Developing physiologically-based toxicokinetic models to assess human exposure to brominated flame retardants and herbicides

A Thesis Submitted in Partial Fulfillment of the Requirements for the Degree of Doctor of Philosophy

By

Alexander Barnabas Cooper MSc

CID: 01037562

Imperial College London

Faculty of Medicine

December 2018

Declaration of Originality

I (Alex Cooper) hereby declare that the work contained within this thesis is my own and that all other work is appropriately referenced.

Copyright Declaration

The copyright of this thesis rests with the author. Unless otherwise indicated, its contents are licensed under a Creative Commons Attribution-Non Commercial 4.0 International Licence (CC BY-NC).

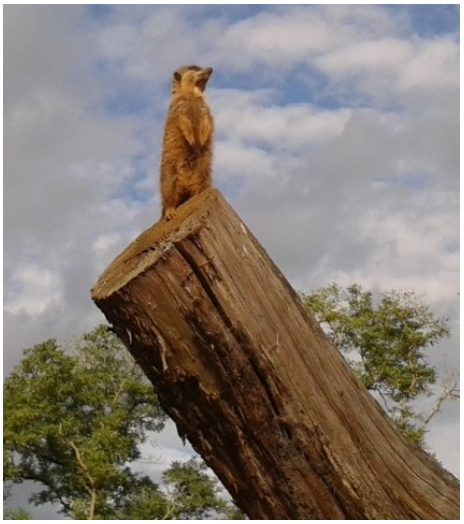
Under this licence, you may copy and redistribute the material in any medium or format. You may also create and distribute modified versions of the work. This is on the condition that: you credit the author and do not use it, or any derivative works, for a commercial purpose.

When reusing or sharing this work, ensure you make the licence terms clear to others by naming the licence and linking to the licence text. Where a work has been adapted, you should indicate that the work has been changed and describe those changes.

Please seek permission from the copyright holder for uses of this work that are not included in this licence or permitted under UK Copyright Law.

Acknowledgements

Special thanks to the Late Dr. Matthew Puncher for the ICRP lung model computer code and uncertainty analysis code. Thanks to Drs. Claire Terry, Manoj Aggarwal, Alistair Morriss and Michael Bartels of Dow AgroSciences for the provision of R&D herbicide reports, analytical samples and review of the paper. Thanks to the 'three Tims': Professor Timothy Gant, Drs. Timothy Ebbels, Timothy Marczylo and also Gwyn Lord for their helpful comments on draft reports and stimulating discussions, and the predoctoral bursary to present at BTS annual congress meetings in Manchester and Liverpool. Many thanks to Public Health England for providing the studentship, and support from NIHR, which made the project feasible and everyone there within the Toxicology department for being so welcoming and supportive throughout, including Nathan, Kirsty and Liz. Lastly, thanks to the meerkats at Beale Park where we did some voluntary work, as they inspired me to keep scanning the horizon.



Publications arising from thesis

Alexander B. Cooper, Manoj Aggarwal, Michael J. Bartels, Alistair Morriss, Claire Terry, Gwyn A. Lord and Timothy W. Gant (2019) PBTK model for assessment of operator exposure to haloxyfop using human biomonitoring and toxicokinetic data. *Regulatory Toxicology and Pharmacology.*

Abstract

Developing physiologically-based toxicokinetic (PBTK) models to assess human exposure to herbicides and brominated flame retardants.

PBTK models are mathematical representations of chemical absorption, distribution, metabolism and excretion (ADME). Each model parameter describes a physiological, physicochemical or biochemical process that affects ADME. Distributions can be assigned to parameters that describe population variability and uncertainty. In this project, PBTK models were developed and calibrated using Bayesian analysis to assess human population exposure to herbicides (picloram and haloxyfop) and a brominated flame retardant (TBBPA). These models allowed assessment of internal exposure at the site of action and therefore an assessment of the risk of toxicity.

For picloram, a rat PBTK model was developed and calibrated. The difference between the predicted and observed toxicokinetic data was interpreted mechanistically leading to transporters being modelled at kidney and liver apical membranes.

For haloxyfop mouse, dog and human PBTK models were built. There were two biologically-plausible approaches to fitting the same toxicokinetic data in the mouse PBTK model, and once extrapolated to humans had different implications for internal exposure assessment. A statistical model was developed to reconstruct operator exposure using experimentally determined LogP, mouse and human toxicokinetic data and human biomonitoring (HBM) data. Of the seven operators, one was calculated to be at potential risk of toxicity from his modelled external and internal exposure levels.

A human PBTK model was constructed for TBBPA (perfusion-limited) and its major metabolite (permeability-limited). Parameter covariance was identified by calibrating the model to human toxicokinetic data. A biomonitoring equivalent (BE) for TBBPA was derived for a hypothetical adult population which was affected by parameter covariance. Comparison of the BE with HBM data suggested low risk of toxicity for individuals with measured TBBPA plasma concentrations.

The findings add to the knowledgebase of PBTK models for use in chemical risk assessment, particularly with regard to the implementation of transporters and the effect of parameter covariance on model extrapolation and prediction.

Table of contents

Declaration of originality……2

Acknowledgements……3

Publications arising from thesis……3

Abstract……4

1.0: INTRODUCTION……18

1.1 Risk assessment and PBTK modelling……18

1.2 An overview of PBTK modelling……20

1.3 Chemicals of a toxicological concern considered in this research project……23

1.3.1 Brominated flame retardants……23

1.3.2 Herbicides……26

1.4 Changes in the exposure assessment of agrochemicals for human risk assessment……29

1.4.1 Modes of toxicity……29

1.4.1.1 Maximum tolerated dose……29

1.4.1.2 From MTD to KMD……31

1.4.2 The utility of TK data in an agrochemical context……32

1.4.2.1 How can TK data reduce uncertainty in chemical risk assessments?……34

1.4.2.2 Regulatory drivers for inclusion of TK……35

1.4.3 Compliance with NC3Rs……36

1.4.4 Use of HBM data to assess exposures……38

1.5 Review of predictive models for pesticide operator exposure used in risk assessment……40

1.5.1 How do the models work?……41

1.5.2 Differences between operator exposure models……42

1.5.3 Passive biomonitoring……44

1.5.4 Relating calculated exposure to risk……45

1.5.5 Risk management……46

1.5.6 Future direction of operator exposure models……48

1.6 Thesis hypothesis and aims……49

2.0: MATERIALS AND METHODS……51

2.1 Bayesian inference……51

2.1.1 Application of Bayesian inference to PBTK modelling……52

2.1.2 Application of MC analysis to PBTK modelling (uncertainty analysis)……55

2.2 LC/MS method development……55

2.2.1 Mass spectrometry method development……55

2.2.2 Liquid chromatography method development……57
2.2.3 Fraction unbound in plasma assay……59
2.2.4 LogP assay……60
3.0: DEVELOPMENT OF PBTK MODELS FOR BFRS AND HERBICIDES (PICLORAM)……61
3.1 Abstract……61
3.2. Introduction……63
3.2.1 Perfusion- and permeability-limited tissue models……63
3.2.2 Gastrointestinal tract models……63
3.2.3 Chapter aims……64
3.2.4 Picloram toxicokinetic data……64
3.3 Methods for constructing PBTK models for herbicides and BFRs……65
3.3.1 Perfusion and permeability-limited tissues……65
3.3.2 Perfusion-limited kidney and liver models……67
3.3.3 Permeability-limited kidney and liver models……69
3.3.4 Gastrointestinal tract (GIT) model……70
3.3.5 Model construction and quality assurance: MCSim vs Gastroplus……72
3.3.6 Preliminary work using picloram toxicokinetic data……74
3.3.6.1 The picloram toxicokinetic data (Nolan *et al.* 1980)……74
3.3.6.2 Preliminary MCMC analysis for model calibration (picloram)……75
3.3.6.3 Sensitivity analyses……76
3.4 Results……77
3.4.1 PBTK model validation……77
3.4.1.1 Perfusion limited model for RBFRs……77
3.4.1.2 Permeability-limited model for herbicides……79
3.4.1.3 Gastro-Intestinal Tract (GIT) model……81
3.4.2 PBTK model calibration and sensitivity analyses (picloram)……84
3.5. Discussion……89
3.5.1 Quality assurance confirms the PBTK models have been accurately coded into MCSim……89
3.5.2 Use of a simplified 4-compartment gut model……91
3.5.3 The PBTK models and risk assessment……92
3.5.4 *In vivo* transporters are present in kidney and possibly liver for picloram……92
3.5.5 PBTK model calibration and sensitivity analyses……93
3.5.6 Summary and conclusions……95
3.5.7 Further work……96

4: DEVELOPMENT OF PBTK MODELS TO ASSESS OPERATOR EXPOSURE TO HALOXYFOP……97
4.1 Abstract……97
4.2 Introduction……99
4.2.1 Toxicology of haloxyfop……99
4.2.2 Mammalian toxicology of haloxyfop……101
4.2.3 Recognised AOEL level……101
4.2.4 Peroxisome proliferation……102
4.2.5 The haloxyfop TK data……104
4.2.6 The Human Respiratory Tract Model (HRTM)……104
4.2.7 Chapter aims……107
4.3 Methods……107
4.3.1 QSAR……107
4.3.2 Construct PBTK model to simulate haloxyfop disposition……108
4.3.3 Metabolite tracking……109
4.3.4 Dermal absorption model……112
4.3.5 Inhalation absorption models……112
4.3.6 Calibration methodology……114
4.3.7 Calibrate model with mouse TK data……115
4.3.8 Calibrate model with dog TK data……116
4.3.9 Extrapolate mouse and dog model to humans……116
4.3.10 Re-calibrate/ validate human model with human TK data……117
4.3.11 Reverse dosimetry with HBM data to populate intake parameters (external exposure assessment)……118
4.3.12 Uncertainty analysis (internal exposure assessment)……119
4.4. Results……119
4.4.1 Mouse PBTK model calibration (approach 1: with optimised fraction bound in liver)……119
4.4.2 Human PBTK model calibration……121
4.4.3 Human reverse dosimetry……123
4.4.4 Reverse dosimetry - uncertainty analysis……125
4.4.5 Octanol: water partition coefficient (haloxyfop-P)……129
4.5. Discussion……130
4.5.1 Different ways of fitting TK data within same species……130
4.5.2 Extrapolating from different species……130
4.5.3 External exposure estimates……131

4.5.4 Parameter correlation……132
4.5.5 Inference of systemic (tissue) exposure……132
4.5.6 Revision to the recognised AOEL?……133
4.5.7 Summary and conclusions……133
4.5.8 Further *in silico* work……134
5.0: DEVELOPMENT OF PBTK WITH STATISTIAL MODELS TO ASSESS OPERATOR EXPOSURE TO HALOXYFOP……135
5.1 Abstract……135
5.2 Introduction……136
5.2.1 Methods of model extrapolation……136
5.2.2 Bayesian statistical models for exposure assessment……137
5.2.3 Chapter aims……138
5.3 Methods……139
5.3.1 PBTK model……139
5.3.2 Statistical models……141
5.3.3 Selection of priors……143
5.3.4 MCMC convergence……145
5.3.5 Rat toxicokinetic data (Smith *et al.* 1982)……149
5.4 Results……150
5.4.1 Mouse-human model extrapolation……150
5.4.1.1 Liver transporter activity……150
5.4.1.2 Systemic exposure estimates……151
5.4.1.3 Sensitivity analysis……152
5.4.1.4 Prior and posterior distributions……153
5.4.2 Rat model calibration……156
5.5. Discussion……160
5.5.1 Mouse-human model calibration……160
5.5.1.1 Liver transporter activity……160
5.5.1.2 Systemic exposure estimates……161
5.5.1.3 Sensitivity analysis……161
5.5.1.4 Prior and posterior distributions……162
5.5.2 Rat calibration……163
5.5.3 Summary and conclusions……164
5.5.4 Further work……164

6.0: DERIVATION OF A BIOMONITORING EQUIVALENT FOR TETRABROMOBISPHENOL A (TBBPA)……165
6.1 Abstract……165
6.2 Introduction……166
6.2.1 Widespread use and occurrence of TBBPA……166
6.2.2 Toxicity of TBBPA……168
6.2.3 Toxicokinetics of TBBPA……169
6.2.4 Biomonitoring equivalents……171
6.2.5. Chapter aims……172
6.3 Methods……173
6.3.1 The human toxicokinetic data……173
6.3.2 PBTK model and calibration……174
6.4 Results……178
6.4.1 *In vitro* data……178
6.4.2 PBTK model calibration……179
6.4.3 Analysis of parameter covariance……183
6.4.4 Model extrapolation to steady-state……185
6.4.5 Calculation of the biomonitoring equivalent at steady-state……186
6.4.6 Review of HBM data for TBBPA……187
6.5 Discussion……189
6.5.1 PBTK model calibration……189
6.5.2 Analysis of parameter covariance……190
6.5.3 Model extrapolation to steady-state……191
6.5.4 Calculation of the biomonitoring equivalent at steady-state……191
6.5.5 Review of HBM data for TBBPA……192
6.5.6 Summary and conclusions……193
6.5.7 Further work……193
7.0: GENERAL DISCUSSION……195
7.1 Background to current research……195
7.2 How research questions have been addressed……196
7.3 Findings from research conducted……197
7.4 Further work……198
7.5 Summary……199

References……201
Appendix 1: Model equations……226
Appendix 2: Glossary of terms……235
Appendix 3: Visual overview of PBTK model calibration process using MCMC……238
Appendix 4: Adverse effect levels relevant to risk assessment……240
Appendix 5: The haloxyfop toxicokinetic and HBM data……241
Appendix 6: Correlation matrices of PBTK model parameters (chapter 5)……244
Appendix 7: PBTK model computer code to simulate toxicokinetics of TBBPA……246
Appendix 8: Permissions to reprint third-party extracts……270

List of Tables

TABLE 1.1: Common and trade names of three herbicides……27

TABLE 1.2: Chronic dietary risk for picloram, triclopyr and haloxyfop-methyl for whole U.S. population……28

TABLE 1.3: Factors affecting operator exposure and corresponding exposure reduction measures…47

TABLE 2.1: Optimisation of ionisation conditions for several RBFRs and haloxyfop……56

TABLE 2.2: MS Detection of RBFR and haloxyfop ions following ionisation……57

TABLE 3.1: *In silico* predictions for physicochemical parameters for BFRs and herbicides……73

TABLE 3.2: Perfusion-limited tissue model with IV route after 30-hour simulation (discrepancy with GastroPlus)……77

TABLE 3.3: Permeability-limited tissue model with IV route after 10-hour simulation (discrepancy with GastroPlus)……80

TABLE 3.4: Discrepancy between GastroPlus and MCSim using 'unidirectional' gastro-intestinal tract model coupled with the perfusion/ permeability-limited model for EBTBPE/ picloram……82

TABLE 3.5: Discrepancy between GastroPlus and MCSim using 'concentration gradient' gastro-intestinal tract model……83

TABLE 3.6: Optimised parameter values for PBPK model with picloram data……88

TABLE 4.1: Haloxyfop products……100

TABLE 4.2: The haloxyfop toxicokinetic (TK) data……104

TABLE 4.3: *In silico* predictions for physicochemical parameters for haloxyfop-P and its glucuronide conjugate (species-unspecific)……110

TABLE 4.4: Estimates for 'fraction absorbed through skin' (Fa_skin)……123

TABLE 4.5: Optimised parameter values for PBPK model with haloxyfop data (approach 1)……128

TABLE 5.1: Prior and posterior distributions for species non-specific model parameters (in natural space)……153

TABLE 5.2: Prior and posterior distributions for mouse-specific model parameters (in natural space)……154

TABLE 5.3: Prior and posterior distributions for human-specific model parameters (in natural space)……155

TABLE 6.1: *In silico* predictions for physicochemical parameters for TBBPA and its glucuronide conjugate (species-unspecific)……178

TABLE 6.2: Prior and posterior distributions for biochemical/ physicochemical PBTK model parameters (in natural space)……181

TABLE 6.3: Prior and posterior distributions for PBTK model parameters (in natural space)……182

TABLE 6.4: Correlation matrix of selected human biochemical and physicochemical PBTK model parameters……183

TABLE 6.5: Correlation matrix of fractional tissue and organ volume variability……184

TABLE 6.6: Correlation matrix of fractional tissue and organ blood flow rate variability……185

APPENDIX TABLE 4.1: Adverse effect levels for haloxyfop-methyl ester relevant to risk assessment……240

APPENDIX TABLE 6.1: Correlation matrix of mouse-human PBTK model parameters……244

APPENDIX TABLE 6.2: Correlation matrix of rat PBTK model parameters……245

List of Figures

FIGURE 1.1: Whole-body PBTK model……22

FIGURE 1.2: Chemical structure of PBBs……23

FIGURE 1.3: Chemical structures of several RBFRs……25

FIGURE 1.4: Chemical structures of several herbicides……27

FIGURE 1.5: Paradigm shift in the way toxicological dose-response analysis is performed……31

FIGURE 1.6: Derivation of chemical-specific adjustment factors (CSAFs) from the original 100 x uncertainty factor for use in risk assessment……35

FIGURE 1.7: Proposed changes to the modelling approach to refine the chemical risk assessment of pesticide operators……48

FIGURE 2.1: Representative LC/ MS calibration graphs for TBBPA and haloxyfop……58

FIGURE 2.2: HPLC gradient elution profiles for TBBPA and haloxyfop……58

FIGURE 3.1: Model for perfusion-limited tissues……66

FIGURE 3.2: Model for permeability-limited tissues……67

FIGURE 3.3: Model for perfusion-limited kidney……67

FIGURE 3.4: Model for perfusion-limited liver……68

FIGURE 3.5: Model for permeability-limited kidney……69

FIGURE 3.6: Model for permeability-limited liver……70

FIGURE 3.7: Concentration gradient gastro-intestinal tract model……72

FIGURE 3.8: Predicted plasma EBTBPE concentration in F344 rat following 14 mg/ Kg iv bolus dose of EBTBPE……78

FIGURE 3.9: Predicted adipose, liver and brain concentrations, and amount excreted in rat for following 14 mg/ Kg iv bolus dose of EBTBPE……79

FIGURE 3.10: Predicted adipose and brain concentrations for picloram (following 14 mg/ Kg iv bolus dose) in F344 rat……81

FIGURE 3.11: GastoPlus vs MCSim: gut lumen concentrations following oral solution ('concentration gradient' model)……84

FIGURE 3.12: MCSim simulation (perfusion-limited model) with high iv dose of 160 mg/ Kg and low iv dose of 14 mg/ Kg……85

FIGURE 3.13: MCSim simulation (permeability-limited model) and picloram data with intravenous dose……86

FIGURE 3.14: MCSim simulation (permeability-limited) and picloram data with an oral dose……86

FIGURE 3.15: Cumulative amount in urine following 9.6 and 1634 mg / Kg oral dose……87

FIGURE 3.16: Prior and posterior distributions for permeability of gastrointestinal tract……89

FIGURE 4.1: Terminology of the haloxyfop variants……100

FIGURE 4.2: Disposition model for HRTM……105

FIGURE 4.3: Dissolution model for HRTM……106

FIGURE 4.4: Overview of workflow for modelling chemical exposure in human health risk assessment……108

FIGURE 4.5: Liver model with metabolite tracking……111

FIGURE 4.6: Model for permeability-limited skin……112

FIGURE 4.7: Adapted HATM model……113

FIGURE 4.8: MCSim simulation (permeability-limited) of mouse toxicokinetic data……120

FIGURE 4.9: MCSim simulation (permeability-limited) of human toxicokinetic data……122

FIGURE 4.10: Reverse dosimetry with scaled human model for assessment of operator exposure..124

FIGURE 4.11: Assessment of maximum tissue exposure for operator G.B. following occupational exposure to haloxyfop-methyl ester……126

FIGURE 4.12: Assessment of maximum systemic (internal) exposure following occupational exposure to haloxyfop-methyl ester……127

FIGURE 4.13: Octanol: water partition coefficient (LogP) assay for haloxyfop-P……129

FIGURE 5.1: Revised liver model……140

FIGURE 5.2: Schematic of enterohepatic recirculation……141

FIGURE 5.3: Hierarchical model for separation of model parameter uncertainty and variability……145

FIGURE 5.4: Statistical model for analysis of mouse/ human toxicokinetic data and human biomonitoring data……146

FIGURE 5.5: Statistical model for analysis of dog/human toxicokinetic and HBM data……147

FIGURE 5.6: Statistical model for analysis of rat toxicokinetic data……148

FIGURE 5.7: Assessment of liver transporter activity in calibrated mouse and human models (apical and basolateral membranes)……150

FIGURE 5.8: Assessment of maximum systemic (internal) exposure following occupational exposure to haloxyfop-methyl ester……151

FIGURE 5.9: Sensitivity analysis of human PBPK model parameters……152

FIGURE 5.10: MCSim simulation (permeability-limited) of female rat toxicokinetic data……156

FIGURE 5.11: MCSim simulation (permeability-limited) of male rat toxicokinetic data……157

FIGURE 5.12: MCSim simulation (permeability-limited) of rat toxicokinetic data……158

FIGURE 5.13: Maximum transporter velocity in rats……159

FIGURE 6.1: Interplay of processes in the GI tract and liver which influence TBBPA toxicokinetics…175

FIGURE 6.2: *In vitro* fraction of TBBPA unbound in human plasma samples……179

FIGURE 6.3: Calibration of the human PBTK model to suitable toxicokinetic data following a single oral dose of 0.1 mg/ Kg……180

FIGURE 6.4: Temporal extrapolation of the calibrated human PBTK model for TBBPPA……186

FIGURE 6.5: Assessment of human plasma TBBPA concentration at steady-state……187

FIGURE 6.6: Review of worldwide human biomonitoring data available for TBBPA……188

APPENDIX FIGURE 3.1: Visual overview of PBTK model calibration process using MCMC……238

APPENDIX FIGURE 3.2: Data visualisation for distributions……239

APPENDIX FIGURE 5.1: Uncertainty analysis of urinary excretion of haloxyfop-P with human PBTK model, calibrated with HBM data……243

List of Abbreviations

ACAT - Advanced compartmental absorption and transit model

ADME - Absorption, distribution, metabolism and excretion

AOEL - Acceptable operator exposure limit

AOEM - Agricultural operator exposure model

BE - Biomonitoring equivalent

BEHTBP - Bis(2-ethyl-1-hexyl)tetrabromophathlate

BFR - Brominated flame retardant

BTBPE - 1,2-Bis(2,4,6-tribromophenoxy)ethane

CF - Composite factor

CSAF - Chemical-specific adjustment factor

DAS - Dow AgroSciences

DBDPE - 1,2-Bis(pentabromophenyl)ethane

EBTBPE - N,N-ethylene bis-(tetrabromophthalimide)

EHC - Enterohepatic circulation

EUROPOEM - European predictive operator exposure model

FUp - Fraction unbound in plasma

GIT - Gastrointestinal tract

HATM - Human alimentary tract model

HBM - Human biomonitoring

HRTM - Human respiratory tract model

Km - Substrate concentration when Vmax is halved (Michaelis-Menten parameter)

KMD - Kinetically-derived maximum dose

Kp - Tissue partition coefficient

LOAEL - Lowest observable adverse effect level

LogP - Octanol/ water partition coefficient

MC - Monte Carlo

MCMC - Markov Chain Monte Carlo

MCSim - Monte Carlo simulation (software)

MTD - Maximum tolerated dose

NC3Rs - National Centre for the Replacement, Refinement and Reduction of Animals in Research

NOAEL - No observable adverse effect level

PBS - Phosphate buffered saline

PBTK - Physiologically based toxicokinetic

Peff - Effective gut permeability

PHED - Pesticide handlers' exposure database

POEM - Predictive operator exposure model

PStc - Permeability-surface area product

RBFRs - Replacement brominated flame retardants

Rbp - Blood/ plasma concentration ratio

RED - Rapid equilibrium dialysis

RfD - Oral reference dose

SF - Safety factor

TBBPA - Tetrabromobisphenol A

TD - Toxicodynamic(s)

TK - Toxicokinetic(s)

TMRC - Theoretical maximum residue concentration

Chapter 1: General Introduction

1.1 Risk assessment and PBTK modelling

Chemical risk assessments are necessary to protect public health. Risk assessment is the process of determining and quantifying harmful effects to humans caused by hazardous substances and activities involving exposure (McClellan 1999). In addition to human health, possible environmental impacts should also be considered (e.g. water contamination), which may indirectly harm human health. Risk assessment is done to establish acceptable human exposure levels, and to assess the health risks associated with particular exposure scenarios. Risk assessment requires an understanding of both the hazard characteristics of the chemical and exposure. It is in exposure analysis that PBTK modelling has an important role to play (Section 1.2). Making a chemical risk assessment requires a multidisciplinary approach that considers hazard, dose-response analysis and exposure (see below). Ultimately, risk assessment allows appropriate precautions to be implemented for the prevention or mitigation of harm.

1) Hazard

A hazard is something which has the potential to harm health, thus the assessment of chemical hazards is a toxicological assessment. Mechanisms of toxicity might be known which provide an understanding of how the chemical harms health and can be important in making cross-species comparisons. Haloxyfop, for example, binds the PPARα receptor as an agonist in mice resulting in peroxisome proliferation causing hypertrophy, hyperplasia and promotion of carcinogenesis (chapter 4). Mechanisms of action can be species-specific due to differences in physiology and biochemistry. Therefore, if toxicity is observed in animals through a particular mechanism, it is not necessarily relevant to human health. Indeed, the expression level of PPARα in humans is very low, thus humans are relatively insusceptible to the peroxisome proliferating effects of haloxyfop. Thus,

at a sufficient dose, toxicity in humans will likely occur through a different mechanism for example involving an oxidative stress pathway.

2) Dose-response relationships

An understanding of the dose-response relationship is helpful for quantifying the chemical's potential for causing harm. If the dose-response is non-linear and exhibits a threshold, then doses below this will not elicit toxicity (the dose would not pose a risk); these are sometimes called 'threshold chemicals'. Many non-genotoxic chemicals exhibit a threshold, whereas genotoxic chemicals are usually considered to exhibit a more linear dose-response where there is no threshold. Thus there would almost always be potential for genotoxicity irrespective of the exposure level. Reference doses such as NOAELs and LOAELs can help characterise the relationship between dose and response; this is usually done in rodents through animal testing. However the precise relationship between dose and response varies between individuals and species. Factors like genetics, age health status and environmental influences can affect an individual's physiology and biochemistry, and hence affect ADME causing different sensitivities to toxicity. For this reason, where the impact of the variability and uncertainty of these factors on toxicological response is unknown, safety factors are used. These are applied to the NOAEL derived from animal studies in order to calculate the reference dose in humans. One safety factor (x 10) is for interspecies differences in ADME and the other (x 10) is for intraspecies differences (variability) in humans.

3) Exposure

Chemical exposure to humans can occur through certain activities associated with the use of the chemical or by accidental exposure, often called bystander exposure. External and internal exposure can be calculated from human biomonitoring data obtained from accessible human samples such as urine or blood, using PBTK models, in a process called 'reverse dosimetry' or 'exposure

reconstruction' (Section 2.1). These models can be used to take account of multiple routes of exposure as they occur in real life scenarios.

PBTK models can be used to calculate 'biomonitoring equivalents'. If an external reference dose is known (e.g. NOAEL or LOAEL), then corresponding tissue concentrations and/or urinary excretion rates can be calculated (Poddalgoda *et al.* 2016). This can be done in humans to assist a chemical risk assessment if HBM data is currently unavailable.

For PBTK modelling, there are some commercial PBTK software packages available such as Simulations Plus™. These packages though often have limitations. For example, Simulations Plus™ is currently unable to simulate multi-route exposures, or perform exposure reconstruction (Simulations Plus 2013). In this work, some of these limitations were overcome for example by coding from Simulations Plus™ into MCSim. MCSim in an open source modelling package that allows Bayesian inference via Markov Chain Monte Carlo simulation. These models can be used to assess chemical exposure which can then be compared to reference doses in order to perform risk assessments.

1.2 An overview of PBTK modelling

Paracelsus (1493-1541) stated that 'all things are poison, and nothing is without poison: the dose alone makes a thing not a poison'. This became the foundation of modern toxicology: 'the dose makes the poison', i.e. toxicity is simply a response to the exposure dose. 'Tissue dose', the concentration of an exposure chemical or its metabolites at target tissues, can be predicted over time (in a process called forward dosimetry) using PBTK models. These are mathematical representations of the processes affecting a chemical's *in vivo* toxicology: absorption, distribution, metabolism and excretion (ADME). These processes are represented by a series of differential equations that are functions of model parameters. The equations describe the rate of change in the amount of a chemical in target organs and blood. To calculate tissue dose over a specified time

period, all differentials are solved simultaneously by integration, which typically must be performed numerically using appropriate software. Subsequently, target tissue dose can be linked to an adverse tissue response. Each parameter in a PBTK model describes a physiological (e.g. ventilation rate), physicochemical (e.g. gut permeability) or biochemical (e.g. metabolic Vmax) process. These properties distinguish PBTK models from more empirical compartment models permitting the following:

- PBTK models can be used to extrapolate toxicokinetic differences within and across species (Wang *et al.* 2000) resulting in greater predictive capability. Consequently, a model can be built using *in vivo* animal data and then mapped onto an equivalent human PBTK structure. This model would use human-specific physiological parameter values and, where appropriate, scaled adjusted biochemical values.
- Distributions can be assigned to each parameter to reflect inter-individual natural variation (Bois *et al.* 2010) and uncertainty regarding the actual population mean value. This means that tissue doses (and possibly levels of toxic response) can be modelled in the target population. Thus, human PBPK models can be built for a population of interest allowing risk assessments to be made on a case-by-case basis.
- The one-to-one correspondence between model parameters and toxicokinetic processes means that many physicochemical and biochemical parameter values of PBTK models can be determined from *in vitro* data.
- Bayesian inference can be used to calibrate the model and also to estimate external exposure and internal doses from human biomonitoring (HBM) data (Section 2.1).

Figure 1.1 gives an example of a PBTK model with target tissue metabolism. The tissues can be modelled as either perfusion-limited (i.e. the rate of uptake into tissues limited by blood flow), suitable for lipophilic compounds, or permeability-limited (i.e. rate of uptake limited by relatively slow permeability across tissue membrane), suitable for non-lipophilic compounds.

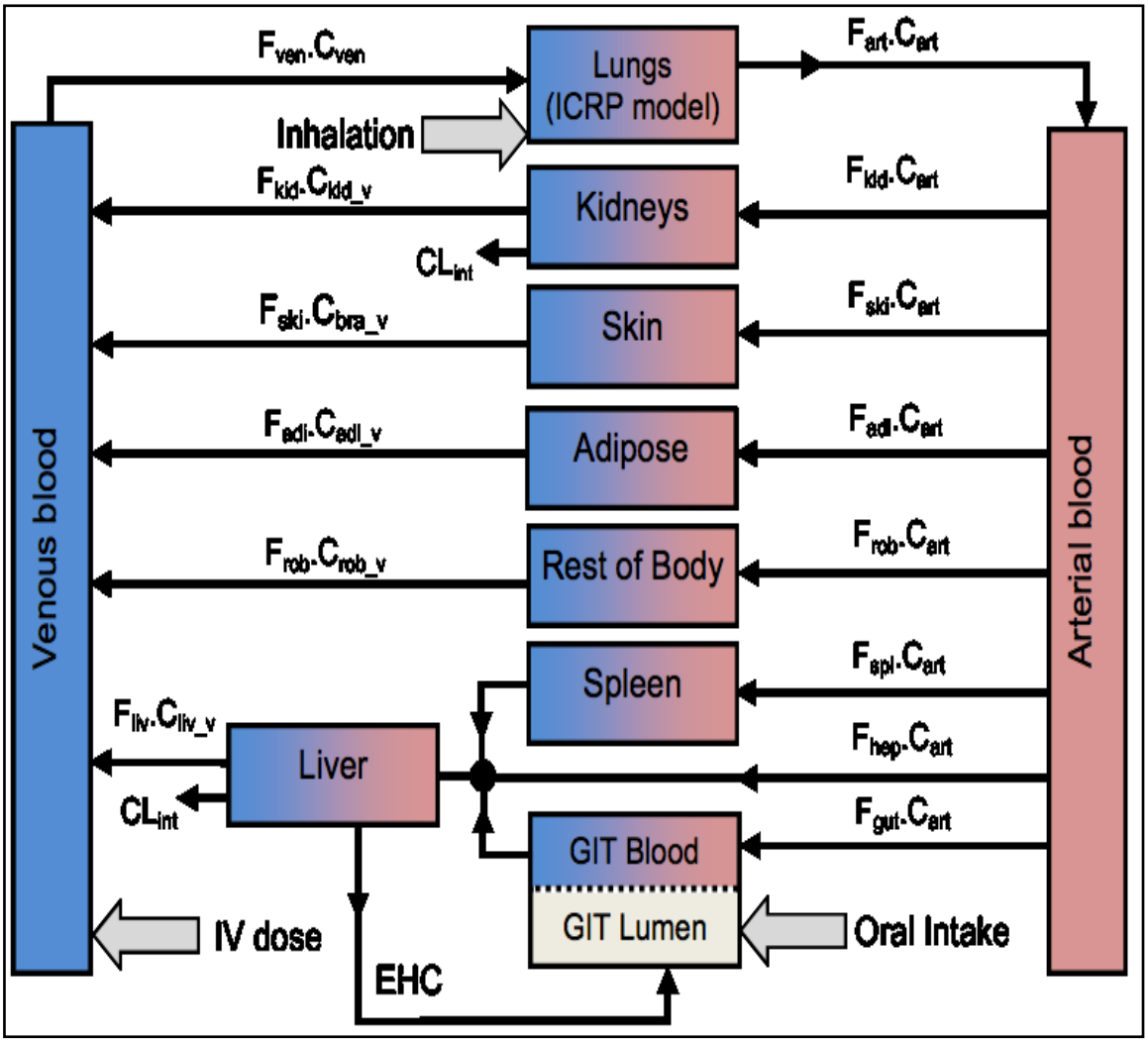


Figure 1.1: Whole-body PBTK model. In this model, intake can occur through the oral, intravenous (IV) or inhalation route. A 'rest-of-body' compartment is used to lump all *in vivo* tissues not modelled. The model structure can be mapped onto humans or animals as required. PBTK model structure adapted from Simulations Plus (2013b).

1.3 Chemicals of a toxicological concern considered in this research project

1.3.1 Brominated flame retardants

Brominated flame retardants (BFRs) are structurally diverse chemicals that contain bromine. Bromine is electrophilic, and accepts electrons from reactive oxygen species that are required for combustion (Kasperma *et al.* 2002). BFRs are incorporated into plastics, foams and fabrics either through covalent binding (e.g. Tetrabromobisphenol A, TBBPA) or addition (e.g. polybrominated -biphenyls/ diphenyl ethers PBBs, PBDEs) to reduce their flammability.

There are 209 possible PBB cogeners (ATSDR 1999) which arise due to different numbers and arrangements of Br atoms around connected benzene rings (Figure 1.2). Bromine at positions 2, 2', 6, and 6' cause bridge rotation making these cogeners non-planar. Most cogeners have unknown toxicology. However, those that are planar can be anticipated to be agonists of the aryl hydrocarbon receptor (AhR).

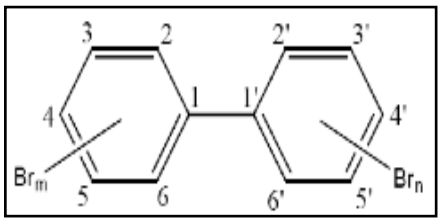


Figure 1.2: Chemical structure of PBBs. Their low vapour pressure and water solubility further decrease as the bromine content increases. Br_m = 1-5, Br_n = 0-5.

There is evidence that PBBs are carcinogenic (NTP 1993). Because a threshold PBB concentration is apparently required for carcinogenesis, a non-genotoxic (possibly epigenetic) mechanism is speculated (IPCS/WHO 1994). Planar/ non-planar cogeners might elicit toxicity through binding aryl hydrocarbon (Brown *et al.* 2004) and constitutive androstane (CAR) (Sakai *et al.* 2009) receptors respectively, thereby inducing gene expression. Thus planar PBBs might behave like dioxin (TCDD) the model AhR agonist, and non-planar PBBs like phenobarbitone the model CAR agonist.

The UK population is continuously exposed to BFRs present in clothes, furniture, flooring, electronic equipment and building insulation (Stuart *et al.* 2008, Besis & Samara 2012). Thus domestic exposure via the dermal route is expected. However, BFRs preferentially partition into dust due to their low vapour pressure (Law *et al.*, 2014). Consequently, an additional route of domestic exposure can be via the lung from dust inhalation (Kefeni *et al.* 2014). BFRs have the potential to bioaccumulate in wildlife and humans due to their lipophilicity (Hites 2004, Schecter *et al*. 2005, Weijs *et al.* 2012). Subsequently, BFRs occur in food of animal origin (Schecter *et al.* 2008), and PBDE transmission occurs via breast feeding (Carrizo *et al.* 2007, Bramwell *et al.* 2014). As a result, the use of pentaBDE, octaBDE (EU 2004), decaBDE (EU 2008a) and all PBBs and PBDEs in electronic and electrical equipment (EU 2002) is now banned within the European Union and pentaBDE, octaBDE and decaBDE have been added to the Stockholm Convention on Persistent Organic Pollutants. However, replacement brominated flame retardants (RBFRs) are being used although their toxicology is poorly defined. Important examples to be investigated in this project include 1,2-Bis(pentabromophenyl)ethane (DBDPE), N,N-ethylene bis-(tetrabromophthalimide) (EBTBPE), 1,2-Bis(2,4,6-tribromophenoxy)ethane (BTBPE), Bis(2-ethyl-1-hexyl)tetrabromophathlate (BEHTBP) and Tetrabromobisphenol A (TBBPA) (Figure 1.3).

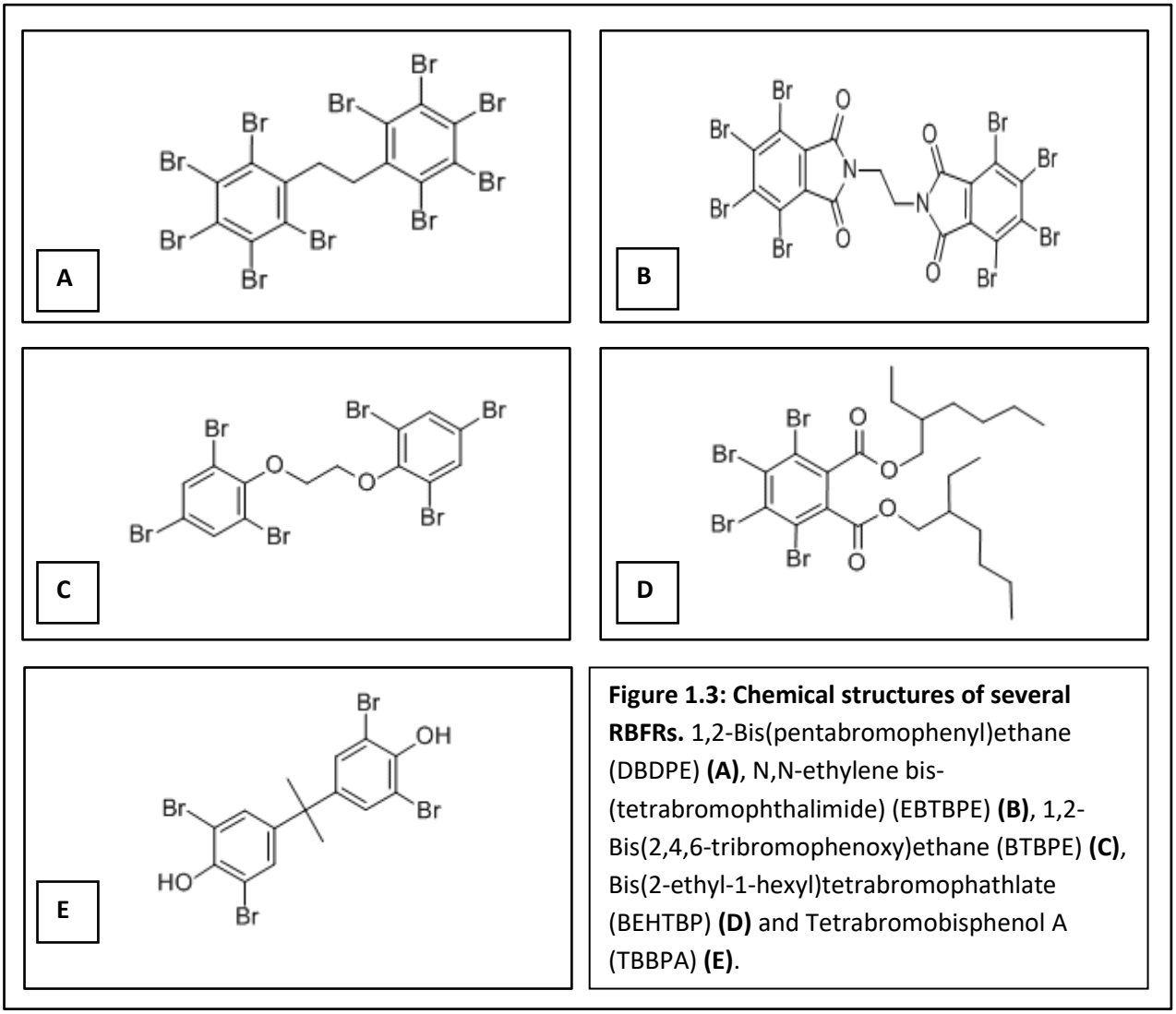


Figure 1.3: Chemical structures of several RBFRs. 1,2-Bis(pentabromophenyl)ethane (DBDPE) **(A)**, N,N-ethylene bis-(tetrabromophthalimide) (EBTBPE) **(B)**, 1,2-Bis(2,4,6-tribromophenoxy)ethane (BTBPE) **(C)**, Bis(2-ethyl-1-hexyl)tetrabromophathlate (BEHTBP) **(D)** and Tetrabromobisphenol A (TBBPA) **(E)**.

This selection is based on level of industrial production, environmental and domestic occurrence, persistence, bioavailability and possible toxicity (Covaci *et al.* 2011). Their toxicology and human exposure levels are largely unknown. DBDPE and EBTBPE are probably resistant to metabolism as relatively non-reactive functional groups are present at all molecule positions where oxidative metabolism (phase 1) might otherwise occur. BTBPE and BEHTBP could be metabolised by phase 1 and phase 2 enzymes, and TBBPA is likely to be predominantly metabolised by phase 2 enzymes. Thus, in addition to their relevance to human exposure and possible health detriment, these chemicals provide a range of complexity in terms of their metabolic profiles that are of interest from a physiologically-based toxicokinetic (PBTK) modelling perspective.

1.3.2 Herbicides

Herbicides are chemicals capable of severely injuring or killing plants. In addition to agricultural use herbicides are used in industrial and domestic settings. Herbicides can be classified according to their mechanism of action, for example 1) mitosis inhibitors (fosamine), 2) photosynthesis inhibitors (hexazinone), 3) amino acid synthesis inhibitors (glyphosate), 4) lipid synthesis inhibitors (haloxyfop) and 5) auxin mimics (picloram and triclopyr). Haloxyfop inhibits acetyl-CoA carboxylase (ACCase) which suppresses *de novo* synthesis of fatty acids in weeds. Auxin mimics are pyridine (C_5H_5N) derivatives, which are structurally analogous to auxin the plant growth hormone, and subsequently elicit uncontrolled lethal growth in target plants. Selectivity of auxin mimics towards weeds over broadleaf crops (e.g. soybeans and sugar beets) is achieved through exploiting their physiological differences: 1) weed growth is reliant on auxin whereas grass growth is not, and 2) weeds generally have greater leaf surface areas than grasses resulting in greater absorption of the herbicide into weeds (Klassen 2008).

Picloram, triclopyr and haloxyfop are sold by Dow AgroSciences (DAS) (Table 1.1 & Figure 1.4). The U.S. EPA considers a minimal chronic dietary risk from food sources containing picloram (U.S. EPA 1995) and triclopyr (U.S. EPA 1998). Although these pesticides have been registered for application on a number of food crops, they have low toxicity profiles and estimated exposures from the diet (Table 1.2). The TMRC values of picloram and triclopyr comprise only 0.9 % and 0.8 % of their reference doses (RfD), respectively, indicating minimal risk of toxicity for the general U.S. population. There is occupational exposure risk for mixers, loaders and applicators of these herbicides through dermal and inhalation routes. Thus the EPA has conducted exposure assessments for herbicide handlers (U.S. EPA 1995, 1998). Regarding inhalation exposure a permissible exposure limit (PEL) of 5 mg/ m^3 (8 hours; respirable fraction) is set for picloram (U.S. OSHA 1994). However, no PELs or threshold limit values (TLVs) have yet been set for triclopyr or haloxyfop-methyl. Registration for

haloxyfop-methyl in the U.S. has so far been unsuccessful (U.S. EPA 2018), which might be due to concerns regarding its observed toxic effects (Appendix Table 4.1). However, foods containing haloxyfop residues are imported from other countries where haloxyfop is registered for use such as New Zealand, China and Brazil (DAS 2018). Thus, a TMRC could be calculated for this herbicide in the U.S. to assess the health risk to consumers of these imported food products.

Table 1.1: Common and trade names of three herbicides.

Common name	Active compounds	Trade names
Picloram	4-amino-3,4,5-trichloropicolinic acid (ATCP)	Tordon®
Triclopyr	3,5,6-Trichloro-2-pyridinyloxyacetic acid N.b. sold as triclopyr triethylamine salt (TEA) or triclopyr butoxyethyl ester (BEE)	USA: Garlon® and Release® UK: SBK®
Haloxyfop	Haloxyfop-ethoxyethyl, haloxyfop-P-methyl ester, haloxyfop-P	Verdict®, Gallant®, Zellek®, Dowco 453 ME® (haloxyfop methyl) and Dowco 453 EE® (haloxyfop ethoxyethyl)

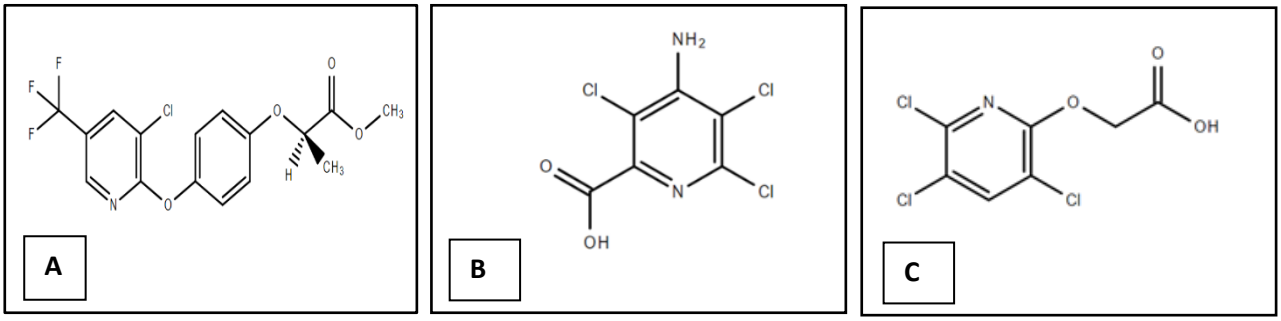


Figure 1.4: Chemical structures of several herbicides. Haloxyfop-methyl ester (R isomer) **(A)**, Picloram **(B)** and Triclopyr **(C)**.

Table 1.2: Chronic dietary risk for picloram, triclopyr and haloxyfop-methyl for the whole U.S. population.

Herbicide	RfD (mg / Kg / day)	TMRC (mg / Kg / day) †	LOAEL (mg / Kg / day)	Effect at LOAEL	Ref.
Picloram	0.2	1.845×10^{-3} (0.92% of RfD)	60	2-year feeding study: increased size and altered tinctorial properties of centrilobular hepatocytes, and increased absolute and/ or relative liver weights in male and female F344 rats	U.S. EPA 1995
Triclopyr	0.05	0.405×10^{-3} (0.81% of RfD)	25	2-generation reproduction study: increased incidence of proximal tubular degeneration of kidneys in male and female P1 & P2 parental F344 rats	U.S. EPA 1998
Haloxyfop-methyl	5×10^{-5}	Not available	0.05	3-generation F344 rat reproduction study: reduced relative kidney weights in F0, F1 and F2b adults. Reduced fertility in F1/ F2b generation.	Jeffries *et al.* 1985

RfD: reference dose; the estimated daily oral exposure level to the human population unlikely to cause deleterious effects during one's lifetime. It is 100 times below the dose causing no observable adverse effect (**NOAEL**) (U.S. EPA 2011). This uncertainty factor accounts for intraspecies variability (x 10) and interspecies extrapolation (x 10). **TMRC:** theoretical maximum residue concentration; the amount in an average person's daily diet, assuming the diet consists of food items containing herbicide residues (U.S. EPA 2011). **LOAEL:** lowest observable adverse effect level. **†** Considering food only.

Chemical risk assessments do not routinely evaluate internal dose. However, it relates more directly (temporally and spatially) to a toxicological response than external dose does and thus provides a better basis for the evaluation of risk. Furthermore, computational approaches can be applied to estimate external dose with systemic exposure data, such as picloram plasma toxicokinetic data from human volunteers (Nolan *et al.* 1983). Also, and of particular interest to DAS, is to use a computational approach to infer external and internal doses from urine biomonitoring data that result from occupational exposure. Such a method provides enhanced understanding from less monitoring or monitoring that is not possible (internal dose at the site of action). This provides an integrated framework for risk assessment centred more on systemic dose and toxicokinetics rather

than external exposure. These computational approaches can be addressed through PBTK modelling (Section 1.2).

1.4 Changes in the exposure assessment of agrochemicals for human risk assessment

There are several paradigm shifts occurring in the risk assessment of agrochemicals: focus on 'modes of toxicity', compliance with NC3Rs, and greater use of human biomonitoring (HBM) data to assess chemical exposures.

1.4.1 Modes of toxicity

A chemical's mechanism of toxicity can change at different dose levels, and overt toxicity can sometimes be the outcome of a number of key events. Understanding these events is central to the concept of 'modes of toxicity' for which there is growing awareness. Indeed, various initiatives have attempted to implement modes of toxicity into risk assessment, so that the relevance of findings from animal studies to humans can be better understood (Boobis *et al.* 2006, 2008). This involves characterising dose-response relationships where possible with a greater focus on 'internal dose' and 'early biological effects' (key events) (Slikker *et al.* 2004a,b, Rhomberg *et al.* 2007).

1.4.1.1 Maximum tolerated dose

Toxicology has traditionally been the science of poisoning, and the primary focus has therefore been on hazard identification such as alterations in body weight or target organ toxicity. This kind of outlook inspired the concept of the maximum tolerated dose (MTD). The MTD is traditionally used in chronic toxicity studies in both the pharmaceutical and non-pharmaceutical sectors in order to conduct safety assessments. It is defined as the external dose which produces an 'acceptable' level of observable toxicity in animals to assist hazard identification, but does not induce mortality thereby jeopardising the study. Testing at a dose that induces toxicity is a regulatory requirement specified in OECD test guidelines (OECD 2016).

The MTD is generally used as a top dose in chronic bioassays such as those performed by the National Toxicology Program (NTP), with lower doses at 50 % and 25 % of the MTD. It is argued that high MTD doses are needed to maximise the chances of detecting chronic toxicity, such as carcinogenesis, using a limited number of animals. However, it may not be suitable to extrapolate these toxic effects to humans, due to dose-dependent transitions in mechanisms of toxicity and/or non-linear toxicokinetic (TK) processes at such high doses causing the observed toxicity that are irrelevant to lower levels of expected human exposure (Counts & Goodman 1995, Slikker *et al.* 2004b, Barton *et al.* 2006, OECD 2010b). At low doses, above threshold effect, one anticipates a linear relationship between dose and systemic exposure. However, as doses increase toward the MTD, this linear relationship can collapse due to the induction, alteration or saturation of processes involved in ADME of the compound. For example, if enzymes involved in metabolism become saturated, then systemic exposure of the parent compound may increase disproportionally with small increases in dose, compared with lower overall doses. Alternatively, systemic exposure may plateau with increasing dose, due to saturation of intestinal absorption for example. In this case, damage might occur to the intestinal epithelium due to prolonged contact with unabsorbed test material although this toxicity may be irrelevant to levels of expected human exposure.

The paradigm shift is moving away from the MTD (and non-linear TK) and towards the establishment of a dose-response relationship at the kinetically-derived maximum dose (KMD, Section 1.4.1.2) which allows the extrapolation of findings to more relevant levels of expected human exposure (Saghir *et al.* 2011). As a consequence of better dose selection, animal tests used to investigate toxic effects at the MTD are no longer required, and those animals used for testing receive a lower dose and are therefore less likely to suffer. These factors represent a reduction and refinement in the use of animals in research, respectively.

1.4.1.2 From MTD to KMD

The concept of 'bioavailability' means that, for various reasons, only a portion of the external dose will be 'available' systemically. Thus, it is easier to relate an internal toxicological response with systemic exposure rather than external exposure (Saghir *et al.* 2006). Therefore, knowledge of systemic exposure better supports understanding of early biological effects for human safety assessment (Figure 1.5). The challenge here though is to understand the level of internal exposure. External exposure can generally be measured easily, internal exposure at most sites less so. However, knowledge of systemic exposure (and how it relates to external dose) can be achieved through the acquisition of TK data (at levels relevant to human exposure) and PBTK modelling.

The KMD is based on the premise that the induction of non-linear TK can be used as an equivalent indicator of biological stress alongside other traditional toxicity endpoints such as tumour formation. The KMD is defined as the top external dose level for use in toxicology studies and corresponds to the 'inflection point' of non-linear TK in repeat-dose studies. The selection of a KMD has been suggested by Barton *et al.* 2006 and Saghir *et al.* 2006 as preferable to the MTD, provided the derived KMD has an adequate margin of exposure over likely human exposures, and the normal physiology of an appropriate test animal is not greatly compromised. Indeed, regulatory authorities could abolish the requirement to demonstrate marked overt toxicity in animal toxicology studies and encourage wider use of the KMD.

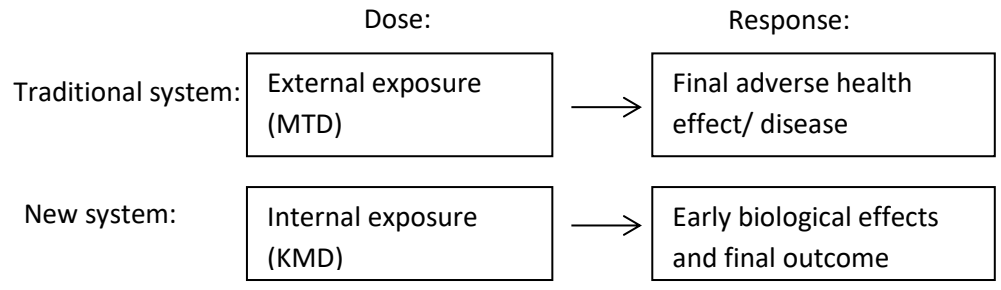


Figure 1.5: Paradigm shift in the way toxicological dose-response analysis is performed. The new system supports a better understanding of 'modes of toxicity' - i.e. how toxicity develops over time at the cellular/ tissue level to elicit disease at levels relevant to human exposure. MTD: maximum tolerated dose. KMD: kinetically-derived maximum dose. See text for details. Adapted from Terry *et al.* 2016.

1.4.2 The utility of TK data in an agrochemical context

The acquisition of TK data can improve the quality of chemical risk assessment in various ways (ICH 1995, OECD 1984). There is increasing recognition that collection of TK data can assist interpretation of toxicity studies for human risk assessment of agrochemicals (Barton *et al.* 2006, Saghir *et al.* 2006). It is also important that animal studies are well designed so that the route, frequency and duration of exposure in rodents are relevant to expected human exposures. The ways in which TK data can assist these aspects of chemical risk assessment are (but not limited to):

- Insight into sensitivities to toxicity between individual animals, genders, species or life stages. For example, it is possible to assess whether the observed sensitivities are related to TK or toxicodynamics (TD). TD is an assessment of how tissue dose relates to the toxicological response. For example, sulfoxaflor induced reproductive toxicity in rats but not rabbits dosed at a level ≥ 400 ppm in the diet. As both species exhibited similar TK, it was possible to determine that this species difference was due to TD (Rasoulpour *et al.* 2012). This understanding helps selection of a test animal (it is standard practice to use the most sensitive relevant animal species for human risk assessment).
- Interpretation of dose-response relationships to support mode-of-action hypotheses about adverse effects seen in animal toxicology studies. For example one could determine that an absent toxicological response is not due to insufficient internal exposure.
- Selection of appropriate concentrations for *in vitro* assays/ aid interpretation of the results.
- Derivation of 'chemical-specific adjustment factors' (CSAFs) to reduce uncertainty in chemical risk assessments (Section 1.4.2.1).

The TK data can be used in combination with a PBTK model to:

- Inform dose selection to derive a KMD and optimal sampling times, or interpret study data where nonlinear TK may explain atypical dose responses (Rhomberg *et al.* 2007). In this

context, it may be necessary to assess the potential of a compound to accumulate upon repeated dosing.

- Extrapolate between exposure routes. Generally for herbicides, animal toxicology studies are conducted via the oral route only. However, extrapolation to assess risks from dermal exposure is useful and reduces the amount of animal testing.
- Extrapolate across/ within species. Extrapolation to humans provides an understanding of human TK which is helpful because the direct acquisition of human TK from intentional dosing is not generally possible.
- Derive biomonitoring equivalents (BEs) to facilitate interpretation of HBM data for health risk assessment (Section 1.4.4).

Barton *et al.* 2006 have proposed a tiered system to guide the routine acquisition and development of agrochemical ADME data. This is a flexible approach and the acquisition of any particular data is not specified as an absolute requirement. In brief, essential studies are performed in tier one and, based on their relevance to expected human exposure and to support study interpretation, additional follow-up studies can be conducted in tiers two and three. For example, in tier one, blood TK data could be collected as part of routine clinical pathology evaluations. Barton *et al.* 2006 suggest an initial 28-day toxicology study in the rat study following a single IV and oral dose, and the collection of TK data in this study would reduce the need for additional groups of animals specifically for investigation of TK. Dow AgroSciences exemplify this practice as TK studies have been integrated into their standard animal toxicology studies since 2006 without the requirement for additional animals (Terry *et al.* 2016). Although male rats have traditionally been for used in TK studies, there is additionally a growing awareness of the importance to also test in females to identify possible reproductive and developmental toxicity in this gender.

1.4.2.1 How can TK data reduce uncertainty in chemical risk assessments?

In order to extrapolate a NOAEL from an animal study to humans for the calculation of an oral reference dose (RfD), an uncertainty factor is required. Its value of 100 was proposed over 60 years ago and is comprised of two 10-fold factors (Lehman & Fitzhugh 1954). Unless there is evidence to show that children are not more sensitive than adults, a further 10-fold factor is used in North America. The first ten-fold factor allows for interspecies differences in ADME (Renwick 1991, 1993), and the second is for intraspecies differences (variability) in humans (Renwick & Lazarus 1998). More recently, division of each of the 10-fold factors into subfactors has been suggested in order to account for variations in TK and TD (WHO 2005) (Figure 1.6). Quantitation of this subdivision is supported by PBTK/ TD modelling studies (Renwick 1993, Renwick & Lazarus 1998). The value of a subfactor can then be replaced with a chemical-specific adjustment factor (CSAF). Guidance has been published for the derivation of CSAFs using appropriate TK and TD data (WHO 2005). For example, it would be possible to use a PBTK model to refine the value of:

- $10^{0.6}$ for AK_{UF} by dividing the mean of a relevant human TK endpoint such as C_{max} by the mean of the animal C_{max}.
- $10^{0.5}$ for HK_{UF} by obtaining an estimate at a particular percentile (e.g. 95th, 97.5th, or 99th) of the population variability distribution of C_{max} and then dividing by the mean.

Consequently a composite factor (CF) could be calculated, to replace the 100 x uncertainty factor: CF = AD_{UF} x AK_{UF} x HD_{UF} x HK_{UF}

The CF could then replace the original 100 x uncertainty factor; if the CF is less than 100 this would represent a reduction in uncertainty in the risk assessment (Meek *et al.* 2003), and recalculation of the RfD would provide a higher level of acceptable human exposure.

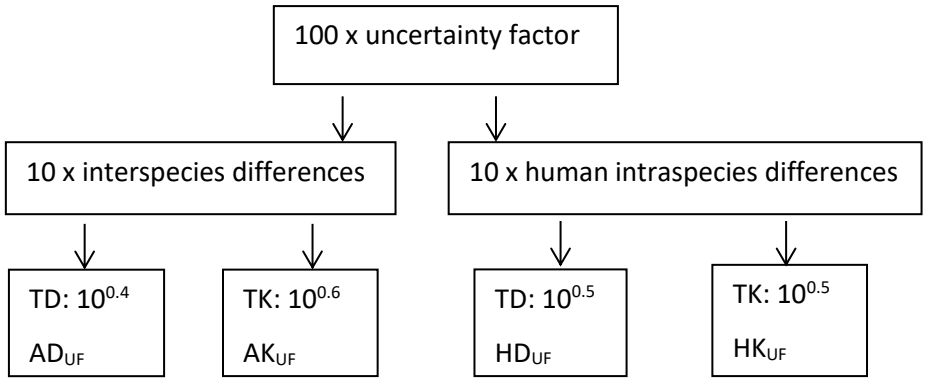


Figure 1.6: Derivation of chemical-specific adjustment factors (CSAFs) from the original 100 x uncertainty factor for use in risk assessment. The product of values assigned to toxicodynamics (TD) and toxicokinetics (TK) subfactors gives the original default values of 10. AD_{UF}: uncertainty factor for animal to human differences in toxicodynamics, AK_{UF}: uncertainty factor for animal to human differences in toxicokinetics, HD_{UF}: uncertainty factor for human variability in toxicodynamics, HK_{UF}: uncertainty factor for human variability in toxicokinetics. Adapted from WHO 2005.

1.4.2.2 Regulatory drivers for inclusion of TK

There has been an international harmonisation of guidelines for the acquisition of TK data for pharmaceutical chemicals, which plays a central role in their safety assessment (Baldrick 2003, ICH 1995). For agrochemicals however, the generation of TK data in risk assessment is less routine. Although many regulatory test guidelines recognise the value of TK, the collection of these data are not generally a regulatory requirement. When TK data is generated, it is usually done on a case-by-case basis to refine a risk assessment. Terry *et al.* (2016) provide an overview of the major regulatory initiatives for the integration of TK data into the risk assessment process of agrochemicals. These are as follows:

- The Agricultural Chemical Safety Assessment (ACSA) from the Health and Environmental Sciences Institute (HESI) proposes an improved approach to assessing the safety of agrochemicals, and advocates the generation and incorporation of ADME and TK data in the chemical risk assessment process (Barton *et al.* 2006, Carmichael *et al.* 2006).

- EU regulation 1107/2009 (which replaced 91/ 414/EEC, the Directive which governs the use of plant protection products within the EU market) states that TK data should be used to inform dose selection, and contains significant new requirements for generation and use of TK data for most types of toxicology studies (EC 2010).
- Guidance documents from REACH outline that the TK profile should be considered as part of the human health hazard assessment, for example by deriving a KMD for use in repeat dose animal studies (ECHA 2008). However, there is no official requirement for TK data due to an insufficient consensus amongst regulators and safety assessors how it would be used (ECHA 2008).
- Both ICH and OECD have recognised that TK data can improve the assessment of internal exposure and thus the quality of chemical hazard and risk assessment (ICH 1995, OECD 1984). OECD has started to incorporate TK into both study design and dose level selection, although the collection of TK data is not an official requirement (OECD 2007, 2009, 2010a). The concept of the KMD is acknowledged in various OECD test guidelines including those used for detecting reproductive toxicity (OECD 2011a, OECD 2011b), and for chronic toxicity and carcinogenicity studies (OECD 2010b).

In summary more organisations within the agrochemical industry should consider adopting TK sampling strategies within their research and development programs. These strategies could be tailored from those already within the pharmaceutical industry which may not otherwise be directly applicable.

1.4.3 Compliance with NC3Rs

The National Centre for the Replacement, Refinement and Reduction of Animals in Research (NC3Rs) is a UK organisation which advocates the principles (3Rs) which underpin the humane use of animals in scientific research and testing within the life sciences sector. Agrochemical exposure science is gradually becoming more aligned with the 3Rs. This may appear somewhat contradictory with

concurrent focus on 'modes of toxicity', as information on internal dose is generally achieved through the acquisition of TK data which involves animal testing. However, analytical technologies and strategies are being developed to reduce and refine animal use, and this is helping to promote the integration of TK within product development programs. These technologies include dried blood spots, microdosing and development of PBTK models.

With dried blood spots, smaller blood volumes (typically 10-20 µl per sample) than are conventionally used (200 µl for mice and 250 µl for rats) are used for the TK study. This allows for serial samples to be obtained from the same animal and should enable a significant reduction in rodent numbers for the generation of TK data.

Microdosing is a relatively new experimental approach being increasingly used in the pharmaceutical industry. It involves administering trace doses of radiolabelled drugs to volunteers at an early stage in drug development to obtain a preliminary assessment of the human ADME profile, using sensitive techniques such as positron emission tomography (PET) (Bauer *et al.* 2008, Garner & Lappin 2006). Furthermore, PET imaging can also provide TD data such as information on receptor binding (Bauer *et al.* 2008). If microdosing can be applied to the agrochemical industry, this has the potential to reduce the need for testing in multiple species (Combes *et al.* 2003), and these data can assist with the development and calibration of human PBTK models. Section 12(a)(2)(P) of the Federal Insecticide, Fungicide and Rodenticide Act (FIFRA) specifies it is illegal to test pesticides in humans unless they volunteer and are fully informed about the potential health effects. Such individuals are more likely to volunteer if there is a lower risk of toxicity following administration of trace doses.

Human PBPK models have been successfully applied in the safety assessment of non-pharmaceutical chemicals such as chloroform (Loizou *et al.* 2008), one of the first generation anaesthetics. However, these models are usually extrapolated using animal data. Conversely, for agrochemicals, it may be possible to build a human PBTK model directly, without extrapolation from rodents. This would involve the acquisition of high quality *in vitro/ silico* (possibly *in vivo*) data to parameterise key model

parameters although this is lacking in some areas (Coecke *et al.* 2013). These data, which could be collected in tier one toxicology studies, might include:

1. *In vitro* metabolism studies. These have not previously been required for registration of agrochemicals, but could be conducted with genetically modified human cell lines. Furthermore *in silico* tools such as Lhasa's Meteor Nexus™ could be used to predict the metabolites formed through phase I and phase II biotransformations occurring in humans.
2. *In vitro* dermal absorption assays. This is the primary route of pesticide exposure for operators (Wolfe 1976) and therefore represents a major concern for risk assessment during product development. Furthermore, this data can facilitate interpretation of toxicological data which is usually obtained through the oral route of administration.
3. Fraction unbound in plasma. This is already done for pharmaceuticals (Levy & Moreland 1984) because serum-binding proteins vary across species, gender, disease states and life stages (Teeguarden & Barton 2004), which can thereby affect bioavailability of the free compound.
4. Transporter assays. If the compound is expected to undergo substantial active transport, this may be necessary.
5. Structure-activity relationships. These may be used to identify 'toxicophores' within metabolites that could serve as structural alerts for predicting toxicity (Green 2002), and predict the octanol/ water partition coefficient (LogP) which is an important model parameter.

1.4.4 Use of HBM data to assess exposures

HBM is the assessment of human chemical exposure, by measuring these chemicals, and/ or metabolites, reaction products thereof (i.e. biomarkers) in human tissues or specimens. These data therefore provide aggregate measures of dose from all sources and exposure pathways, and can be

used to provide evidence of human exposures to a xenobiotic(s). Saliva was explored as a medium for monitoring pesticide exposures (Nigg & Wade 1992), as it is anticipated to have a close association with tissue bioavailability. However, urine is the most frequently used biological specimen, due to its non-invasive nature, ease of collection and importance as a route of excretion for many analytes. HBM data is becoming increasingly available for agrochemicals due to increased numbers of these studies. Surveillance strategies may include field studies in an occupational context for farmers and professional applicators (Nolan *et al.* 1991), studies of human exposures under normal conditions of use (Krieger *et al.* 2001), or integrated into routine medical examinations.

HBM data are typically statistically weak because a single measurement of a chemical/ metabolite in human specimens is usually provided per individual, although measurements are usually collected from a large number of individuals from the exposed population of interest, usually as part of a survey. For example, in the US, biomonitoring programs include Children's Total Exposure to Persistent Pesticides and Other Persistent Organic Pollutants (CTEPP) (U.S. EPA 2002), and the National Health and Nutrition Examination Survey (NHANES); the latter provides concentrations of over 70 pesticide analytes in blood and urine. The Canadian Health Measures Survey (CHMS) measures 17 pesticide analytes in blood and urine amongst the Canadian population. Although these programs have generated vast amounts of data, it can be difficult to interpret because:

- The measured metabolite may not be specific to a particular parent compound. The metabolite may be shared by numerous agrochemicals within the same class. For example, 3-phenoxybenzoic acid is a common metabolite of numerous pyrethroids (Terry *et al.* 2016). A ‘cumulative’ risk assessment is required if this metabolite is involved in a common mechanism of toxicity.

- Many agrochemicals are degraded in the environment to the same metabolites formed in humans. Therefore detecting the metabolite in human biofluids does not differentiate whether exposures occurred to the metabolite or parent compound (Terry *et al.* 2016).
- Many agrochemicals have short half-lives and exposures occur infrequently, resulting in large intraindividual, within-day variations in urine concentrations (Aylward *et al.* 2012).
- Some pesticides are highly volatile and may evaporate from the urine before detection.

Interpretation of HBM can be facilitated with a suitable PBTK model, which can be used to identify and quantify corresponding exposure pathways. This is called 'exposure reconstruction' or 'reverse dosimetry' (Tan *et al.* 2007) and, for example, has been used to estimate exposure to chloroform in tap water, from chloroform measurements in blood (Lyons *et al.* 2008). However, it is not currently possible for the analysis of HBM data to give any information on the exposure scenario such as the duration or frequency of exposures (Sohn *et al.* 2004).

PBTK models can help contextualise HBM data through the derivation of BEs. This involves 'forward dosimetry' and is the calculation of chemical concentration within a readily accessible human biofluid (such as urine or blood) for a known external reference dose (Hays *et al.* 2008). Interpretation of HBM data is easier if a BE is available for that particular chemical, because a margin of safety (MOS) can be calculated (BE/ HBM). Chemicals for which human internal exposures exceed BE values (or pass a MOS threshold) could be given priority for follow up and health risk assessment/ management (Phillips *et al.* 2014).

1.5 Review of predictive models for pesticide operator exposure used in risk assessment

Pesticides are used to make agricultural practices more sustainable. They are categorised according to the type of organisms they control. The primary categories of pesticides are insecticides, herbicides and fungicides. Chemical risk assessments are required for the approval, registration and

labelling of pesticides and for making suitable recommendations concerning the use of personal protective equipment (PPE). In the European Union (EU), Directive 91/414/EEC identifies three subpopulations for which non-dietary risk assessments must be conducted. These are operators (individuals involved in activities relating to pesticide application), workers (those exposed through re-entry activities such as harvesting) and bystanders (individuals whose presence is unrelated to pesticide work). The process of conducting a chemical risk assessment is multidisciplinary because hazard, dose-response and exposure are assessed (Section 1.1). Here the exposure assessment of operators working in an agricultural context is reviewed.

1.5.1 How do the models work?

Generic databases are collections of exposure data representative of varying scenarios of pesticide use and climatic conditions. These data are from controlled field studies and are an example of passive biomonitoring (Section 1.5.3). As the information in the database is generally treated for operator exposure assessment, these databases are also called 'predictive operator exposure models' (POEM) and are used as a tool by regulators to determine whether the pesticide should be approved for registration.

POEMs have been constructed under the assumption that the spread of pesticide aerosols is determined by the way in which work activities are performed rather than the pesticide's chemical properties. Therefore selection of the 'use scenario' is the first and most important step when assessing operator exposure. The use scenario considers factors such as the type of formulation (emulsifiable concentrate, aqueous suspension, solution, wettable powder or granular), application equipment (e.g. vehicle-mounted sprayers which can be open or closed systems, or hand-held sprayers), and the degree of PPE worn and the activities performed by an operator. The work activities include mixing-loading, application, flagging to assist aerial application and maintenance/ decontamination of application equipment.

Mixing-loading involves measuring the concentrated product, mixing with a diluent and then loading the pesticide into application equipment. Mixing and loading are normally done sequentially by the same person and are usually considered together in exposure models. The exposure during mixing/ loading depends on the amount of a particular formulation used, size and neck width of the container and the loading technique. There is significant potential for exposure during mixing-loading, mainly to forehead, forearms and hands because the formulation is highly concentrated. During application of the pesticide onto crops, all body parts of the operator are at risk for exposure. The extent of exposure largely depends on the application technique which can be upward spray (for fruit trees) or downward onto field crops (PHED 1992). Upward spray greatly increases the risk of dermal and inhalation exposure (Thornhill *et al.* 1996).

Estimation of daily exposure is calculated in terms of the amount of active ingredient (a.i.) handled during mixing/ loading (mg a.i./ kg a.i. handled) and the work time during application (mg or ml / hr work). 'Potential' exposure (amount of pesticide on PPE and uncovered skin) is calculated which is transformed into 'actual' exposure (amount of pesticide on the skin after penetrating PPE) through the use of exposure reduction factors that account for PPE. Subsequently, 'absorbed dose' is calculated through the use of dermal absorption factors and compared with the AOEL (see below). Although operator exposure to pesticides is predominantly through the dermal route, pesticide aerosols can also be inhaled and efficiently absorbed in the lung (Kolmodin-Hedman & Akerblom 1987). Therefore 'absorbed dose' is calculated as a summation from both inhalation and dermal routes of exposure. Matthews 2002 provides a worked example of an estimate for operator exposure, which is dependent on additional factors such type of equipment used and the pesticide concentration in use.

1.5.2 Differences between operator exposure models

Various national models are available for estimating operator exposure which includes the German model (Lundehn *et al.* 1992), UK-POEM model (PSD 1992) and the Dutch model (Van Hemmen

1992). Further updates to these national exposure models are unlikely because multinational models are becoming more widely used for risk assessments. These are the pesticide handlers' exposure database (PHED) (PHED 1992) for use in North America and the European POEM (EUROPOEM) (EUROPOEM 1997). The segregation of these databases relates to differences in the size of farms and agricultural methods between North America and the EU. Although EUROPOEM allows for evaluations of pesticide exposure at the European scale, different subsets of the database may be used to support differences in climate and working practices in different member states. The development of these large databases has allowed for increased confidence of exposure estimates. They have also prompted the harmonisation of methodologies used for generating passive biomonitoring data, as well as the modelling of operator exposure for example through the use of harmonised values for dermal absorption and exposure reduction factors. However these databases need upgrading with modern working conditions, and the development of new formulations and application techniques such as microencapsulated pesticides and computerised spraying systems. In this regard the Agricultural Operator Exposure Model (AOEM) has recently been developed for use in the EU (Großkopf *et al.* 2013).

The diversity of models available for estimating operator exposure seems to reflect national and zonal differences in work culture and safety practices. These differences relate to the source of datasets, assumptions made about the area of land treated per day, the clothing worn by an unprotected operator, glove penetration factors and the percentile used for calculating exposure estimates. Therefore comparison of the models with similar use scenarios gives different exposure estimates for use in risk assessment (Kangas & Sihvonon 1996).

The German and PHED models provide the central tendency value (i.e. geometric mean, median or arithmetic mean depending on the data distribution). Thus, registration is made in terms of operators exposed at the average level even though approximately half of operators are anticipated to exceed this. Conversely the Dutch model is based on the 90th percentile: 90 % of operators are

included in the exposure assessment and 10 % have higher exposure. Dutch authorities apply a high level of protection due to a relatively small exposure database and the assumption that most operators do not follow product label recommendations. The UK model is rather intermediate and uses the 75th percentile. In EUROPOEM and AOEM the percentile used for exposure estimates is variable. EUROPOEM is based on the 75th percentile when at least 50-100 data points from at least ten studies are available in the subset. The 90th percentile is used when less exposure data is available (Van Hemmen 1998). In the AOEM either the 75^{th} or 95^{th} percentile can be used. This follows recommendations from EFSA that the 95^{th} percentile is used for estimation of acute exposure (i.e. occurs in a single day) and the 75^{th} percentile is used for longer term exposures (EFSA 2014).

1.5.3 Passive biomonitoring

Passive biomonitoring measures the amount of pesticide that comes into contact with the skin, clothing and breathing zone of operators in a field study (Wolfe 1976, Davis 1980). Inhalation can be monitored using personal air pumps and fixed site air collectors. Dermal exposure sampling methods range from surrogate skin techniques (e.g. patches, coveralls worn next to the skin), chemical removal techniques (e.g. skin washes/ wipes) and fluorescent tracer techniques (Fenske 1993a). These measurements are added to databases, which can be used to relate certain operator activities to external dose. It is also desirable to collect additional data on variables which affect the amount and rate of dermal absorption, such as the area of unprotected skin, duration of dermal exposure, and climatic factors such as humidity and air temperature.

The field studies carried out for registration purposes are controlled and conducted according to label requirements. This may introduce observational bias (if workers change their behaviour with awareness of being under scrutiny) and motivational bias (if volunteers feel the need to conduct activities more carefully if they are paid). However, under actual conditions of use, substantial dermal exposure may occur through improper use, deterioration and contamination of PPE.

Consequently, regulators take various approaches to avoid underestimating worker exposure. For example, U.S. EPA and the Pest Management Regulatory Agency (PMRA) normalise exposure study data by using 1) the maximum application rate, 2) upper bound values for the amount of active ingredient used and area treated, and 3) default values of 100 % dermal absorption and 100 % inhalation absorption to avoid underestimating worker exposure. As the quality of data in exposure databases is being improved, including surveillance exposure data obtained under actual conditions of use, it may be possible to reduce some of these conservatisms to facilitate product registration.

1.5.4 Relating calculated exposure to risk

According to Directive 97/57/EC, the acceptable operator exposure limit (AOEL) is defined as 'the maximum amount of active ingredient to which the operator may be exposed without any adverse health effects' (EC 2006). AOELs relate to the internal (absorbed) dose available for systemic distribution from any absorption route and are expressed as internal levels (mg/ kg bw/ day) (EC 2006). It can be expressed as the ratio NOEL/ SF, where the NOAEL is the no observed effect level in the most sensitive relevant animal species, and the SF is the safety factor accounting for uncertainties in the extrapolation of toxicological data. Chemical risk can be described as the difference between absorbed dose and the AOEL using a 'tier approach'. In the tier approach, each successive tier requires more refined data and hence provides a more accurate measure of exposure (EUROPOEM 1997). This approach economises resources and focuses effort on chemicals of greatest concern, and is similar to the RISK21 matrix (http://www.risk21.org) which has been developed under a program of the Health and Environmental Sciences Institute.

Tier one involves estimating exposure using a predictive exposure model with generic data and conservative default assumptions (e.g. 100 % dermal absorption). If this exposure estimate is below the AOEL, the exposure is considered acceptable (not associated with unacceptable health risks) and the product may gain approval. If the exposure exceeds the AOEL a refinement in tier two may be made based on various considerations such as the physicochemical properties of the substance

(mainly lipophilicity and chemical structure) and the scientific database. This helps to refine variables such as dermal absorption, daily areas treated, effectiveness of protective clothing and engineering controls leading to more realistic exposure data. If the Tier 2 exposure estimate exceeds the AOEL, a field study may be conducted in tier three. In most cases, a tier three study involves a biomonitoring (and/ or passive biomonitoring) study supported by knowledge of the human toxicokinetic profile to provide more accurate exposure estimates. When such a study is not available, one might look for a reference study carried out with another pesticide with a similar use scenario. Ideally the assessment of tier three data should be probabilistic in nature.

1.5.5 Risk management

If the predicted absorbed dose exceeds the AOEL then it may be necessary to implement exposure reduction measures (Table 1.3) which are mandated by worker protection standards (WPS) (U.S. EPA 1992). Such risk management is required for pesticide registration and post registration stewardship and includes informing operators about the hazards of pesticides.

Table 1.3: Factors affecting operator exposure and corresponding exposure reduction measures.

Type of equipment used. Mixing and loading of pesticides can result in substantial exposures over brief periods. Applications such as air-blast sprayers produce much higher exposures than applications with ground-boom equipment.	Engineering controls: closed cab and mixing/ loading systems with ventilation systems. Restricting the usage of certain types of equipment associated with high exposure. Ensure operators receive adequate training.
Formulation of the pesticide. Liquids, such as emulsifiable concentrate solutions, and aqueous suspensions are prone to splashing and spillage. Conversely, wettable powders and granules may present a plume of dust while being loaded into application equipment posing a respiratory hazard and exposures to the face and eyes. Nanoformulations may increase inhalation exposure.	Use appropriate formulation types and packaging. Use PPE, gloves, respirators where necessary. Availability of emergency washing facilities.
Packaging. The size and shape of liquid containers may affect the potential for spillage and splashing after opening.	Limiting the amount of pesticide that can be sold or handled.
Environmental conditions. Temperature and humidity may influence chemical volatility, perspiration rate and use of protective clothing. Wind can cause the spray to drift. Sunshine and heat may increase blood flow to the skin and therefore enhance dermal absorption (Fiserova-Bergerova 1993).	Avoid mixing and spraying during windy conditions.
Personal protective equipment (PPE). Includes chemical-resistant gloves and coveralls and respiratory protection.	Proper use and maintenance of PPE as part of hygienic behaviour. The use of protective clothing is a legal requirement for many compounds (U.S. EPA 1992).
Duration of activity. The frequency and duration of exposures can affect operator exposure.	Limiting the uses for the product and managing worker time schedules on a seasonal and lifetime basis.

1.5.6 Future direction of operator exposure models

The aforementioned POEMs have no temporal aspect and do not account for the time dependent nature of dermal or inhalation absorption or other ADME processes which affect absorbed dose and hence toxicity. The dose that is bioavailable, or the systemic exposure of the primary toxicant, has a greater association with the toxicological response, and therefore a better comparator to the AOEL than predicted absorbed dose for the assessment of chemical risk (Figure 1.7). In this respect, it would be ideal to calculate maximum systemic exposure, which may occur at a certain time point following or during initial exposure. Compartmental models such as TK Modeler (McCoy *et al.* 2012) or PBTK models are required for this purpose. In a PBTK model, the dose applied on the skin surface can be slowly absorbed over time which affects systemic exposure. Additionally, concurrent elimination will reduce the bioavailability of the toxicant over time leading to less risk of toxicity. Another advantage of the PBTK model is that it can take into account variability and uncertainty on dermal absorption rates which will also affect the prediction of systemic exposure.

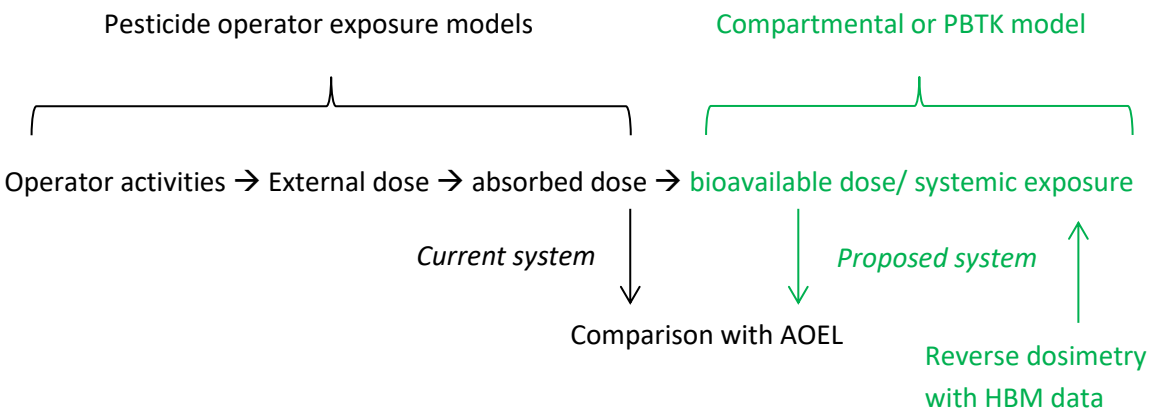


Figure 1.7: Proposed changes (green) to the modelling approach to refine the chemical risk assessment of pesticide operators. A pesticide operator exposure model can be used to predict absorbed dose. A compartmental or PBTK model can be coupled to a pesticide operator exposure model. This allows prediction of the corresponding bioavailable dose, or systemic exposure, which has a greater association with the toxicological response than absorbed dose. Additionally, for some pesticides, it may be possible to include urine HBM data from operators in databases. Reverse dosimetry can be done with this data to assess systemic exposure for comparison with estimates using the forward dosimetry approach.

Oral exposure is considered to be low relative to dermal and inhalation exposures and therefore is neglected in operator exposure models. However, inhaled pesticides may enter the gastrointestinal tract through swallowed phlegm. Additionally, under actual conditions of use, pesticides may enter the mouth if hygienic aspects are ignored such as eating with unwashed hands. Oral exposure can be taken into account with appropriate data and a PBTK model.

There is a transition away from using a deterministic modelling approach where conservative default parameter values are used (which can overestimate worker exposures), towards using a probabilistic approach involving Monte Carlo analysis, where distributions are used reflecting variability and uncertainty in worker exposure patterns (Hamey 2001). Although large databases are required to build the necessary distributional data, this will allow more realistic estimates of operator exposure. Work on developing newer exposure databases such as EUROPOEM II will facilitate this transition.

1.6 Thesis hypothesis and aims

Hypothesis:

PBTK models can be calibrated and used to accurately calculate tissue exposures and applied in risk assessment.

Aims:

The project will develop PBTK models for RBFRs and herbicides to assess human exposure to these chemicals. Briefly the project will:

1. Acquire *in vivo* rat toxicokinetic and appropriate *in vitro* data to build and calibrate rat PBTK models for representative RBFRs and herbicides (using toxicokinetic data supplied by DAS).
2. Scale rat PBTK models to produce human equivalent PBTK models, validating the models using human toxicokinetic data where available. For the herbicides, additional human toxicokinetic data are available from DAS.

3. Perform uncertainty analyses to model internal and external exposures of the UK population to RBFRs and herbicides, using a calibrated human PBTK model and appropriate HBM data (Section 2.1.2).

4. Apply PTBK herbicide models to estimate body burdens from occupational exposures, and to integrate this approach into the DAS risk assessment procedure (Section 1.3.2).

Chapter 2: Materials and methods

2.1 Bayesian inference

Bayesian inference has been widely applied across scientific disciplines for interpreting data. It is based on Bayes' theorem:

$$P(X|M) \propto P(M|X) \times P(X) \quad [1]$$

- P(X) is a probability distribution representing the state of current knowledge regarding the system of interest (i.e. the PBTK model structure and its parameter value distributions, represented by X in equation 1) before experimental or other additional data (M) are considered. Thus P(X) is termed a 'prior' probability distribution.
- The quantity P(M|X) is a likelihood function which gives the probability of obtaining M given the model and parameters, X. I.e., P(M|X) represents mathematically the measurement process and measurement uncertainty associated with M. Higher values of P(M|X) occur when X values better explain the data. Hence the likelihood function refines the model's prior parameter distributions based on M, thereby generating a 'posterior' probability distribution P(X|M).
- P(X|M) thus represents the new knowledge state regarding the model after new data are considered.

Bayesian inference can be applied using a numerical method such as Monte Carlo integration using Markov Chains (MCMC). MCMC analysis can be performed using Metropolis-Hastings sampling (Hastings 1970, Metropolis *et al.* 1953). The steps of this algorithm (presented visually in Appendix Figure 3.1) are as follows:

1. Specify random seed number (initiate chain),
2. Randomly take (and record) a sample from a proposal distribution,
3. Calculate current and proposal probability densities,

4. Calculate probability of accepting move (proposal probability density/ current probability density). Thus, if the probability density is greater at proposal point, definitely accept proposal and return to step 2. Conversely, if the probability density is lower at proposal point, accept proposal with low probability (otherwise remain at current point).

These iterative samples are recorded for each unknown parameter which forms the Markov Chain. After a sufficient number of iterations ('burn-in'), the chain converges where the proposal distribution becomes the posterior distribution. Convergence can be monitored by calculating potential scale reduction factors (PSRFs). PSRFs calculate the level of variance within and between proposal distributions from three independent MCMC chains seeded with different random numbers and starting values of model parameters. During convergence, the proposal distributions from the three chains begin to overlap; when the PSRF for each parameter is < 1.2 then convergence is considered to have occurred (Gelman & Rubin 1992).

2.1.1 Application of Bayesian inference to PBTK modelling

Bayesian analysis can be applied to PBTK modelling in two ways:

1) Model calibration:

Approaches to model calibration range from visual analysis (comparing fitted model predictions with data) (e.g. Lilly *et al.* 1998) to use of more statistically rigorous methods. A common algorithm is the 'least-squares fit': model output is calculated with an initial value of the parameter being calibrated (optimised) and then squaring the difference between the model predictions and observed data at each time point, and summing these differences. This is repeated with different parameter values until the summed differences are minimised and the 'least squares' fit is obtained, thereby

generating a single optimised value (Campbell *et al*. 2012). This procedure can be applied to many model parameters simultaneously. This is helpful because PBPK models are highly parameterised. The use of Bayesian inference for model calibration has two unique advantages: the fit of each parameter is 1) a posterior probability distribution of values, rather than a point estimate, which takes account of measurement uncertainty, and variability of parameter values; and 2) informed by both experimental data and prior knowledge (Jonsson & Johanson 2003).

In the Bayesian approach, the likelihood function (equation 1) identifies model parameter values that best describe the experimental data; these are further weighted by the prior distribution to give the posterior parameter distributions (Gilks *et al.* 1996). Prior knowledge can be summarised by assigning appropriate prior distributions to various PBTK model parameters, to reflect population variability and uncertainty. Such prior knowledge can be obtained from the literature, although it is often incomplete. For example, many model parameters are 'physicochemcial' in nature - their values are dependent on both organismal physiology and the chemical itself. This incompleteness makes it necessary to acquire additional (chemical-specific) experimental data. Analysing these data with prior knowledge generates 'posterior' distributions. Posterior distributions are a balance between previous ('prior') knowledge about the parameter, and the new information provided through the experimental data. Hence the posterior parameter distributions, in conjunction with model validation procedures, define the calibrated model. The calibrated model can undergo further rounds of Bayesian analyses (the posterior becomes a prior distribution) for further model refinement with additional experimental data sets. Hack (2006) provides an overview of using Bayesian analysis for PBTK model calibration.

2) Modelling population exposure from HBM data:

Human biomonitoring (HBM) is the assessment of human chemical exposure, by measuring these chemicals, and/ or metabolites, reaction products thereof (i.e. 'biomarkers') in human tissues or specimens (e.g. blood and urine). Hence, HBM data provides aggregate measures of dose from all sources and exposure pathways. PBTK models can be used with HBM data to identify and quantify these exposure pathways. Depending on the HBM database used, this can be done to assess domestic, environmental or occupational exposures. Consequently, exposure levels through these pathways can be varied for relevant exposure scenarios and the PBTK models can predict the quantitative effect on tissue dose. Generally, BFRs are not extensively metabolised and accumulate in adipose, thus the parent compound (in urine for example) is a potential biomarker of BFR exposure.

HBM data are typically weak because a single measurement of a chemical/ metabolite in human specimens is usually provided per individual, although measurements are usually collected from a large number of individuals from the exposed population of interest, usually as part of a survey (e.g. the U.S. National Health and Nutrition Examination Survey, NHANES (NHANES 2015). Therefore it is important to develop statistical methods that improve estimates of parameters governing exposure level such as daily intake rate, and also to ensure that the predicted exposures reflect adequately the significant measurement uncertainty inherent in the data themselves. One approach is to couple MCMC with a calibrated human PBTK model to infer (internal and external) exposure at the population level from HBM data collected from a sample of the exposed population. A joint analysis performed on all the data simultaneously can also yield better estimates of input parameters and reduce uncertainty on dose estimates at the individual and population level. This is known as dose reconstruction or reverse dosimetry (Tan *et al.* 2007) and, for example, has been used to estimate exposure to chloroform in tap water, from chloroform measurements in blood (Lyons *et al.* 2008).

2.1.2 Application of MC analysis to PBTK modelling (uncertainty analysis)

Posterior parameter vectors from Markov chains can be used in further simulations to calculate distributions of tissue doses. The conventional approach, however, is to perform Monte Carlo (MC) analysis without Markov chains. This involves randomly sampling from distribution(s) assigned to model parameter(s), and iteratively calculating model output such as tissue concentration. This can be done to perform uncertainty analyses to predict ranges of tissue doses, and HBM values expected from a specified (possibly uncertain) intake regime. Given high confidence in the PBTK model's predictions, then 1) mechanistic interpretations can be inferred from significant deviations between predicted and observed toxicokinetic data, and 2) implications for public health risk can be assessed. The latter accounts for uncertainties on internal and external parameters as well as interindividual variability in parameter values. The assessment of tissue dose variability is useful in chemical risk assessments performed for heterogeneous populations.

2.2 LC/MS method development

2.2.1 Mass spectrometry method development

Atmospheric pressure chemical ionisation (APCI) and atmospheric pressure photo ionisation (APPI) are suitable methods for the ionisation of nonpolar analytes with a low molecular weight (< 1000 Da) prior to mass spectrometry (MS). Therefore APCI and APPI were used for the ionisation for BFRs which fulfil both criteria. Heated electrospray ionisation (HESI) was used for TBBPA and haloxyfop, however, which are relatively polar. High-resolution mass spectrometry (HRMS) methodology was developed using a Q Exactive™ plus Orbitrap mass spectrometer (Table 2.1). Under the ionisation conditions, various ionised molecules of the parent chemical are formed and these are ultimately detected in the MS in terms of their mass: charge (m: z) ratios (Table 2.2). Many of the BFR anions

are debrominated and/ or oxygenated. The ionisation conditions were optimised to generate a high and stable anion signals, helping to improve the HPLC-MS limits of detection and quantification.

Table 2.1: Optimisation of ionisation conditions for several RBFRs and haloxyfop.

Setting	**TBBPA**	**DBDPE**	**BTBPE**	**BEHTBP**	**Haloxyfop**
Ionisation probe	HESI	APCI	APPI	APCI and APPI	HESI
Infusion concentration (ng/ mL)	50	100	100	100	50
Infusion rate (µL/ min)	10	20	5	5	10
Flow rate (mL/ min)	0.400	0.550	0.400	0.400	0.400
Mobile phase ratio (for tuning)	100% MeOH	9:1 MeOH, H_2O	9:1 MeOH, H_2O	9:1 MeOH, H_2O	100% MeOH
Probe position	D	D	C	C	D
Scan range	150-2000	900-915	300-360	635-650	150-2000
Sheath gas pressure (psi)	20	50	24	45	5
Aux gas (psi)	7	5	4	7	15
Sweep gas (psi)	0	0	4	4	1
Discharge current (kV)	5 (Spray voltage)	6	10	7.00	2.7 (Spray voltage)
Capillary temperature (° C)	290	240	250	210	230
Vaporiser temperature (° C)	290 (Aux gas heater)	200	250	270	240 (Aux gas heater)
Signal obtained	550 - 600 x 10^3	3.0 - 5.5 x 10^3	15 - 20 x 10^3	0.9 - 1.0 x 10^6	200 - 300 x 10^3
Polarity	Negative	Negative	Negative	Negative	Positive

Table 2.2: MS Detection of RBFR and haloxyfop ions following ionisation.

Compound	**Molecular Formula (parent compound)**	**Anion formed**	**m: z**
TBBPA	$C_{15}H_{12}Br_4O_2$	$(M-H)^-$	542.74,540.74,544.74
DBDPE	$C_{14}H_4Br_{10}$	$(M-Br+O)^-$	906.28, 908.28
BTBPE	$C_{14}H_8Br_6O_2$	$(C_6H_2Br_3O)^-$	328.76,332.76
BEHTBP	$C_{24}H_{34}Br_4O_4$	$(M-Br+O)^-$	640.99,642.99
Haloxyfop	$C_{15}H_{11}ClF_3NO_4$	$(M+H)^+$	362.039

2.2.2 Liquid chromatography method development

During APCI the HPLC mobile phase is nebulised with inert nitrogen gas by heating the probe's vaporiser. The vapour then interacts with a corona of electrons (generated by a needle) at atmospheric pressure. The electrons initiate a chain of chemical reactions that are dependent on the analyte and mobile phase composition, but ultimately elicits ionisation of the analyte. In HESI, the analyte must be an ion in solution (hence polar). A voltage is then applied across the ESI needle to remove (or add) protons and leaves charged ions to enter the MS capillary. Conversely, in APPI, a UV lamp is used to generate photos which elicit analyte ionisation instead of electrons.

The HPLC column for TBBPA was 100 x 2.1 mm and the stationary phase comprised of 2.6 µM solid core Accucore PFP particles maintained at 30 °C. The retention time was 3.4 minutes. Six calibration samples were used (0 - 1000 ng/ mL) immediately before running unknown samples to minimise the effect of intraday variability of detection sensitivity (Figure 2.1A). For haloxyfop, the HPLC column was 100 x 2.1 mm and the stationary phase comprised of 2.5 µM solid core ACE C18 particles maintained at 30 °C. The retention time was 6.0 minutes. Seven calibration samples were used (0 - 4000 ng/ mL) immediately before running unknown samples (Figure 2.1B).

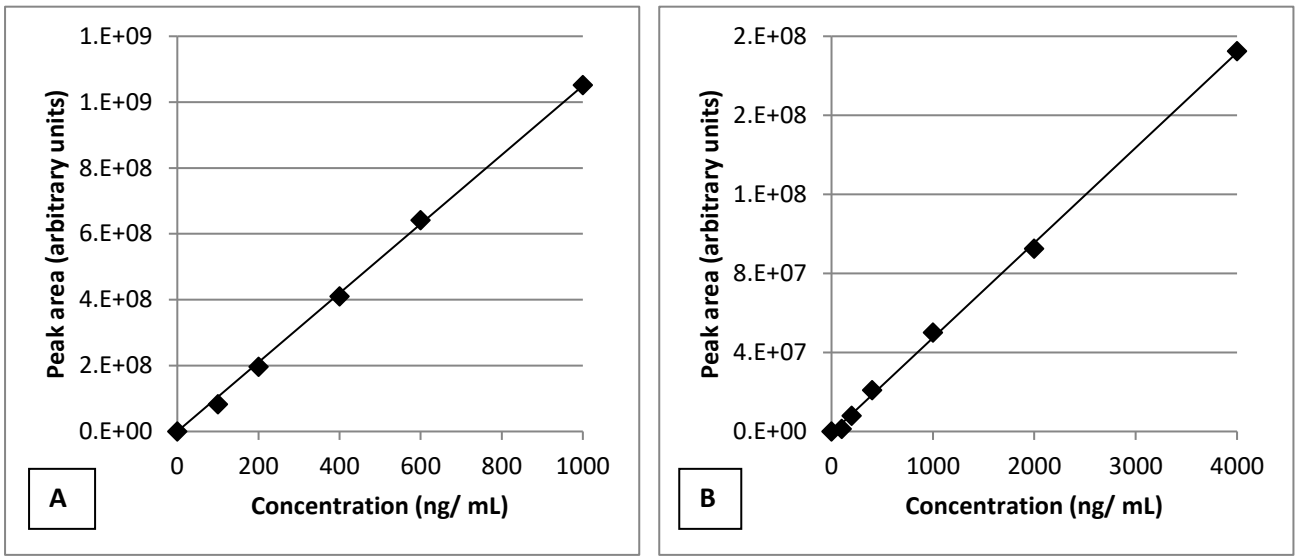


Figure 2.1: Representative LC/ MS calibration graphs for TBBPA **(A)** and haloxyfop **(B)**.

The eluent system comprised of mobile phase A (water containing 5 % methanol, v/v) and mobile phase B (methanol) with an injection volume of 10 µL (Figure 2.2).

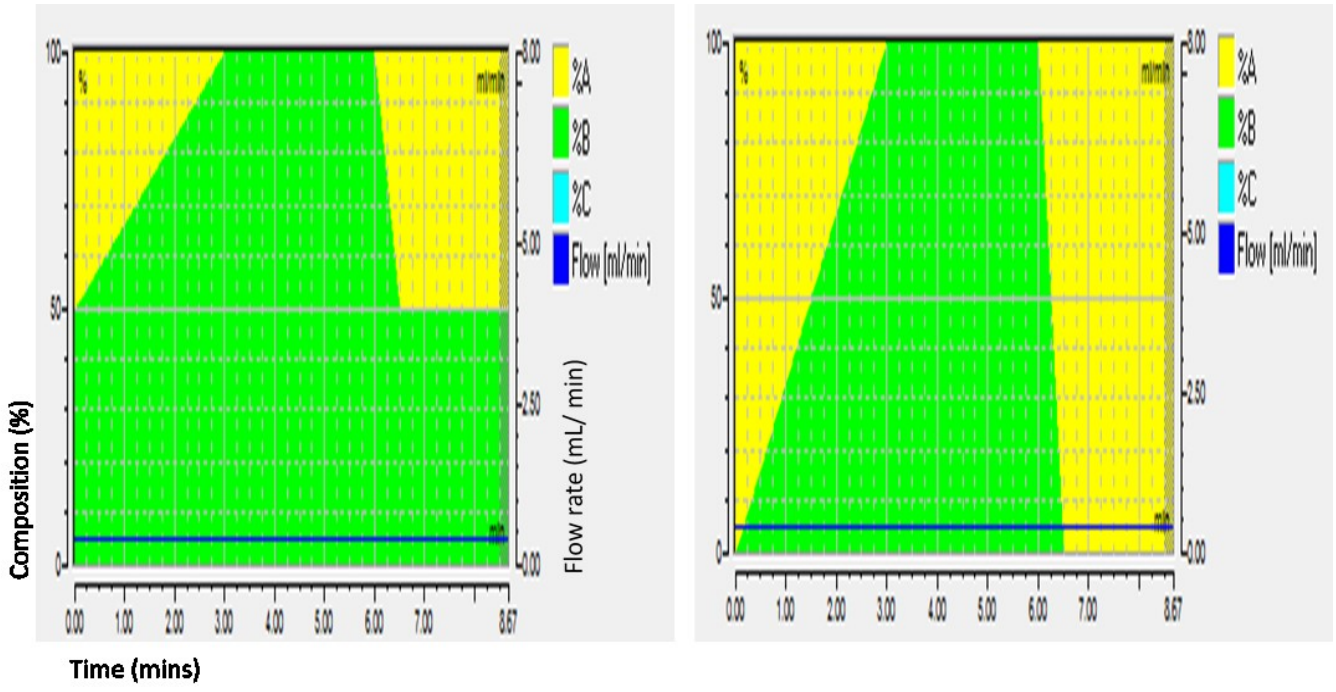


Figure 2.2: HPLC gradient elution profiles for TBBPA (left) and haloxyfop (right). Mobile phase A was water containing 5% methanol, and mobile phase B was 100 % methanol (v/v). The flow rate was 0.4 mL/ min.

The following *in vitro* assays were performed for both TBBPA and haloxyfop to provide additional biochemical data for model calibration.

2.2.3 Fraction unbound in plasma assay

To determine the fraction of TBBPA unbound in plasma, the rapid equilibrium dialysis (RED) system was used with an 8 kDa molecular weight cut off membrane (Thermo Scientific). 100 µL of thawed plasma was added to the sample chamber. Plasma samples were taken from healthy human volunteers (n = 4), each performed in sextuplicate to ascertain measurement error. To the buffer chamber, 297.2 µL of 1 x PBS buffer and 2.8 µL of 1 mg/ mL TBBPA solution (100 % methanol) was added. Unequal volumes in chambers were essential to avoid sample volume changes. The dialysis tubes were sealed with parafilm and then incubated at 23 °C on a Thriller® orbital shaker (Peqlab) at 300 rpm for 12 hours.

After equilibration, 25 µL from the buffer chamber was added to 300 µL of 50 % methanol solution in an Eppendorf. This was incubated for 30 minutes at -18 °C and subsequently centrifuged for 10 minutes at 13,000 g to remove plasma lipids and proteins below 8 kDa from the buffer. The supernatant was then analysed for quantification using LC/MS.

To calculate fraction unbound in plasma (FUp), the following working was used:

- 2.8 µL of 1 mg/ mL TBBPA solution used, so 2.8 µg TBBPA added to buffer.
- Amount in buffer chamber = concentration in buffer chamber x volume.
- To calculate the concentration in buffer chamber, the concentration determined by LC/MS (e.g. 10 ng/ mL) was multiplied by 12 to compensate for the dilution of 25 µL into 300 µL.
- Thus, concentration in buffer chamber = 10 ng/ mL x 12 = 120 ng/ mL, and amount in buffer chamber = 120 ng/ mL x 0.3 mL = 36 ng

- After equilibration, amount in plasma chamber = amount TBBPA initially added - amount in buffer chamber = 2800 ng - 36 ng = 2764 ng
- Concentration in plasma chamber = amount in plasma chamber / volume = 2764 ng / 0.1 mL = 27640 ng/ mL
- FUp = concentration in buffer / concentration in plasma = 120 / 27640 ng/ mL = 0.0043

2.2.4 LogP assay

The LogP assay was performed for haloxyfop as described in OECD (1995) with modifications. Each Eppendorf comprised of 1000 µL of aqueous solution, 840 µL of octanol and 160 µL of 50 µg/ mL haloxyfop (99.3 % purity, in 99 octanol: 1 methanol) which were sealed with parafilm before shaken with a tube revolver (Thermo Scientific) at 40 rpm for 12 hours. The first experiment (n = 10) used water for aqueous at room temperature and the second experiment (n = 10) used 1 x PBS pH 7.4 for aqueous incubated at 37 °C to resemble physiological conditions.

After equilibration, a needle syringe was then used to aspirate the aqueous layer to avoid contamination with octanol. Eppendorf lids were opened to avoid pressure changes during aspiration. The aqueous sample was analysed for quantification using LC/MS. With the PBS aqueous, the solvent front containing PBS salts were diverted to waste to avoid changes to detection sensitivity.

To determine LogP values, the concentration determined by LC/MS (e.g. 650 ng/ mL) was subtracted from 8000 ng/ mL to determine concentration in octanol. Log P values were calculated as Log_{10} (concentration in octanol/ concentration in aqueous).

Chapter 3: Development of PBTK models for BFRs and herbicides

3.1 Abstract

In this chapter, models were built to assess internal exposure to two types of environmental chemical hazards: herbicides (using the representative member picloram) and a class of chemicals called the brominated flame retardants (BFRs). The UK population can be exposed to BFRs that are incorporated into many consumer products such as plastics, synthetic fibres and polyurethane foam used in furniture (Stapleton *et al.* 2009) and baby products (Stapleton *et al.* 2011). Physiologically-based toxicokinetic (PBTK) models can be used to assess internal human exposure to BFRs from expected external doses and indirectly via human bio-monitoring data. PBTK models are mathematical representations of processes affecting a chemical's *in vivo* toxicology: absorption, distribution, metabolism and excretion (ADME). Because internal dose has a more direct temporal and spatial relationship with toxicological response than external dose, PBTK models can potentially inform chemical risk assessment and form an important part of the risk characterisation.

In this chapter, PBTK models were developed to assess UK domestic exposures to BFRs and environmental and occupational exposures to herbicides. Initial work develops rat PBTK models using Bayesian methods with *in vivo* and *in vitro* data.

BFRs are lipophilic, so their tissue uptake is limited by tissue blood flow rather than membrane permeability, hence 'perfusion-limited' models were constructed for BFRs. Conversely, a 'permeability-limited' model was developed for the herbicides (picloram) reflecting relatively slow permeability through tissue membranes, a consequence of its hydrophilicity. These rat PBTK models were coded into simulation and modelling software MCSim, and quality assured by performing

discrepancy tests with the same models built in GastroPlus PBPKPlus^{TM} software. Monte Carlo Markov chain (MCMC) analysis was applied to calibrate the picloram model: prior distributions were assigned to physicochemcial and biochemical model parameters reflecting population variability (Bayesian prior) and convoluted with rat pharmacokinetic data to obtain posterior distributions of optimised parameter values (Bayesian posterior). A permeability- (vs perfusion-) limited model best described picloram pharmacokinetic data; the permeability-surface area product was optimised to 3.32 - 4.03 x 10^{-4} mL/ sec/ mL-tissue (95% range). Stomach permeability and blood/ plasma concentration ratio were found to be sensitive physicochemical PBTK parameters, which require accurate laboratory determination (normalised sensitivity coefficients 0.89 and 1.00 respectively). The difference between predicted and observed pharmacokinetic data was interpreted mechanistically: transporters were modelled at kidney and liver apical membranes.

3.2. Introduction

3.2.1 Perfusion- and permeability-limited tissue models

BFRs are highly lipophilic (Hites 2004, Schecter *et al.* 2005, Weijs *et al.* 2012). Subsequently, their rate of uptake into tissues following exposure is not limited by their membrane permeability (which is high), but by the blood flow rate to that tissue. Therefore, perfusion-limited models are expected to best describe the *in vivo* disposition of these chemicals. Herbicides are less lipophilic than BFRs, and their rate of uptake into tissue cells following exposure is limited by their relatively slow permeation through the tissue basolateral membrane. Thus, permeability-limited models are likely to be more suitable than perfusion-limited models for simulating the toxicokinetics of herbicides.

3.2.2 Gastrointestinal tract models

Huang *et al.* (2009) provide an overview of the GIT models used in PBTK modelling, which vary in complexity in terms of the number of toxicokinetic processes they model. For example the Grass model is relatively simple. It includes GIT transit, dissolution (for ingestion of chemicals in solid form), and passive diffusion (Grass 1997). The gastrointestinal tract absorption (GITA) model is more complex as it integrates the aforementioned toxicokinetic processes in addition to metabolism occurring within enterocytes (Kadono *et al*. 2002). The advanced compartmental absorption and transit (ACAT) model in GastroPlus extends the GITA model with, for example, the inclusion of active transport (Simulations Plus 2013a). Due to the complexity of the ACAT model and its implementation within the GastroPlus software, this model was selected as the appropriate model to use within MCSim.

3.2.3 Chapter aims

- In MCSim, build and validate perfusion- and permeability-limited tissue models and a suitable gastrointestinal tract model.
- Calibrate the permeability-limited rat PBTK model to picloram toxicokinetic data using Bayesian analysis.

3.2.4 Picloram toxicokinetic data (reproduced with permission of the rights holder, Dow AgroSciences).

The toxicokinetics of 14C-labeled picloram was investigated in male Fischer 344 rats by Nolan *et al.* (1980) and radioactivity was quantified by liquid scintillation spectrometry. As picloram is not extensively metabolised, radioactivity can be used to measure the kinetics of picloram as the parent compound. 9.6 mg/ Kg and 1634 mg/ Kg doses of picloram dissolved in solution (as potassium salt) were administered via oral gavage to 3 and 2 rats, respectively. 14 mg/ Kg and 160 mg/ Kg doses of picloram were administered via intravenous (iv) injection (2-3 minutes infusion time) through jugular cannulas to 3 and 2 separate rats, respectively. Rats were housed in glass metabolism cages permitting urine and faeces collection. Rat chow and tap water were provided ad libitum, and rats were not fasted before dosing. The concentration of radioactivity in the plasma and excrement was recorded over 48 hours (used for PBTK model calibration). Rats were subsequently sacrificed and the concentrations in several tissues (e.g. liver and adipose) determined.

The report of Nolan *et al.* (1980) indicates picloram is rapidly excreted (predominantly via the urine) and little accumulates in body tissues. 48 hours after oral administration of the 9.6 mg/ Kg dose, 84.72 ± 7.20 % of the dose was excreted in urine, whilst 10.67 ± 4.69 % was excreted in faeces. Furthermore, by 48 hours after iv administration of the 14 mg/ Kg dose, 90.59 ± 0.74 % of the dose

was excreted in urine, and 2.66 ± 1.22 % in faeces. With this dose, the concentration of radioactivity in all tissues (except the GI tract) was ≤ the limit of detection (0.02 mg/ Kg; based on sample size, background radioactivity and activity of administered 14C-picloram). The authors observed that, following iv administration of 14 mg/ Kg, the clearance of picloram from the plasma (34.3 mL/ min/ Kg) 1) exceeded the glomerular filtration rate (3-10 ml/ min/ Kg), and 2) was similar to the clearance rate of para-aminohippurate (approximately 30.7 mL/ min/ Kg; Lote *et al.* 1985) known to be actively secreted by the kidney proximal tubules (Tanner & Isenberg 1970). Therefore, active secretion of picloram as the parent compound in the kidney was inferred and modelled here.

3.3 Methods for constructing PBTK models for herbicides and BFRs

Equations 1-10, 13, 19, 23-28, 31, 34, 39, 42-43 and 49-52 (Appendix 1) were taken with permission directly from the GastroPlus manual (Simulations Plus 2013b). Equations 44-45 were adapted from Shelia 2012. Remaining equations are not in the manual so were adapted from Simulations Plus.

3.3.1 Perfusion and permeability-limited tissues

A perfusion-limited model structure was adopted for BFRs (Figure 3.1). Unlike permeability-limited models, transporters along the tissue's cell membrane are not modelled: it is assumed the rate of passive diffusion greatly exceeds the rate of active transport across the membrane. Thus, the extracellular and intracellular spaces constituting the tissue are not modelled as separate compartments. Poulin and Theil's homogenous method was used for calculating partition coefficients (Kp's) (Poulin & Theil 2000, Appendix 1). Under *in vitro* conditions, Kp is calculated as the concentration in a specific tissue divided by the concentration in plasma under steady-state conditions using rapid equilibrium dialysis, thereby giving a quantitative indication of chemical

accumulation in that tissue. Hence Kp is an example of a physicochemcial parameter, as it is reliant on both the physiology and the chemical itself.

A 'permeability-limited' model structure was adopted for herbicides (Figure 3.2). The extracellular space is modelled as an additional compartment separating the intracellular space from the vascular space. Kp relates to the chemical partitioning through the vascular membrane into the extracellular space, thus Kp is calculated differently for permeability-limited tissues using Poulin & Theil's extracellular method (Poulin & Theil 2000). The permeability-surface area product (PStc, in mL/ sec/ mL-tissue), the physicochemical parameter that describes the rate of permeation across the tissue basolateral membrane, was scaled according to intracellular tissue volumes.

For perfusion and permeability-limited tissues, a constant RAtp value was assumed for all tissues except adipose (N.b. Permission not received to reproduce values from rights holder Simulations Plus, Inc. Values available at Simulations Plus (2013a)). Ratp is the ratio of albumin concentration in tissue over plasma, and is used in the Poulin equation (Poulin & Theil 2002) to calculate fraction unbound in tissue (Appendix 1). An equation published by Leo *et al.* (1971) and modified by GastroPlus (Simulations Plus 2013b) was used to calculate logP_adi: the logarithm of the vegetable oil: water partition coefficient of neutral drug molecules for adipose.

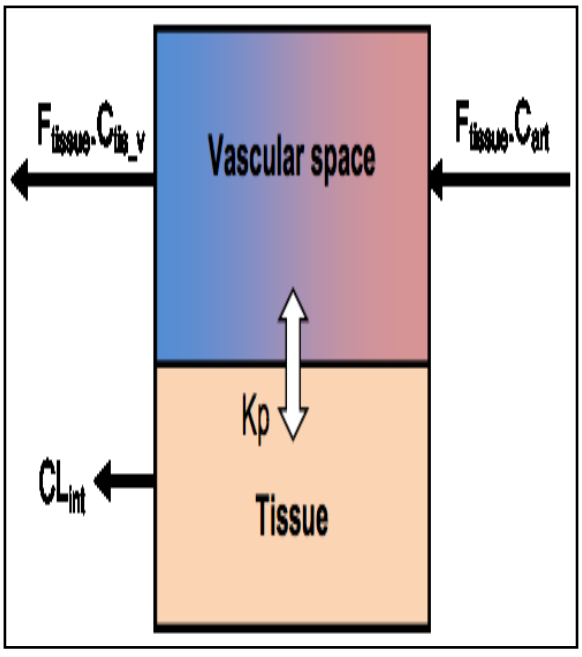


Figure 3.1: Model for perfusion-limited tissues. The rate of chemical entry into the tissue is given by the product of blood flow rate (F_{tissue}) and arterial concentration (C_{art}). Conversely, the rate of chemical exit from the tissue is given by the product of F_{tissue} and the venous tissue concentration (C_{tis_v}), which is calculated as a function of the tissue partition coefficient (Kp). C_{tis_v} decreases when there is intrinsic tissue clearance (CL_{int}). The bi-directional arrow indicates the chemical can diffuse in either direction across membranes. Figure adapted with permission from Simulations Plus 2013b.

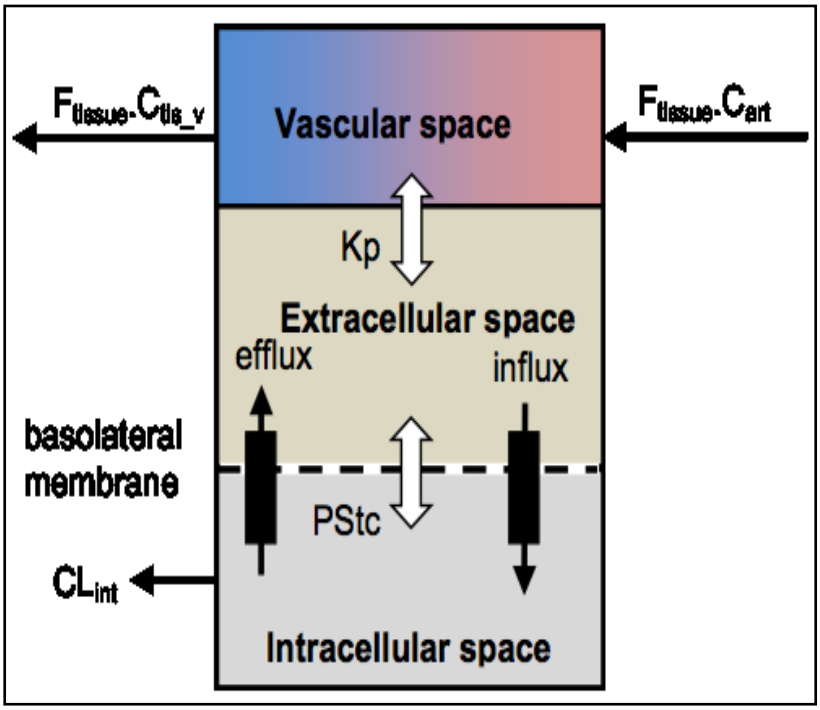


Figure 3.2: Model for permeability-limited tissues. Herbicides are less lipophilic than BFRs so their rate of uptake into tissue cells (where possible enzymatic clearance occurs, CL_{int}) is limited by their permeability across the basolateral membrane, where efflux and influx transporters can be situated. Figure adapted with permission from Simulations Plus 2013b.

3.3.2 Perfusion-limited kidney and liver models

The model for the kidney has additional functionality, reflecting its unique role in excretion (Figure 3.3). This model extends the perfusion-limited tissue model with the inclusion of a compartment for the kidney tubule. Uptake into the kidney tubule occurs through two main routes: glomerular filtration and permeability through the apical membrane.

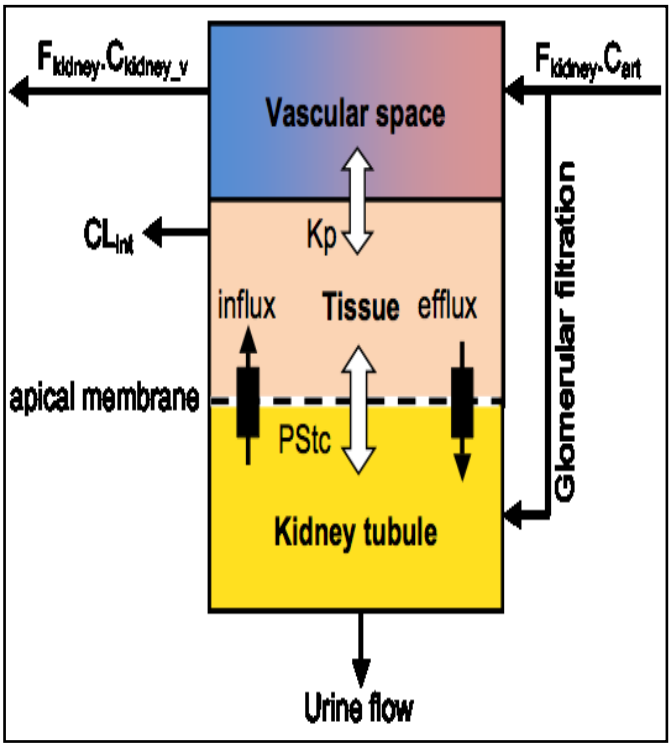


Figure 3.3: Model for perfusion-limited kidney. Permeability through the apical membrane can be categorised into both active transport (transporter mediated) and passive diffusion (a function of the permeability-surface area product, PStc). Michaelis-Menten kinetics are used to describe the activity of influx and efflux transporters, and also enzymes present in the tissue eliciting CL_{int}. Thus a unique approach is taken for kidney and liver where uptake into the kidney tubule and bile canaliculi respectively is described in terms of permeability of the apical membrane where transporters can be specified. The urine flow rate is modelled as a function of both glomerular filtration and permeability through the tissue apical membrane. Figure adapted with permission from Simulations Plus 2013b.

Given its important role in metabolism and excretion, the liver also has additional functionality compared with the more generic compartments. The *in vivo* liver is perfused by the portal vein (which is innervated by the splenic vein) and the hepatic artery. The i*n silico* approach taken here models a hepatic junction which is innervated by the hepatic artery, the splenic vein and the 'gut blood' separately before entering the vascular space of the liver (Figures 1.1 & 3.4). The vascular space thus represents the mixing of arterial and venous blood along hepatic sinusoids.

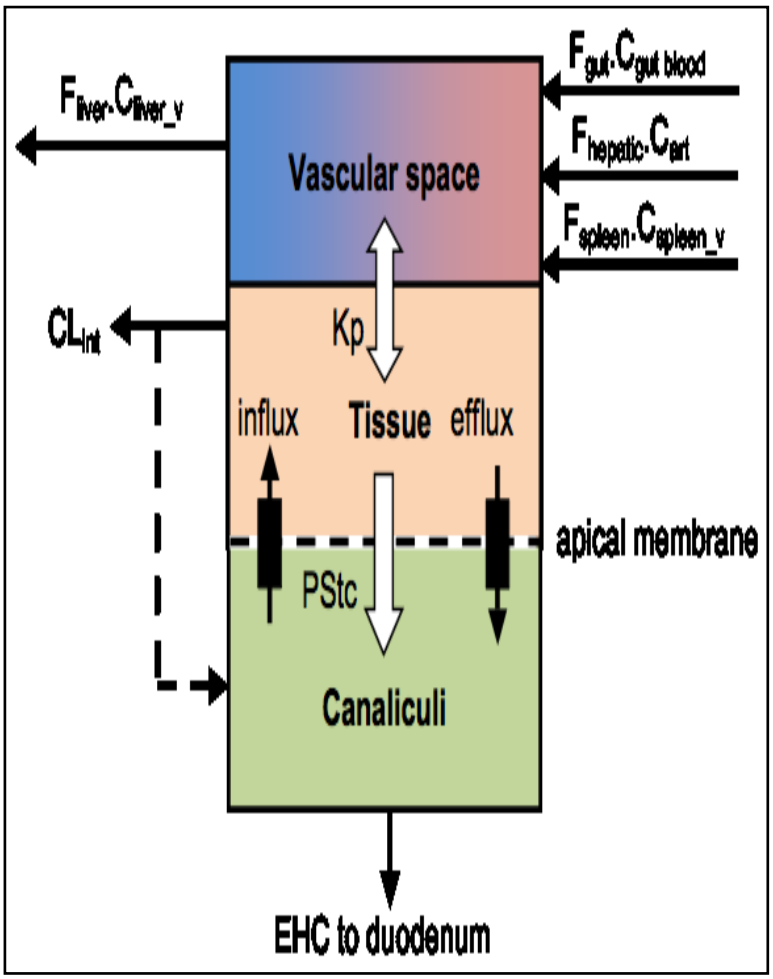


Figure 3.4: Model for perfusion-limited liver. The liver is perfused by the 'gut blood', splenic vein and hepatic artery. Similar to the kidney model (Figure 3.3), a separate compartment is included for bile canaliculi. Uptake into this compartment is defined in terms of permeability of the apical membrane (i.e. active transport and passive diffusion) or as a constant fraction of total enzymatic clearance, CL_{int} (dashed arrow). The chemical cannot diffuse from canaliculi to tissue due to binding bile salts. If enterohepatic circulation (EHC) is 'switched on' for simulation, bile flows into the duodenum dissolved compartment (Figure 10), where the chemical is available for reabsorption. Figure adapted from Simulations Plus 2013b.

3.3.3 Permeability-limited kidney and liver models

The permeability-limited kidney model differs from the perfusion-limited kidney model, as permeability across the basolateral membrane of kidney cells is modelled in addition to permeability across the apical membrane (Figure 3.5).

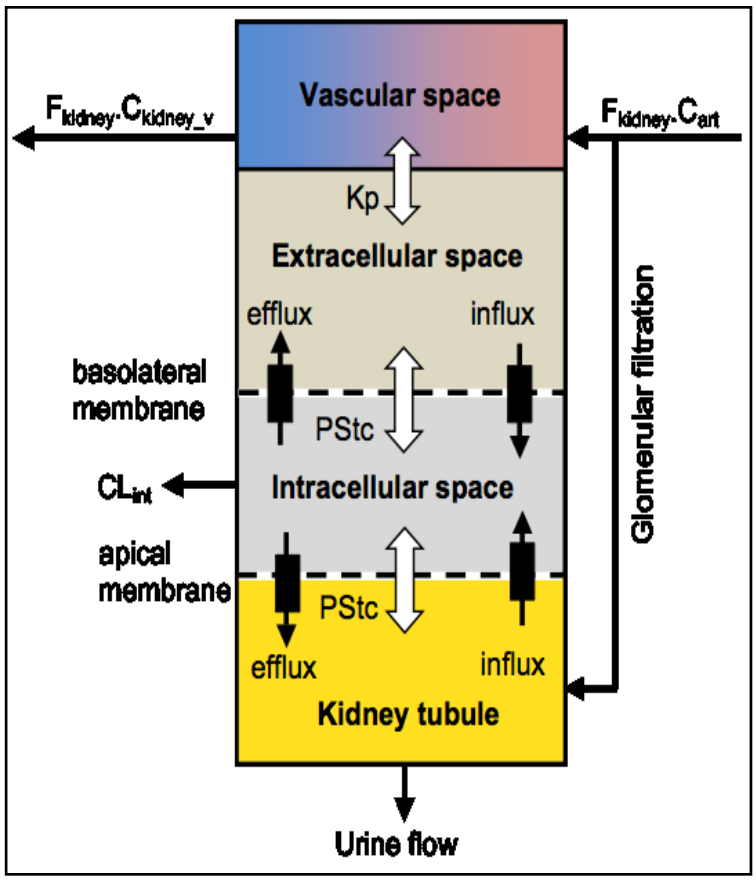


Figure 3.5: Model for permeability-limited kidney. The chemical present in the vascular space can partition across the vascular membrane into extracellular space, where it can diffuse across the basolateral membrane and/ or be actively transported into the intracellular space via influx transporters therein. Once in the intracellular space, it can be metabolised, transported or diffuse back into the extracellular space, or transported or diffuse into the kidney tubule. Figure adapted with permission from Simulations Plus 2013b.

A liver permeability model includes a basolateral membrane (interfacing extra- with intracellular spaces) (Figure 3.6). Transport across this membrane can occur via passive diffusion and possibly active transport.

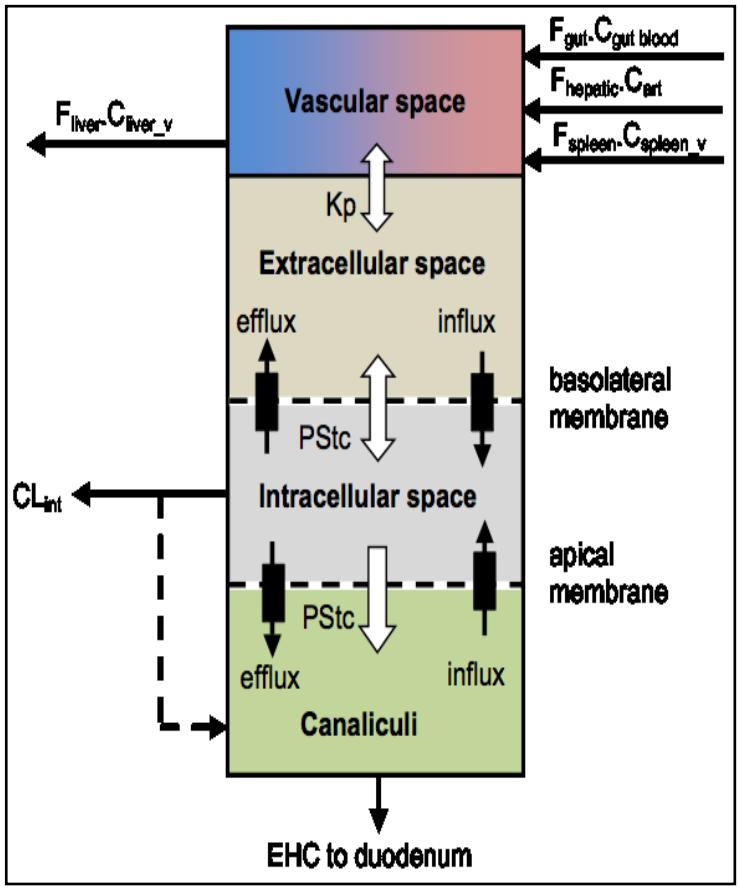


Figure 3.6: Model for permeability-limited liver. There are three rates of chemical entry: directly from the gut, spleen and hepatic artery. Once the chemical has partitioned into the extracellular space (Disse space) it can then diffuse into the intracellular space. Subsequently, it can undergo metabolism, diffuse and/ or be actively transported into the bile canaliculi. Uptake into canaliculi can be defined as a fraction of total metabolised (CL_{int}; dashed arrow) instead of via apical membrane permeability. Figure adapted from Simulations Plus 2013b.

3.3.4 Gastrointestinal tract (GIT) model

The ACAT model developed by Simulations Plus, and implemented in their software GastroPlus, has nine sequential compartments for the GIT: stomach, duodenum, jejunum 1-2, ileum 1-4 and colon (Simulations Plus 2013a). In this project, the nine compartments of the ACAT model were implemented into MCSim for both perfusion and permeability-limited models. Initially, Fick's first law of passive diffusion was not implemented at the gut membrane. This facilitated the validation of equations relating purely to chemical transit along the GIT. Subsequently Fick's law, which determines bi-directional flow across plasma membranes, was implemented at the gut endothelial

membrane where enterocyte compartments were also modelled. This is termed the 'concentration gradient GIT model' (Simulations Plus 2013b). For calibration of the picloram model, the concentration gradient GIT model was simplified (Figure 3.7) so that a single compartment represented GIT compartments jejunum 1 to ileum 4 - that is, a four compartment GIT model (use of simplified vs full ACAT model is discussed later).

A relatively short stomach transit time (0.1 hr) was used for oral solution (*cf.* tablet) administration. The Johnson model was used for dissolution rate (Lu *et al.* 1993). Enterohepatic circulation (EHC) was activated given evidence for picloram EHC (Nolan *et al.* 1980) - discussed below. The quantity excreted in bile was calculated in terms of permeability (both diffusion and active transport) across the liver apical membrane, instead of a constant fraction (Fbcl) of that metabolised in hepatocytes, as there is no evidence for hepatic metabolism of picloram (Nolan *et al.* 1980). A constant flow of bile into the dissolved duodenum compartment was modelled (rats have no gall bladder), where reabsorption of picloram into gut blood was permitted. Effective permeabilities (Peffs) and surface enhancement factors (SEFs) for each GIT compartment are modelled. Whereas Peff relates to changes in porosity along the gut endothelial membrane, SEF relates to changes in surface area/ volume ratio along the gut (e.g. due to the presence of cilia). Both are involved in calculating gut absorption constants (Appendix 1) and are amenable to optimisation via MCMC analysis (Section 3.3.6.2).

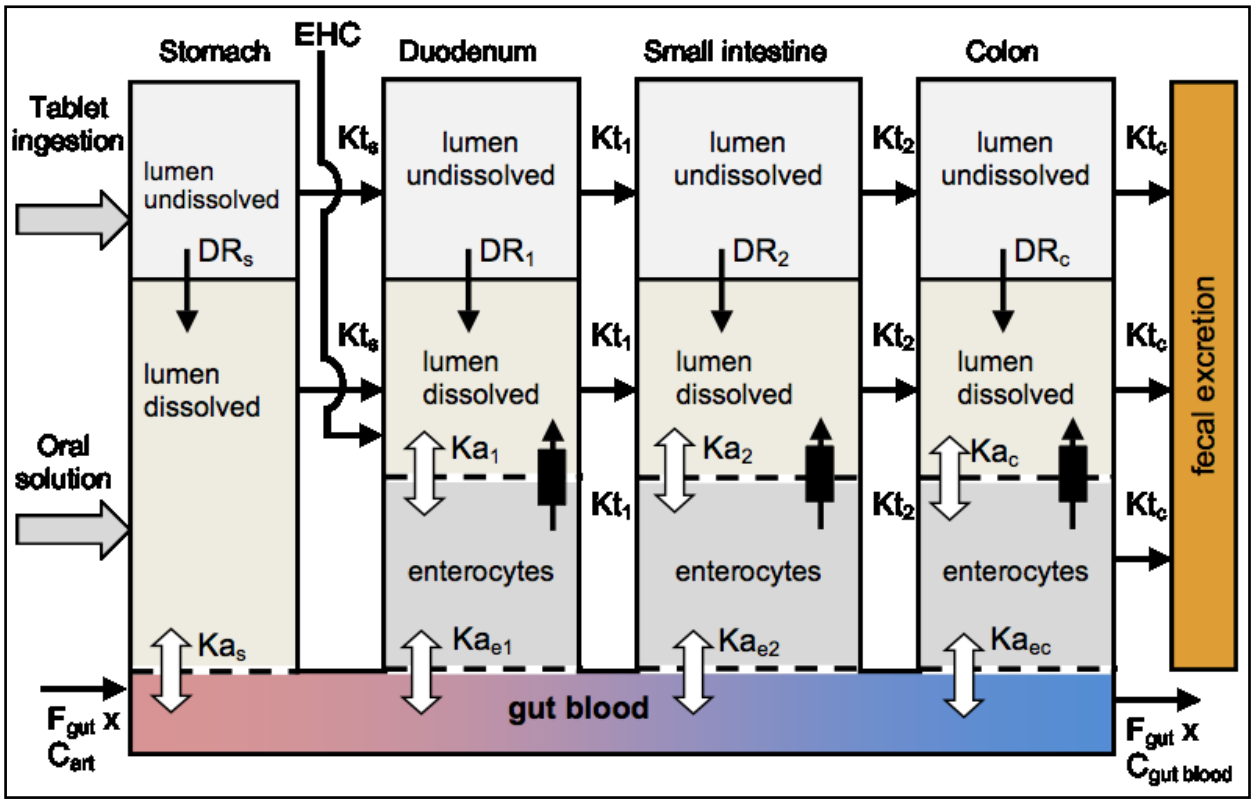


Figure 3.7: Concentration gradient gastro-intestinal tract model. Fick's first law of passive diffusion is implemented at gut endothelial and apical enterocyte membranes. Animals can ingest chemicals in liquid ('solution') or solid ('tablet') form. The former enters the 'stomach lumen dissolved' compartment where it can be absorbed into the 'gut blood'. The latter enters the 'stomach lumen undissolved' compartment where it is subject to a dissolution rate (DR_s). The chemical can enter the 'duodenum lumen dissolved' compartment through multiple pathways described in Appendix 1. The amount of chemical excreted is calculated as the total amount in all colon compartments multiplied by the colon transit time (Kt_c). Efflux transporters have been modelled at apical enterocyte membranes. Figure adapted with permission from Simulations Plus 2013b.

3.3.5 Model construction and quality assurance: MCSim *vs* Gastroplus

PBTK models were coded into the simulation and modelling code MCSim V.5.3 which uses LSODES as the differential equation solver (Hindmarsh 1983) and Metropolis-Hastings sampling for MCMC simulation (Hastings 1970, Metropolis *et al.* 1953). These PBTK models were quality assured by performing discrepancy tests with the same models built in GastroPlus PBPKPlus™ software (i.e.

calculating the percentage difference between the two predictions) (Simulations Plus 2013a). GastroPlus Absorption, Distribution, Metabolism, Elimination and Toxicity (ADMET) property predictor was used to generate *in silico* predictions for physicochemical parameters for all BFRs and herbicides. These include the blood/ plasma concentration ratio (rbp), the logarithm of octanol/ water partition coefficient of neutral drug molecules for tissues (logP_tis), and the experimental fraction unbound in plasma ($f_{up,exp}$). These were subsequently used to calculate partition coefficients (Table 3.1).

Table 3.1: *In silico* predictions for physicochemical parameters for BFRs and herbicides.

Chemical	logP_tis	Rbp	$F_{up,exp}$	Kp			
				Liver	Adipose	Brain	Kidney
EBTBPE	5.67	1.02	0.0389	6.65	74.41	16.05	6.05
DBDPE	10.08	1.13	0.0399	6.66	74.49	16.05	6.06
TBBPA	6.84	0.85	0.0124	6.66	74.49	16.05	6.06
BEHTBP	9.33	0.63	0.0797	6.66	74.49	16.05	6.06
BTBPE	7.70	1.02	0.0538	6.66	74.49	16.05	6.06
Picloram	2.09	0.72	0.0659	0.53	0.20	0.53	0.53
Triclopyr	2.72	0.63	0.0421	0.52	0.18	0.52	0.52
Haloxyfop-methyl	3.93	0.55	0.0173	0.51	0.16	0.51	0.51

In silico predictions reproduced with permission of the rights holder, Simulations Plus Inc.

3.3.6 Preliminary work using picloram toxicokinetic data

Picloram, triclopyr and haloxyfop R&D toxicology reports were obtained from DAS. Permeability limited and perfusion limited models were constructed assuming rat physiology, specifically F344 rats because these were used to generate the herbicide toxicokinetic data in Nolan *et al*. (1980) (described in Section 3.2.3). Parameter values for this strain are implemented in GastroPlus. F344 rat parameters were taken from Hosseini-Yeganeh & McLachlan 2002 and Simulations Plus 2013a.

3.3.6.1 The picloram toxicokinetic data (Nolan *et al.* 1980; reproduced with permission of the rights holder, Dow AgroSciences).

In the pilot study of Nolan *et al.* 1980, evidence was acquired for enterohepatic circulation (EHC), where 0.4 % of a 1400 mg / Kg oral dose administered to a bile-cannulated male F344 rat was excreted in bile 24 hours post-dose. This data was not provided in the main study and so this information was used to generate surrogate measurements for the subsequent IV and oral studies whose data were used to calibrate the PBTK model for picloram in this study. It was assumed the value of 0.4 % is independent of dose, thus for the 9.6 and 1635 mg/ Kg oral doses, it was assumed that 0.0096 and 1.634 mg (respectively) are excreted in bile 24 hours post-dose assuming a 250 g rat.

GrabIt™ V1.5 data capture software was used to extract the toxicokinetic data including measurement uncertainties from graphs in Nolan *et al.* 1980. For computational convenience, incremental urine data were combined to give cumulative amounts excreted in urine during the time-course of the study (the PBTK model as coded does not model cumulated amounts excreted over discrete time intervals, e.g. over 24 hours). Standard deviations specific to each data point were assigned to plasma, urine and bile likelihoods reflecting primarily inter-individual variability.

3.3.6.2 Preliminary MCMC analysis for model calibration (picloram)

The combination of nominal picloram permeability systemic model and simplified four compartment ACAT model were adopted for calibration. Physiological parameters were fixed at values specific for F344 rats, but physicochemical and biochemical parameters were calibrated: prior distributions were assigned to 1) Peff_sto, 2) Peff, 3) SEF, and 4) kidney and liver transporter V_{max}, and 5) PStc. The distributions reflect population variability and are based on an initial literature review (Table 3.6). The prior distribution for rat Peff was informed by Fagerholm *et al.* 1996, who reported rat Peffs for ten compounds (not including picloram) with a suitably broad range of physicochemical properties. Prior distributions for SEFs were based on the range of values permissible as input to the GastroPlus gut model (Simulations Plus 2013a). These values were based on data from Snipes 1997 and Wilson 1967, and were derived by optimising against experimental data for drugs with measured parameters such as solubility, logP, permeability, percent absorbed, bioavailability and plasma toxicokinetic data. A nominally wide prior distribution was assigned to transporter Vmax. Transporter expression level and Km were kept constant at 0.01 (mg transporter/g-tissue) and 0.05 (µg/ mL), respectively. The estimation of tissue-specific PStc values for PBTK modelling is not well established due to poorly understood physiological aspects of specific tissues such as cell surface areas. The method of scaling PStc values to tissue cell volumes implemented here is recent (Lukacova *et al.* 2011) and PStc values are not widely reported in the literature. Therefore a suitably wide prior distribution was assigned to PStc. To avoid numerical errors arising from negative parameter values during the MCMC calculations, truncated normal prior distributions were used and left truncated at zero. They were also right truncated at very high maximum values because MCSim requires that both upper and lower bound truncation points are specified when a truncated distribution is adopted. Left truncation does not significantly affect the shape of the distributions because the chosen mean and standard deviations cause negative values to arise with very low probability. Proposal distributions were selected and tuned autonomously in MCSim.

MCMC was performed using the Metropolis algorithm as implemented in the code MCSim (Bois & Maszle 2008) to calibrate the model (Section 2.1). Physicochemical and biochemical parameters (above) were calibrated with low IV and oral dose data (9.6 and 14 mg/ Kg respectively) simultaneously through a joint analysis, where saturation of toxicokinetic processes is less likely. Calibration was verified by visually assessing the model's ability to fit plasma and urine data after low, and high IV and oral doses (160 and 1634 mg/ Kg respectively) (Nolan *et al.* 1980), assuming posterior mean values of parameters.

Markov chain convergence was confirmed by running multiple independent chains seeded with different random numbers and starting values of model parameters. Stationary distributions were obtained after around 300,000 iterations. Convergence was monitored by comparing posterior means every 100,000 iterations. The first 30,000 iterations were discarded as 'burn-in'. This choice is consistent with Geyer 1992 who suggested a burn-in of 1 - 2 % of total chain length is adequate. Microsoft Excel was used to perform all statistical analyses. Fractional coefficients of variation were calculated for prior and posterior distributions (stdev/ mean) to show the extent of variability about their respective means (Table 3.6), i.e. the 'broadness' of the distribution.

3.3.6.3 Sensitivity analyses

Sensitivity analyses were done to assess the influence of each model input parameter on model predictions. Calculated sensitivity coefficients (SC) were considered to indicate a significant response if the value was ≥ 0.1 (Table 3.6) (Shelia 2012). These values facilitate 1) validation of the MCMC analysis (i.e. parameters with high SC should have narrower posteriors and vice versa) and 2) prioritising which parameters to include in the MCMC analysis. The central difference method was used:

$$SC = ([f(I + \Delta I) - f(I - \Delta I)] \div 2\Delta I) \times (I \div f(I)) , \qquad [2]$$

where the difference above f(I + ΔI) and below f(I - ΔI) a central value for the input parameter (I; optimised mean, Table 3.10) are considered with respect to a model function (f) (Shelia 2012), in this case the maximum venous plasma concentration (C_{max}). The sensitivity coefficient (SC) was normalised (I ÷ f(I)) for easy comparison and ΔI was 2 %.

3.4 Results

3.4.1 PBTK model validation

3.4.1.1 Perfusion limited model for RBFRs

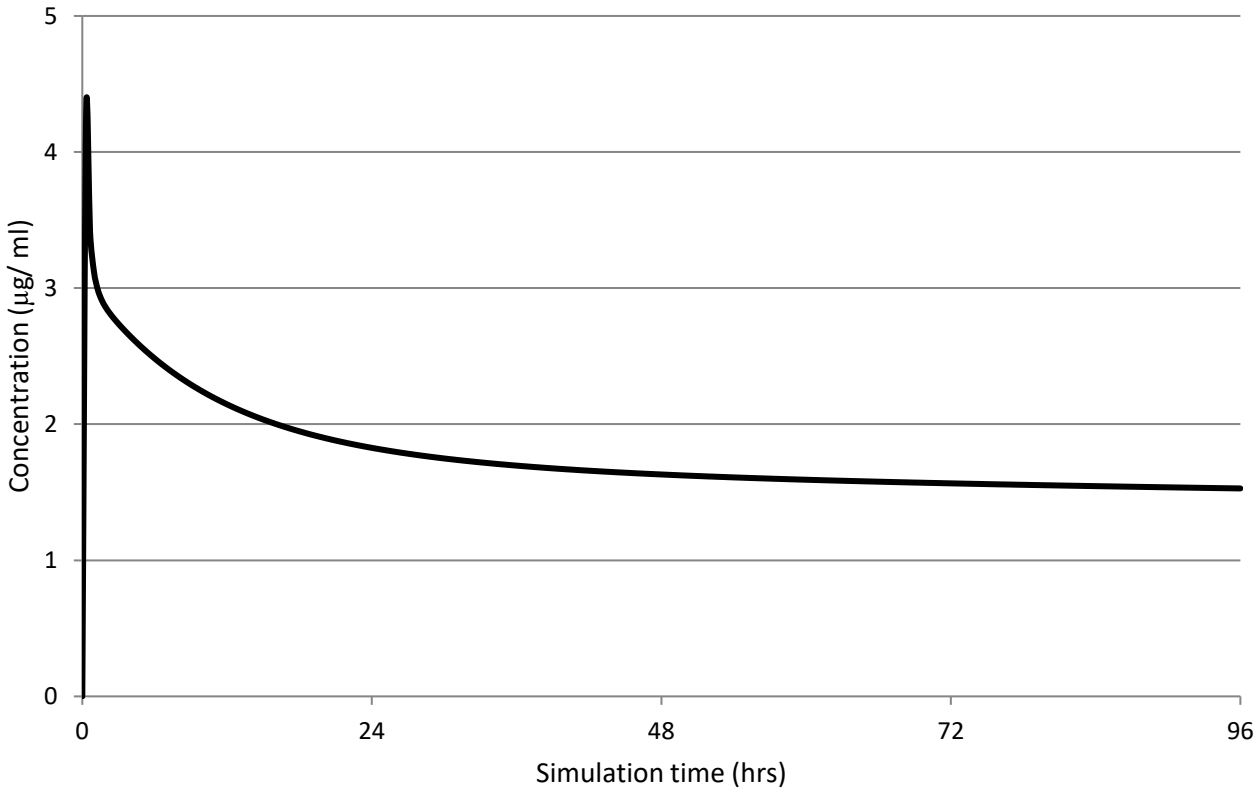
The perfusion-limited model coded into MCSim was quality assured by comparing simulation output with the same model built in GastroPlus PBPKPlus™ software (both using the same input settings). Table 3.2 shows low percentage difference between the two predictions after a 30-hour simulation, indicating good agreement between the two codes.

Table 3.2: Perfusion-limited tissue model with IV route after 30-hour simulation (discrepancy with GastroPlus).

Tissue Concentration	% Absolute Discrepancy
Adipose	2.75×10^{-3}
Liver	6.60×10^{-3}
Brain	4.33×10^{-3}
Kidney	4.52×10^{-3}
Rest-of-body	2.23×10^{-3}

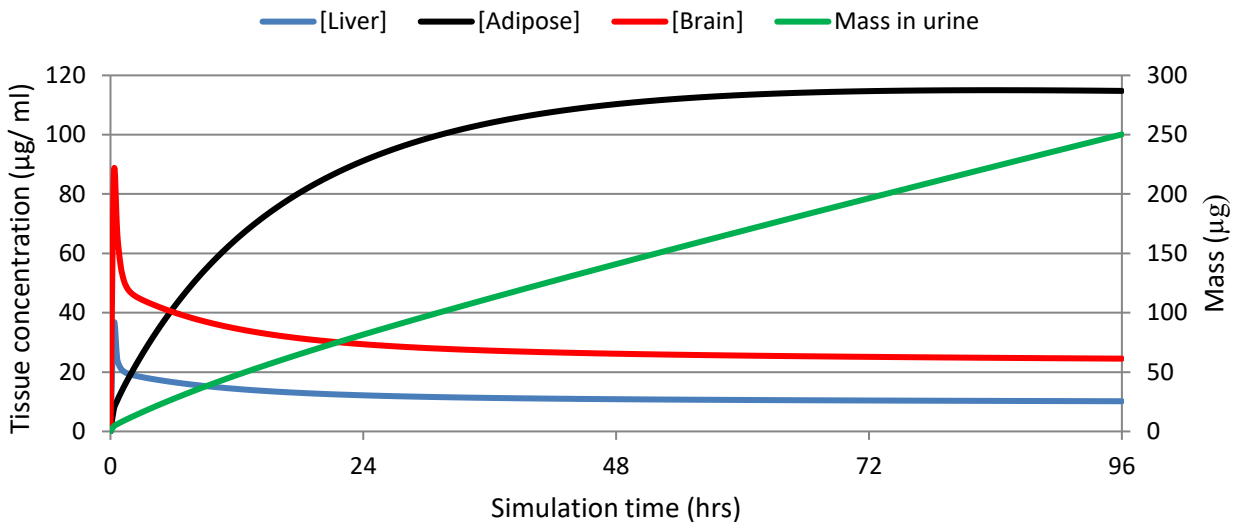
Preliminary systemic disposition of BFRs was simulated, using predicted physicochemical values (Table 3.1). Following an intravenous bolus dose of 14.0 mg/ Kg of EBTBPE to an F344 rat (at t = 0 hrs), EBTBPE is slowly cleared from the body. Bioavailability remains high (assuming no metabolism or active transport/ secretion in any tissues), as evident from Figure 3.8 which gives plasma clearance for EBTBPE.

Figure 3.8: Predicted plasma EBTBPE concentration in F344 rat following 14 mg/ Kg iv bolus dose of EBTBPE.



Corresponding tissue concentrations for liver, adipose and brain are displayed in Figure 3.9. EBTBPE is slowly excreted via kidneys as the parent compound, which is described by a simple first-order process (Appendix 1).

Figure 3.9: Predicted adipose, liver and brain concentrations, and amount excreted in rat for following 14 mg/ Kg iv bolus dose of EBTBPE.



3.4.1.2 Permeability-limited model for herbicides

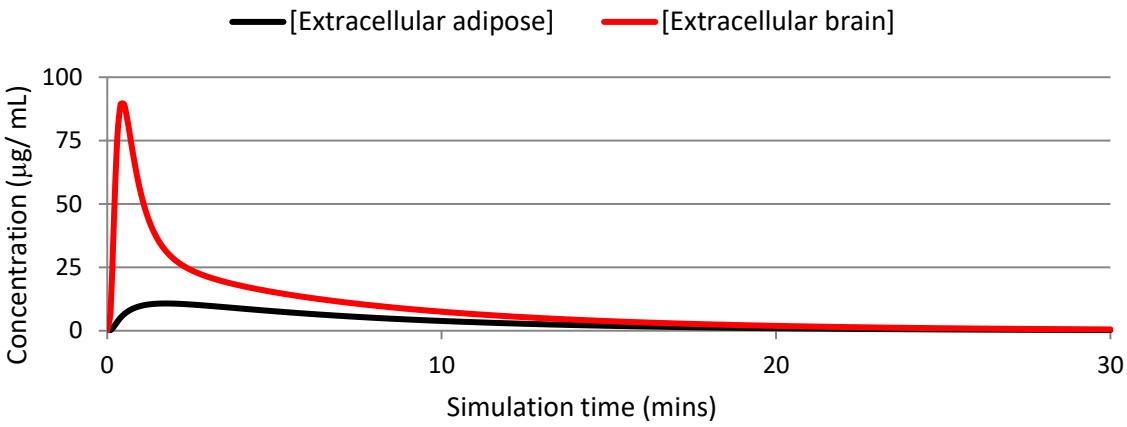
The permeability-limited model coded into MCSim was quality assured by performings discrepancy tests with the same model built in GastroPlus PBPKPlus™ software. Table 3.3 shows low percentage difference, and hence good agreement, between the two predictions after a 10-hour simulation.

Table 3.3: Permeability-limited tissue model with IV route after 10-hour simulation (discrepancy with GastroPlus).

Tissue Concentration	Tissue Compartment	% Absolute Discrepancy
Adipose	extracellular	4.90×10^{-3}
	intracellular	4.91×10^{-3}
Liver	extracellular	4.87×10^{-3}
	intracellular	5.00×10^{-3}
Brain	extracellular	4.90×10^{-3}
	intracellular	4.84×10^{-3}
Kidney	extracellular	4.97×10^{-3}
	intracellular	4.91×10^{-3}
Rest-of-body	extracellular	4.90×10^{-3}
	intracellular	4.98×10^{-3}

Preliminary systemic disposition of picloram was simulated, using predicted physicochemical values (Table 3.1), and assuming the posterior mean value of PStc (Table 3.6). Following an iv dose of 14.0 mg/ Kg to an F344 rat, picloram is quickly cleared from the body. Because it permeates slowly through tissue membranes, extracellular tissue concentrations are low and transient (Figure 3.10).

Figure 3.10: Predicted adipose and brain concentrations for picloram (following 14 mg/ Kg iv bolus dose) in F344 rat



3.4.1.3 Gastro-Intestinal Tract (GIT) model

Prior to simplification (see discussion), the additional gastrointestinal compartments were also modelled to validate the implementation of the ACAT model in MCSim. Table 3.4 displays the discrepancy between MCSim and GastroPlus model outputs when the 'unidirectional' GastroPlus gut model was used. I.e., Fick's first law of passive diffusion was not implemented at the gut endothelial membrane, and enterocyte compartments were not modelled.

Table 3.4: Discrepancy between GastroPlus and MCSim using 'unidirectional' gastro-intestinal tract model coupled with the perfusion/ permeability-limited model for EBTBPE/ picloram.

Gut lumen concentration (dissolved)	% Absolute Discrepancy (1 d.p.)
Duodenum	4.9×10^{-4}
Jejunum 1	2.9×10^{-4}
Jejunum 2	5.0×10^{-5}
Ileum 1	2.3×10^{-4}
Ileum 2	1.2×10^{-4}
Ileum 3	8.1×10^{-5}
Ileum 4	6.9×10^{-5}
Colon	7.4×10^{-5}

Simulation conditions: 1 hr simulation**,** intake via oral solution (2.4 mg), Peff's = 0 cm/ sec. EHC off.

Table 3.5 displays the discrepancy between MCSim and GastroPlus model outputs when the 'concentration gradient' GastroPlus gut model was used. I.e., Fick's first law of passive diffusion was implemented at the gut endothelial membrane, and enterocyte compartments were modelled.

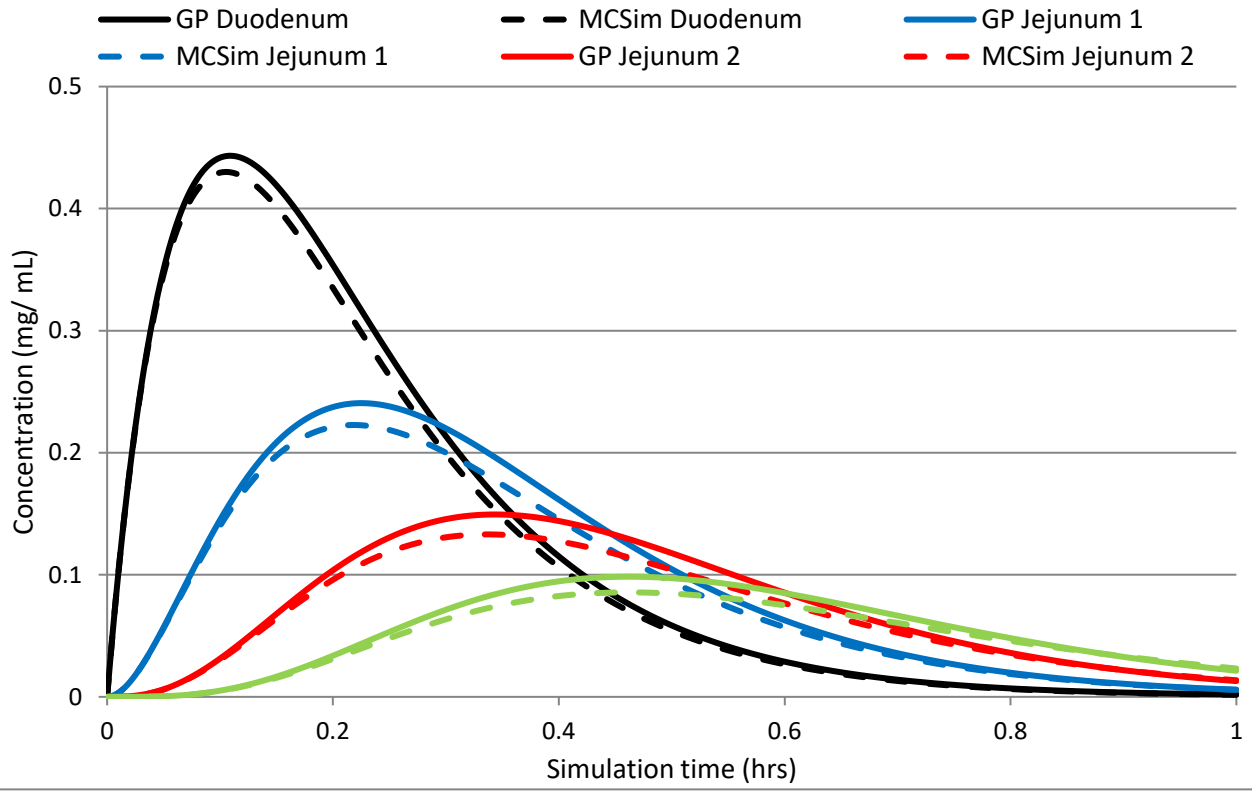
Table 3.5: Discrepancy between GastroPlus and MCSim using 'concentration gradient' gastro-intestinal tract model.

Gut lumen concentration (dissolved)	% Discrepancy (1d.p.)[1]	% Discrepancy (1d.p.)[2]
Duodenum	11.7	12.4
Jejunum 1	2.4	3.8
Jejunum 2	-5.2	-3.3
Ileum 1	-8.6	-6.1
Ileum 2	-8.3	-5.4
Ileum 3	-5.5	-2.3
Ileum 4	-1.3	2.1
Colon	15.2	18.7
(Venous plasma)	2.3	2.4

Simulation conditions: 1 hr simulation, intake via **1)** oral solution (2.4 mg) or **2)** tablet (2.4 mg), Peff's = 1.3 x 10^{-4} cm/ sec, SEF's = 1, perfusion-limited body compartments. EHC activated.

Figure 3.11 shows a visual comparison between GastroPlus and MCSim with the 'concentration gradient' gut model. Despite substantial discrepancy (Table 3.5), similar integration curves were obtained. For clarity, concentrations within the first the three gut compartments are displayed.

Figure 3.11: GastoPlus *vs* MCSim: gut lumen concentrations following oral solution ('concentration gradient' model).



3.4.2 PBTK model calibration and sensitivity analyses (picloram)

To verify that a perfusion-limited model would be unsuitable for picloram, preliminary simulations were run using this structure and predicted tissue Kp values for picloram. These are shown in Figure 3.12. However, it was less able to fit the toxicokinetic data (from Nolan *et al.* 1980) than the permeability-limited model (Figure 3.13). Using the perfusion-limited model, the sum of squared residuals for the low and high doses were 755.8 and 233829.0, respectively. With the permeability-limited model, the sum of residuals for low and high doses were 17.7 and 90115.2, respectively.

Subsequently, the permeability-limited model was selected for calibration with picloram toxicokinetic data.

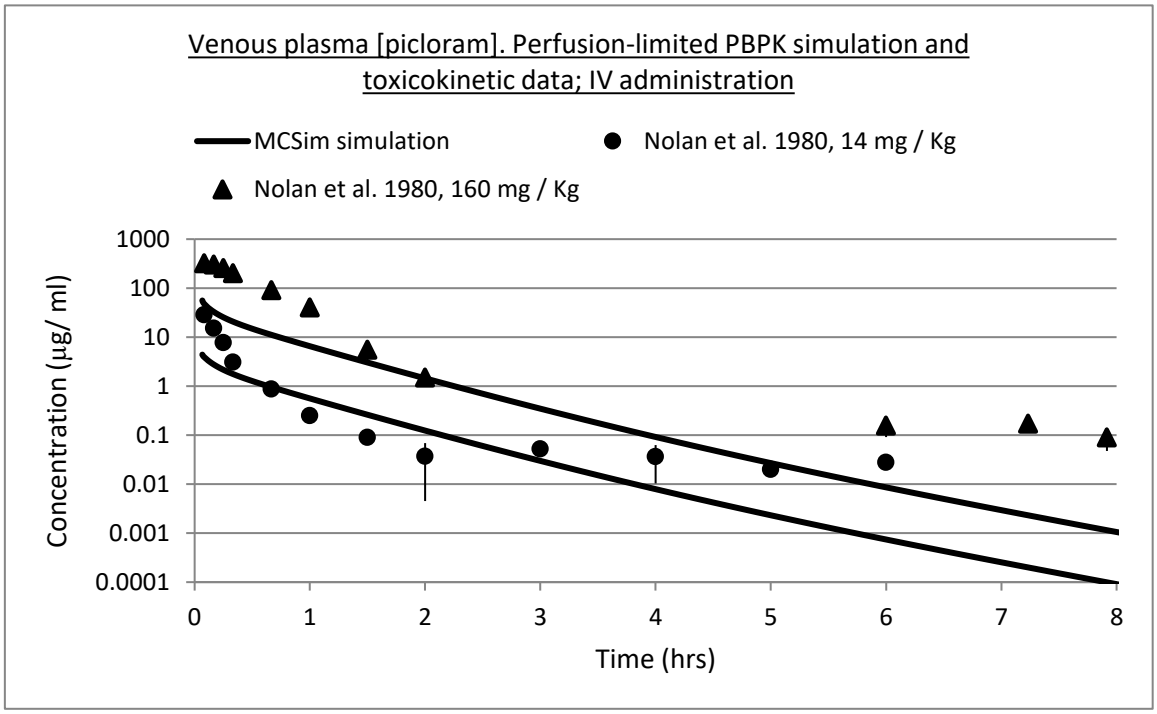


Figure 3.12: MCSim simulation (perfusion-limited model) with high iv dose of 160 mg/ Kg (upper line) and low iv dose of 14 mg/ Kg (lower line). Data represent mean ± SD for 3 low and 2 high dosed male Fischer 344 rats. Toxicokinetic data reproduced with permission of the rights holder, Dow AgroSciences.

MCMC analysis was done to calibrate the permeability-limited PBTK model with the iv and oral toxicokinetic data (combined into a single dataset for a joint analysis, using realistic errors) from Nolan *et al.* (1980). Thus, physiologically-realistic distributions were assigned to SEFs and Peffs for each GIT compartment, and also PStc and transporter V_{max} (Table 3.6). Good fits were obtained (Figure 3.13) indicating correctness of model structure.

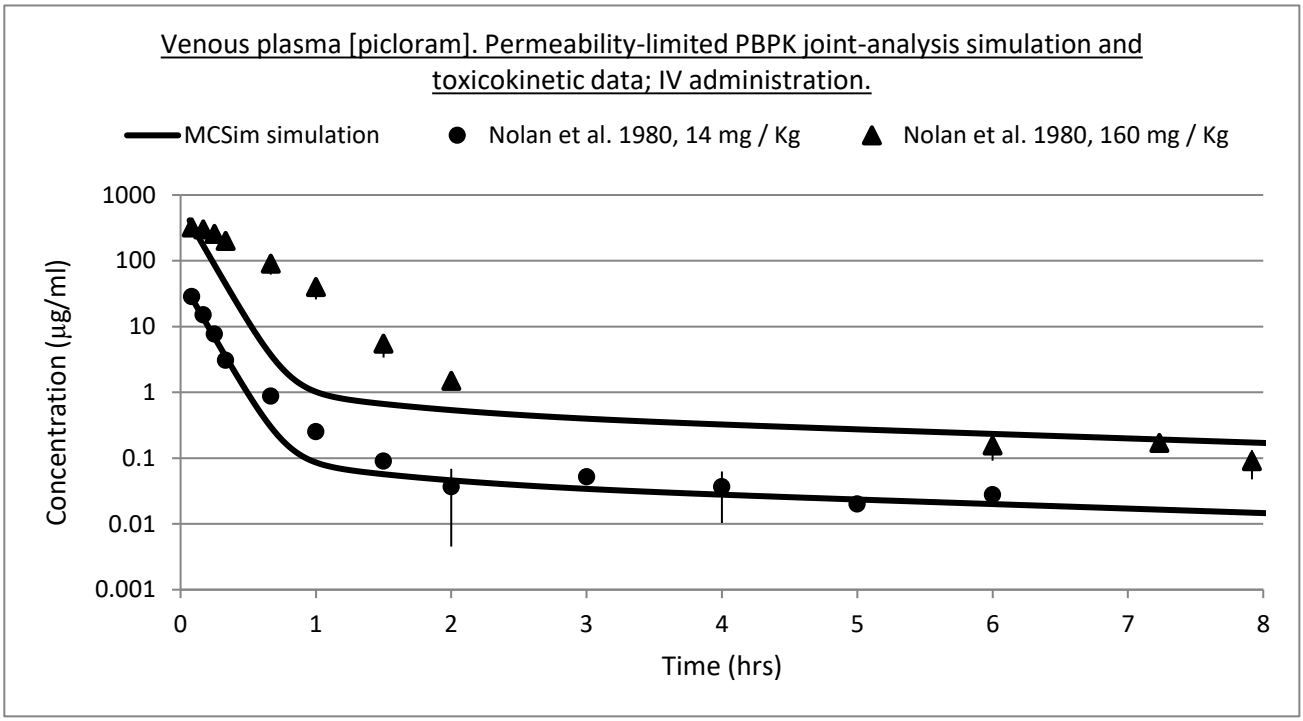


Figure 3.13: MCSim simulation (permeability-limited model) and picloram data with intravenous dose. Data represent mean ± SD for 3 low and 2 high dosed male Fischer 344 rats. Toxicokinetic data reproduced with permission of the rights holder, Dow AgroSciences.

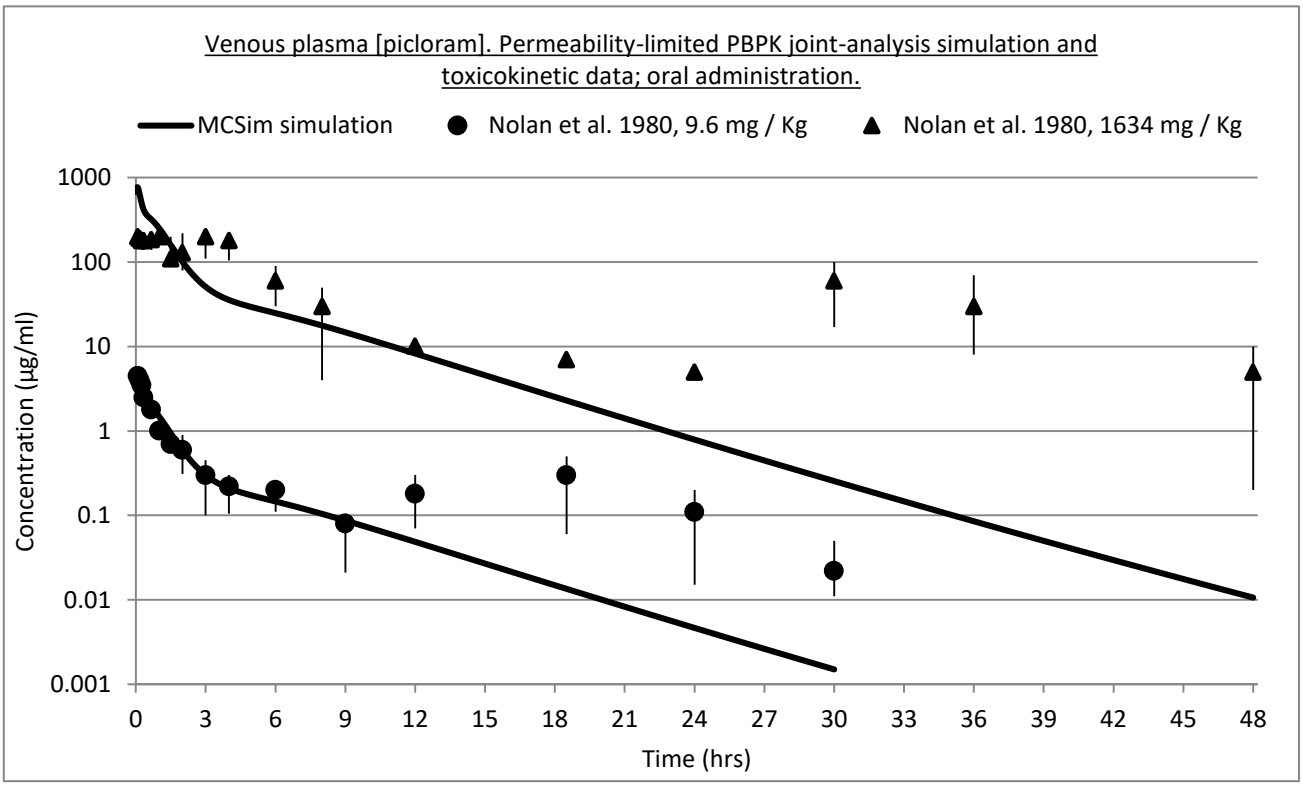


Figure 3.14: MCSim simulation (permeability-limited) and picloram data with an oral dose. Data represent mean ± SD for 3 low and 2 high dosed male F344 rats. Toxicokinetic data reproduced with permission of the rights holder, Dow AgroSciences.

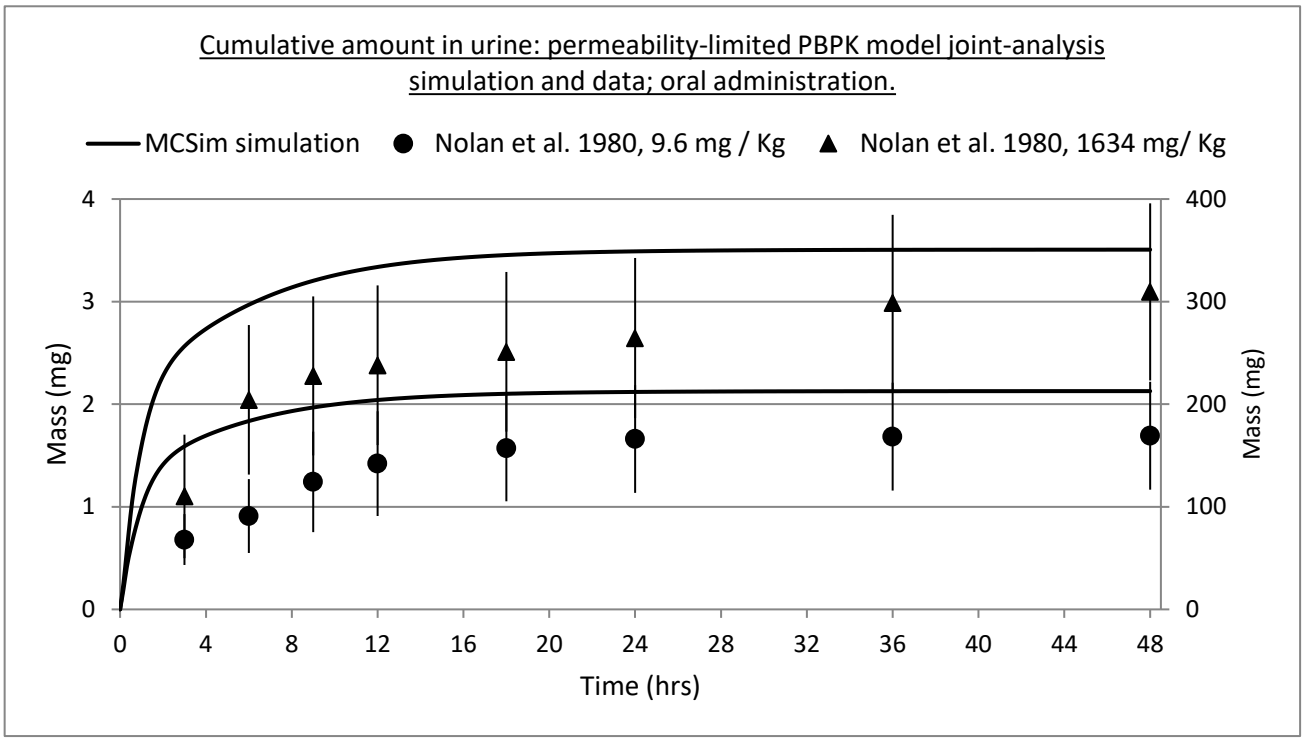


Figure 3.15: Cumulative amount in urine following 9.6 and 1634 mg / Kg oral dose. Data represent mean ± cumulative SD for 3 low and 2 high dosed male F344 rats. Toxicokinetic data reproduced with permission of the rights holder, Dow AgroSciences.

The posterior values from the joint analysis are given in Table 3.6. Parameters with posteriors that are significantly different from their priors are highlighted in bold. Of these three parameters, only Peff_sto has a significant sensitivity coefficient.

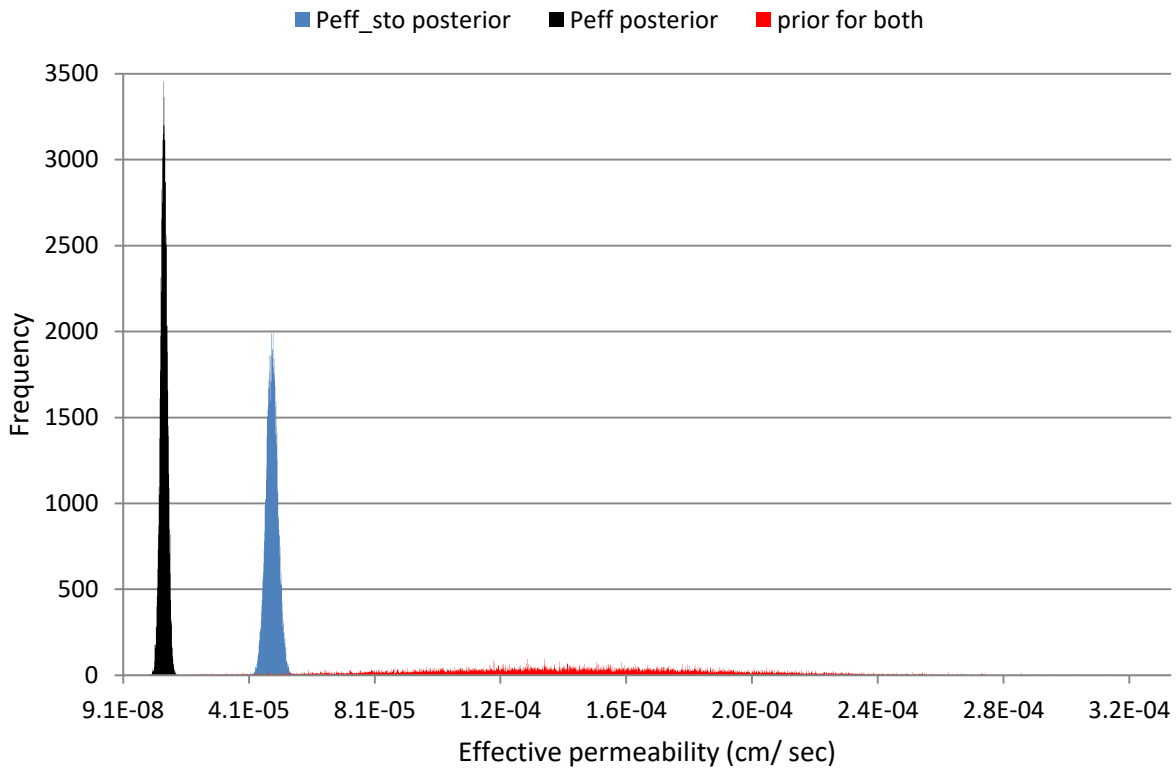
Table 3.6: Optimised parameter values for PBPK model with picloram data.

Parameter[1]	Prior		Posterior			SC[6]
	Distribution[2]	CV[3]	Mean[4]	Distribution[5]	CV[3]	
PStc	**Normal (5.0×10^{-3}, 1.0×10^{-3})**	**0.200**	**3.676×10^{-4}**	**(3.324×10^{-4}, 4.027×10^{-4})**	**0.048**	**0.000**
V_max_kid_b[2]	Normal (3.0, 0.7)	0.233	3.034	(1.655, 4.413)	0.227	0.000
V_max_kid_a[2]	Normal (3.0, 0.7)	0.233	3.043	(1.648, 4.437)	0.229	0.000
V_max_liv_a[2]	Normal (3.0, 0.7)	0.233	3.039	(1.662, 4.417)	0.227	0.000
Peff_sto	**Normal (1.4×10^{-4}, 5.0×10^{-5})**	**0.357**	**4.801×10^{-5}**	**(4.421×10^{-5}, 5.181×10^{-5})**	**0.040**	**0.889**
Peff	**Normal (1.4×10^{-4}, 5.0×10^{-5})**	**0.357**	**1.313×10^{-5}**	**(1.086×10^{-5}, 1.539×10^{-5})**	**0.086**	**0.033**
SEF_duo	Normal (5, 1)	0.200	6.618	(4.885, 8.350)	0.131	0.016
SEF_SI	Normal (5, 1)	0.200	1.064	(0.837, 1.491)	0.140	0.001
SEF_col	Normal (5, 1)	0.200	3.901	(1.771, 6.032)	0.273	0.000

1) See glossary (Appendix 2) for description and units. **2)** (*a, b*), *a* = mean, *b* = standard deviation (stdev); *n.b.* minimum values of zero specified for distribution (1 d.p). **3)** Coefficient of variation (CV). **4)** Mean of the posterior from three independent 100,000 iteration chains. Convergence was good because the average % difference between posterior means was 3.2 %. **5)** 95% range; (*a, b*) = mean ± (2 x stdev). **6)** Sensitivity coefficient (SC; normalised). *N.b.* SC (Rbp) = 0.997. All 3 d.p unless stated otherwise.

To aid visual assessment, Figure 3.16 was constructed for effective gut permeabilities (Peff_sto and Peff) before and after calibration.

Figure 3.16: Prior and posterior distributions for permeability of gastrointestinal tract



3.5. Discussion

3.5.1 Quality assurance confirms the PBTK models have been accurately coded into MCSim

The quality assurance confirms that the PBTK models in both MCSim and GastroPlus agree. The models developed in MCSim (Figures 3.1 and 3.2) exhibit very low discrepancy with GastroPlus (Tables 3.2 and 3.3). Thus confidence is high in these PBTK models (in terms of structure and equations used). Subsequently, when fitting data, differences between predicted and observed may be interpreted mechanistically. Furthermore, the PBTK models are suitable for subsequent modelling work as necessary, as the model structure can be simplified or extended to include e.g. tissue-specific enzymes as indicated by *in vitro* data.

The substantial sources of discrepancy in the ACAT model relate to equations which are, for proprietary reasons, undisclosed by GastroPlus (Simulations Plus 2013b) and were therefore coded from first principles. This includes the model for mass transfer across the gut basolateral membrane into portal vein (Figure 3.7). Fick's first law of passive diffusion is implemented by GastroPlus, where the unbound chemical fraction can diffuse across the endothelial gut membrane in either direction. Despite the discrepancy with GastroPlus (Table 3.5), this 'concentration gradient' gut model was used for simulation because Fick's first law 1) is described by a simple first-order process facilitating incorporation into the MCSim gut model (Appendix 1), and 2) reflects real physiology (e.g. following IV dose drug potentially enters gut lumen).

Overall, the adaptations described above do not appear to introduce undue amounts of discrepancy for the sake of modelling chemical disposition following oral dosing, because 1) the discrepancies in Table 3.5 do not appear cumulative, indicating the discrepancy is not a result of a model systematic error, and 2) any model of a biological system is a reflection of the perception of it, and the GastroPlus gut model is not necessarily 'absolutely correct' in its own right, i.e. GastroPlus could be wrong. Simpler gut models will be tested, however, to assess whether these make any difference to model calibration (Principle of Parsimony; Section 3.5.2).

The preliminary BFR model simulates very different chemical disposition to the herbicide model. EBTBPE accumulates in fatty tissues i.e. adipose owing to its lipophilicity (Figure 3.9). This may indicate a toxicological concern particularly for obese humans dieting - sufficient decrease in adipose volume may cause BFR release followed by adipose re-uptake, hence increasing BFR concentration therein to potentially toxic levels. This mechanism is called bioamplification and can occur with for example persistent organic pollutants (POPs) in larval fish under weight-loss scenarios. Here the chemical partitioning capacity exceeds the rate at which POPs are eliminated from the body (Daley 2013). EBTBPE accumulation occurs somewhat in liver (as it is not likely to be extensively

metabolised therein) and brain, perhaps posing a neurotoxicological concern particularly to the developing fetus (it is likely BFRs are capable of crossing the placenta due to their lipophilicity). These preliminary simulations using the prototype model for EBTBPE generate tissue and plasma retention data that will be useful for planning *in vivo* work to further calibrate the models using rat data, and also a useful indication of the likely biological medium that could be used for human biomonitoring. Conversely, there is little accumulation of picloram in tissues (Figure 3.10) because picloram is 1) less lipophilic thus permeation across tissue membranes is slow, and 2) rapidly excreted in urine. Thus, picloram exposure is somewhat less of a toxicological concern than EBTBPE exposure from the perspective of long-term exposure.

3.5.2 Use of a simplified 4-compartment gut model

Originally a nine compartment gut model was implemented that is as close as possible to the ACAT model in GastroPlus™. However it was found that a four compartment gut model was, after calibration, also able to fit the picloram toxicokinetic data. The duodenum, although part of the small intestine, was modelled as a separate compartment because it receives bile from the liver canaliculi (Figure 3.4). The subsequent small intestine compartments (jejunum 1 to ileum 4) were combined into a single compartment, because they are likely to be physiologically and toxicologically indistinguishable with respect to the chemicals being modelled in this project. Conversely, the colon was modelled as distinct compartment owing to its physiological differences with the small intestine, particularly its larger radius affecting the absorption constant therein (Appendix 1). This modelling approach is consistent with the Principle of Parsimony, i.e. the model should be as simple as possible for its purpose but no simpler (Campbell *et al.* 2012). This facilitates identification of additional model parameters necessary to fit data and subsequently their values through calibration (Andersen *et al.* 1995). Despite this, absorption from the gut is a long and complex process involving several parameters (e.g. SEF's and Peff's) requiring the level of complexity modelled here. Thus a balance

was reached between biological plausibility and parsimony. It is likely that the simplified gut model will suffice for calibration of haloxyfop and RBFR toxicokinetic data (chapters 4-6). For these chemicals, the systemic toxicokinetics is of primary concern, and the GIT therefore primarily functions as a conduit between external dose and systemic distribution. However, it is likely that the simplified model would also suffer a similar (albeit small), difference with its GastroPlus equivalent (if it existed), because the GastroPlus gut model still implements Fick's law. As noted (Section 3.5.1), simpler gut models will be coded and compared to determine if the choice of model affects model calibration, internal dosimetry and exposure assessment.

3.5.3 The PBTK models and risk assessment

The PBTK models coded into MCSim are better suited than those used in GastroPlus for modelling environmental exposures because multiple routes of exposure (e.g. ingestion, inhalation and dermal) can be modelled simultaneously (Figure 1.1), making them better suited for general chemical risk assessment. An additional advantage is the ability to perform MCMC with these models. Currently GastroPlus utilises a standard non-linear fitting algorithm to find the best fitting values of specified parameter values. However, it does not provide an indication of the uncertainty on fitted values (i.e. the Bayesian posterior) nor does it account for prior information on the parameters (i.e. the Bayesian prior). Additionally, MCSim can be applied to perform Bayesian inference on multiple datasets simultaneously, as described here for picloram, including HBM data collected from a large population.

3.5.4 *In vivo* transporters are present in kidney and possibly liver for picloram

To fit the picloram data transporters were modelled as follows:

Kidney transporters

Nolan *et al.* 1980 inferred active secretion or transport of picloram into urine by the kidney (Section 3.3.6.1). Indeed, the amount excreted in urine was not reached through simulation when the amount entering the kidney tubule results only from passive diffusion and glomerular filtration (Figure 3.5). Subsequently transporters were modelled that influx through the kidney basolateral membrane and efflux through the kidney apical membrane into the kidney tubules.

Liver transporters

Based on a pilot study performed by Nolan *et al.* 1980, it was assumed for 9.6 and 1635 mg / Kg oral doses, 0.0096 and 1.634 mg, respectively, are excreted in bile 24 hours post-dose (Section 3.3.6.1). These levels were not reached through simulation (0.0030 and 0.56 mg respectively). Therefore an efflux transporter was modelled at the hepatocyte apical membrane. The inclusion of this transporter exemplifies mechanistic interpretation from the discrepancy between observed and predicted toxicokinetic data. However the 0.4 % scaling assumption with a single value reduces confidence in this pilot study and subsequently the transporter modelled.

3.5.5 PBTK model calibration and sensitivity analyses

After running permeability-limited and perfusion-limited models with low/ high IV picloram doses, the permeability-limited model was better able to fit the plasma data (Figures 3.12 and 3.13). A functional explanation is provided by the structure of picloram which contains a carboxylic acid group making the chemical more water-soluble and less lipophilic. Thus its rate of uptake into tissues is limited by its slow permeability. If uptake is described as perfusion limited, picloram quickly perfuses into kidney tubules and is rapidly excreted in urine, explaining the steep decline in simulated plasma concentration (Figure 3.12).

Through MCMC analysis and calibration of the permeability-limited PBTK model, PStc was optimised to 3.676 x 10^{-4} mL/ sec/ mL-tissue (mean; Table 3.6). Relative to the mean of its nominal prior distribution, this optimised value suggests picloram has low tissue permeability, contributing to low tissue accumulation (Figure 3.10) which is consistent with Nolan *et al*. 1980 (Section 3.3.6.1). The posterior distribution for PStc is narrow indicating pharmacokinetic data used for MCMC analysis was informative for PStc. However, the toxicokinetic data may not be representative of true population variability due to the low number of rats used. Subsequently, it might be necessary to assign greater standard deviation to the data for the MCMC analyses. Conversely, posteriors for transporter V_{max} resembled their priors, hence their sensitivity coefficients (SC) were zero (Table 3.6). Assuming less uncertainty of the urine data elicited narrow V_{max} posteriors shifted away from the prior mean. This indicates that this toxicokinetic data, with lower measurement uncertainty (or more measurements over the same time period) can potentially be informative for this parameter. This illustrates the importance of minimising reducible uncertainties during data acquisition.

Calibration of the gut model generated optimised values for effective permeabilities of the stomach (Peff_sto) and gut (Peff) (Table 3.6). Relative to their prior distribution, posterior values were lower for Peff_sto and Peff (Figure 3.16) indicating low permeability through the stomach wall and gut endothelium. However Peff_sto is greater than Peff. Indeed, picloram has a pKa of 3.6 (an acid) (Yang & Pursch 2015) which is similar to rat stomach pH: 3.2 (fed) and 3.9 (fasted) (McConnell *et al.* 2008). Hence a substantial proportion of the administered picloram is likely to be in the non-ionised state within the stomach (approximately 50 %), facilitating absorption through the stomach wall (Duffus & Worth 2006). This is generally the case for acidic drugs administered to rats e.g. salicylic acid, the active ingredient of aspirin (Schanker *et al.* 1957). Conversely, rat ileal pH is slightly alkaline (pH 7-8) (Heijnen *et al.* 1993), thus more will be ionised leading to a lower absorption rate through the ileal endothelium. Relative to its prior distribution, high values were generated for SEF_duo relating to the high density of cilia increasing the surface area in the duodenum.

SC's and coefficients of variation (CV's) for posterior distributions are generally inversely correlated, i.e. sensitive parameters (high SC) have low CV's, which is consistent with the MCMC analysis. This relationship is strong for Peff_sto, but less so for Peff (Table 3.6): peff_sto is sensitive (SC = 0.889) and has low CV (0.040), whereas Peff is less sensitive (SC = 0.033) and accordingly has a higher CV than Peff_sto (0.086). In contrast, PStc appears to be informed by the toxicokinetic data but has an SC of zero. A possible explanation is that the nominal prior for PStc was unsuitable and by coincidence resembles the true posterior. In addition to Peffs, Table 3.6 indicates Rbp (legend) is sensitive (SC = 0.997), i.e. greatly influences tissue concentration. Further work will assign a suitable prior to this parameter. To improve to model's predictive ability, these parameters require accurate laboratory determination.

The joint analysis generated an inaccurate fit to oral plasma and urine data (Figures 3.14 and 3.15 respectively), indicating an inconsistency between the PBTK model and toxicokinetic data. To reconcile this difference, additional parameters can be varied (e.g. Rbp, a particularly sensitive parameter) and prior distributions can be assigned to physiological parameters to reflect animal variability. Furthermore, a hierarchal model approach can be tested, whereby uncertainties regarding population mean values for parameters are included in the MCMC analyses.

3.5.6 Summary and conclusions

1. Prototype PBTK models have been built and tested using MCSim and the GastroPlus software.

2. Toxicokinetic data has been used to perform preliminary calibration of the PBTK model for picloram.

3. The permeability-limited PBTK model developed for rats adequately predicts picloram toxicokinetics (given certain discrepancy as discussed).

4. *In vivo* transporters are present in kidney and possibly liver for picloram, and need to be factored into the modelling.

5. Rbp and Peff are calculated to be sensitive physicochemical PBTK parameters, and thus require accurate laboratory determination.

3.5.7 Further work

Additional development of the rat PBTK model for picloram is required, for example, to obtain a better fit to the plasma toxicokinetic data from 12 hours post administration of 9.6 mg/ Kg and 1634 mg/ Kg oral doses (Figure 3.14). This discrepancy may be attributed to additional enteroheptatic circulation of picloram not included in the current model.

After further development and calibration of the rat PBTK model, it could then be extrapolated to humans. Furthermore, an uncertainty analysis could be performed with the permeability-limited PBTK model (with kidney and liver transporters) to assess levels of tissue exposure that correspond to likely levels of operator external exposure. In this chemical risk assessment, the risk of toxicity could be assessed for operators handling this particular pesticide under different exposure scenarios. As the model parameter Rbp (concentration ratio between blood and plasma) was determined to be sensitive, its value could be determined in the lab using a number of human blood samples to ascertain the level of variability. A distribution of values, to reflect this variability, could then be used in the PBTK model to improve model calibration.

Chapter 4: Development of PBTK models to assess operator exposure to haloxyfop

4.1 Abstract

This project develops physiologically-based toxicokinetic (PBTK) models (with experimental data) to assess occupational exposures to herbicides.

PBTK models are mathematical representations of chemical absorption, distribution, metabolism and excretion (ADME). Each parameter in a PBTK model describes a physiological, physicochemical or biochemical process that affects ADME. To each parameter, distributions can be assigned to reflect inter-individual natural variation and uncertainty regarding the population mean value. With these distributions in place, Bayesian inference using a numerical method such as Markov Chain Monte Carlo (MCMC) can then be applied to calibrate the model, and to estimate external exposure and internal doses from human biomonitoring (HBM) data. Using these models, tissue doses of a chemical can be simulated in a target population allowing the models to be used for chemical risk assessment.

'Permeability-limited' mouse and dog PBTK models were developed for the herbicide (haloxyfop-methyl ester, HME) reflecting relatively slow permeation through tissue membranes, a consequence of its hydrophilicity. MCMC analysis was applied to calibrate these models: prior distributions were assigned to physicochemcial and biochemical model parameters reflecting population variability (Bayesian prior) and convoluted with mouse and canine HME toxicokinetic (TK) data, respectively, to obtain posterior distributions of optimised parameter values (Bayesian posterior). Two different biologically-plausible approaches were adopted to fit the same mouse TK data (*viz.* peroxisome proliferation), and once extrapolated to humans, had different implications for internal exposure assessment.

Extrapolation to humans was performed by substituting in human physiological parameter values and validating against human TK data. Dermal and inhalation absorption routes were modelled: the Human Respiratory Tract Model (HRTM), from the International Commission on Radiological Protection (ICRP), was incorporated into the whole-body PBTK model. Reverse dosimetry was done to assess external human exposure to HME, using a calibrated human PBTK model and appropriate HBM data. Uncertainty analyses were performed to infer exposure in target tissues of interest. Of the seven individuals participating in the occupational exposure study, one may be at potential risk of toxicity from inferred internal exposure levels.

4.2 Introduction

4.2.1 Toxicology of haloxyfop

Haloxyfop-methyl ester is the active ingredient in various herbicide formulations produced and sold by Dow AgroSciences (DAS) (Table 4.1). It was developed as a selective post-emergence herbicide to control annual and perennial grass weeds amongst broadleaf crops (e.g. carrots, rapeseed, soy bean and sugar beet). Haloxyfop-methyl ester exists as both R and S enantiomers. In plants and mammals, these are rapidly hydrolysed to the R and S enantiomers of haloxyfop (Figure 4.1). Haloxyfop is the International Organisation of Standardisation (ISO) approved name for the isomerically unresolved (R/S)-2-{4-[3-chloro-5-(trifluoromethyl)-2-pyridyloxy]phenoxy}propionic acid. Haloxyfop belongs to a class of chemicals called 'aryloxyphenoxypropionates', which includes clodinafop, fenoxaprop-P and fluazifop-P (EFSA 2009). These chemicals inhibit the enzyme acetyl-CoA carboxylase (ACCase). This enzyme is present in both weeds and broadleaf crops. However, in broadleaf crops, ACCase is less sensitive (Stoltenberg *et al*. 1989).

The R-enantiomer of haloxyfop is the herbicidally-active form (ISO name 'haloxyfop-P'), while essentially no herbicidal activity is associated with the S isomer of haloxyfop (Gerwick *et al.* 1988). In plants, haloxyfop-P inhibits acetyl-CoA carboxylase (ACCase) which suppresses *de novo* synthesis of fatty acids. In plants, conversion of the (S)- to the (R)- enantiomer does not occur (Gerwick *et al.* 1988); this step is mediated by soil microbes. Hence, commercially produced haloxyfop-R methyl ester contains a minimum of 98% of R-isomer and a maximum of 2% S-enantiomer.

In mammals, S-form haloxyfop undergoes rapid stereochemical inversion to the R form (Bartels & Smith 1988) indicating toxicokinetic studies conducted with racemic haloxyfop or haloxyfop-P are mutually supportive

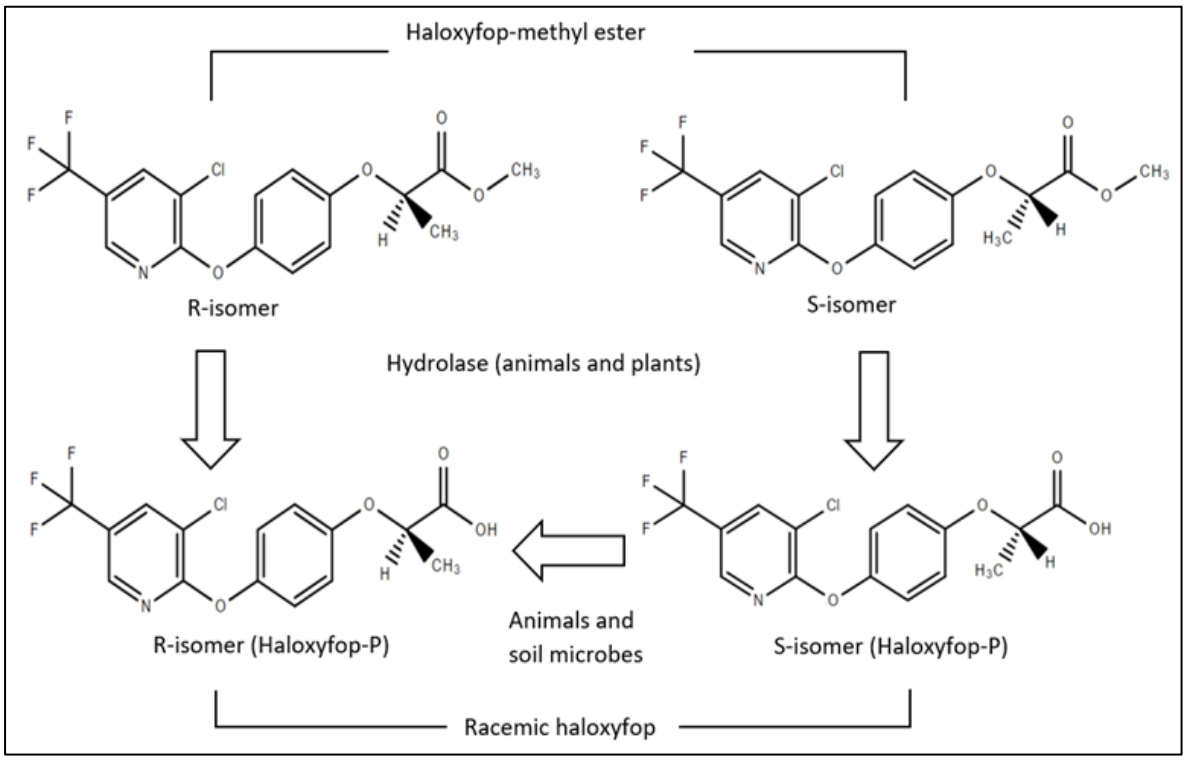


Figure 4.1: Terminology of the haloxyfop variants.

Table 4.1: Haloxyfop products

Trade name	Active compound (in water)
Verdict™ 520	Haloxyfop-methyl ester (520g/ L)
Gallant™ Super	Haloxyfop-methyl ester (108g/ L)
Gallant™ 2000	Haloxyfop-methyl ester (108g/ L)
Eloge™	Haloxyfop-methyl ester (108g/ L)

4.2.2 Mammalian toxicology of haloxyfop

Toxicology studies have identified hepatotoxicity, renal toxicity, carcinogenicity, reproductive and developmental toxicity in rodents, unexplained rabbit mortality, hepatotoxicity in Beagle dogs, and kidney, liver and thyroid toxicity in Cynomolgus monkeys (Appendix 4). The no observable adverse effect levels (NOAELs) differ markedly between different animal species, indicating substantial inter-species differences in susceptibility to toxicity to haloxyfop. Because several tissues are implicated in animal toxicity, such as heart, kidney and reproductive organs, it is useful to calculate the individual tissue doses in humans such that the risk assessment can be derived for the most sensitive tissue. Calculation of individual tissue doses can be achieved through PBTK modelling.

4.2.3 Recognised AOEL level

Operators are individuals involved in activities relating to the application of plant protection products. This includes mixing/ loading products into application machinery, and its operation (EC 2006). According to Directive 97/57/EC, the acceptable operator exposure limit (AOEL) is defined as 'the maximum amount of active substance to which the operator may be exposed without any adverse health effects' (EC 2006). AOELs relate to the internal (absorbed) dose available for systemic distribution from any route of absorption and are expressed as internal levels (mg/ kg bw/ day) (EC 2006).

The acceptable operator exposure level (AOEL) is 0.005 mg/ Kg bw/ day for haloxyfop. This is based on the NOAEL of 0.5 mg/ kg bw/ day from the 1-year Beagle dog study, and applying the 100 x uncertainty factor (EFSA 2009). This uncertainty factor accounts for intraspecies variability (x 10) and interspecies extrapolation (x 10). In this non-good laboratory compliant (GLP) study, groups of six male and six female dogs were fed a diet containing racemic haloxyfop acid (99.6 % purity) providing

doses of 0, 0.05, 0.5 or 5 mg/kg bw/ day. The LOAEL was 5 mg/ Kg bw/ day for significantly increased serum ALT (alanine transaminase) and AST (aspartate transaminase) activities in females at 12 months indicating hepatotoxicity. Serum cholesterol concentration was significantly decreased in males at 1, 6, 9 and 12 months. At autopsy (12 months), no treatment-related effects on histopathology (light microscope) or organ weights were observed (Barna-Lloyd *et al*., 1983 & 1984). Liver electron micrographs (from three males and three females of each group) of the centrilobular area at 8000 × magnification showed no effects on histopathology or peroxisomal volume density (expressed as a percentage of cytoplasmic volume) (Barnard *et al.* 1986).

4.2.4 Peroxisome proliferation

Peroxisomes are sub-cellular organelles present in virtually all eukaryotes. Peroxisomes catabolise long fatty acids via β-oxidation, providing energy for peripheral tissues. They also detoxify various compounds through production and removal of reactive oxygen species. Peroxisome proliferator-activated receptors (PPARs) are nuclear transcription factors which regulate gene expression. There are three types: alpha, gamma and delta. PPARα is expressed predominantly in the liver (Tyagi *et al.* 2011). Endogenous PPARα ligands include fatty acids (Wilson *et al.* 2000); hence, peroxisomes are known to proliferate under high concentrations of unsaturated fatty acids. Synthetic ligands (peroxisome proliferators) include various herbicides such as haloxyfop: they bind PPARα and ultimately increase peroxisome number and size in the tissue. This may cause hypertrophy, hyperplasia and carcinogenesis (Tyagi *et al.* 2011).

The ability of haloxyfop to induce peroxisome proliferation was investigated with a primary culture of hepatocytes from male B6C3F1 mice (n = 5). Pirinixic acid (PPARα agonist) was used as a positive control (100 µmol/ L) for inducing peroxisome proliferation, which was quantified by measuring cyanide-insensitive oxidation of palmitoyl CoA (Lazarow & De Duve 1976). There was a highly significant ($p < 0.001$) increase in the rate of oxidation of palmitoyl CoA at concentrations ≥ 30 µmol/

L indicating peroxisome proliferation (Elcombe 2002a). The same study performed with hepatocytes sampled from three humans showed no consistent effect of haloxyfop (30, 300 and 1000 µmol/ L) on peroxisome proliferation (Elcombe 2002b), indicating human hepatocytes are not susceptible to the peroxisome proliferating effects of haloxyfop. These data accord with those for other peroxisome proliferators such as fenofibrate and gemfibrozil, where humans appear relatively nonresponsive to peroxisome proliferation at dose levels that produce a substantial response in rats and mice (Moody *et al.* 1991, Bentley *et al*. 1993).

It is unclear how differences in interspecies susceptibility to peroxisome proliferation are mediated. Walgren *et al.* 2000 have shown the level of PPARα protein in human liver samples as variable but considerably lower than mouse (n = 6), although one sample had levels similar to the mouse. Indeed, there is ten times less PPARα mRNA in human liver versus rat or mouse (Palmer *et al.* 1998, Tugwood *et al.* 1998). Additionally, interspecies differences in the ability of PPARα-RXRα heterodimers to bind the peroxisome proliferator response element (PPRE) is suggested (Rodriguez *et al.* 2000). There may also be interspecies differences in PPRE responsiveness once activated by the heterodimer.

In conclusion, peroxisome proliferation in mice is irrelevant in a risk assessment for humans (Klaunig *et al.* 2003). The hepatotoxicity and carcinogenicity in rodents (Appendix 4) is also irrelevant to humans because these toxicological effects are likely mediated through the proliferation of peroxisomes. Thus, non-rodent studies where peroxisome proliferation does not occur, provide more relevant findings for assessment of human health hazard and in calculating reference doses such as AOEL. Hence the AOEL for haloxyfop was based on a NOAEL from the 1-year Beagle dog study (EFSA 2009).

4.2.5 The haloxyfop TK data

The studies available from DAS which investigate the toxicokinetics of haloxyfop in various animal species are summarised in Table 4.2 (see Appendix 5 for details).

Table 4.2: The haloxyfop toxicokinetic (TK) data

Experimental study	**Dosage of ^{14}C-labelled haloxyfop (mg/ Kg)**	**No. subjects**	**Biospecimens collected**	**Reference**
Beagle dog	Single oral: 1.99, 2.74	2	Blood, faeces, urine, liver, kidney, perirenal fat	Nolan *et al.* 1987
Mice	Single oral: 5	42	Blood, faeces, urine, liver, kidney	Smith *et al.* 1984
Human volunteers	Single oral: 0.2 Single dermal: 0.8	8	Blood, urine	Nolan *et al.* 1985
Operators	Unknown	8	Urine	Nolan *et al.* 1991

N.b. Data reproduced with permission of the rights holder, Dow AgroSciences.

4.2.6 The Human Respiratory Tract Model (HRTM)

International Commission on Radiological Protection (ICRP) publication 130 gives the scientific basis of the revised Human Respiratory Tract Model (HRTM) (Smith *et al.* 2014). Reference values of rate constants were derived, as far as possible, from human studies as particle transport rates vary substantially across mammalian species. Figure 4.2 shows the model structure.

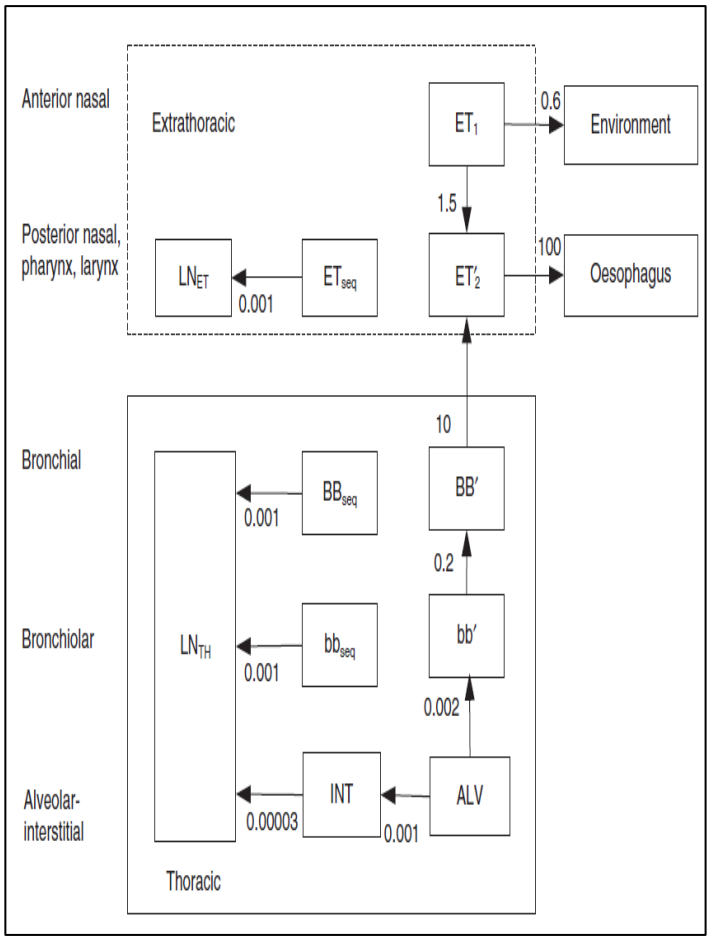


Figure 4.2: Disposition model for HRTM. The respiratory tract is modelled as the extrathoracic (ET) and thoracic (TH) airways. These are subdivided, based on their different sensitivities to radiation. The ET regions are the anterior nasal passage (ET1), posterior nasal passage, pharynx & larynx (ET2), and the ET lymph nodes (LNET). The TH regions are bronchial (BB: trachea & bronchi), bronchiolar (bb), alveolar interstitial (AI), and the TH lymph nodes (LNTH). Model assumptions: 1) All clearance rates are independent of age & sex, 2) particle transport rates are the same for all materials, & 3) absorption into blood occurs at the same rate in all HRTM compartments, except ET1 where no absorption occurs. Figure taken with permission from the rights holder, ICRP (2015).

The model describes several routes of clearance from the respiratory tract. During nose-breathing, approximately 65% of the deposit in the ET airways is deposited in ET1. This is cleared at an overall rate of 2.1 d^{-1} (e.g. by nose- blowing). In other regions, clearance is competitive between absorption into blood and particle movement via the mucociliary escalator. Absorption into the blood from HRTM is determined by the physicochemical properties of the deposited material (Figure 4.3). Simultaneously, most particles deposited in ET2 (or transferred to it from other regions) are cleared by mucociliary action to the throat (the phlegm is subsequently swallowed). This is represented by clearance from compartment ET2 to the oesophagus at a rate of 100 d^{-1}. Mucus velocities generally increase towards the trachea. This is represented by clearance rates of 0.2 d^{-1} (bb to BB) and 10 d^{-1} (BB to ET2).

Approximately 50% of the deposit remains in the AI region of human lung one year post inhalation (ICRP 1994). This is represented by deposition in the alveolar compartment (ALV), which clears to bb (rate 0.002 d^{-1}), and to the interstitial compartment (INT; rate 0.001 d^{-1}). The INT compartment clears very slowly to the regional lymph nodes (rate 0.00003 d^{-1}) (Figure 4.2). Consistent with animal inhalation studies, it is assumed 0.2% of material deposited in regions ET2, BB and bb sequesters in airway walls (ETseq, BBseq, and bbseq, respectively). Material is cleared from these compartments to regional lymph nodes at a rate of 0.001 d^{-1}.

In the HRTM, absorption is treated as a two-stage process: 1) dissolution of deposited particles into material that can be absorbed into pulmonary blood, and 2) absorption into blood of soluble material (Figure 4.3). Material deposited in the respiratory tract is initially assigned to a compartment called 'particles in initial state' in which it dissolves at a constant rate (sp). Material is transferred simultaneously (at a constant rate, spt) to a compartment called 'particles in transformed state' in which it has a different dissolution rate (st). To represent time-dependent uptake, it is assumed a fraction (fb) of the dissolved material is retained in the 'bound' state, from which it enters blood at a rate sb, while the remaining fraction (1 – fb) enters blood instantaneously. Default parameters values are recommended, according to whether the absorption is considered fast (F), moderate (M), or slow (S) (ICRP 1994).

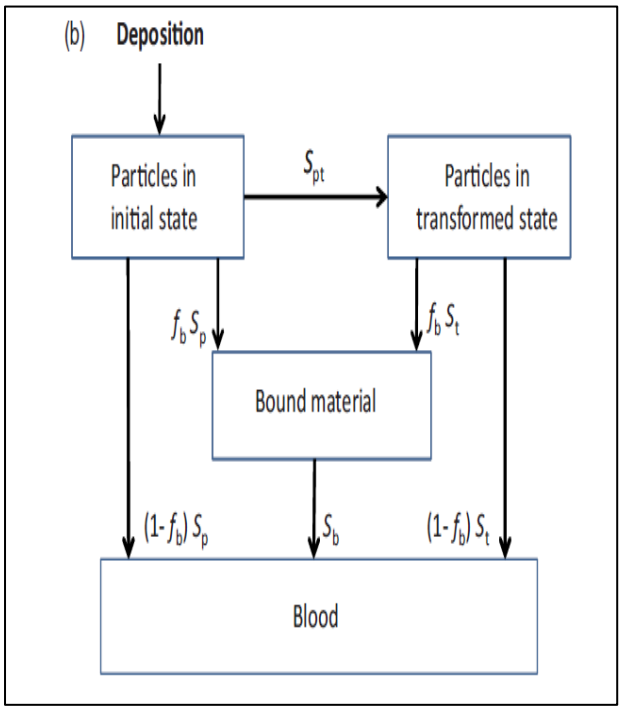


Figure 4.3: Dissolution model for HRTM. Material deposited in the respiratory tract is initially assigned to a compartment called 'particles in initial state'. N.b. particles in 'transformed' & 'initial' states are subject to identical particle transport rates. Furthermore, 'bound material' is not subject to particle transport; it is only cleared by absorption into blood. fr: fraction of the deposit dissolving rapidly, at a rate sr; (1- fr): fraction of deposit dissolving less rapidly, at rate ss; fb: fraction of dissolved material retained in bound state; sr: rate of rapid dissolution; ss: rate of slow dissolution; sb: transfer rate from bound state to blood; spt: transfer rate of material from 'particles in initial state' to 'particles in transformed state'; sp: dissolution rate of material from compartment 'particles in initial state'; st: dissolution rate of material from compartment 'particles in transformed state'. Figure taken with permission from the rights holder, ICRP (2015).

4.2.7 Chapter aims

- To investigate if there are different biologically-plausible approaches to fitting TK data in the same rodent PBTK model, and once extrapolated to humans, whether these have different implications for internal exposure assessment.
- To investigate if human exposure assessment is influenced by the animal species being extrapolated from.

4.3 Methods

4.3.1 QSAR

The project uses *in silico* QSAR predictions and *in vivo* mouse and dog haloxyfop TK data (supplied by DAS) to build and calibrate PBTK models for haloxyfop. These models are then scaled to produce human equivalent PBTK models, which are validated using human haloxyfop TK data available from DAS. Reverse dosimetry is then performed to assess external exposure of operators to haloxyfop. Furthermore, uncertainty analysis is used to estimate body burdens from occupational exposure. A discussion of how this modelling approach can be integrated into the DAS risk assessment procedure follows (Figure 4.4).

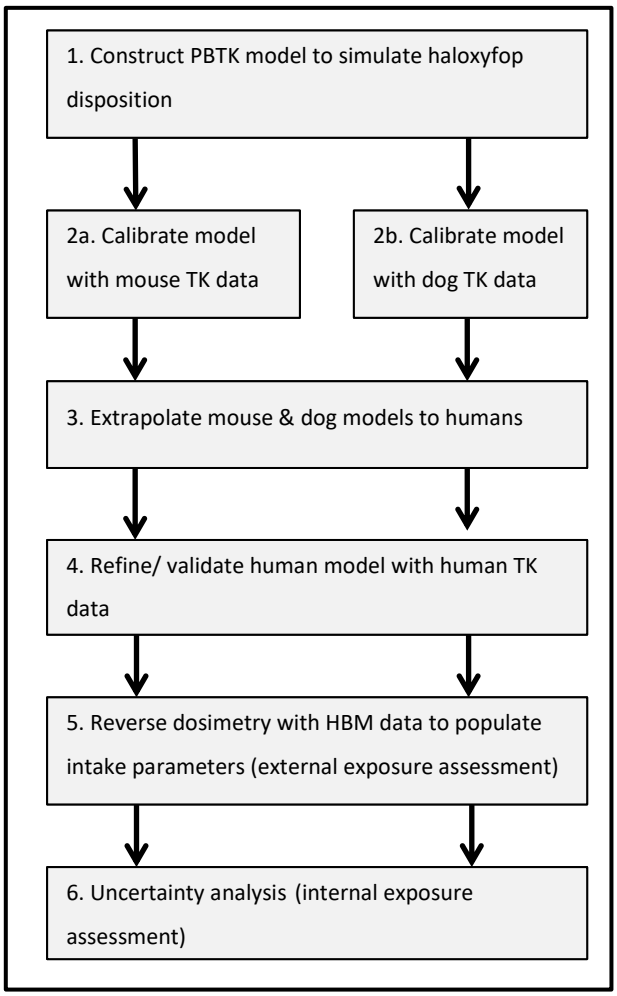


Figure 4.4: Overview of workflow for modelling chemical exposure in human health risk assessment (see text for details).

4.3.2 Construct PBTK model to simulate haloxyfop disposition

Haloxyfop-P is hydrophilic, and subsequently is likely to permeate more slowly through tissue basolateral membranes (interfacing intra- and extracellular spaces) relative to more hydrophobic chemicals. Thus, a 'permeability-limited' model structure was adopted. Quality assurance confirms 1) the models developed in MCSim exhibit very low discrepancy against GastroPlus (chapter 3), and 2) a working mass balance (summation of the chemical amounts in all model compartments is always equal to the dose administered).

To ensure mass balance despite variability of tissue blood flows and tissue volumes, these parameters were described as fractions of cardiac output and body weight, respectively. Samples

were then constrained to ensure constant cardiac output and total tissue volume during MC simulations: tissue flow = (fractional tissue flow ÷ ∑fractional tissue flows) x cardiac output. Similarly, tissue volume = (fractional tissue volume ÷ ∑fractional tissue volumes) x body weight (Lyons *et al.* 2013).

The permeability-surface area product PStc (mL/ sec/ mL-tissue), the physicochemical parameter that describes the rate of permeation across the tissue basolateral membrane, was scaled according to intracellular tissue volumes. Kp relates to the chemical partitioning through the vascular membrane into the extracellular space, and is calculated using Poulin & Theil's extracellular method (Poulin & Theil 2000).

4.3.3 Metabolite tracking

Given evidence for the formation of a metabolite of haloxyfop (Smith *et al.* 1984, Nolan *et al.* 1985), metabolite tracking functionality was implemented into the permeability-limited PBTK model (Figure 4.5). GastroPlus Absorption, Distribution, Metabolism, Elimination and Toxicity (ADMET) Property Predictor™ (Simulations Plus 2013a) was used to generate *in silico* predictions for physicochemical parameters for haloxyfop-P and its glucuronide conjugate. These include the blood: plasma concentration ratio (rbp), the logarithm of octanol: water partition coefficient of neutral drug molecules for tissues (logP_tis), and the experimental fraction unbound in plasma ($f_{up,exp}$); subsequently, these were used to calculate partition coefficients (Table 4.3) using Poulin & Theil's extracellular method (Poulin & Theil 2000). *N.b.* Rbp and fup_exp are theoretically species-specific parameters (*i.e.* influenced by species-specific plasma protein and hematocrit levels); however, the ADMET Property Predictor currently only generates these predictions for humans (Simulations Plus 2013a). Subsequently, fup_exp was optimised (Table 4.5). Rbp was used as predicted. The fact GastroPlus predicts values only for humans may have an impact on the mouse calibration, but this impact cannot be assessed until rodent-specific data become available.

Table 4.3: *In silico* predictions for physicochemical parameters for haloxyfop-P and its glucuronide conjugate (species-unspecific).

Chemical	logP_tis	Rbp	$F_{up,exp}$	Kp			
				Liver	Adipose	Brain	Kidney
Haloxyfop-P	3.93	0.55	0.0173	0.51	0.16	0.51	0.51
Haloxyfop-P glucuronide	1.86	0.63	0.0845	0.54	0.22	0.54	0.54

In silico predictions reproduced with permission of the rights holder, Simulations Plus Inc.

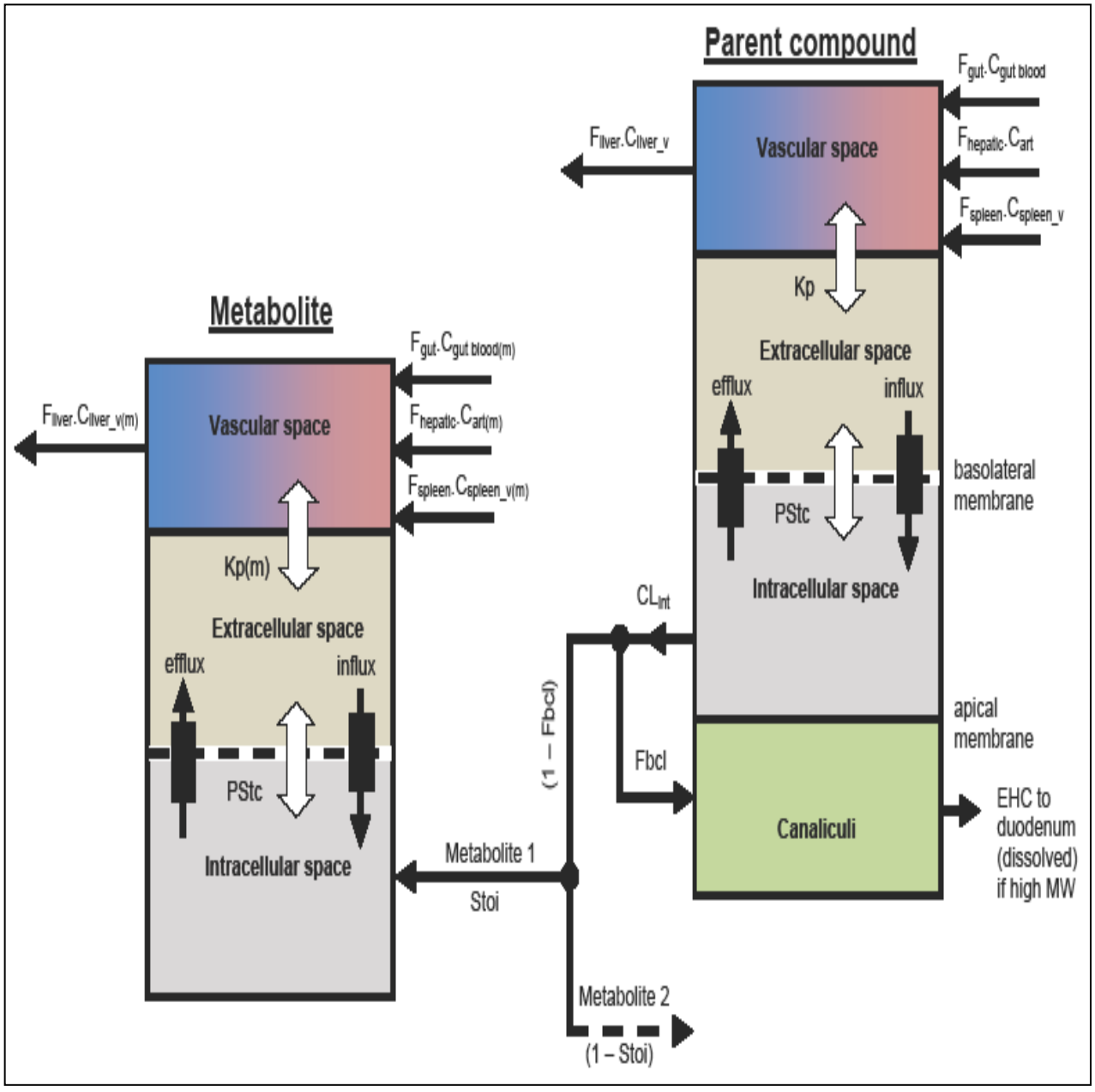


Figure 4.5: Liver model with metabolite tracking. The parameter Fbcl is used - the metabolite fraction undergoing biliary clearance. This fraction enters the duodenum where bile is deposited. The other portion (1 - Fbcl) remains in the liver, subsequently described as a sub-model (m) in order to track the metabolite. The metabolite can enter hepatic blood for systemic circulation and ultimately the kidneys for elimination. Given evidence for at least two haloxyfop metabolites (Smith *et al.* 1984), reaction stoichiometry (stoi) was implemented (which ≤ 1). For example, if 'stoi' is 0.5, half the metabolised amount of parent compound forms metabolite 1, half forms metabolite 2. The metabolites' physicochemical properties can be specified - they are likely to be more water soluble than the parent compound facilitating their elimination. The enterohepatic circulation (EHC) of the metabolite can be activated if the metabolite's molecular weight (MW) is likely to exceed the threshold MW required for biliary excretion, else it remains in the liver from where it accesses systemic circulation. PStc is currently assumed to be identical between parent compound and metabolite. There are no QSAR models or *in vitro* assays currently available for PStc prediction/ determination, so the optimised PStc for the parent compound provides the best estimation for metabolite PStc. Figure adapted from Simulations Plus 2013b.

4.3.4 Dermal absorption model

The dermal absorption model was developed, based on the generic permeability-limited tissue structure available from GastroPlus, with the addition of an upper liquid compartment to which the dermal dose is applied (Figure 4.6). The dose permeates through the skin at a rate determined by 1) the permeability coefficient (mg/ sec/ cm^2 -skin), 2) the surface area of exposed skin (cm^2) and 3) the skin: liquid partition coefficient. The dose available for absorption is dependent on the rate of crystallisation (mg/ sec), whereby the aqueous dose precipitates into solid which is unavailable for absorption. The fraction absorbed over time is calculated in terms of the net quantity permeating into skin cells.

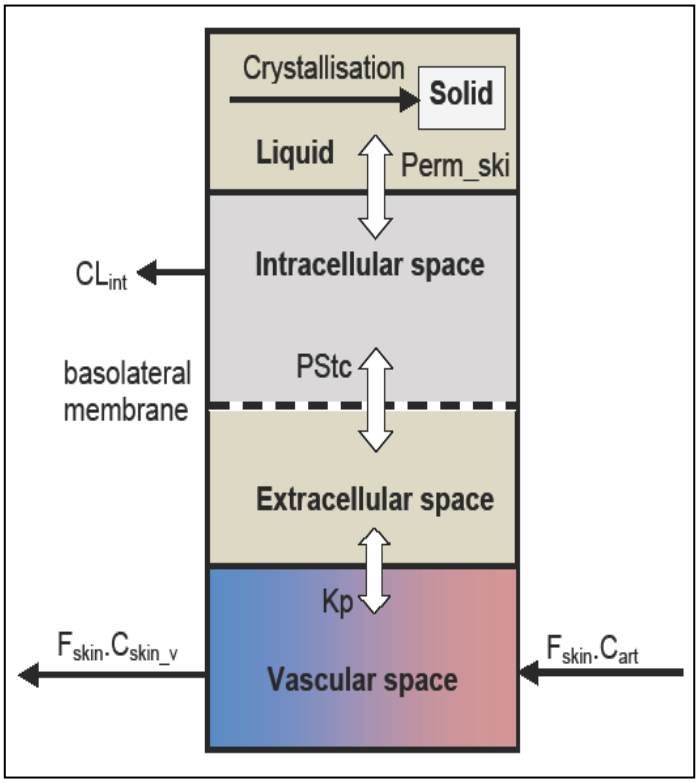


Figure 4.6: Model for permeability-limited skin. The rate of chemical entry into the skin is given by the product of blood flow rate (Fskin) and arterial concentration (Cart). Conversely, the rate of chemical exit from the tissue is given by the product of Fskin and the venous tissue concentration (Cskin_v), which is calculated as a function of the tissue partition coefficient (Kp). Cskin_v decreases when there is intrinsic tissue clearance (CL_{int}). The bi-directional arrows indicate the chemical can diffuse in either direction across the tissue's cell membranes. Figure adapted from Simulations Plus 2013b.

4.3.5 Inhalation absorption models

The HRTM (Figures 4.2 and 4.3) was implemented into the human PBTK model. HRTM was developed for all aerosol sizes of practical interest (0.6 nm - 100 µm), and a median aerodynamic diameter of 5 µm was assumed for haloxyfop-methyl ester. Type F was assumed for inhaled

particulates due to an absence of information on which assignment to another absorption type could be made. Hence, values for Fr (1.0 d^{-1}), Sr (30.0 d^{-1}) and Ss (0.0 d^{-1}) were used. Fb (0) was used for both HRTM and HATM.

ICRP publication 100 gives the scientific basis of the revised Human Alimentary Tract Model (HATM) (ICRP 2006). This model simplifies the complex processes involved in the transfer of material along the gut lumen; however, it provides a reasonably accurate representation of the residence times of swallowed material in each gut segment. The model implemented into the human PBTK model is adapted from the HATM model (Figure 4.7). The gut transit times are the same as those used for the ACAT model (chapter 3). Absorption of inhaled material from HATM into blood is specified as a fraction of the amount entering the alimentary tract, denoted here as f1 (0.0005). Initially, the phlegm from the HRTM was designed to enter the ACAT model. However, this would introduce the assumption that inhaled material trapped within the phlegm would undergo dissolution (and absorption into portal blood) at the same rates as ingested material. To avoid this, the phlegm was designed to go into its own HATM model.

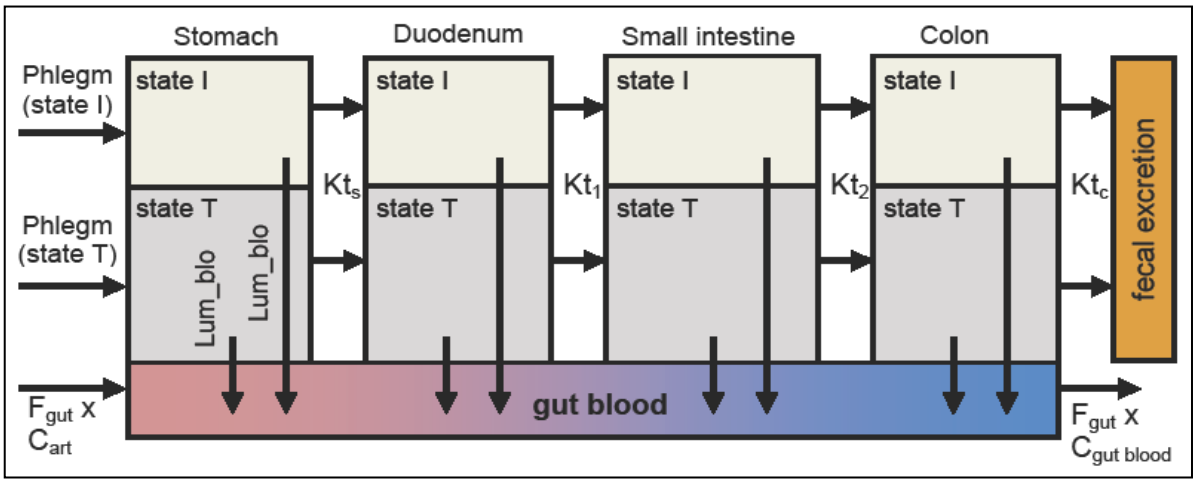


Figure 4.7: Adapted HATM model. Inhaled material is subject to the mucociliary escalator. The phlegm produced can enter the stomach via the oesophagus (in the HRTM). Thus, inhaled materials, in both 'initial' & 'transformed' states enter their respective stomach compartments. As these quantities travel down the gastro-intestinal tract, they are subject to state-dependent rates of absorption into gut blood. Unlike the ACAT model, Fick's first law of passive diffusion is not implemented at the gut endothelial membrane.

The simplified four-compartmental gastrointestinal tract (GIT) model (chapter 3) was developed to include gut precipitation, which occurs if the local concentration exceeds the chemical's solubility (Appendix 1), and the precipitate subsequently undergoes dissolution. This is particularly relevant for BFRs which have low solubility, hence precipitation following oral ingestion may be likely.

4.3.6 Calibration methodology

The combination of nominal haloxyfop permeability-limited systemic model, simplified four-compartmental GIT model (chapter 3) and adapted HATM model were adopted for calibration. An attempt was made to calibrate the perfusion-limited systemic model (chapter 3), however this produced poor fits to either mouse or dog TK data. This is because haloxyfop is relatively hydrophilic, so tissue uptake is limited by the slow rate of permeation through tissue membranes, rather than the rate of blood perfusion.

The estimation of tissue-specific PStc values for PBTK modelling is not well established due to poorly understood physiological aspects of specific tissues such as cell surface areas. The method of scaling PStc values to tissue cell volumes implemented here is recent (Lukacova *et al.* 2011), and PStc values are not widely reported in the literature. Therefore a suitably wide prior distribution was assigned to PStc. To avoid numerical errors arising from negative parameter values during the MCMC calculations, truncated normal prior distributions were used: left truncated at zero. They were also right truncated at very high maximum values because MCSim requires that both upper and lower bound truncation points are specified when a truncated distribution is adopted. Left truncation does not significantly affect the shape of the distributions because the chosen mean and standard deviations cause negative values to arise with low probability. Proposal distributions were selected and tuned autonomously in MCSim.

MCMC was performed using the Metropolis algorithm as implemented in the code MCSim (Bois & Maszle 2008) to calibrate the model (Section 2.1). Markov chain convergence was confirmed by

running three independent chains seeded with different random numbers and starting values of model parameters; stationary distributions were obtained after approximately 150,000 iterations. The first 20,000 iterations were discarded as 'burn-in'; this choice is consistent with Geyer 1992 who suggested a burn-in of 1 - 2 % of total chain length is adequate. Convergence was monitored by comparing posterior means every 50,000 iterations. Potential scale reduction factors (PSRFs) were calculated for parameters using the Gelman-Rubin convergence diagnostic (Gelman & Rubin 1992). Microsoft Excel was used to perform all statistical analyses. Calibration was verified by visually assessing the ability of the mouse and dog models to fit respective TK data, assuming values of parameters sampled from their posterior distributions.

4.3.7 Calibrate model with mouse TK data

The PBTK model was populated with mouse physiology, specifically B6C3F1 mice because these were used to generate the herbicide TK data in Smith *et al*. 1984. Corresponding parameter values are implemented in GastroPlus. Mouse parameters were taken from Brown *et al.* (1997), Davies & Morris (1993), Kyselova *et al.* (2003) & Simulations Plus (2013a). Haloxyfop-P and its glucuronide conjugate were identified in murine bile (Smith *et al*. 1984), thus EHC was activated in the mouse PBTK model. Physiological parameters were fixed at values specific for B6C3F1 mice, however physicochemical and biochemical parameters were calibrated: prior distributions were assigned, for example, to 1) Fbcl, Fup_exp, PStc and (Table 4.5). In order to fit the kidney TK data, a low level of active secretion is modelled within the kidney, hence prior distributions were assigned to V_max_kid_a and Km_kid_p_a. A uniform prior was assigned to fup_exp, thus no reliance was placed on the ADMET predictor for this parameter. These distributions were either normally or uniformly distributed, to reflect current knowledge regarding the variability of these parameter values in the population, based on an initial literature review (Table 4.5). For metabolite tracking, the reaction 'stoichiometry' parameter was set to 1, given a lack of information relating to the identity and quantity of the second metabolite formed (Smith *et al.* 1984).

There were two different biologically-plausible ways of fitting the mouse liver TK data, where liver concentrations were greater than expected. The first approach involved raising the liver partition coefficient from the QSAR prediction (through the use of MCMC) by assuming a greater fraction bound in liver (Poulin & Theil 2000). This may to a small degree reflect additional binding to the PPARα receptor therein (see discussion). The second approach involved using the original QSAR prediction of liver partition coefficient, but having influx transporter activity in the liver basolateral membrane leading to sequestration of haloxyfop within hepatocytes. Both models were extrapolated to humans to assess implications for human internal exposure assessment.

4.3.8 Calibrate model with dog TK data

These PBTK models assumed Beagle dog physiology, because these were used to generate the herbicide TK data in Nolan *et al*. 1987. Corresponding parameter values, implemented in GastroPlus (Simulations Plus 2013a), were taken from Brown *et al.* (1997), Davies & Morris (1993), Paltiel *et al.* (2002) and Jurvelin *et al.* (1988). To fit the plasma, urine and faeces TK data, it was not necessary to model any active transport processes.

4.3.9 Extrapolate mouse and dog model to humans

The calibrated mouse and dog PBTK models were scaled to humans, by substituting in fixed human age-related physiology, specifically male Caucasians average age 42 years (individual ages of volunteers unreported in Nolan *et al*. 1985). Human parameter values were based on age-related population data for 11,039 Americans (50 % female) from the National Health and Nutrition Examination Survey (NHANES) database. As the molecular weight of haloxyfop-glucuronide (537.8 g/ mole) almost exceeds the molecular weight cut-off of 500 ± 50 g/ mole for anions in humans (Millburn *et al.* 1967, Millburn 1970), EHC was activated in the human PBTK model.

4.3.10 Re-calibrate/ validate human model with human TK data

The posterior distributions of optimised mouse and dog physicochemical and biochemical parameters were specified as univariate prior distributions in the human models. Monte Carlo sampling was done to ensure the specified priors were identical to the optimised mouse and dog posteriors. The optimised fraction bound in mouse liver was not used in the human model (assuming PPARα binding occurs at a lower/ negligible level in humans). Furthermore, due to substantial differences in gut permeability between animal species (e.g. rats and humans; Fagerholm *et al.* 1996, Zakeri-Milani *et al*. 2007), uniform (flat) priors were assigned to parameters of the human gut model, i.e. Peffs and SEFs (Table 4.5). Currently, due to the absence of published mathematical interspecies correlations for this parameter, this interspecies difference is not taken into account during the extrapolation process.

A further round of Bayesian analysis was applied to the human model for further model refinement with human TK datasets (Hack 2006a). The TK data from each human were pooled at each time point to create estimates of the mean and standard deviation (Nolan *et al*. 1985). This data was used in a joint Bayesian analysis to calibrate the PBTK model using oral (0.2 mg/ Kg) and dermal dose (0.8 mg/ Kg) TK datasets (plasma haloxyfop-P concentrations and urine amounts). The dermal exposure was assumed to last ten minutes. Once the human model was convoluted with the TK data, secondary posterior distributions of optimised parameter values were obtained (Table 4.5). Calibration of the human model was validated by its ability to fit additional human TK data (Figure 4.9).

4.3.11 Reverse dosimetry with HBM data to populate intake parameters (external exposure assessment)

The calibrated human model was used to estimate operator external exposure, by performing a Bayesian analysis with operator urine HBM data (Nolan *et al.* 1991). Reverse dosimetry was done for operators G.B. and J.Q. based on the amounts of haloxyfop-P excreted in their urine (which were above the analytical limit of quantification (LoQ)). Reverse dosimetry was also done for individuals J.H., M.D., D.R., J.W. and G.D. collectively, who did not excrete quantifiable amounts of haloxyfop-P in their urine. Their urine measurements were set to the LoQ thus providing a conservative estimate of body burden. It was assumed that 1) the average duration of dermal exposure for operators was 108 mins (Scortichini *et al.* 1987), 2), the body weight of each operator was 70 Kg (EFSA 2012b), 3) the area of exposed skin was 100 cm^2, 4) exposure occurred only through inhalation and dermal routes and 5) there was no crystallisation on the skin surface (see discussion). The sampled MCMC parameter values derived from the reverse dosimetry fit the urine data (Appendix 5) (Nolan *et al.* 1991).

A hierarchical statistical model was used to assess individual exposures. This model works by sampling first from top-level parameters, in this case, the systemic model parameters (Table 4.5) - these samples are identical for all operators. For each iteration of the algorithm, samples were also taken from lower- (subject) level parameters. These parameters ('dermal' and 'inhalation') were assigned uniform priors (0 - 1); they scale the NDoses function which specifies chemical exposure through each route. The NDoses function for operators was specified to equal 1 mg/ Kg, over a time period of expected exposure (108 minutes). Because the 'dermal' and 'inhalation' parameters are multiplied by one, their respective posteriors become expected exposure.

4.3.12 Uncertainty analysis (internal exposure assessment)

A computer code was obtained and adapted to perform iterative simulations, assuming parameter values sampled from the converged MCMC chain. Subsequently, the model output data was banded based on the median, lower and upper 95% distribution range (maintaining the correlation between parameters).

To relate to the AOEL (mg/ kg bw/ day) (EC 2006), an equation was developed for systemic exposure. It calculates the internal (absorbed) dose available for systemic distribution from any route of absorption and is expressed as internal levels (mg/ kg bw). The equation is based on the mass balance equation, minus the chemical quantities in compartments considered external to the body (e.g. residue on the skin, exhaled material, gut lumen contents and faeces) (Appendix 1).

4.4. Results

4.4.1 Mouse PBTK model calibration (approach 1: with optimised fraction bound in liver)

MCMC analysis was done to calibrate the permeability-limited mouse PBTK model with oral TK data from Smith *et al.* 1984. Predictions of haloxyfop physicochemcial parameters were used (Table 4.3). Physiologically-realistic distributions were assigned to parameters including SEFs and Peffs for each GIT compartment and PStc (Table 4.5). Good fits were obtained assuming posterior mean values of parameters (Figure 4.8), indicating correctness of model structure. The posterior values from the Bayesian analysis are given in Table 4.5.

To fit the liver TK data, it was necessary to raise the liver partition coefficient from the QSAR prediction by assuming a greater bound fraction in liver (Fb_liv) (Poulin & Theil 2000). The corresponding deviation from the QSAR prediction (99.25 to 99.91 %) is approximately 0.7 % (this distribution is recorded in Table 4.5). In order to fit the kidney TK data it was necessary to model a

low level of active secretion at the kidney apical membrane, hence prior distributions were assigned to transporter Vmax and Km.

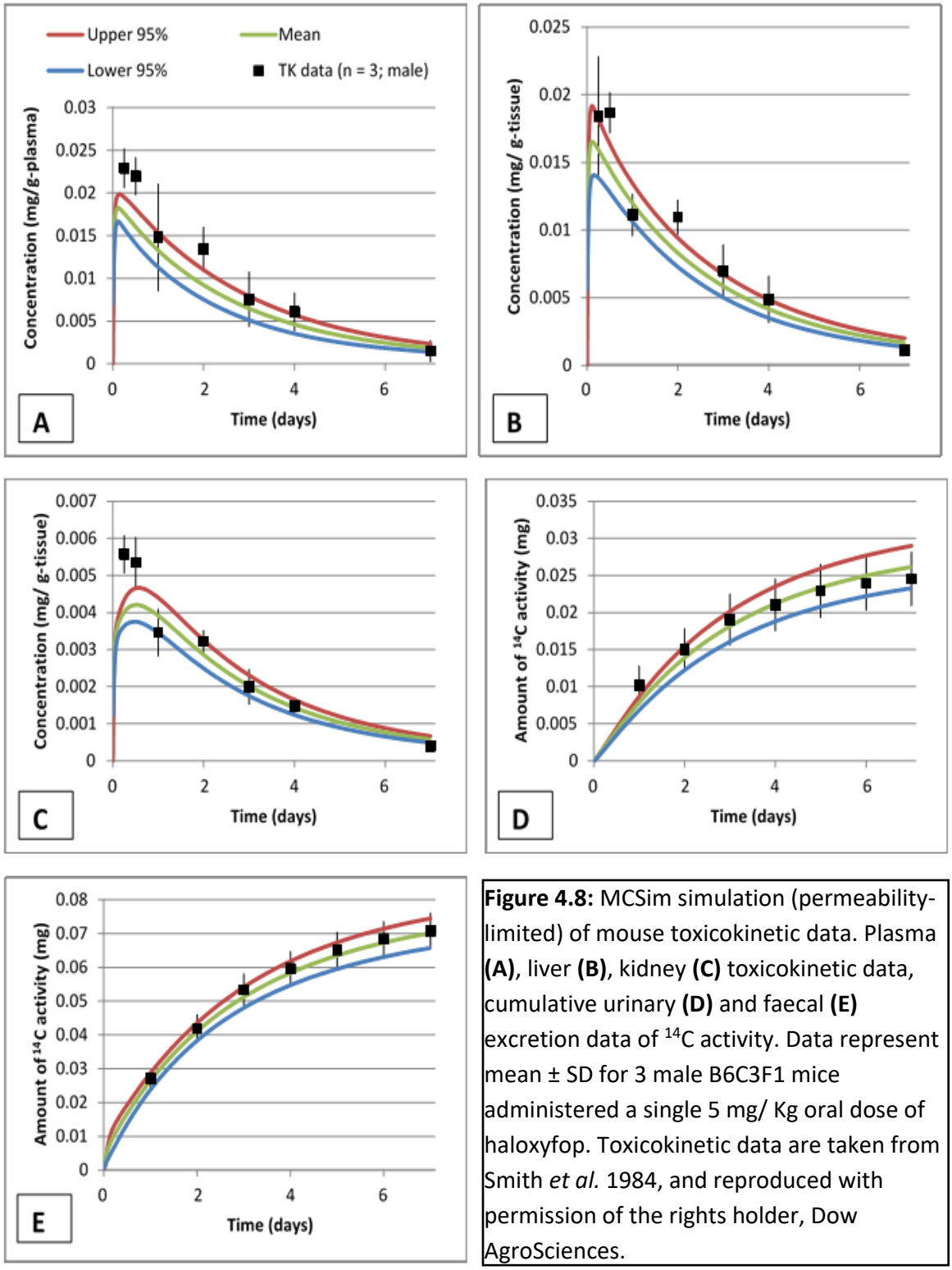


Figure 4.8: MCSim simulation (permeability-limited) of mouse toxicokinetic data. Plasma **(A)**, liver **(B)**, kidney **(C)** toxicokinetic data, cumulative urinary **(D)** and faecal **(E)** excretion data of ^{14}C activity. Data represent mean ± SD for 3 male B6C3F1 mice administered a single 5 mg/ Kg oral dose of haloxyfop. Toxicokinetic data are taken from Smith *et al.* 1984, and reproduced with permission of the rights holder, Dow AgroSciences.

4.4.2 Human PBTK model calibration

The calibrated mouse PBTK model (approach 1) was extrapolated to humans, by substituting in human age-related physiology, specifically male Caucasians average age 42 years. The optimised fraction bound in mouse liver was not used in the human model assuming PPARα binding occurs at a lower/ negligible level in humans. The posterior distributions of optimised mouse parameters were specified as priors in the human model (Table 4.5). The human TK data was used in a joint Bayesian analysis to calibrate the PBTK model using oral (0.2 mg/ Kg) and dermal dose (0.8 mg/ Kg) TK datasets (plasma concentrations and urine amounts) (Nolan *et al*. 1985). Figure 4.9 shows corresponding fits to plasma and urine TK data following oral and dermal doses of haloxyfop.

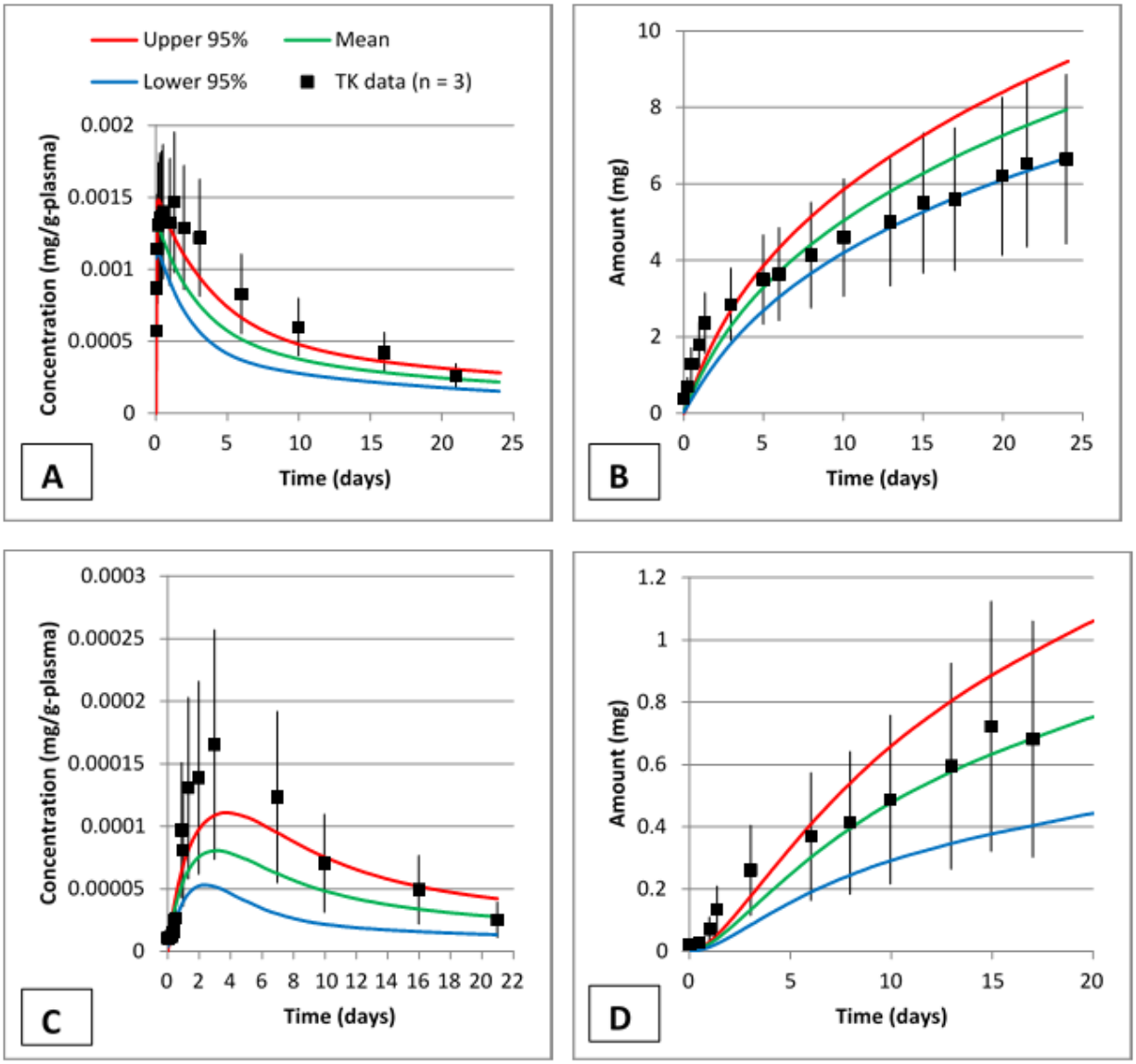


Figure 4.9: MCSim simulation (permeability-limited) of human toxicokinetic data. Plasma data **(A)** & urinary excretion data **(B)**; data represent mean ± SD for 3 adult male volunteers administered a single 0.2 mg/ Kg oral dose of haloxyfop. MCSim simulation of human plasma toxicokinetic data **(C)** & urinary excretion data **(D)**; data represent mean ± SD for 4 adult male humans administered a single 0.8 mg/ Kg dermal dose of haloxyfop-methyl ester. Toxicokinetic data are taken from Nolan *et al.* 1985, and reproduced with permission of the rights holder, Dow AgroSciences.

The calibrated model was then run forward to assess fraction absorbed through the skin (Fa_skin), calculated as the net quantity permeating into skin cells. The estimates for Fa_skin are within the expected range (Table 4.4); based on the amount of haloxyfop-P excreted in urine approximately 3 % of the dermal dose was absorbed (Nolan *et al*. 1985).

Table 4.4: Estimates for 'fraction absorbed through skin' (Fa_skin)

Calibration type	**Fa_skin (% of dermal dose) (mean, stdev)**
Human calibration (0.8 mg/ Kg dermal dose)	1.98, 0.67
Reverse dosimetry (occupational exposure)	1.08, 0.00058

4.4.3 Human reverse dosimetry

Reverse dosimetry was done with the validated human model (above) to assess the external exposure of operators. A Bayesian analysis was performed with operator urine HBM data (Nolan *et al.* 1991), using a hierarchical statistical model to assess individual exposures. Figure 4.10 shows the external dermal exposure to haloxyfop-methyl ester for the operators.

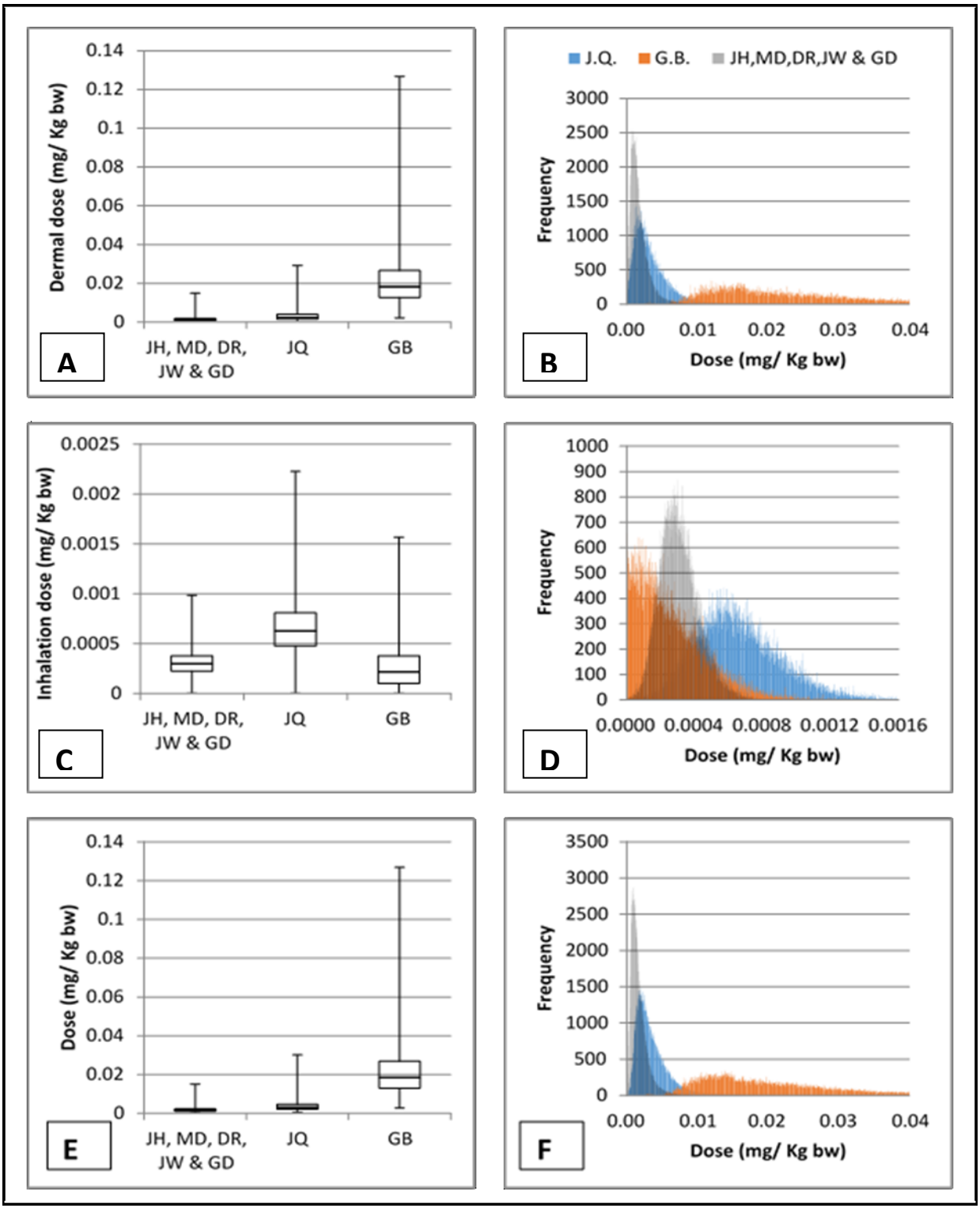


Figure 4.10: Reverse dosimetry with scaled human model for assessment of operator exposure. Operator **A, B)** dermal exposure, **C, D)** inhalation exposure and **E, F)** total external exposure (both absorption routes). Inhalation exposure was substantially below the dermal exposure estimates.

4.4.4 Reverse dosimetry - uncertainty analysis

An uncertainty analysis was done to assess maximum exposure in various tissues for operator G.B, the individual who was likely exposed to the greatest amount of haloxyfop methyl-ester. This was done in triplicate for the different modelling approaches (see methods). Reproductive toxicity was indicated in Sprague-Dawley rats (Nitschke *et al.* 1985), hepatotoxicity in Beagle dogs (Barna-Lloyd *et al.* 1983, 1984), renal toxicity in B6C3F1 mice (Gorzinski *et al.* 1982a), F344 rats (Gorzinski *et al*. 1982b) and Cynomolgus monkeys (Yano *et al.* 1987). Thus an exposure assessment of corresponding tissues in humans is of particular interest to assess possible human health detriment.

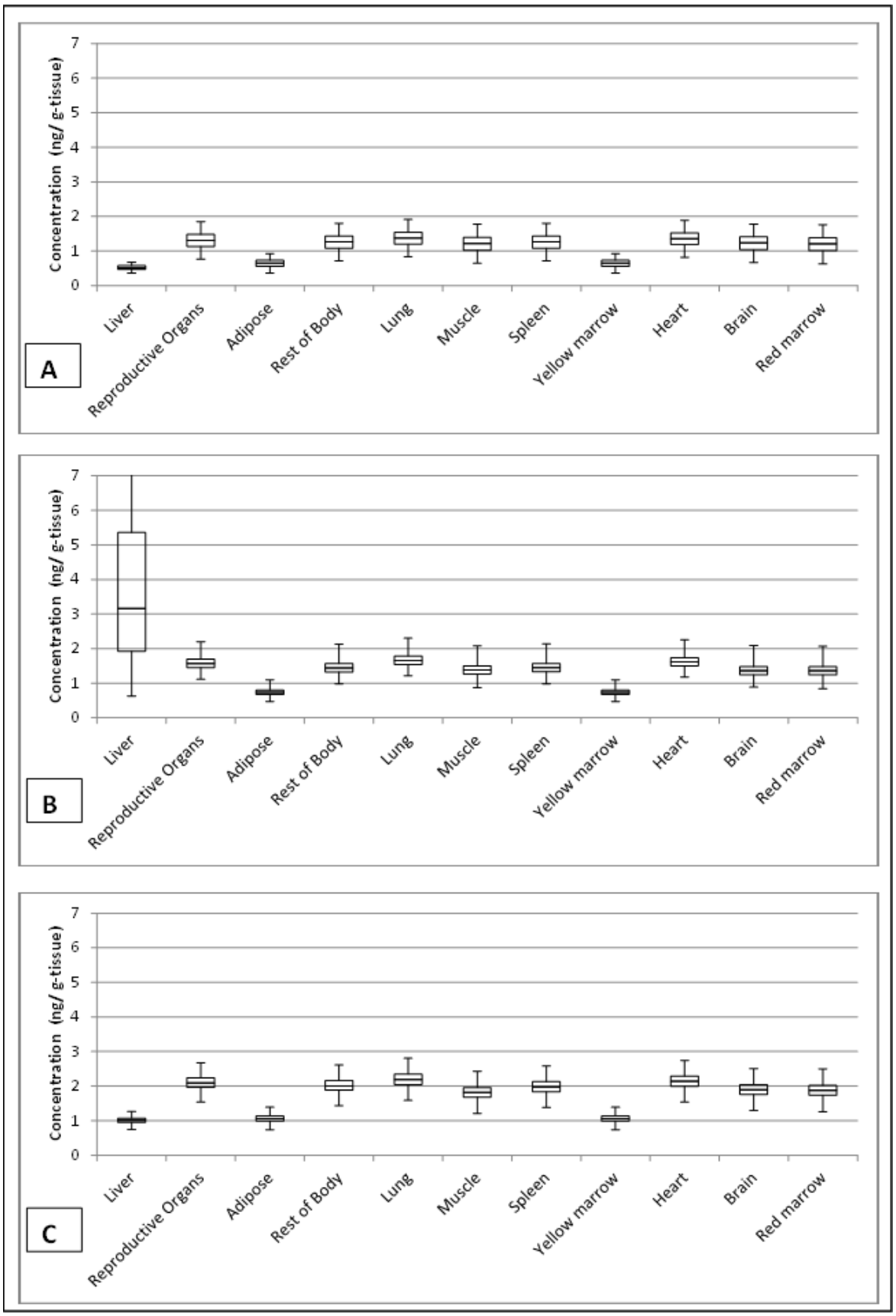


Figure 4.11: Assessment of maximum tissue exposure for operator G.B. following occupational exposure to haloxyfop-methyl ester. A) Approach 1, **B)** approach 2, and **C)** from dog extrapolation (see text for details). *N.b.* concentrations are bound and unbound fractions.

Figure 4.12 shows the systemic exposure for each operator, obtained in triplicate for the different modelling approaches.

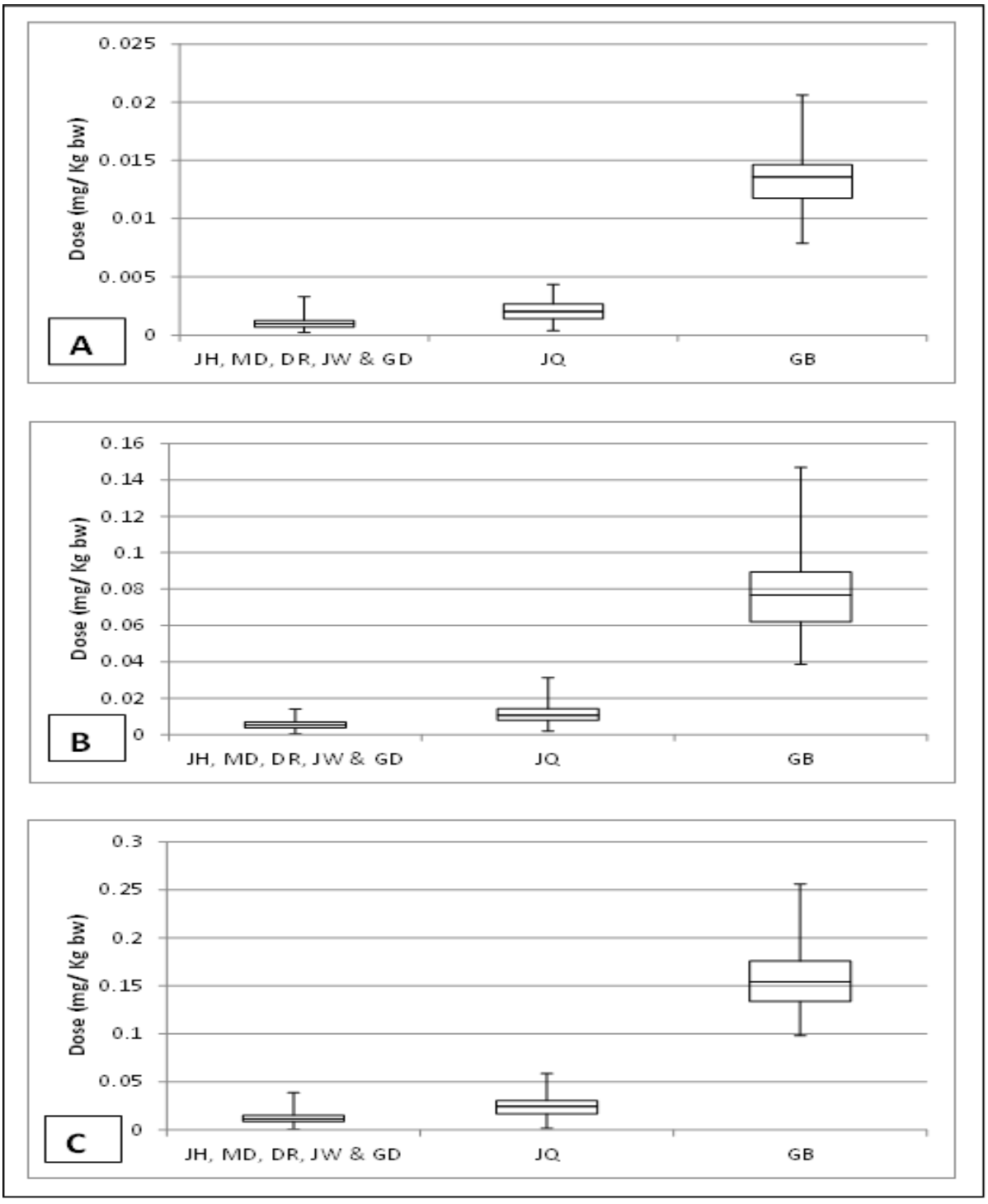


Figure 4.12: Assessment of maximum systemic (internal) exposure following occupational exposure to haloxyfop-methyl ester. A) Approach 1, **B)** approach 2, and **C)** from dog extrapolation. See text for details. The 10 x uncertainty factor for interspecies differences in risk assessment appears to cover the variability seen in the modelling.

Table 4.5: Optimised parameter values for PBPK model with haloxyfop data (approach 1)

In summary:

- The PBTK model was populated with mouse physiology.
- Prior distributions were assigned to physicochemical and biochemical parameters undergoing calibration, e.g. Fbcl, Fup_exp and PStc to (column 1).
- Once calibration was complete, posterior distributions were generated for these parameters (column 2).
- The calibrated mouse PBTK model was scaled to humans, by substituting in fixed human age-related physiology.
- The posterior distributions of optimised mouse parameters were specified as priors in the human model.
- A further round of Bayesian analysis was applied to the human model with human TK datasets. Once the human model was convoluted with the TK data, secondary posterior distributions were obtained (column 3).

	Prior distribution (mouse)			1° posterior distribution (mouse)			2° posterior distribution (human)		
Parameter[1]	Shape	min	max	Shape	Descriptor 1	Descriptor 2	Shape	Descriptor 1	Descriptor 2
Fbcl	Uniform	0.00E+00	1.00E+00	Uniform	0.00E+00	1.00E+00	Uniform	0.00E+00	1.00E+00
Peff_sto	Uniform	0.00E+00	1.00E-03	Log Normal	3.51E-04	1.44E+00	Log Normal[2]	1.20E-06	4.50E+00
Peff	Uniform	0.00E+00	1.00E-03	Normal	1.98E-05	5.95E-06	Log Normal[2]	6.01E-05	1.69E+00
SEF_duo	Uniform	1.00E+00	1.00E+01	Log Normal	1.57E+00	1.41E+00	Uniform[2]	1.00E+00	1.00E+01
SEF_SI	Uniform	1.00E+00	1.00E+01	Log Normal	2.49E+00	1.71E+00	Uniform[2]	1.00E+00	1.00E+01
SEF_col	Uniform	1.00E+00	1.00E+01	Log Normal	1.10E+00	1.09E+00	Uniform[2]	1.00E+00	1.00E+01
fup_exp	Uniform	0.00E+00	2.00E-02	Normal	4.98E-03	4.91E-04	Normal	8.34E-03	1.30E-03
PStc	Uniform	0.00E+00	1.00E-03	Normal	8.01E-05	1.95E-05	Normal	7.20E-05	1.82E-05
V_max_liv_e	Uniform	0.00E+00	1.00E+01	Uniform	0.00E+00	1.00E+01	Uniform	0.00E+00	1.00E+01
Km_liv_e	Uniform	0.00E+00	1.00E+01	Uniform	0.00E+00	1.00E+01	Uniform	0.00E+00	1.00E+01
fut_liv	Uniform	0.00E+00	1.00E+00	Normal	8.84E-04	7.39E-05	NA	NA	NA
V_max_kid_a	Uniform	0.00E+00	1.00E+01	Normal	1.76E-03	8.09E-04	Normal	2.01E-03	7.51E-04
Km_kid_a	Uniform	0.00E+00	1.00E+01	Uniform	0.00E+00	1.00E+01	Uniform	0.00E+00	1.00E+01
Kp_ski_liq	NA	NA	NA	Uniform	0.00E+00	5.00E+00	Uniform	0.00E+00	5.00E+00
Perm_co	NA	NA	NA	Uniform	0.00E+00	1.00E-02	Normal	2.60E-04	1.48E-04
Cry	NA	NA	NA	Uniform	0.00E+00	1.00E+01	Normal	4.21E-01	1.97E-01

1) See glossary (Appendix 2) for description and units. 2) 1° posterior distribution. Descriptors 1 and 2: Uniform (min, max). Normal (mean, stdev). Log Normal (geometric mean, geometric stdev). Convergence of model calibrations was good as parameter PSRFs were generally < 1.2.

Key notes on Table 4.5:

- Gut permeability (Peff) is ~ 3.5 times greater in human *vs* mouse.
- Fraction unbound in plasma (Fup_exp) is ~ 1.7 times greater in humans *vs* mouse, indicating small interspecies differences for this parameter.
- The primary and secondary posterior distributions for permeability-surface area product (PStc) are almost identical, indicating reliable interspecies 'scalability' for this parameter.
- The metabolism parameters are unaffected by calibration, indicating TK data of parent compound is uninformative for metabolite TK.

4.4.5 Octanol: water partition coefficient (haloxyfop-P)

The octanol: water partition assay was performed for haloxyfop-P to provide additional biochemical data for model calibration. The assay was performed as described in OECD (1995), and modified to resemble physiological conditions (37 °C, using PBS pH 7.4 for the aqueous layer). There was no significant difference between the two experimental conditions ($p = 0.85, \alpha = 0.05$; $n = 10$).

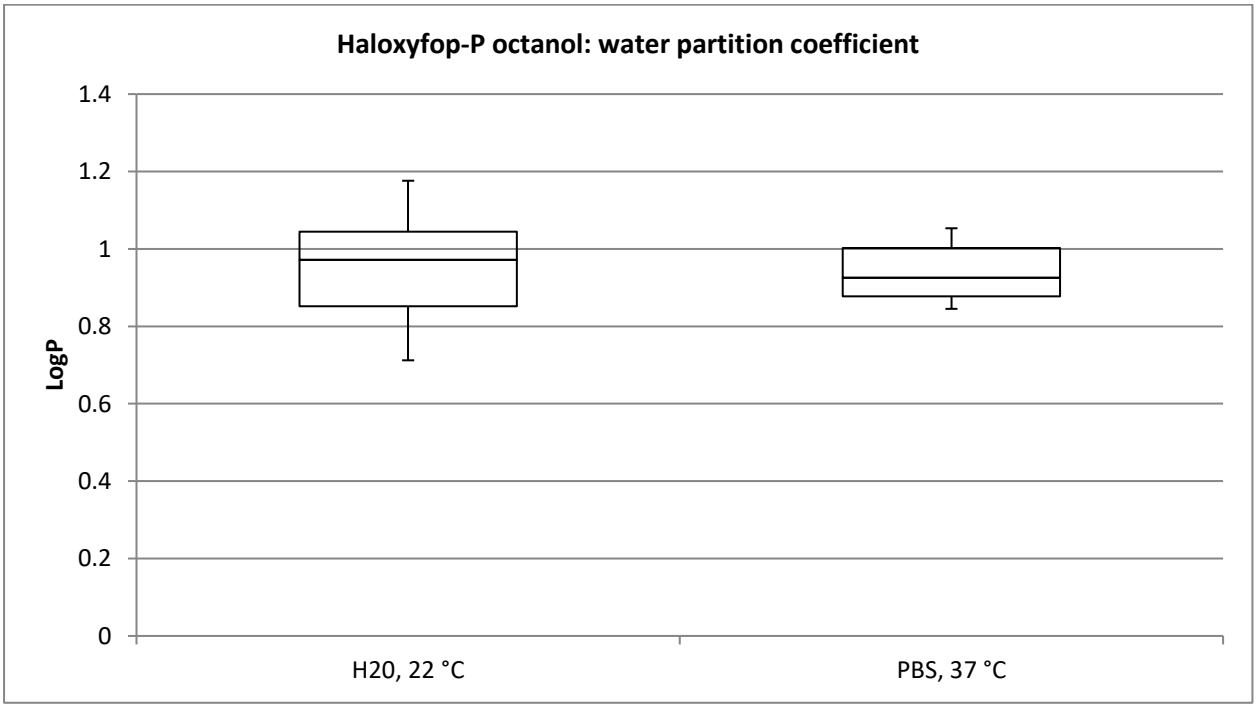


Figure 4.13: Octanol: water partition coefficient (LogP) assay for haloxyfop-P.

4.5. Discussion

4.5.1 Different ways of fitting TK data within same species

Haloxyfop hepatotoxicity has been observed in Beagle dogs (Barna-Lloyd *et al.* 1983, 1984) and Cynomolgus monkeys (Yano *et al.* 1987), and may occur in humans given sufficient exposure. Hence it is important to understand internal exposure at the liver from measures in biofluids, which can be done through PBTK models.

Figure 4.11 indicates human internal exposure assessment is affected by how the TK data is modelled within the same rodent species (mice). Approaches; 1) the discrepancy between predicted and optimised fraction bound in hepatocytes (~ 0.7 %) is interpreted mechanistically by inferring that haloxyfop is binding to PPARα (peroxisome proliferator-activated receptor) in hepatocytes. This binding is not modelled in humans, so there is no such accumulation in human hepatocytes. 2) Maximum liver exposure is substantially greater: PPARα receptor binding is not modelled in mice but instead transporter activity (influxing into hepatocytes). Once this activity is extrapolated to humans, it causes sequestration of haloxyfop within hepatocytes, leading to elevated enterohepatic circulation and greater systemic exposure (Figure 4.12). Xenobiotics can induce the expression of hepatic transporters if they undergo biliary excretion (Gant *et al.* 1995); such a positive feedback mechanism may be operating with haloxyfop and affect its disposition.

4.5.2 Extrapolating from different species

When calibrating to the dog TK data, it was not necessary to model active transport processes relating to haloxyfop elimination. Therefore the extrapolated human model did not have any active transport processes, ultimately leading to a greater systemic burden following occupational exposure (Figure 4.12). Interestingly, haloxyfop concentrations in fatty tissues such as adipose and yellow marrow are markedly lower than other tissues, as this chemical is relatively hydrophilic.

4.5.3 External exposure estimates

It is unclear whether MCMC can distinguish between inhalation and dermal exposure, since the prior distributions for both routes are identical. However, if the reverse dosimetry is done assuming only dermal exposure, then this produces worse fits to the operator HBM data.

A dermal exposure study has been performed with haloxyfop-methyl ester, the form to which operators have potential exposure: Perkins 2004 generated 'flux constants' across the skin (µg/ hr/ cm^2 -skin). These values do not appear compatible with the dermal model for calibration (Figure 4.6), as the flow-through diffusion cell does not distinguish the permeability coefficient from the basolateral membrane permeability (which are modelled separately, and each would contribute to the 'flux constant' in the set-up of Perkins 2004). For operator reverse dosimetry crystallisation was not modelled, resulting in lower systemic exposure estimates. Verdict™ is diluted in water which has a slower evaporation rate than xylene (Nolan *et al.* 1985), making crystal formation less likely. Furthermore, sweat produced during manual labour may dissolve any crystals formed on the skin surface.

Previous estimates of general operator exposure to haloxyfop-methyl ester using the 'German' model and 'UK-POEM' model are 12.2 % and 169 % of the AOEL, respectively (with PPE, i.e. gloves and coverall) (EFSA 2009). Previous estimates for amounts of haloxyfop-methyl ester absorbed for operators J.Q. and G.B. are 0.00033 and 0.0014 mg/ Kg bw, respectively (Nolan *et al.* 1991), according to a compartmental TK model (Nolan *et al.* 1985). Estimates obtained here through reverse dosimetry are substantially greater (Figure 4.12). This reflects the different modelling and statistical approaches used in this project. However, it may be due to loss of parameter correlation (Section 4.5.4).

4.5.4 Parameter correlation

Significant correlation between parameters is lost when extrapolating to humans (not shown). This may be due to the adopted method of specifying posterior distributions of optimised mouse and dog physicochemical and biochemical parameters as marginal priors in the human model. Independence between parameters cannot be assumed in this way because the posterior distribution is highly dimensional (multivariate). Other possible causes include:

- Recalibrating gut parameters (Peff_sto, Peff and SEF's) to the human TK data.
- Omitting a calibrated parameter when extrapolating to humans (e.g. fraction bound in liver) or in reverse dosimetry (i.e. dermal crystallisation).
- Introducing a human-specific model parameter and calibrating it (e.g. skin permeability coefficient)

It is known that perturbing marginal posterior distribution(s) in the ways above can affect the correlation matrix (Bois 1999, Hack 2006a). As there is no way to directly specify a multivariate distribution in MCSim, one way of preserving parameter correlations may be through utilising hierarchical modelling, in which both mice and humans are included (some parameters common to both, others specific to mice or humans) (F. Bois, pers. comm.).

4.5.5 Inference of systemic (tissue) exposure

For operators J.Q., J.H., M.D., D.R., J.W. and G.D., their maximum systemic exposure (occurring approximately 180 minutes after initial exposure) is within the AOEL (Figure 4.12; approach 1), indicating minimal toxicological risk. Furthermore, the estimates for operators J.H., M.D., D.R., J.W. and G.D are an overestimate of actual exposure, because their surrogate HBM data is based on the analytical LoQ. However, the maximum systemic exposure for operator G.B. is approximately three times greater than the AOEL, indicating potential toxicological risk. The reason why G.B. excreted substantially more than other operators is unclear since the air and patch data suggest his external

exposure was similar to other participants (Scortichini *et al.* 1987). Despite this, Figure 4.10 indicates substantial dermal exposure. One possibility is that operator G.B. was not compliant with wearing personal protective equipment (PPE) while mixing, loading and/ or spraying Verdict™. Although professional operators should access to PPE, amateur operators (i.e. home garden users) are not considered to have access to appropriate PPE (EC 2006). Thus the amateur use of Verdict™ is not recommended.

4.5.6 Revision to the recognised AOEL?

The extrapolated human model accurately predicts human TK data (Figure 4.9). Subsequently, the 10 x uncertainty factor for interspecies variability, used in calculating the AOEL from the NOAEL, could be abolished/ reduced (M. Aggarwal pers. comm.). Thus the AOEL could potentially be raised by a factor of ten from 0.005 to 0.05 mg/ Kg bw/ day. This would still allow 10 x uncertainty (for intraspecies variability) below the NOAEL of 0.5 mg/ Kg bw/ day. Subsequently, systemic exposure of operators is more likely to fall within acceptable levels for risk assessment.

As operator exposure is predominantly *via* dermal and inhalation routes, the relevance of NOAELS and LOAELs determined through oral routes for the exposure risk assessment of operators is questionable. The Beagle dog study could be performed again using the dermal and/ or inhalation routes of exposure.

4.5.7 Summary and conclusions

PBTK models can be calibrated and used to accurately calculate tissue exposures and be used in risk assessment:

1. There are different biologically-plausible approaches to fitting toxicokinetic data in the same rodent PBTK model, and once extrapolated to humans, these have different implications for internal exposure assessment.

2. Human exposure assessment is informed by the animal species being extrapolated from.

3. Reverse dosimetry can be used to assess external human exposure, using a calibrated human PBTK model and appropriate HBM data.

4. A calibrated PBTK model can be used to infer exposure in target tissue(s) of interest.

5. Out of the seven operators participating in the occupational exposure study (Nolan *et al.* 1991), only one operator (G.B.) was potentially at risk of toxicity from his external and internal exposure levels (approach 1).

4.5.8 Future *in silico* work

- Develop regression/ allometric models for scaling rodent/ canine gut permeability to humans, so that it is unnecessary to recalibrate this parameter to human TK data.
- Include additional sources of physiological variability into the analysis. For example, when scaling the calibrated mouse and dog PBTK models to humans, fixed age-related physiology was substituted into the model (average age 43 years), because the individual ages of operators were unreported in Nolan *et al*. 1985. The physiological parameter values change substantially over the age range of the volunteers (21 - 55 years), so further analytical work could implement this variability into the Bayesian analysis.
- Potentially model induction of liver transporters to investigate effects on chemical disposition.
- Implement uncertainty regarding parameter mean into the analysis, and separate from variability through a hierarchical statistical model.
- Investigate use of hierarchical modelling as a means of maintaining parameter correlations when performing interspecies extrapolations and reverse dosimetry (chapter 5).

Chapter 5: Development of PBTK with statistical models to assess operator exposure to haloxyfop

5.1 Abstract

The MCMC algorithm has been used to calibrate PBTK models and to identify parameter covariance in terms of how the parameters vary in proportion to each other (Bois 1999). In chapter four, posteriors of mouse PBTK parameters were used in the human PBTK model as marginal (univariate) priors (parameter distributions that vary independently of each other). However, independence between parameters cannot be assumed in this way because the Bayesian posterior distribution is highly dimensional (multivariate). Neglecting parameter covariance when extrapolating to another species can result in highly improbable combinations of values being selected, and therefore unrealistic model physiology being adopted (Bernillon & Bois 2000). This leads to improbable model predictions (Bois 2000b), and confidence intervals in the model's predictions becoming over-estimated (Portier & Kaplan 1989). In other words, estimates of internal exposure can become overestimated. In this chapter, statistical models were built to combine both rodent and human PBTK models in a joint Bayesian analysis thus creating a single multivariate distribution from which exposure assessments could be made. This study used both animal and human PBTK models jointly to derive human exposure information. Maintaining correlations between model parameters in this way was shown to affect estimates of human systemic exposure. The new estimates of human systemic exposure were significantly lower with a hierarchical statistical model versus without ($p < 0.001$; $\alpha = 0.05$, student's t-test).

5.2 Introduction

5.2.1 Methods of model extrapolation

The physiological nature of PBPK models permits inter-species extrapolations. Therefore, a rodent model can be calibrated to a toxicokinetic dataset for a particular chemical and subsequently extrapolated to humans. The first use of a PBPK model to perform an interspecies extrapolation (rodents to humans) for an agency risk assessment was done by the U.S. EPA with methylene chloride in 1987 (Andersen *et al.* 1987). The methods of extrapolation involved 1) replacing fixed rodent parameter values with human values obtained from the literature or experimental data, and 2) use of allometry (see next paragraph). These methods have subsequently been used in a number of literary publications, for example, to extrapolate a rat model to humans for the assessment of toluene exposure (Tardif *et al.* 1997). De Buck *et al.* 2007 showed this approach was reasonably successful in predicting human toxicokinetics for 26 drugs from calibrated rat models.

Allometric scaling is the use of a regression equation involving body weight to predict a parameter of interest in a different animal species (Lindstedt & Schaeffer 2002). This is applied in PBPK modelling to scale animal parameters to humans (Ings 1990). The general allometric equation takes the form $y = a(\text{body weight})^b$, where y is the model parameter of interest. These parameters typically include absorption and metabolism rates. However the inherent uncertainty/ variability of body weight and the allometric coefficient (a) and exponent (b) is often not taken into account (Bois 1999, Bois 2000b).

Parameters describing xenobiotic metabolism can be difficult to extrapolate across species because kinetic constants do not necessarily follow a predictable pattern, and there may be unknown interspecies differences in metabolism. Therefore, metabolic data should ideally be obtained from the species of interest (humans), although opportunities to collect data in human subjects are limited. Subsequently, *in vitro* studies are popular for determination of metabolic parameters (V_{max}

and Km), which then get scaled for use in a PBPK model (Lipscomb & Poet 2008). This process is called *in vitro* to *in vivo* extrapolation (IVIVE). This is not allometry, but instead relies on an understanding of the experimental and biological factors that influence *in vivo* estimation. For example, a value of Vmax derived from *in vitro* assays using isolated hepatocytes is sometimes expressed as metabolism rate per million cells (mg/ sec/ 10^6 cells). Subsequently a scaling factor, hepatocellularity per gram of liver (HPGL), is required to estimate the rate for the whole liver (Kenyon 2012):

Whole liver Vmax (mg/ sec) = Vmax (mg/ sec/ 10^6 cells) x HPGL (cells/ g-liver) x liver weight (g) [1]

A 'parallelogram' approach can be used for predicting metabolic rate constants for the human PBPK model from 1) *in vivo* rodent studies, and 2) *in vitro* studies using rodent and human tissues. Subsequently, a ratio between rodent *in vitro*/ *vivo* measures is calculated, and used to derive the 'missing' human *in vivo* parameter (Knudsen *et al.* 2016). Vmax can be scaled in an allometric manner, using an exponent of 0.75 (West *et al.* 2002), based on *in vitro* data (i.e. IVIVE) or derived by fitting a rodent model to *in vivo* data. However this method provides a crude approximation, and should only be performed when other methods are infeasible. Km is sometimes assumed not to require to inter-species scaling, as Km describes the affinity between enzyme and substrate (Ward *et al*. 1988, Chiu *et al.* 2009). However this assumes that the same enzyme is involved in both species.

5.2.2 Bayesian statistical models for exposure assessment

The aforementioned extrapolation techniques often calibrate a subset of parameters while keeping others fixed. This is problematic when correlations exist between parameters (Bernillon & Bois 2000). Values being selected by the optimisation algorithm may provide a good fit to the data, but may not have a meaningful correspondence to the real biological system they are intended to represent. Another major difficulty in performing inter-species scaling arises from parameters having distributions rather than fixed values. For example, Watanabe & Bois 1996 calibrated rat and human

PBTK models to respective toxicokinetic data independently, and obtained distributions of optimised parameter values. Three different approaches were used to extrapolate rat distributions to humans: 1) multiplicative (rat model scaling coefficients multiplied by the ratio of the mean values between humans and rats), 2) additive (scaling coefficients extrapolated by adding the difference between average human value and the average rat value to the rat parameter value) and 3) allometric scaling from rat to human. Unfortunately, all three extrapolations poorly predicted human toxicokinetics (when compared to the human model which was independently calibrated to the human toxicokinetic data). This may be because a degree of parameter covariance was lost in the extrapolation process.

These issues relating to parameter covariance can be addressed using Bayesian analysis, through the use of appropriate prior distributions assigned to model parameters, and the use of a suitable statistical model. Hierarchical models in a Bayesian framework have been used to calibrate individual species models, without inter-species extrapolation (Bois 2000b, Hack *et al.* 2006b, Chiu *et al.* 2009). This approach is useful for providing insight towards the identification of species-specific parameters like gut permeability or transporter activity levels. The primary aim of this chapter was to use animal toxicokinetic data to help inform human exposure assessment through the use of a suitable Bayesian statistical model which preserves parameter covariance.

5.2.3 Chapter aims

- To use hierarchical statistical models to derive estimates of operator exposure using animal and human toxicokinetic data as well as HBM data.
- To compare estimates of operator systemic exposure without (chapter 4) and with (chapter 5) use of hierarchical statistical models.
- To investigate the sex difference in plasma toxicokinetics in F344 rats using a suitable statistical model.

5.3 Methods

5.3.1 PBTK model

A PBTK model was developed with biological plausibility a primary objective and one that in particular would allow the further interrogation of liver transporter activity. The previous liver PBTK model (specified in chapter 4) included the parameter 'Fbcl', which stands for 'fraction (of the metabolised portion) entering biliary clearance'. This parameter is assigned a value between 0 - 1 (it is a fraction). This portion includes the amount of chemical entering the bile canaliculi via passive diffusion and active transport (through the apical membrane). Hence, by using the term 'Fbcl', the model can be simplified but may be an example of model over-simplification at the expense of biological plausibility. Therefore the model structure was modified to describe uptake into bile canaliculi in terms of passive diffusion and active transport (Figure 5.1). Indeed, transporters (particularly at the apical membrane) are anticipated to play an important role in chemical disposition. The transporter and enzyme-mediated activity was assumed to follow Michaelis-Menten kinetics.

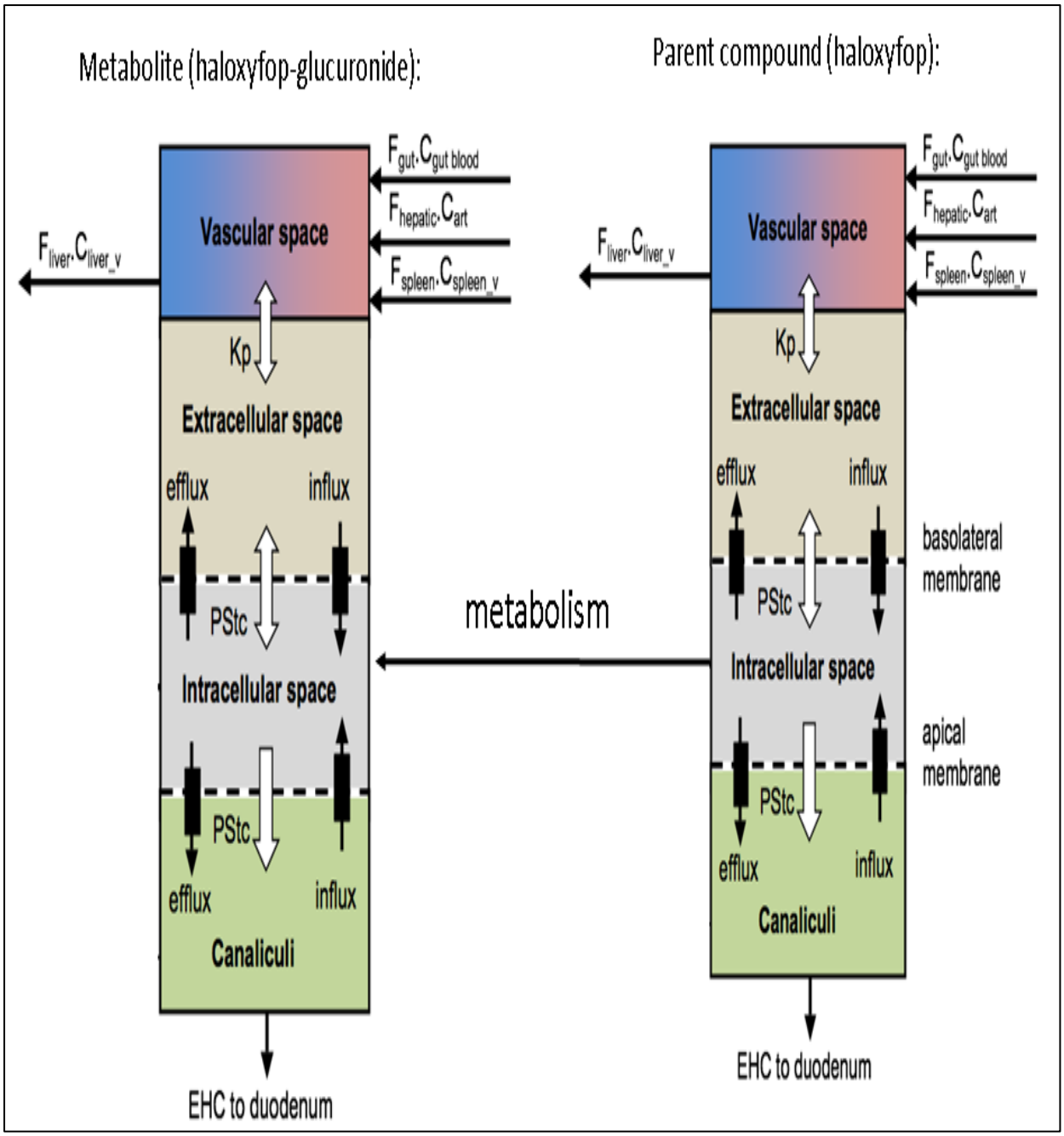


Figure 5.1: Revised liver model. The model describes uptake into the bile canaliculi in terms of passive diffusion and active transport across the apical membrane. Although the term 'passive diffusion' is used, diffusion across the membrane is considered to occur one-way due to the chemical binding bile salts within the canaliculi *in vivo* which prevents backwards transport. The amount metabolised within hepatocytes (described in terms of Michaelis-Menten kinetics) remains in the liver (now described as a sub-model to allow metabolite tracking), where it has access to systemic circulation, or can also enter the bile. (N.b. metabolite disposition was not assessed with the calibrated PBTK model, because the glucuronide conjugate of haloxyfop is unlikely to be toxic, even at relatively high levels). Figure adapted from Simulations Plus 2013b.

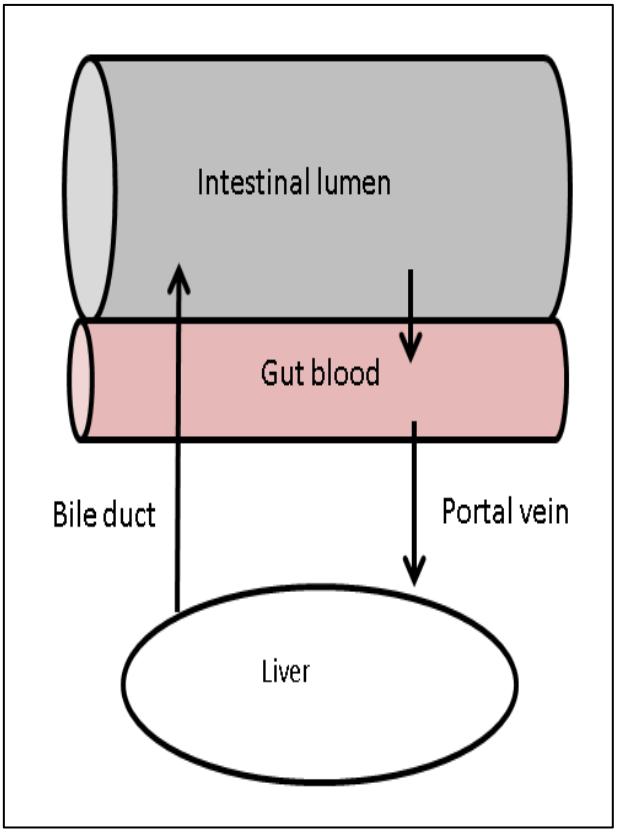


Figure 5.2: Schematic of enterohepatic recirculation. The parent compound may undergo metabolism in the liver - for example, it may be conjugated to glucuronide which increases water solubility and facilitates elimination from the body. Biliary excretion is more likely after conjugation which increases the compound's molecular weight, thus it may enter the duodenum via the bile duct. In humans, bile is stored in the gall bladder between meals, however rats do not have a gall bladder, therefore the model (for both species) is a simplification. Gut flora produce β-glucuronidase, which hydrolyses haloxyfop-glucuronide present in bile, converting it back to the parent molecule (haloxyfop-P), and hence can be reabsorbed into portal blood. A chemical undergoing enterohepatic recirculation may prolong its plasma half-life.

5.3.2 Statistical models

A statistical model is often required in conjunction with a PBTK model to ensure appropriate analysis of toxicokinetic data. Bois (2013) gives a useful overview of the application of statistical models in PBTK modelling. The hierarchical statistical model was built to allow the MCMC vector to draw samples from all parameters undergoing calibration using their joint (combined) probability distribution (Gelman *et al.* 1996). This was done using all haloxyfop measurement data allowing both mouse and human models to be calibrated simultaneously. In Figure 5.4, the toxicokinetic data was aggregated at the species level thus two layers were used to encompass mouse and human toxicokinetic datasets separately, lumping interindividual variability with measurement and model uncertainty. These toxicokinetic datasets were analysed to calibrate species-specific (θ_1), and species non-specific PBTK model parameters (θ_2) which were assigned prior distributions. The latter (θ_2) allowed mouse toxicokinetic data to inform operator exposure assessment; further symbols in equation 2 (below) are defined in Figure 5.4. Whereas PStc for example is species non-specific, the

gut permeability parameter is species-specific and interspecies regression equations vary making extrapolation difficult (Fagerholm *et al.* 1996, Zakeri-Milani *et al.* 2007). The HBM data is nested within the human model such that exposure reconstruction adopts values from θ_1 and θ_2. The data likelihood, P(E|H), becomes:

$$P(TK, HBM_i, logP \mid f(\theta_1, \theta_2, C_{u,i}, \xi, t, C), \sigma_1, \sigma_2, \sigma_3) \quad [2]$$

The mathematical hypothesis (terms RHS of the vertical bar) consists of the following: 'f' (deterministic PBTK model), '$C_{u,I}$' (unknown exposure concentration for an individual operator), 'ξ' (species-specific physiology), 't' (measurement times of toxicokinetic data), and 'C' (exposure concentration). The 'experimental evidence' for Bayes theorem (terms LHS) comprises of the terms 'TK' (toxicokinetic data), 'HBM_i' (human biomonitoring data, as amounts excreted in an individual's urine following unknown occupational exposure), and 'logP' (experimental data on octanol: water partition coefficient, a model parameter). σ1,2,3 are the standard deviations used to describe the variabilities and measurement errors for the evidence, including the modelling error.

Bayes' theorem, $P(H|E) \propto P(E|H) \times P(H)$, then takes the form:

$$P(f(\theta_1, \theta_2, C_{u,i}, \xi, t, C), \sigma_1, \sigma_2, \sigma_3 \mid TK, HBM_i, logP) \propto$$

$$P(TK, HBM_i, logP \mid f(\theta_1, \theta_2, C_{u,i}, \xi, t, C), \sigma_1, \sigma_2, \sigma_3) \times P(f(\theta_1, \theta_2, C_{u,i}, \xi, t, C), \sigma_1, \sigma_2, \sigma_3) \quad [3]$$

The likelihood function identifies model parameter values that best describe the experimental data - these are further weighted by the prior distribution to give the posterior parameter distributions (Gilks *et al.* 1996).

The statistical models can be displayed using a directed acyclic graph (DAG), which serves to deconvolve variabilities present in the toxicokinetic data. The 'nodes' (circles) represent unknown model parameters to be 'updated' using Bayes' theorem. These entities replace the term for the hypothesis in the equation above; they input into a deterministic PBTK model (f). The entities in

squares represent known (measured) information - for example, the prior distributions assigned to model parameters, the toxicokinetic data and corresponding measurement times.

Some arrows in DAG graphs indicate conditional dependencies (stochastic relationships), others represent deterministic relationships. For example in Figure 5.4, parameter values (θ) are distributed around mean (μ) and standard deviation (∑). I.e., the conditional dependence of Cu on μ and ∑ is indicated by arrows. For the graph to be coherent it must be acyclic, so arrows leading away from a node cannot loop back to the same node. Because the toxicokinetic data used for model calibration was aggregated at the species level (i.e. with multiple subjects), the statistical model used lumps measurement error with inter-individual variability (Bois 2000a,b). GrabIt™ V1.5 data capture software was used to extract the toxicokinetic data including measurement uncertainties from graphs in Smith *et al.* 1984, Nolan *et al.* 1985, 1991. For computational convenience, incremental urine data were combined to give cumulative urine excreted during the time-course of the study (the PBTK model as coded does not model cumulated excreted over discrete time intervals, e.g. over 24 hours). Standard deviations specific to each data point were assigned to plasma, urine and bile likelihoods reflecting primarily inter-individual variability.

5.3.3 Selection of priors

The operator 'population' exposure parameter (C_u), the 'hyper-prior', was assigned an uninformative (uniform) distribution reflecting minimal previous knowledge on operator external exposure. This distribution was truncated at zero to avoid numerical errors arising from negative parameter values during the MCMC calculations. The values of physicochemical parameters (e.g. gut permeability) are dependent on the chemical's characteristics (as well as physiology), therefore determining relevant priors from the literature is not straightforward. Therefore uniform distributions were also assigned to various biochemical and physicochemical parameter distributions, and the analysis was performed to 'speak' about these parameters. This method contrasts with previous model

calibrations where prior distributions were based on visual fitting or previous analysis (Bois 2000a, Hack *et al.* 2006). This is problematic because the same toxicokinetic data is used to obtain both prior and posterior distributions. Uniform distributions were left truncated at zero and right truncated to ensure only physiologically-meaningful values were selected (Bois 2013). The interval was set very wide reflecting uncertainty in inter-species extrapolation (Yang *et al.* 2010), and to minimise potential bias. Since almost all available *in vivo* haloxyfop toxicokinetic data was utilised in the analysis, posterior distributions may be accurate despite several priors having uninformative distributions. As described in Chiu *et al.* 2009, the metabolism parameters were assigned uniform prior distributions; the same approach was taken here including transporter parameters.

It is important in model calibration to separate parameter uncertainty and variability, as both affect the confidence of model predictions. This was done using a suitable hierarchical model (Figure 5.3) for fractional blood flow rates and tissue volumes whose prior distributions are assumed to be normally distributed (Hack *et al.* 2006b). These prior distributions were assigned CVs of 50 % to reflect intra-individual adult variability across different ages (Hack 2006b, Yang *et al.* 2010), normal truncated at ± 3 standard deviations (Yang *et al.* 2010). Corresponding uncertainties are displayed in Tables 5.2 - 5.3. Fractional coefficients of variation (CVs) were calculated for posterior distributions (stdev ÷ mean) to show the extent of population variability about their respective population means (greater CVs indicate 'broader' distributions). Fractional coefficients of uncertainty (CUs) were calculated in the same manner as CVs, but describe the uncertainty distribution of the population mean. Blood flows are lesser known than tissue volumes (Hack 2006b), thus CU's of 30 % were applied to blood flows, and CU's of 20 % to tissue volumes (Mezzetti *et al.* 2003, Hack 2006b).

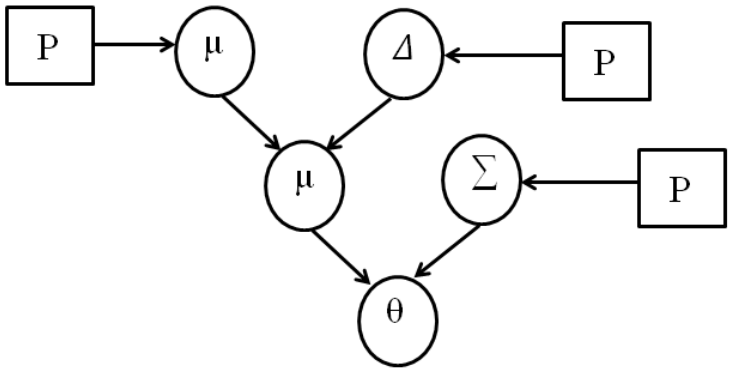


Figure 5.3: Hierarchical model for separation of model parameter uncertainty and variability. The PBPK model parameter (θ) has a mean (μ) and variability (∑) in the population. The variability is described by the standard deviation, ∑. The uncertainty of the location of the mean (*Δ*) is taken into account. It is possible to extend this model by incorporating uncertainty of the variability in the population (e.g. Jonsson & Johanson 2002, Hack *et al.* 2006b, Yang *et al*. 2010). Prior information (P) is positioned at the open ends of the hierarchical model. Adapted from Bois 2013.

5.3.4 MCMC convergence

MCMC was performed using the Metropolis-Hastings algorithm (Hastings 1970) as implemented in the code MCSim (Bois & Maszle 2008) to calibrate the model (Section 2.1). Markov chain convergence was confirmed by running three independent chains seeded with different random numbers. Stationary distributions were obtained after running approximately 10,000 iterations so these iterations were discarded as 'burn-in'. Convergence was monitored by calculating potential scale reduction factors (PSRFs) for parameters using the Gelman-Rubin convergence diagnostic (Gelman & Rubin 1992). Microsoft Excel was used to perform all statistical analyses. Calibration was verified by visually assessing the model's ability to fit relevant toxicokinetic data, assuming values of parameters sampled from their posterior distributions.

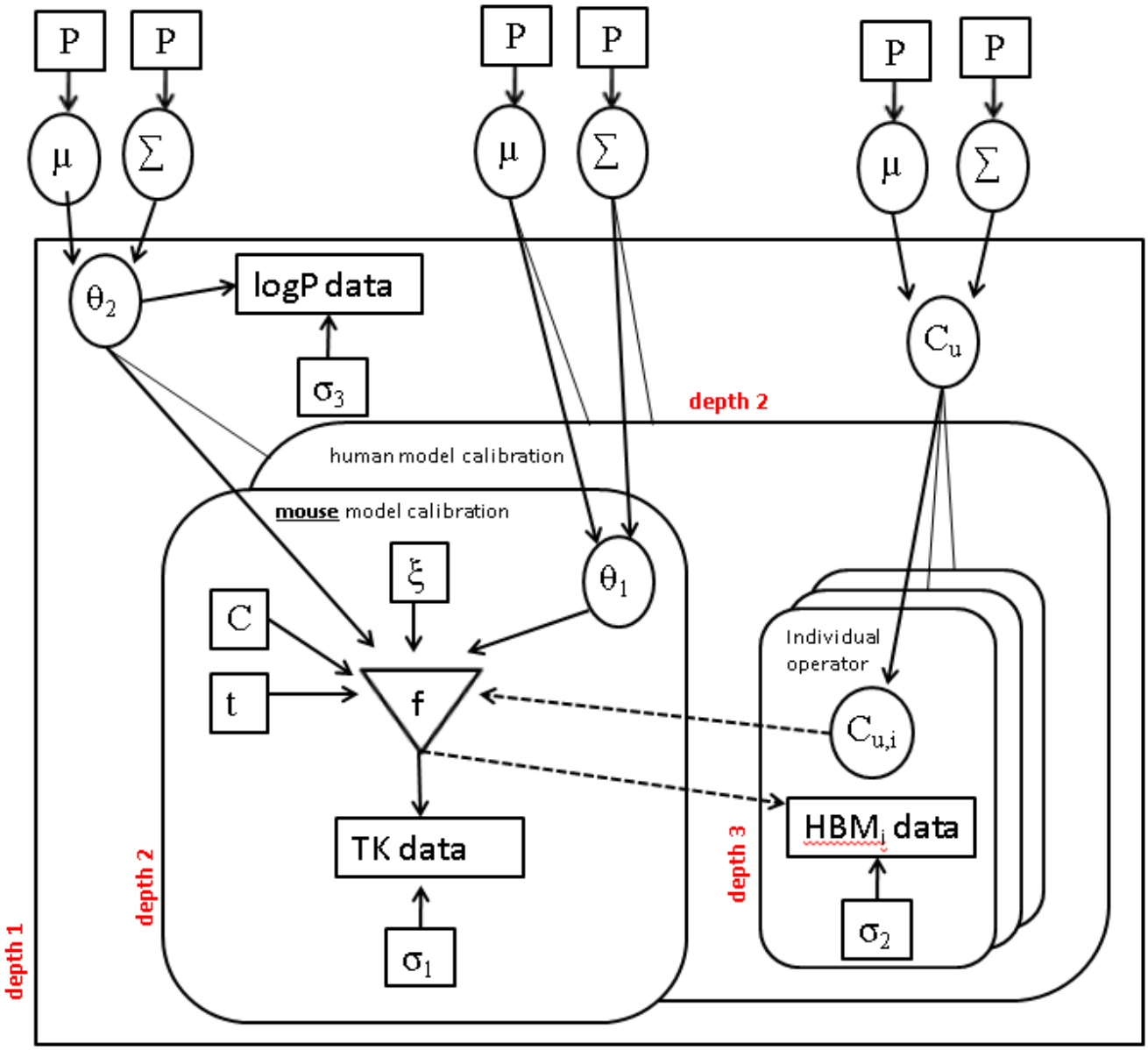


Figure 5.4: Statistical model for analysis of mouse/ human toxicokinetic data and human biomonitoring data. C: exposure concentration. $\mathbf{C_{u,i}}$**:** unknown exposure concentration, for individual operator. **f:** deterministic PBTK model. $\mathbf{HBM_i}$ **data**: human biomonitoring data (amounts excreted in individual's urine following unknown occupational exposure). **logP:** experimental data on octanol: water partition coefficient (model parameter). **TK data:** toxicokinetic data; **t:** measurement times thereof. **ξ:** species-specific physiology. $\mathbf{\theta_1}$**:** species-specific PBTK model parameters (e.g. gut permeability). $\mathbf{\theta_2}$**:** species non-specific PBTK model parameters (e.g. rate of passive diffusion through tissue membranes). **σ1,2,3:** data variability, measurement & modelling error. **P:** prior distributions; **μ, ∑:** mean & standard deviation - see Figure 5.3 for details. Plain arrows represent model calibration, and the dashed arrow represents exposure inference (exposure reconstruction).

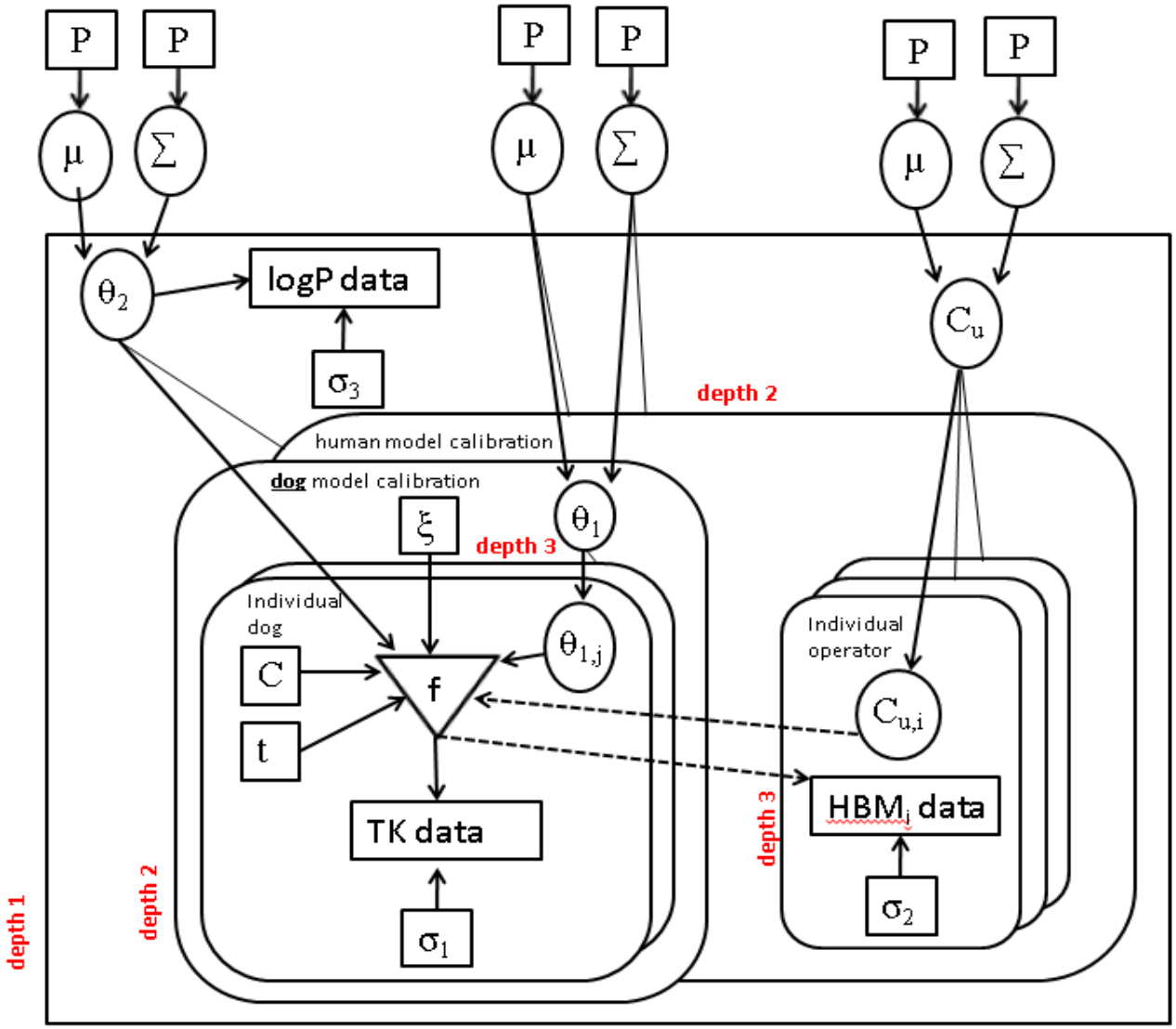


Figure 5.5: Statistical model for analysis of dog/human toxicokinetic and HBM data. The toxicokinetic data from the two dogs cannot be pooled because the dogs were administered different doses. Therefore, a population model was necessary for the dogs; each dog's toxicokinetic data is modelled (and calibrated) on an individual basis. $\boldsymbol{\theta_1}$**:** species-specific PBTK parameters. $\boldsymbol{\theta_{1,j}}$**:** dog-specific PBTK parameters.

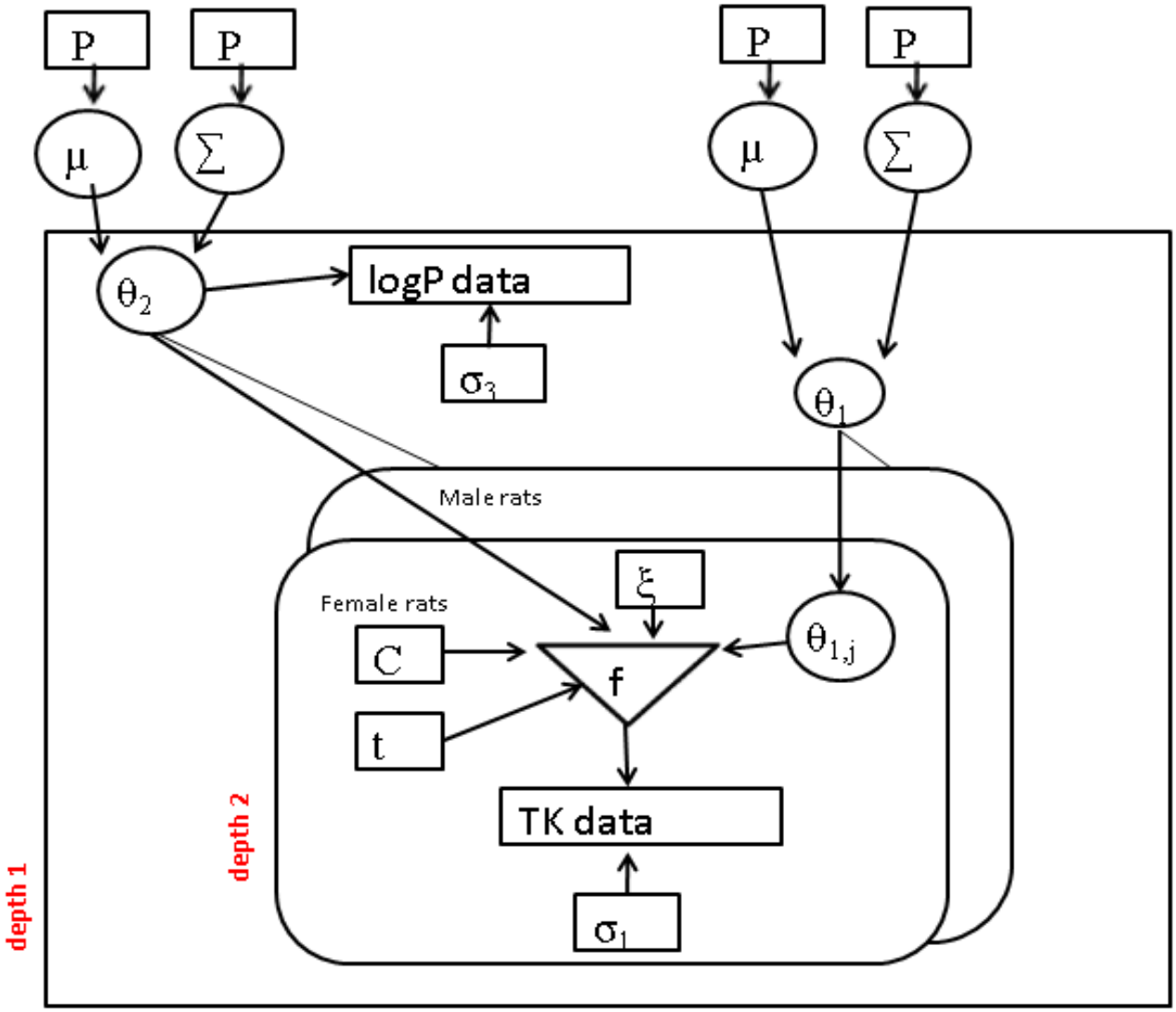


Figure 5.6: Statistical model for analysis of rat toxicokinetic data. C: exposure concentration. **f:** PBTK model. **logP:** experimental data on octanol: water partition coefficient (model parameter). **TK data:** toxicokinetic data; **t:** measurement times thereof. **ξ:** species-specific physiology. **θ_1:** gender-specific parameters (e.g. kidney transporter Vmax). **θ_2:** gender non-specific model parameters (e.g. rate of passive diffusion through tissue membranes). **$\sigma_{1,3}$:** data variability, measurement & modelling error. **P:** prior distribution; **μ, ∑:** mean and standard deviation. See text for details.

5.3.5 Rat toxicokinetic data (Smith *et al*. 1982; reproduced with permission of the rights holder, Dow AgroSciences)

A range finding study was conducted in females administered 10 mg/ Kg haloxyfop orally, and another group intravenously. Blood was collected at 6, 8, 12, 24, 30, 48, 54 and 72 hours post-dose. This toxicokinetic data indicates clearance of radioactivity from the plasma is first-order, with half-lives of 1.1 and 1.0 days for orally and intravenously dosed rats, respectively. Based on this study, a definitive study was done.

In the definitive study, F344 rats (24 of each sex) were administered a single oral dose (0.1 mg/ Kg) of ^{14}C- labelled haloxyfop (radiochemical purity > 98 %). Rats were housed in metabolism cages permitting the collection of urine and faeces. Rats were fasted overnight before dosing. Tap water and rat chow were provided ad libitum 4 hours after dosing. Plasma toxicokinetic data was collected over a period of 21 days (females) and 24 days (males). Rats were euthanised (in groups of 3) at 1, 4, 7, 10, 13, 16, 21 and 24 (males) and 1, 2, 3, 4, 5, 10, 16 and 21 (females) post-dose. Subsequently, autopsies were performed and concentrations in various tissues determined (liver, kidney, heart, skin and spleen). Radioactivity was quantified using liquid scintillation spectrometry. Analysis of bile and urine was performed using LCMS.

Haloxyfop was rapidly and completely absorbed from the GI tract, indicating the ^{14}C activity in faeces is due to biliary excretion. In both sexes, biliary and urinary ^{14}C comprises the parent compound and a metabolite from which the parent compound was liberated following acid hydrolysis, indicative of a glucuronide conjugate. Plasma concentration of ^{14}C activity decreased in a monophasic log-linear fashion. However, significant sex differences were observed in the toxicokinetic data: half-lives of ^{14}C activity clearances from plasma were 1.2 and 5.6 days for female and male rats, respectively. Autopsies indicated low-level sequestration in the liver, kidney, heart, skin and spleen as the parent compound.

5.4 Results

5.4.1 Mouse-human model extrapolation

5.4.1.1 Liver transporter activity

Michaelis-Menten kinetics includes the term 'maximum transporter velocity' (Vmax) to describe transporter activity. After model calibration, Vmax is greater in the basolateral (inwards) vs apical (outwards) membrane leading to accumulation of haloxyfop within liver cells (Figure 5.7). Km, the parameter that describes substrate concentration when Vmax is halved, is approximately equal in both membranes indicating equal affinity between substrate and transporter in both membranes.

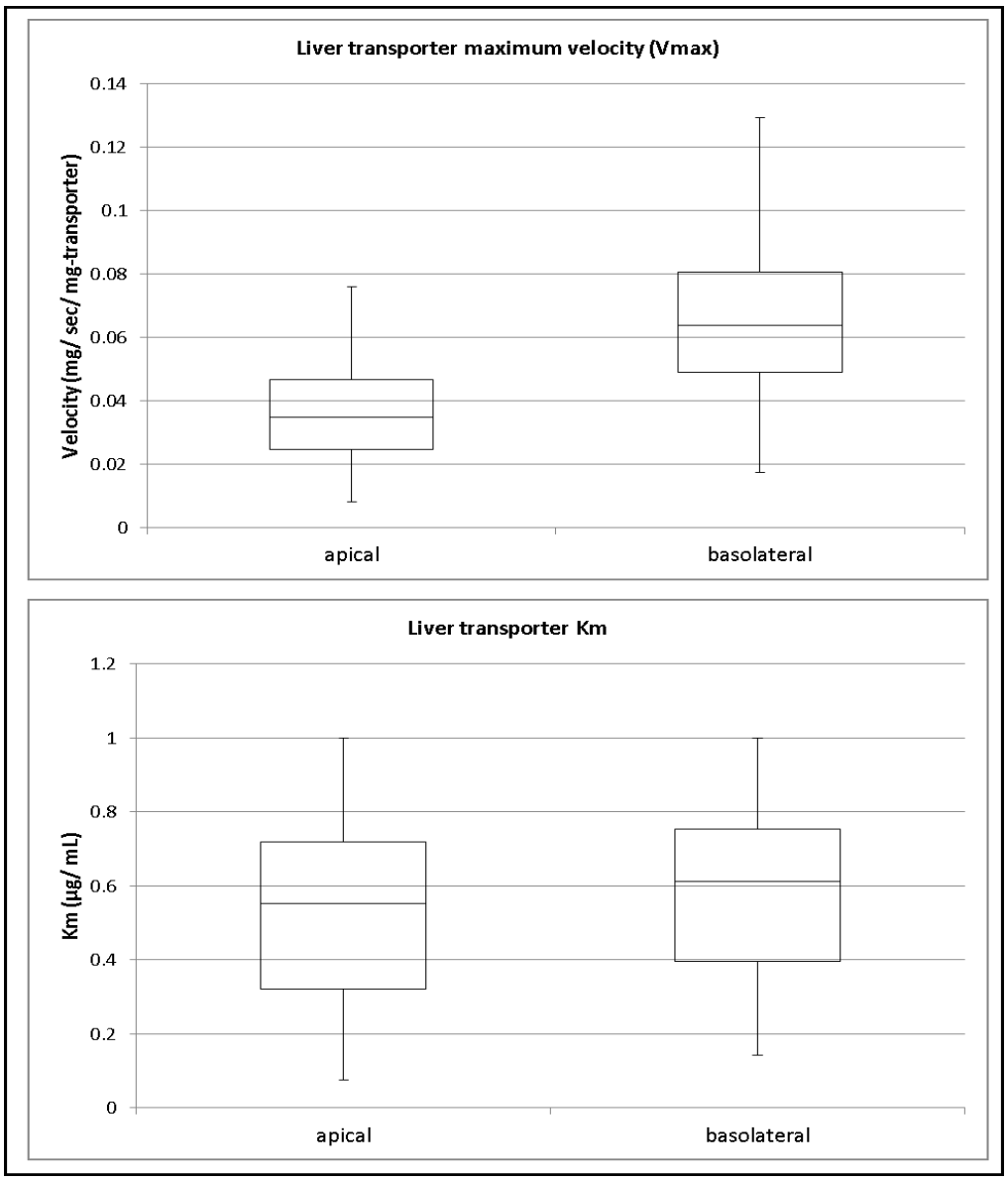


Figure 5.7: Assessment of liver transporter activity in calibrated mouse and human models (apical and basolateral membranes).

5.4.1.2 Systemic exposure estimates

The new estimates of systemic exposure after model calibration (below) are significantly lower using the hierarchical statistical model (Figure 5.4) ($p < 0.001$; $\alpha = 0.05$, student's t-test). As shown in Figure 5.8, systemic exposure estimates for all operators (excluding G.B.) are below the AOEL of 0.005 mg/ Kg bw/ day, indicating minimal toxicological risk. Conversely, the systemic exposure estimate for operator G.B., although lower with use of the statistical model, still exceeds the AOEL.

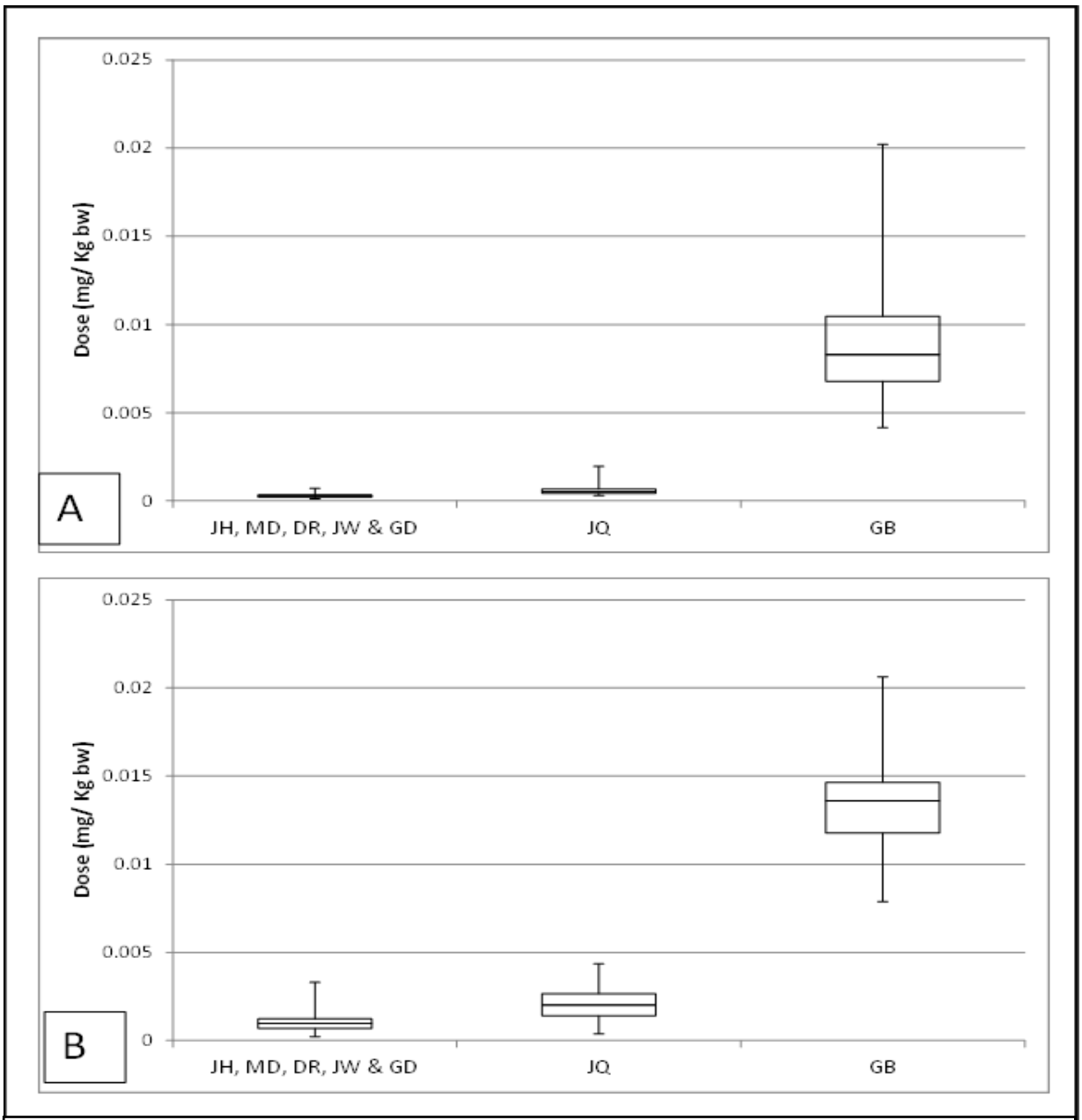


Figure 5.8: Assessment of maximum systemic (internal) exposure following occupational exposure to haloxyfop-methyl ester. A) Using the statistical model with both animal and human PBTK models. **B)** Without the use of a statistical model (leading to greater, inaccurate exposure estimates). N.b. extrapolation was done from a calibrated mouse model with liver transporter activity.

5.4.1.3 Sensitivity analysis

A 'local' sensitivity analysis was done on the calibrated human model on all model parameters, using equation 2 (Section 3.3.6.3), to identify parameters with the greatest influence on the model's prediction (Figure 5.9). This process involves changing the value of one parameter while other parameters are held constant. Of 122 model parameters, 22 were sensitive (i.e. sensitivity coefficient ≥ 0.1, Shelia 2012). Ideally, sensitivity analysis should be performed with respect to the toxicokinetic data being fitted (Bois 1999). However, in this Bayesian analysis, toxicokinetic data from various tissues were fitted simultaneously, therefore, sensitivity analysis was done with respect to plasma concentration only. Baseline values for parameters were adopted from a sampling vector of the converged MCMC chain.

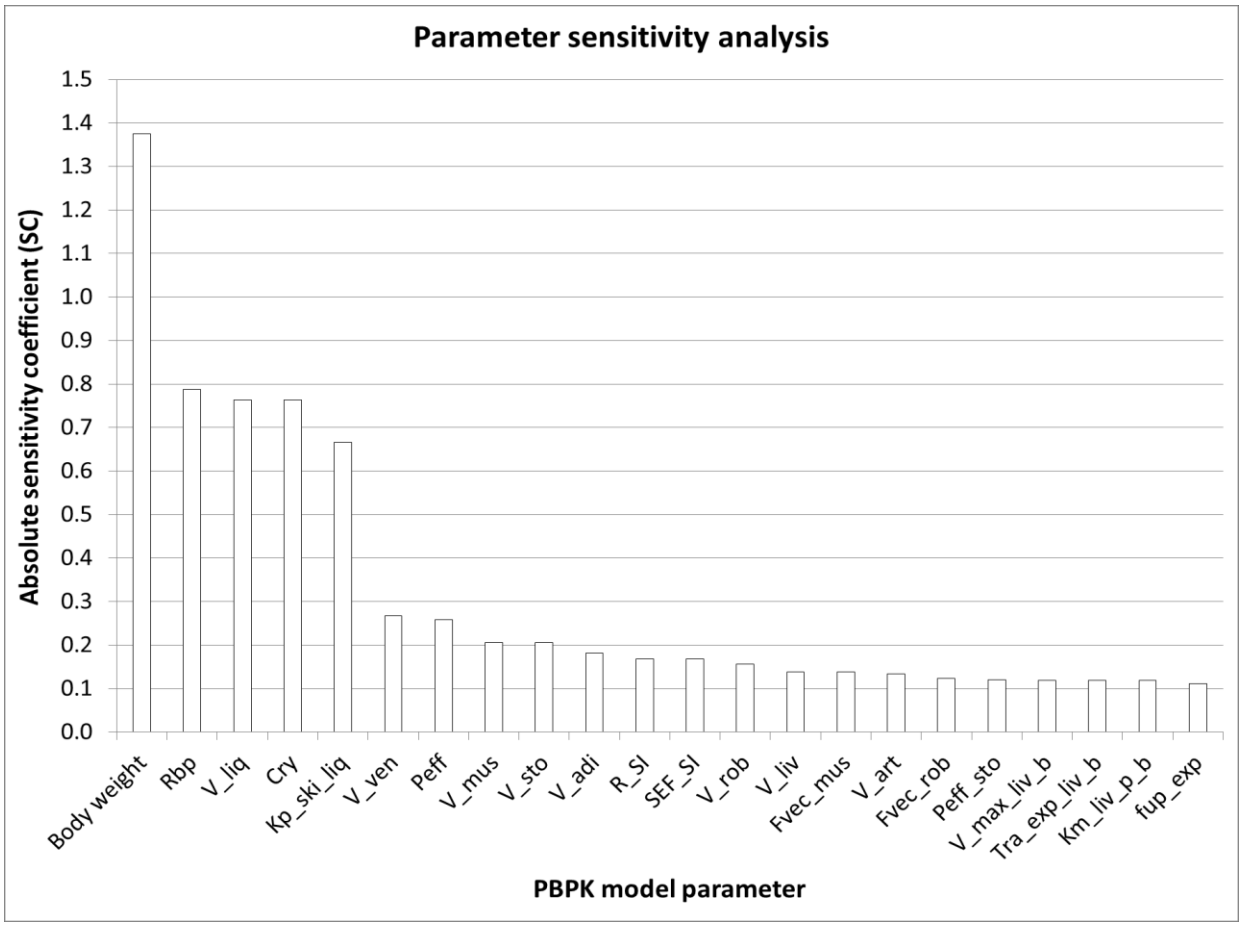


Figure 5.9: Sensitivity analysis of human PBPK model parameters. See glossary (Appendix 2) for definitions of terms and units.

5.4.1.4 Prior and posterior distributions

Uniform prior distributions were assigned to biochemical and physicochemical parameters listed in Table 5.1. After MCMC convergence, posteriors were obtained. The toxicokinetic data was not informative for several parameters (e.g. liver enzyme Km and basolateral transporter Km) as posteriors were equivalent to their priors.

Table 5.1: Prior and posterior distributions for species non-specific model parameters (in natural space).

Parameter‡	**Prior‡**	**Posterior shape**	**Posterior mean‡**	**Posterior CV**
PStc*	0, 0.001	Normal	3.84×10^{-5}	0.36
V_max_liv_e*	0, 1	Lognormal	0.90	1.11
Km_liv_p_e*	0, 1	Uniform	NA	NA
V_max_liv_b*	0, 1	Lognormal	1.43	1.10
Km_liv_p_b*	0, 1	Uniform	NA	NA
V_max_liv_a*	0, 1	Uniform	NA	NA
Km_liv_p_a*	0, 1	Uniform	NA	NA
Fup_exp*	0, 0.1	Normal	4.63×10^{-3}	0.10
Cry*	0, 1	Lognormal	0.23	0.80
logP_pla†	0.94, 0.08	Normal	0.94	0.08

* Uniform distribution (min, max). † Normal distribution (mean, standard deviation); derived from experimental data. ‡ See glossary (Appendix 2) for description and units. Correlation coefficients between PBPK model parameters presented in Appendix 6.

Posterior distributions of fractional blood flow rates and tissue volumes are generally consistent with prior distributions (Tables 5.2 - 5.3). This suggests the model structure is ‘correct’ (i.e. a good representation of the real biological system) and there are no inconsistencies in the toxicokinetic data.

Table 5.2: Prior and posterior distributions for mouse-specific model parameters (in natural space).

Parameter‡	Population mean				Population variability	
	Mean‡		CU		CV	
	Prior	Posterior	Prior	Posterior	Prior	Posterior
Peff_sto	0 - 0.001	2.9×10^{-4}	NA	NA	NA	0.73
Peff	0 - 0.001	1.9×10^{-5}	NA	NA	NA	0.40
Fr_F_kid	0.19	0.20	0.30	0.29	0.50	0.48
Fr_F_ski	0.09	0.10	0.30	0.29	0.50	0.48
Fr_F_adi	0.01	0.01	0.30	0.29	0.50	0.48
Fr_F_rob	0.05	0.05	0.30	0.29	0.50	0.48
Fr_F_gut	0.23	0.23	0.30	0.28	0.50	0.47
Fr_F_mus	0.14	0.14	0.30	0.29	0.50	0.48
Fr_F_hep	0.03	0.03	0.30	0.29	0.50	0.48
Fr_F_spl	0.01	0.01	0.30	0.35	0.50	0.49
Fr_F_yel	0.01	0.01	0.30	0.28	0.50	0.47
Fr_F_bra	0.07	0.07	0.30	0.29	0.50	0.49
Fr_F_rep	0.004	0.005	0.30	0.28	0.50	0.47
Fr_F_red	0.124	0.129	0.30	0.29	0.50	0.48
Fr_V_kid	0.016	0.016	0.20	0.19	0.50	0.44
Fr_V_nep	0.0002	0.0002	0.20	0.20	0.50	0.49
Fr_V_ski	0.14	0.13	0.20	0.20	0.50	0.65
Fr_V_adi	0.08	0.08	0.20	0.19	0.50	0.37
Fr_V_rob	0.05	0.06	0.20	0.19	0.50	0.46
Fr_V_ven	0.05	0.04	0.20	0.21	0.50	0.73
Fr_V_art	0.02	0.02	0.20	0.20	0.50	0.60
Fr_V_lun	0.01	0.01	0.20	0.21	0.50	0.48
Fr_V_mus	0.37	0.40	0.20	0.18	0.50	0.25
Fr_V_spl	0.004	0.004	0.20	0.19	0.50	0.46
Fr_V_yel	0.02	0.02	0.20	0.19	0.50	0.43
Fr_V_hea	0.004	0.004	0.20	0.21	0.50	0.49
Fr_V_bra	0.02	0.02	0.20	0.19	0.50	0.45
Fr_V_rep	0.01	0.01	0.20	0.20	0.50	0.45
Fr_V_red	0.03	0.03	0.20	0.20	0.50	0.43

‡ See glossary for description and units (Appendix 2)

Table 5.3: Prior and posterior distributions for human-specific model parameters (in natural space).

Parameter‡	Population mean				Population variability	
	Mean‡		CU		CV	
	Prior	Posterior	Prior	Posterior	Prior	Posterior
Peff_sto	0 - 0.001	2.8 X 10^{-5}	NA	NA	NA	1.10
Peff	0 - 0.001	2.6 X 10^{-4}	NA	NA	NA	1.00
Perm_co	0 - 0.1	4.9 X 10-4	NA	NA	NA	0.73
Fr_F_kid	0.17	0.18	0.30	0.27	0.50	0.43
Fr_F_ski	0.04	0.04	0.30	0.28	0.50	0.48
Fr_F_adi	0.11	0.12	0.30	0.28	0.50	0.43
Fr_F_rob	0.05	0.06	0.30	0.28	0.50	0.44
Fr_F_gut	0.14	0.12	0.30	0.35	0.50	1.36
Fr_F_mus	0.11	0.11	0.30	0.27	0.50	0.42
Fr_F_hep	0.09	0.09	0.30	0.28	0.50	0.47
Fr_F_spl	0.03	0.03	0.30	0.28	0.50	0.47
Fr_F_yel	0.02	0.02	0.30	0.28	0.50	0.48
Fr_F_rep	0.001	0.001	0.30	0.26	0.50	0.49
Fr_F_red	0.06	0.06	0.30	0.28	0.50	0.47
Fr_V_kid	0.004	0.004	0.20	0.19	0.50	0.47
Fr_V_nep	0.0001	0.0001	0.20	0.19	0.50	0.55
Fr_V_ski	0.03	0.03	0.20	0.19	0.50	0.36
Fr_V_adi	0.49	0.49	0.20	0.20	0.50	0.41
Fr_V_rob	0.16	0.16	0.20	0.19	0.50	0.43
Fr_V_ven	0.07	0.07	0.20	0.19	0.50	0.45
Fr_V_art	0.03	0.03	0.20	0.20	0.50	0.46
Fr_V_lun	0.03	0.02	0.20	0.20	0.50	0.46
Fr_V_mus	0.31	0.33	0.20	0.19	0.50	0.39
Fr_V_spl	0.002	0.002	0.20	0.24	0.50	0.51
Fr_V_yel	0.05	0.05	0.20	0.20	0.50	0.45
Fr_V_hea	0.005	0.005	0.20	0.19	0.50	0.46
Fr_V_bra	0.03	0.03	0.20	0.20	0.50	0.45
Fr_V_rep	0.0005	0.0005	0.20	0.19	0.50	0.41
Fr_V_red	0.02	0.02	0.20	0.19	0.50	0.46

‡ See glossary for description and units (Appendix 2)

5.4.2 Rat model calibration

MCMC was used to calibrate the permeability-limited rat PBTK model. Predictions of haloxyfop physicochemcial parameters were used (Table 4.3, chapter 4), although additional experimental data for logP (octanol: water partition coefficient) was obtained and used in the analysis. Figures 5.10 - 5.11 show the corresponding fits to plasma and tissue toxicokinetic data following oral (0.1 mg/ Kg) and intravenous (10 mg/ Kg) doses of haloxyfop, assuming values of parameters sampled from their posterior distributions.

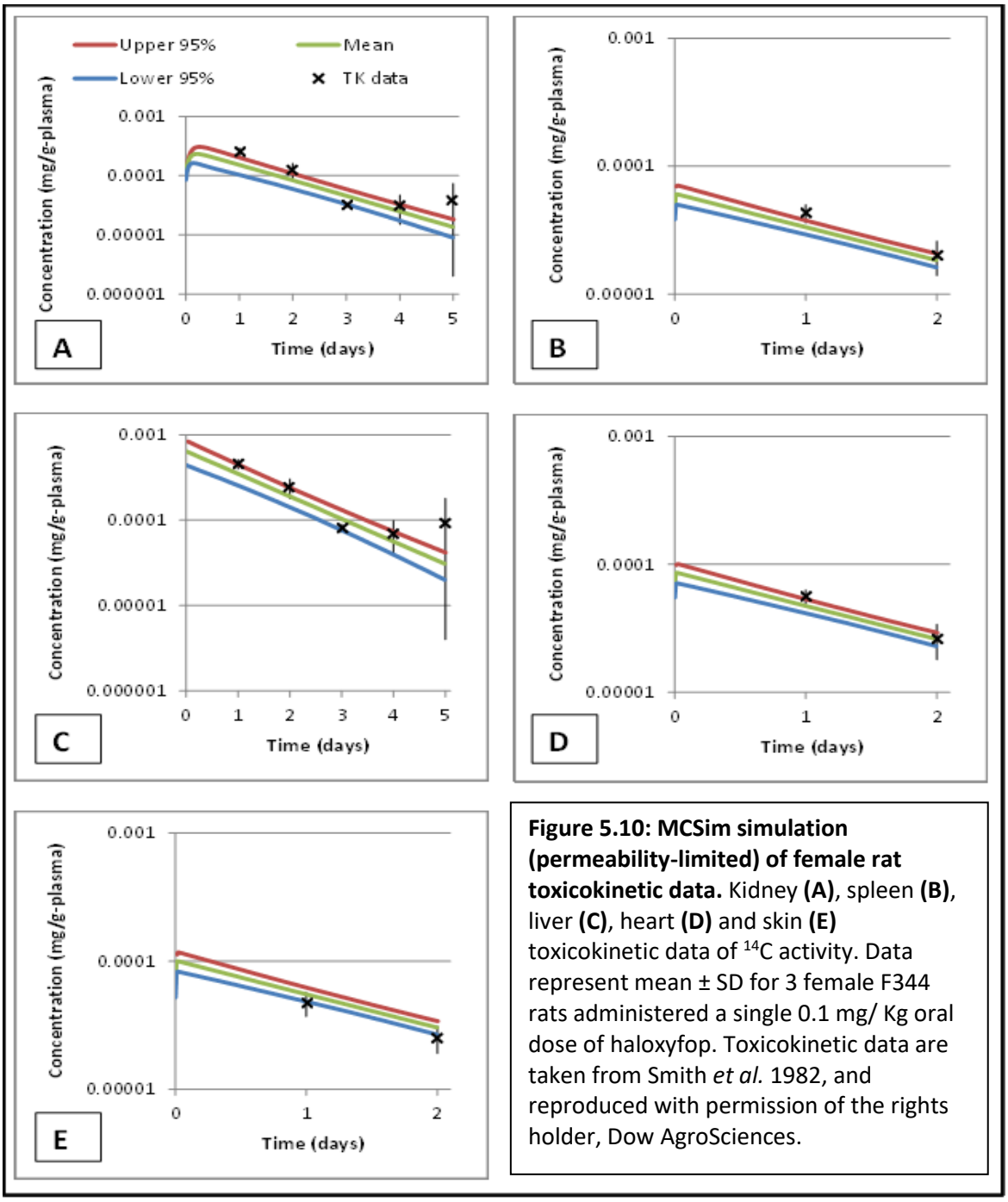


Figure 5.10: MCSim simulation (permeability-limited) of female rat toxicokinetic data. Kidney **(A)**, spleen **(B)**, liver **(C)**, heart **(D)** and skin **(E)** toxicokinetic data of ^{14}C activity. Data represent mean ± SD for 3 female F344 rats administered a single 0.1 mg/ Kg oral dose of haloxyfop. Toxicokinetic data are taken from Smith *et al.* 1982, and reproduced with permission of the rights holder, Dow AgroSciences.

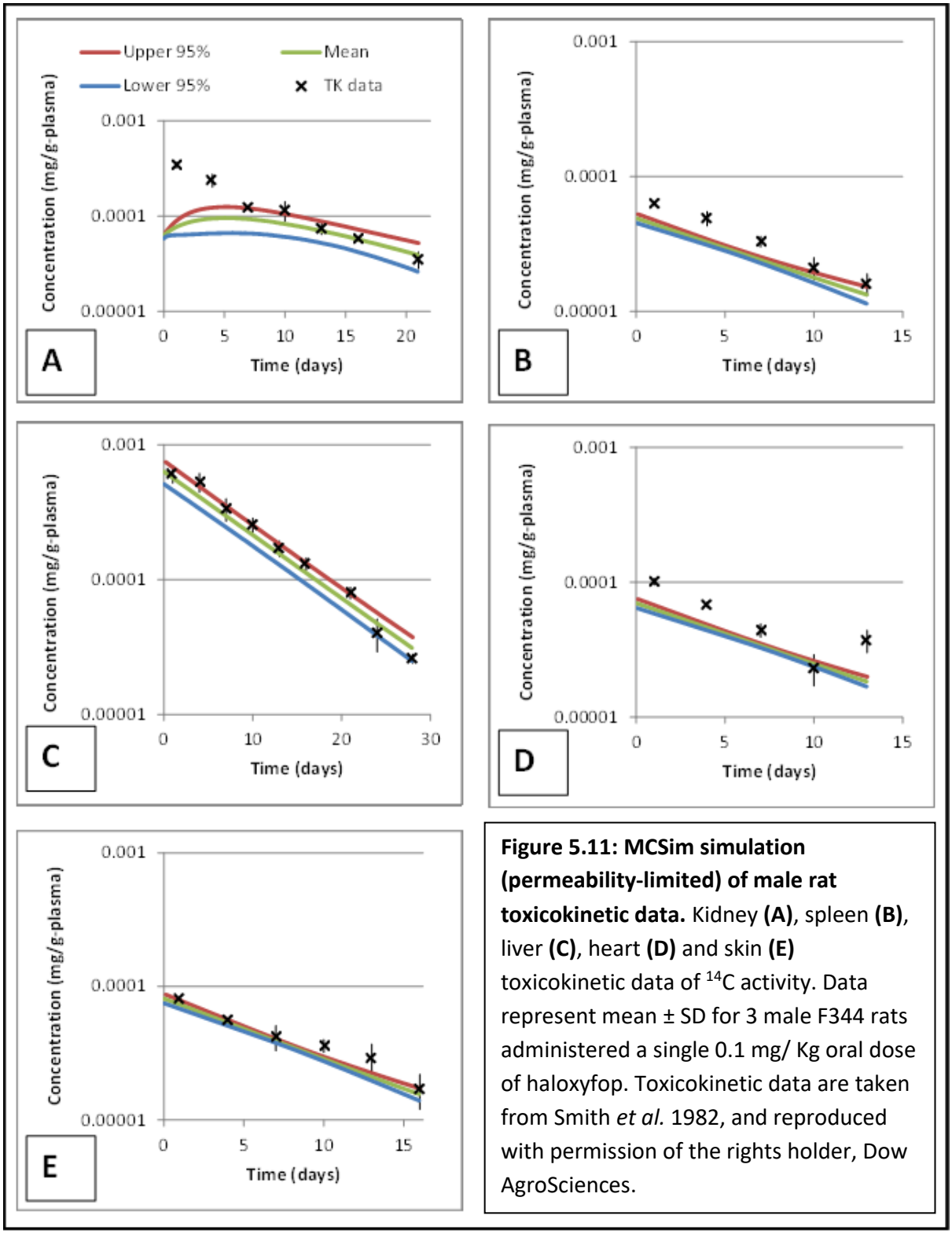


Figure 5.11: MCSim simulation (permeability-limited) of male rat toxicokinetic data. Kidney **(A)**, spleen **(B)**, liver **(C)**, heart **(D)** and skin **(E)** toxicokinetic data of ^{14}C activity. Data represent mean ± SD for 3 male F344 rats administered a single 0.1 mg/ Kg oral dose of haloxyfop. Toxicokinetic data are taken from Smith *et al.* 1982, and reproduced with permission of the rights holder, Dow AgroSciences.

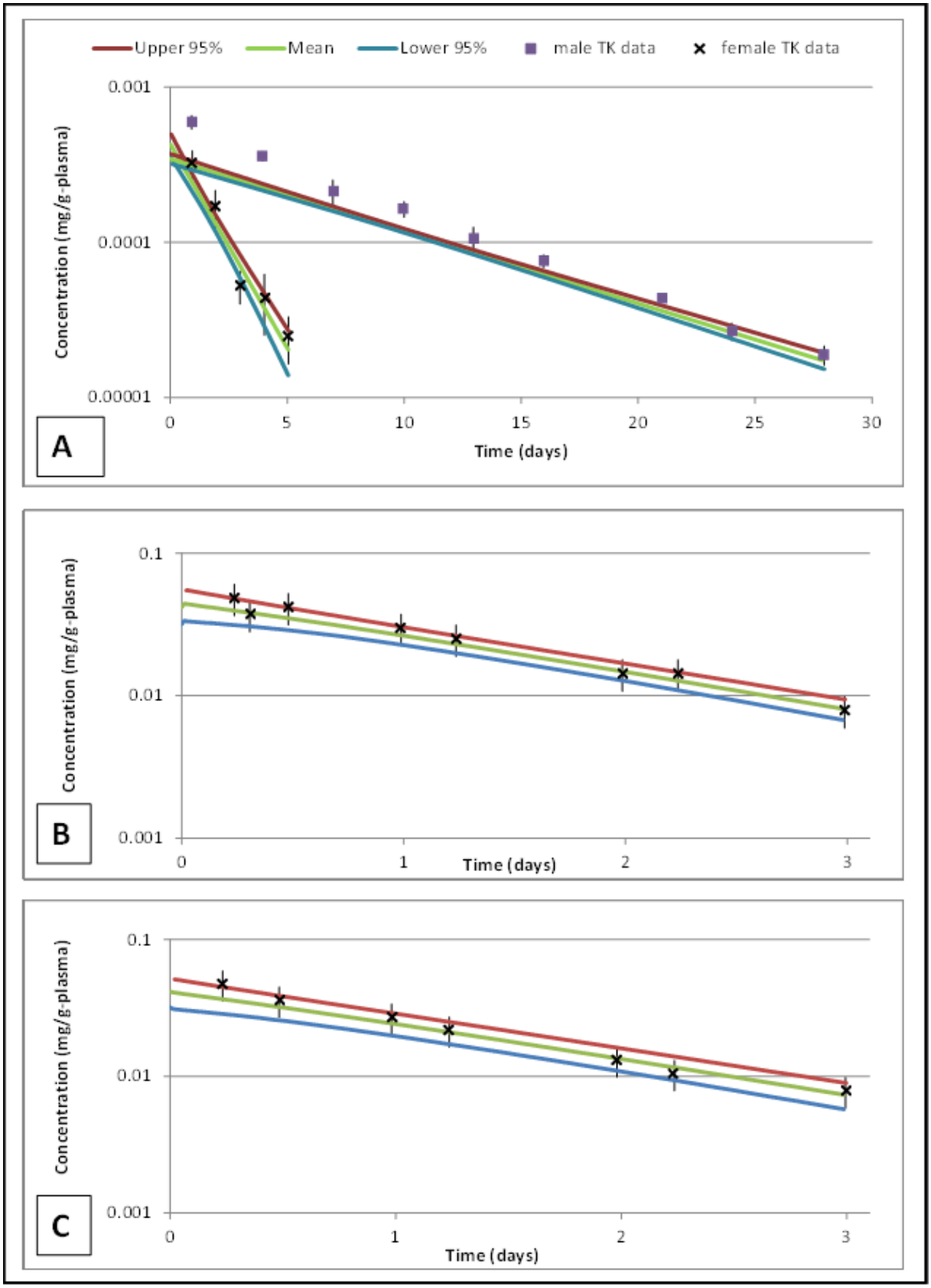


Figure 5.12: MCSim simulation (permeability-limited) of rat toxicokinetic data. Male and female plasma toxicokinetic data of ^{14}C activity following 0.1 mg/ Kg oral dose of haloxyfop **(A)**, female plasma toxicokinetic data after 10 mg/ Kg oral dose **(B)**, and female plasma TK data following 10 mg/ Kg iv dose **(C)**. Data represent mean ± SD for 3 male F344 rats. Toxicokinetic data are taken from Smith *et al.* 1982, and reproduced with permission of the rights holder, Dow AgroSciences.

In order to fit the plasma TK data (Figure 5.12) it was necessary to model a low level of active secretion in the liver and kidney, hence prior distributions were assigned to transporter Vmax and Km therein. The corresponding posterior distributions are presented below.

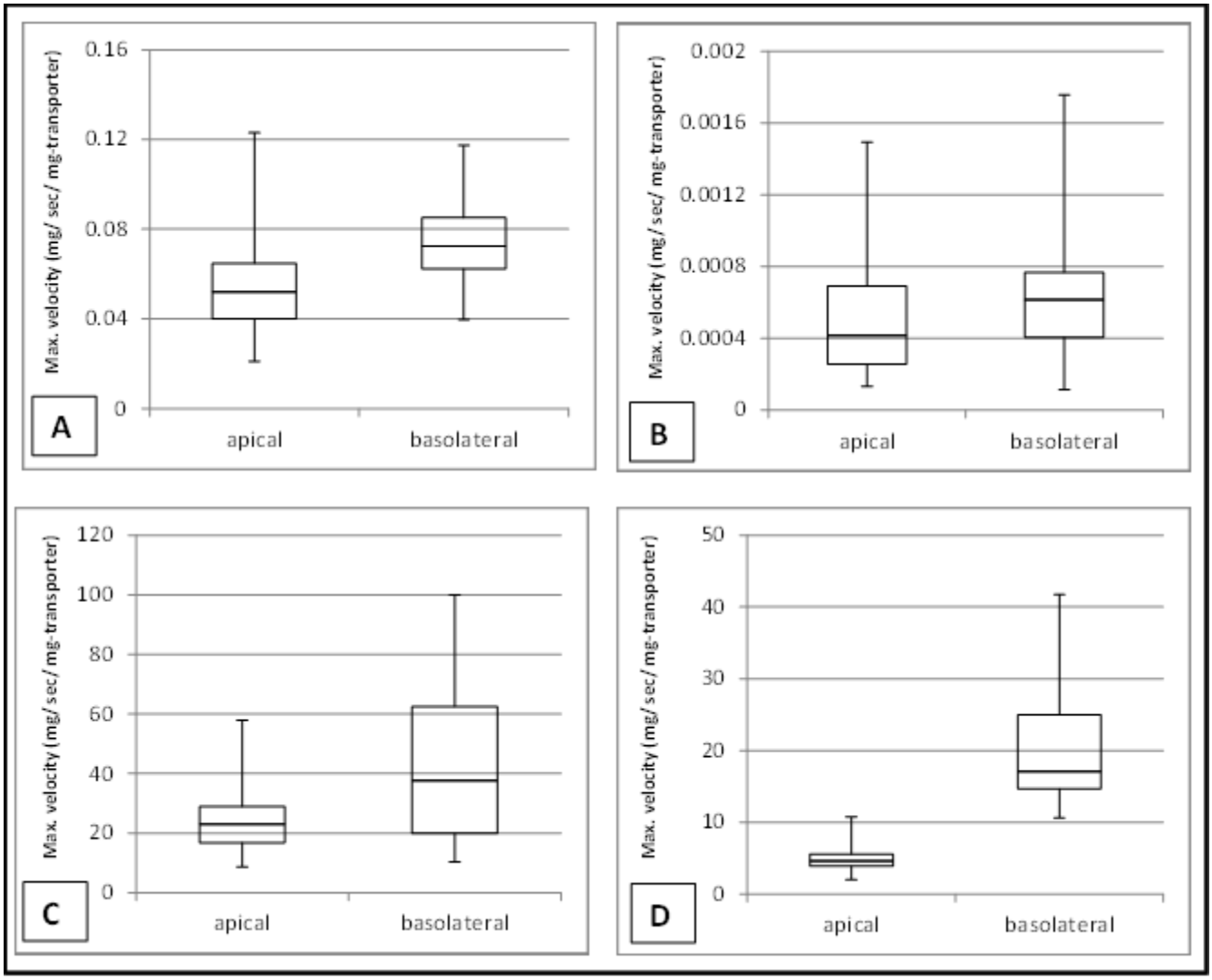


Figure 5.13: Maximum transporter velocity in rats. Female **(A)** and male **(B)** rat kidney, and in female **(C)** and male **(D)** rat liver.

5.5. Discussion

5.5.1 Mouse-human model calibration

5.5.1.1 Liver transporter activity

Molecular transporters play an important role in toxicokinetic processes but are not always included in PBTK models. This is an active area of research which will inevitably improve the accuracy of predictions made by PBTK models. Transporters are notoriously difficult to obtain *in vitro* activity data for, so finding *in silico* ways of determining their values is useful. This method (model calibration) utilises mouse liver toxicokinetic data to obtain values for mouse transporter activity levels (Vmax). The same Vmax levels can then be assumed for humans (if doing so provides a good fit to human data). Because the maximum velocity of transport (in mg/ sec/ mg-transporter) is directly proportional to liver volume (greater volume means more transporter mg), Vmax should be scaled to humans. This scaling approach is similar to IVIVE (Section 5.2.1), but the '*in vitro*' Vmax measurements are actually '*in silico*' predictions which the model then scales to humans by accounting for different liver volumes (Appendix 1). Figure 5.13 indicates the maximum rate of liver transporter velocity (Vmax) is greater for influx transporters than efflux transporters. Modelling in this work suggests this biochemical difference between transporters leads to accumulation of haloxyfop within hepatocytes. Although it may be possible to perform accurate exposure reconstruction from a calibrated human model only, the advantage of this modelling approach (calibrating mouse and human models simultaneously) is that information obtained within the extensive rodent toxicokinetic data can also inform human toxicokinetics and exposure reconstruction.

5.5.1.2 Systemic exposure estimates

The estimates of operator systemic exposure are significantly lower with the statistical model vs without ($p < 0.001$; $\alpha = 0.05$) (Figure 5.8). Systemic exposure estimates for all operators (excluding G.B.) are below the AOEL of 0.005 mg/ Kg bw/ day, indicating minimal risk of toxicity. Conversely, the systemic exposure estimate for operator G.B., although lower with use of the statistical model, still exceeds the AOEL. Whether this indicates a potential for toxicity is questionable however. The NOAEL of 0.5 mg/ Kg on which the AOEL is based (Barna-Lloyd *et al*. 1983, 1984) may not be the 'true' NOEL. There may be doses above the NOAEL which do not elicit toxicity, but are still below the LOAEL. Benchmark dosing might be useful in this respect, to identify possible ranges of the 'true' NOAEL (Filipsson *et al.* 2003). Furthermore, given the availability of human toxicokinetic data, the x 10 uncertainty factor for interspecies differences in ADME could be reduced (EFSA 2006). Thus the AOEL could potentially be raised tenfold from 0.005 to 0.05 mg/ Kg bw/ day, thus systemic exposure estimates of operators are more likely to be within acceptable levels. Finally, working patterns of operators must be considered in the context of occupational exposure which affects the risk assessment. In countries with temperate climates, it is unlikely that operators will use the same herbicide longer than three months in any one year (during the growing season). Therefore, use of toxicity studies of up to 90 days duration is normally appropriate for deriving AOELs for operator exposures working in temperate regions (EC 2006). However in tropical countries where herbicides can be applied year round, operators may experience longer chronic exposures with less recovery time, indicating greater toxicological risk.

5.5.1.3 Sensitivity analysis

There are various ways in which the modelling and risk assessment process can be improved in this case study. The outcome of the local sensitivity analysis indicates which model parameters strongly influence model output. This was done by changing a parameter whilst holding all other parameters

fixed. However varying a single parameter should cause all other parameters to change, because PBPK model parameters vary in proportion to each other. Hence, results from the sensitivity analysis should be interpreted with some caution. Further work could focus on developing a 'non-local' sensitivity analysis algorithm which takes into account parameter covariance. Furthermore, there are various model parameters which were assigned fixed values, but are sensitive e.g. rbp (blood/plasma concentration ratio). Thus, these parameters should have their prior distributions accurately determined. Occasionally these data are not readily available in the literature, in which case a 20% coefficient of variation can be applied to reflect population variability (Mezzetti *et al.* 2003).

5.5.1.4 Prior and posterior distributions

Table 5.1 indicates the toxicokinetic data used for model calibration was informative for most of the parameters assigned uniform distributions, such as PStc (permeability-surface area product). This is encouraging because PStc is an important model parameter (used to describe the rate of passive diffusion into tissues), and *in vitro* assays are currently unavailable for measuring PStc. Other parameters, for example transporter Km are not 'updated' by the toxicokinetic data. I.e. their posterior distributions are equivalent to their priors. This may be a computational issue called parameter 'non-identifiability' described elsewhere (Bernillon & Bois 2000). Briefly, if X = a/b (in this case) and neither a or b appear elsewhere in the model code, there are many possibilities for a and b to make X. n.b. Because the algorithm cannot 'identify' a or b (only X), it may be necessary in future to put a prior distribution on Vmax/Km (i.e. X), rather than each parameter individually. This is important especially for those non-identifiable (transporter) parameters which also appear to be sensitive (McLanahan *et al.* 2012).

5.5.2 Rat calibration

The discrepancy between the simulated and measured male rat kidney concentrations at one and four days post dose (Figure 5.11) may be attributed to additional active transport processes within the kidney affecting the disposition of haloxyfop *in vivo*, but for simplicity not modelled.

There is a sex difference in the plasma toxicokinetics of haloxyfop in F344 rats (Figure 5.12). Half-lives of ^{14}C activity clearances from plasma are 1.2 and 5.6 days for female and male rats, respectively. Male rats eliminate haloxyfop more slowly than females, possibly because males do not possess the active transport mechanism to the extent females do. Model calibration suggests transporter activity is substantially lower in males than females in both the kidneys and liver (Figure 5.13), and these differences provide a good fit to the toxicokinetic data. Thus, the transporter expression levels may differ across genders and/ or male rat transporters may be less inducible than female transporters. It is unclear whether the male or female rat could be extrapolated to humans (which gender is the better model). Gender differences in the rat have been observed with PFOA (Heuvel 1991); half-lives of 14C activity clearances from the body were < 1 day and 15 days for female and male rats, respectively. Indeed, male rats are more susceptible to PFOA-induced toxicity (Griffith & Long 1980). Heuvel found no evidence for metabolism of PFOA in either males or female Sprague-Dawley rats, hence the difference in urinary excretion rates was not due to differential metabolism. It was concluded an active secretion mechanism was active in female kidneys, but at a much lower level in male rats (Hanhijarvi *et al.* 1982, Ylinen *et al.* 1990, Heuvel 1991). The observed difference in elimination between rat genders may not be specific to certain xenobiotics (e.g. haloxyfop or PFOA) and deserves further investigation, for example modelling transporter inducibility with relevant literary data.

5.5.3 Summary and conclusions

- Use of both animal and human PBTK models jointly affects the accuracy of exposure reconstruction in human.
- The gender difference in plasma haloxyfop toxicokinetics in F344 rats is likely mediated by transporter differences.

5.5.4 Further work

In the absence of human TK data, it may be possible to directly extrapolate a rodent model to humans. However, it is still a challenge to extrapolate species-specific parameters where suitable regression equations are unavailable in the literature. For example, there are substantial differences in gut permeability between rodents and humans, and published mathematical interspecies regression equations vary significantly (Fagerholm *et al.* 1996, Zakeri-Milani *et al.* 2007). Subsequently, it is difficult to extrapolate these parameters, and to predict human toxicokinetics (without human data). Human toxicokinetic data remains very useful for several reasons: 1) to eliminate the uncertainty associated with an inter-species extrapolation, 2) validate the extrapolation approach, and 3) inform exposure reconstruction analysis (in this study). Human TK data may be unavailable or difficult to obtain; however, with the advent of microdosing and highly sensitive analytical instruments, this is becoming more possible. Another difficulty is performing exposure reconstruction with disparate HBM data. There may only be one piece of human biomonitoring data per individual, and usually the times and duration of exposure are unknown. Further work with these statistical models with other xenobiotics requires knowledge of which parameters are species-specific and which are species non-specific. This might be possible to identify by calibrating each model individually then looking for significant differences in parameter values.

Chapter 6: Derivation of a biomonitoring equivalent for tetrabromobisphenol A (TBBPA)

6.1 Abstract

Tetrabromobisphenol A (TBBPA) is a widely used brominated flame retardant (BFR) incorporated into various combustible materials to reduce their flammability. A physiologically-based toxicokinetic (PBTK) model was developed for TBBPA and its major glucuronide conjugate. Distributions were assigned to model parameters to reflect adult population variability and uncertainty regarding mean values. The model was calibrated using Bayesian analysis to human toxicokinetic data of the urinary glucuronide conjugate to allow the identification of parameter covariance. A biomonitoring equivalent (BE) was calculated for TBBPA at steady-state (approximately 150 days) using an oral reference dose of 0.6 mg/ Kg body weight/ day and parameter covariance (0.23 ± 0.24 SD mg of TBBPA/ g plasma lipids). Comparison of this BE with human biomonitoring (HBM) data available in the scientific literature suggests a low risk of toxicity for those individuals with measured TBBPA plasma concentrations. Furthermore, the effect of parameter covariance has a statistically significant effect on the prediction of the BE ($p < 0.001$; $\alpha = 0.05$, student's t-test).

6.2 Introduction

6.2.1 Widespread use and occurrence of TBBPA

Brominated flame retardants (BFRs) are chemicals used to make combustible materials less flammable. Use of pentaBDE, octaBDE (EU 2004), decaBDE (EU 2008a) and all PBBs and PBDEs in electronic and electrical equipment was banned within the European Union due to their toxicity (EU 2002). Subsequently, other BFRs have been synthesised to replace the banned BFRs, such as tetrabromobisphenol A (TBBPA, 2,2',6,6'-Tetrabromo-4,4'-isopropylidene diphenol). TBBPA may be classified as an 'emerging' BFR as it has been identified in the environment, wildlife, food and humans. For example, Abdallah & Harrad (2011) identified TBBPA in 12 of 34 human milk samples from Birmingham (UK), indicating potential exposure to newborns through breastfeeding. This classification distinguishes it from 'novel' BFRs which have confirmed presence in materials but not identified within the wider environment (EFSA 2012a). However, different authors define 'novel' in different ways. For example, Covaci *et al.* (2011) define 'novel' as being new to the market *or* recently observed in the environment. Various other terms exist in the literature, such as 'alternative', 'replacement' and 'new', and thus standardisation is required when referring to these compounds.

TBBPA is now the BFR with the largest production volume worldwide with over 170 kilotons manufactured in 2004 (ECB 2008). This is primarily because of its effectiveness as a flame retardant, its apparent low hazard profile and the regulatory requirement to meet fire safety standards. TBBPA is used predominantly as a reactive BFR in resins of printed circuit boards, and is therefore found in electronic equipment such as computers and mobile phones. Here, TBBPA is covalently bound to the material and therefore does not migrate out of the material. For this reason, a risk assessment performed within the EU identified no health or environmental health risks when TBBPA is used

reactively (EU 2008b). However, the polymerisation process may be incomplete: Sellström & Jansson (1995) reported that up to 4 μg/ g of TBBPA used in the circuit board might be unreacted and therefore capable of migrating out of the material. TBBPA is also used additively (non-reactively) in Acrylonitrile-Butadiene-Styrene (ABS) plastic casings, which is problematic because it can potentially partition out into the environment at any time during the product's production, lifetime or destruction. TBBPA can subsequently adhere to particulate matter namely dust due to its low vapour pressure (6.24×10^{-6} Pa) and hydrophobicity (EU 2006).

TBBPA has been identified in indoor dust samples in twelve countries (Wang *et al.* 2015). Therefore exposure to TBBPA is anticipated to occur through the inhalation route. In domestic settings, children may be at particular risk due to greater hand-to-mouth contact; indeed, Abdallah *et al*. (2008) calculated the average toddler (6-24 months) is exposed to TBBPA through dust inhalation at a rate of 100 pg per day. Within an occupational context, an elevated level of TBBPA was identified in plasma from workers at an electronics dismantling facility, compared with laboratory personnel in Norway (Thomsen *et al.* 2001). TBBPA has also been detected in indoor air samples from the dismantling area of an electronics recycling plant in Sweden (30 ng/ m^3) (Sjödin *et al.* 2001). Such occupational exposure is becoming a greater problem because the recycling of electronic goods is a growing industry.

TBBPA is not thought to occur naturally in the environment, so its environmental presence is due to anthropogenic activity. TBBPA can enter the environment at production sites through industrial wastewater and landfill sites. It was first detected in the environment in 1983 in Japanese river sediments (Watanabe *et al.* 1983) and has since been found in Swedish river sediments (Sellström & Jansson 1995) and Canadian municipal sewage sludge (Lee & Peart 2002) for example. TBBPA has been measured in various biota worldwide particularly in the aquatic food web and piscivorous birds. This may be due to the limited water solubility of TBBPA (octanol: water partition coefficient

4.5 - 5.3) and hence concentration within living organisms particularly fatty fish. For example, Morris *et al.* (2004) analysed cod (*G. morhua*) and cormorant (*P. carbo*) liver and harbour porpoise blubber (*P. phocoena*) from the North Sea and reported concentrations of up to 1.8, < 14 and 418 ng/ g lipid, respectively. Despite this, TBBPA was not found in any of the 19 food groups representing a typical UK diet, at levels above the limit of detection (0.02 - 0.2 ng/g) (Driffield *et al*. 2008). This may suggest UK human exposure is predominantly through dust inhalation rather than ingestion of food contaminated with TBBPA.

6.2.2 Toxicity of TBBPA

Mammalian exposure to TBBPA is a concern due to evidence for toxicity. TBBPA is structurally similar to the thyroid pro-hormone thyroxine (T_4) due to the presence of two phenyl groups in the molecule. T_4 is converted to the active form of the hormone T_3 (Marsili *et al.* 2011). Exposure to TBBPA was found to significantly reduce circulating levels of T_4 in SD rats (Cope *et al.* 2015). TBBPA can bind human transthyretin (Iakovleva *et al*. 2016), a protein which transports T_4 in the serum, and may displace T_4 for subsequent degradation in the plasma (Lai *et al*. 2015). It is unclear why accompanying alterations in T_3 levels or overt hypothyroidism are absent, however (Cope *et al.* 2015). Additionally, the high TBBPA dose required to cause T_4 reduction is bio-irrelevant (NOAEL 10 mg/ Kg bw/ day). Taken together, there is little concern for thyroid hormone perturbation regarding expected human TBBPA exposures (Canada 2013).

In a terminal two-year oral study, TBBPA was administered in corn oil to male and female Wistar Han rats and B6C3F1/N mice by gavage at doses of 0, 250, 500 or 1000 mg/ Kg bw for five days per week. In female rats dosed 500 or 1000mg/ Kg bw, there was a significant increase in the incidence of uterine epithelial tumours (NTP 2014) which followed a positive trend. At a lower incidence and statistical significance, tumours of the large intestine were observed in male mice only which also

followed a positive trend (NTP 2014). Although the precise mechanism of tumorigenesis here is unknown, it may involve altered estrogen levels (Dunnick *et al.* 2015).

TBBPA is a halogenated derivative of bisphenol A, a typical xenoestrogen (Krishnan *et al.* 1993). It is not surprising perhaps that TBBPA should exhibit direct estrogenic activity. In studies using an estrogen-dependent cancer cell line, TBBPA enhanced proliferation, although only at bio-irrelevant doses of 10-30 µM (Samuelsen *et al.* 2001) or 10-100 µM (Kitamura *et al.* 2002), suggesting TBBPA has a very low affinity to the estrogen receptor. Furthermore, because the *in vivo* TBBPA glucuronidation pathway *via* glucuronyltransferases (see below) is shared with estrogen for their elimination (Raftogianis *et al*. 2000), TBBPA exposure may indirectly result in elevated estrogen levels (Lai *et al.* 2015). Additionally, *in vivo* metabolism of TBBPA may include the formation of reactive free radicals leading to oxidative damage (Chignell *et al.* 2008). Due to 'sufficient evidence of carcinogenicity in experimental animals' and mechanistic evidence, the International Agency for Research on Cancer (IARC) has recently upgraded this flame retardant to group 2A (probably carcinogenic to humans) (Grosse *et al.* 2016).

6.2.3 Toxicokinetics of TBBPA

The health concerns of TBBPA have driven various toxicokinetic studies to investigate the disposition of this chemical in animals. Most toxicokinetic studies use oral administration since oral intake is considered the major pathway for potential human exposure (EFSA 2011). Although inhalation exposure predominates, 96 % of the TBBPA dust particles are > 15 µm in diameter (ECB 2006) and hence do not reach alveoli but instead undergo mucociliary transport and are deposited in the GI tract as phlegm is swallowed. Additionally, in *vitro* dermal exposure studies have shown that TBBPA can be absorbed by human skin, although the level is low (< 1% of the applied dose) (ECB 2006). Dermal contact with TBBPA may represent a small but important exposure route (Knudsen *et al.* 2015).

Hakk *et al.* (2000) demonstrated that, at an oral dose of 2 mg/kg, TBBPA is readily absorbed from the GI tract of male Sprague Dawley (SD) rats where it undergoes substantial first-pass metabolism. The presence of the two hydroxyl groups in TBBPA facilitates biotransformation by conjugation reactions in mammals which occur in both the GI tract and/ or liver. TBBPA was metabolised in rat and human liver subcellular fractions without major qualitative differences (Zalko *et al.* 2006), indicating that rats may be an appropriate metabolism model for humans. The resulting O-glucuronide and O-sulphate conjugates were identified in bile, and these metabolites undergo biliary elimination (Hakk *et al.* 2000, Knudsen *et al*. 2014). Indeed, 71 $\pm$ 7.2 % of the dose administered to eight bile-duct cannulated rats was excreted in bile by 72 hours (Hakk *et al.* 2000). Due to the high molecular weight of TBBPA-glucuronide (720 Da), which exceeds the thresholds for biliary elimination in both rats (>350 Da) and humans (>500 Da), this conjugate is eliminated from the liver via the bile duct and thus excreted with faeces (Colnot *et al.* 2014). However, TBBPA was eliminated in the faeces predominantly as the parent compound (Hakk *et al.* 2000) indicating intestinal deconjugation back to the parent compound, a step probably mediated by bacterial microflora. Elimination was delayed when a high single oral dose of 1000 mg/ Kg was administered. This is presumably due to the saturation of conjugation reactions leading to the process of enterohepatic circulation becoming rate-limiting (Knudsen *et al.* 2014).

The enterohepatic recirculation of TBBPA in both rodents and humans results in a low systemic bioavailability of TBBPA as the parent compound (Kuester *et al.* 2007, Colnot *et al.* 2014). Indeed, TBBPA (a lipophilic chemical) was undetected in lipophilic tissues such as the adipose or testis post exposure (Hakk *et al.* 2000), and only a small percentage (1-2 %) of TBBPA (and its metabolites) was eliminated in urine following oral or intravenous administration (Kang *et al.* 2009, Kuester *et al.* 2007, Schauer *et al.* 2006). These low systemic exposures reduce the potential for bioaccumulation and hence toxicity of this chemical within mammals. Indeed, the half-life of TBBPA in humans is

approximately just 48 hours (Schauer *et al.* 2006). Figure 6.1 shows the interplay of processes in the GI tract and liver thought to affect TBBPA toxicokinetics (see Methods).

6.2.4 Biomonitoring equivalents

Human exposure assessment to TBBPA is necessary because of its scale of use, environmental persistence and toxicity. One method of exposure assessment is through the derivation of biomonitoring equivalents (BEs). The original BE approach was developed by Hays *et al.* 2007, and is the calculation of chemical concentration within a readily accessible human biofluid (such as urine or blood) for a known external exposure for example the oral reference dose (RfD). The RfD is the maximum acceptable daily oral intake rate with minimal risk of developing an adverse health effect over one's lifetime. The corresponding BE can then be compared alongside human biomonitoring (HBM) data to facilitate interpretation of this data for health risk assessment purposes. For example, if an individual's HBM data is substantially above the BE corresponding to the RfD, then a certain toxicological risk may be inferred for that individual (Phillips *et al.* 2014). Furthermore, if HBM data is currently unavailable within a certain country (as is the case with the UK), then the derived BE can be used for rapid interpretation when it does become available.

In order to calculate a BE, a model is required that deterministically links external dose with exposure at the physiological site of interest. To our knowledge, a PBTK model has not been developed to assess exposure to TBBPA. Recent developments in the field include using PBTK models with parameters with fixed values (Hays *et al. 2012*) leading to parameters having distributions (Phillips *et al.* 2014). The latter is particularly important to calculate ranges of plausible BE values, taking population physiological heterogeneity into account. However, the parameter distributions are often treated as univariate without relationships existing between them (Phillips *et al.* 2014). From the previous chapter, it is apparent that relationships do exist between various

parameter distributions. These inter-parameter correlations were expressed in terms of Pearson correlation coefficients, and were identified by running a suitable algorithm such as MCMC (Monte Carlo integration using Markov Chains) in order to calibrate the model to a toxicokinetic dataset.

A number of PBTK studies have ignored parameter covariance, but instead utilise a so-called 'traditional' Monte Carlo approach which is Monte Carlo analysis without Markov Chains (Portier & Kaplan 1989, Clewell & Andersen 1996, Thomas *et al.* 1996). This involves randomly sampling from univariate parameter distributions to calculate a model output of interest. However there are no correlations identified between these distributions, and therefore the accuracy of the model predictions may be quite questionable. Some notable studies where univariate distributions were used in PBTK models include:

- risk assessment for chloroform; indeed, 'potential correlations among most of the parameters were ignored' (Allen *et al.* 1996).
- the effect of glutathione transferase polymorphism on the estimates of dichloromethane in humans (El-Masri *et al.* 1999).
- the level of carcinogenic methyleugol metabolites formed in the human population by taking variability in key bioactivation and detoxification reactions into account (Al-Subeihi *et al.* 2015).

6.2.5. Chapter aims

The aim of this chapter is to assess whether parameter covariance in PBTK models affects the prediction of BEs. This will be done in three stages:

1) Identify parameter covariance by calibrating the PBTK model to a human TK dataset available for TBBPA (Schauer *et al.* 2006).

2) Calculate a BE in blood for TBBPA with and without parameter covariance.

3) Compare the derived BE with available HBM data available for TBBPA for their interpretation for health risk assessment purposes.

6.3 Methods

A literature review was done to 1) identify human toxicokinetic data for TBBPA with which to calibrate the model to (and subsequently identify parameter covariance), and 2) collate the HBM data available for TBBPA. For comparative purposes, the units of HBM data were converted, where necessary, to ng/ g plasma lipids, assuming 0.63 % lipid composition and 1.025 g/ mL density of plasma.

6.3.1 The human toxicokinetic data

Schauer *et al.* (2006) administered a single oral dose of 0.1 mg/ Kg of TBBPA to five adult humans (3 males, 2 females). Blood and urine samples were collected over a period of 178 hours, and TBBPA and its metabolites were quantified by LC/MS. Parent TBBPA was not detected in any human plasma samples although its metabolites were.

TBBPA-glucuronide was detected in blood from all individuals: maximum plasma concentrations (16 nmol/ L) were obtained between 2 and 6 hours after administration. Plasma clearance appeared to be monophasic with a half-life of approximately 48 hours. TBBPA-glucuronide was slowly eliminated in urine to reach the LOD 124 hours after administration. Only a minor part (< 0.1 %) of the administered dose was recovered in urine as TBBPA-glucuronide. Based on analysis of MS fragmentation patterns, the glucuronide appeared to be conjugated to one or both of the two

hydroxyl groups of TBBPA although not quantified, thus only the monoglucuronide conjugate was modelled.

TBBPA-sulphate was detected only in blood samples from two male individuals. Here, maximum concentrations of approximately 20 µmol/ L were present 4-6 hours after oral administration of TBBPA, which rapidly declined to reach the LOD after 8 hours. Detailed toxicokinetic data was not provided therefore this metabolite was not modelled.

In summary, these results suggest that absorption of TBBPA from the GI tract occurs following oral exposure. However, due to efficient metabolism and biliary excretion of the conjugates formed, systemic bioavailability of the parent compound is very low, and only a minor portion of the dose is excreted in urine.

GrabIt™ V1.5 data capture software was used to extract the toxicokinetic data including measurement uncertainties from the graphs in Schauer *et al.* (2006). For computational convenience, incremental urine data were combined to give cumulative urine excreted during the time-course of the study (the PBTK model as coded does not model cumulated amounts excreted over discrete time intervals, e.g. over 24 hours), and units of data were converted from moles to mass. Standard deviations specific to each data point were assigned to plasma and urine likelihoods reflecting primarily inter-individual variability.

6.3.2 PBTK model and calibration

The PBTK model for TBBPA, the parent compound, was described as perfusion-limited due to the lipophilicity of this chemical. Another model (nested beneath the first) was built for the main metabolite (TBBPA-glucuronide), and described as permeability-limited due to its relative

hydrophilicity (Figure 6.1). Metabolism was modelled within both the gut endothelial cells and the liver. Since the rate of metabolite formation (TBBPA-glucuronide) is rapid, and liver exposure to parent compound is insufficient to achieve this rate, an additional site of metabolism (intestinal epithelium) was modelled. This is consistent with the review of data by Colnot *et al.* 2014.

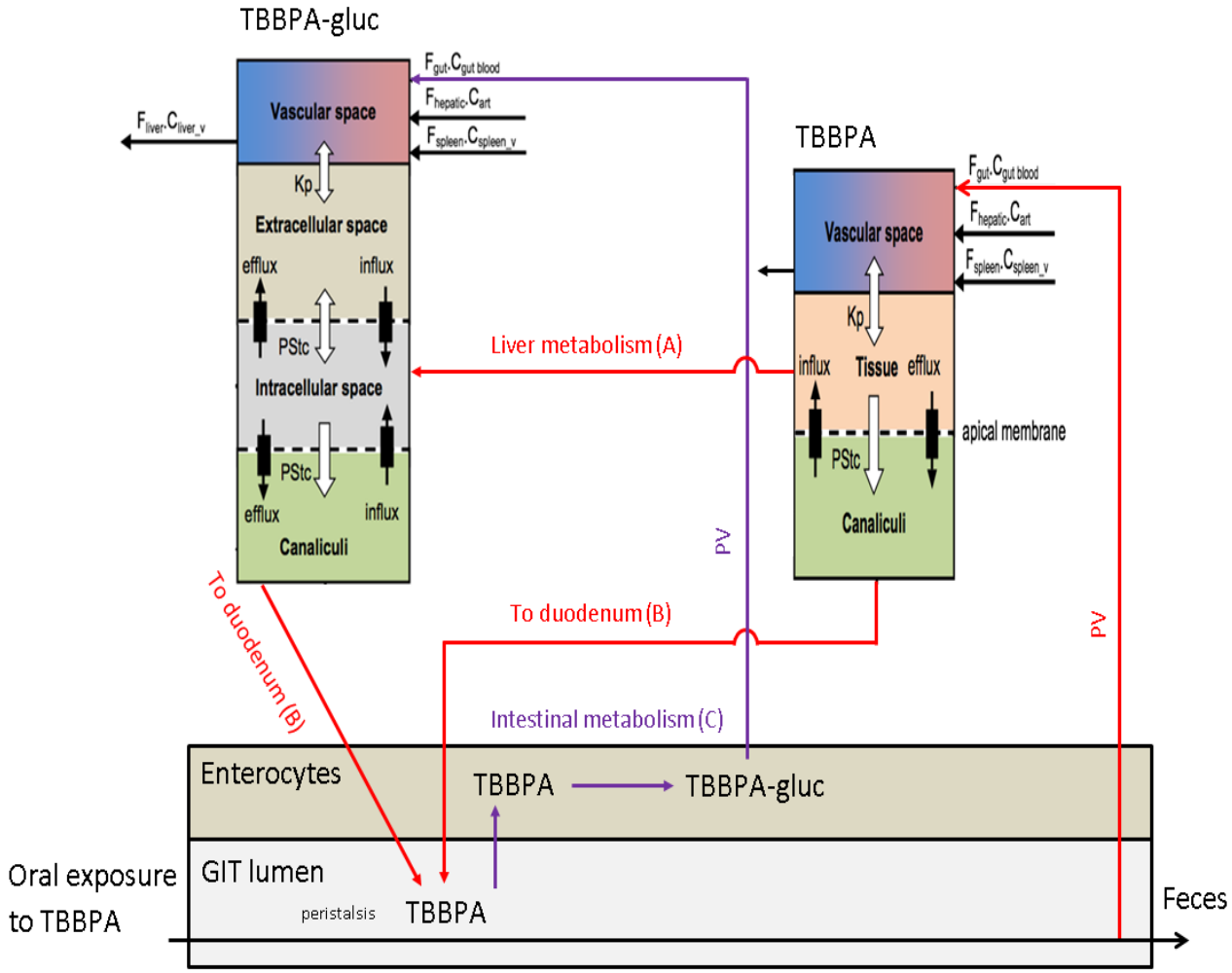


Figure 6.1: Interplay of processes in the GI tract and liver which influence TBBPA toxicokinetics. The process of enterohepatic recirculation (red arrows) causes a prolongation of systemic exposure to both TBBPA and its glucuronide conjugate. Metabolism within enterocytes followed by absorption of the glucuronide conjugate (purple arrows) means that systemic exposure to the conjugate is much greater than the parent compound. TBBPA was shown not to be a substrate for BCRP, P-gp, MRP1 or MRP4 transporters (Dankers *et al.* 2013); indeed, transporters for TBBPA were not required in the parent model. However, transporter activity was required for TBBPA-glucuronide in the kidney apical and basolateral membranes (not shown), as well as the liver apical membrane. For processes labelled A-C see text for details. Figure adapted from Simulations Plus 2013b.

The amount of metabolite within the liver intracellular space was calculated using the equation below. It is calculated by the difference between basolateral and apical membrane permeabilities (of the metabolite model), with the addition of the quantity metabolised from the parent model (process A) which is described using first-order Michaelis-Menten kinetics:

$$V_{liv_i}\ x\ \frac{dC_{i_liv_m}}{dt} =$$

$$perm_liv_bas_m - perm_liv_api_m + \sum^{nEnz}\left[\frac{V_{\max_w_liv_e}\ x\ C_{i_liv}\ x\ f_{ut,tis}}{K_{m_liv_e} + \left(C_{i_liv}\ x\ f_{ut,tis}\right)}\right] \quad [1]$$

The equation below gives the amount of parent compound within the duodenum lumen. It is assumed the metabolite from apical liver permeability ($perm_liv_api_m$) undergoes instantaneous conversion to the parent compound due to β-glucuronidase deconjugation activity of intestinal microflora. The duodenum also receives input from the parent liver apical membrane permeability (perm_liv_api) (process B) and inflow from the stomach (Kt_s x Q_sto_{dis}). The amount leaving the duodenum lumen is due to peristaltic flow to the small intestine (Kt_{duo} x Q_duo_{dis}) and absorption into the portal vein (perm_duo_api):

$$V_{duo,lum}\ x\ \frac{dC_duo}{dt}$$

$$= (Kt_s\ x\ Q_sto\ ) + perm_liv_api_m + perm_liv_api - (Kt_{duo}\ x\ Q_duo\ )$$

$$- perm_duo_api \quad [2]$$

The amount of metabolite in the small intestinal endothelial cells is given by the equation below. It is determined by the difference in enterocyte membrane permeabilities, in addition to the quantity metabolised therein from the parent model (process C):

$$V_{ent,SI}\ x\ \frac{dC_ent_m_{SI}}{dt} = perm_SI_api_m - perm_SI_bas_m + \sum^{nEnz}\left[\frac{V_{max_w_gut_e}\ x\ C_ent_{SI}\ x\ f_{ut,tis}}{K_{m_gut_e} + \left(C_ent_{SI}\ x\ f_{ut,tis}\right)}\right] \quad [3]$$

Prior distributions for model parameters were selected as described previously, and a suitable statistical model was used to separate parameter uncertainty and variability for fractional blood flow rates and tissue volumes (Section 5.3.3). MCMC was performed using the Metropolis algorithm as implemented in the code MCSim (Bois & Maszle 2008) to calibrate the model to the human TBBPA toxicokinetic data (Schauer *et al.* 2006). Markov chain convergence was confirmed by running three independent chains seeded with different random numbers and starting values of model parameters; stationary distributions were obtained after approximately 85,000 iterations. The first 10,000 iterations were discarded as 'burn-in'; this choice is consistent with Geyer 1992 who suggested a burn-in of 1 - 2 % of total chain length is adequate. Convergence was monitored by calculating potential scale reduction factors (PSRFs) for parameters using the Gelman-Rubin convergence diagnostic (Gelman & Rubin 1992). Microsoft Excel was used to perform all statistical analyses. Calibration was verified by visually assessing the ability of the model to fit the human toxicokinetic data, assuming values of parameters sampled from their posterior distributions. The converged chain was thinned by a factor of four to prevent interference from auto-correlation (Chiu *et al.* 2009), and the last 5000 iterations of sampled parameter values were used to calculate the biomonitoring equivalent. This process was repeated without the use of the Bayesian likelihood for MCMC iterations, thereby obtaining uncorrelated samples from posterior distributions in a traditional Monte Carlo fashion without parameter covariance.

To calculate the biomonitoring equivalent, an oral reference dose (RfD) of 0.6 mg/ Kg/ day was used (Wikoff 2014); this is based on the significant increase in uterine endometrial hyperplasias and

tumours in Wistar Han rats (NTP 2014). HBM data for TBBPA is expressed in terms of plasma concentrations (ng/ g lipid), so this was selected as the model output of interest. Plasma concentrations at steady-state were calculated, consistent with guidelines from Hays *et al.* (2007). Exposure to TBBPA was assumed to occur only during the daytime. Therefore, the daily oral dose of 0.6 mg/ Kg was administered continuously over 12 hours in each 24 hour period; this process was performed with and without the parameter covariance.

Table 6.1: *In silico* predictions for physicochemical parameters for TBBPA and its glucuronide conjugate (species-unspecific).

Chemical	logP_tis	Rbp	$F_{up,exp}$	Kp			
				Liver	Adipose	Brain	Kidney
TBBPA	6.82	0.61	0.0021	2.74	30.67	6.61	2.49
TBBPA glucuronide	3.59	0.59	0.013	0.50	0.16	0.50	0.50

In silico predictions reproduced with permission of the rights holder, Simulations Plus Inc.

6.4 Results

6.4.1 *In vitro* data

Figure 6.2 shows the results from the rapid equilibrium dialysis experiment to determine the fraction of TBBPA unbound in plasma (Section 2.2.3). This assay was repeated several times with plasma from various healthy human volunteers to ascertain measurement error (indicated by the box plots below) as well as variability (across the box plots). There is a slight discrepancy against the *in silico* prediction of 0.0021 for this chemical.

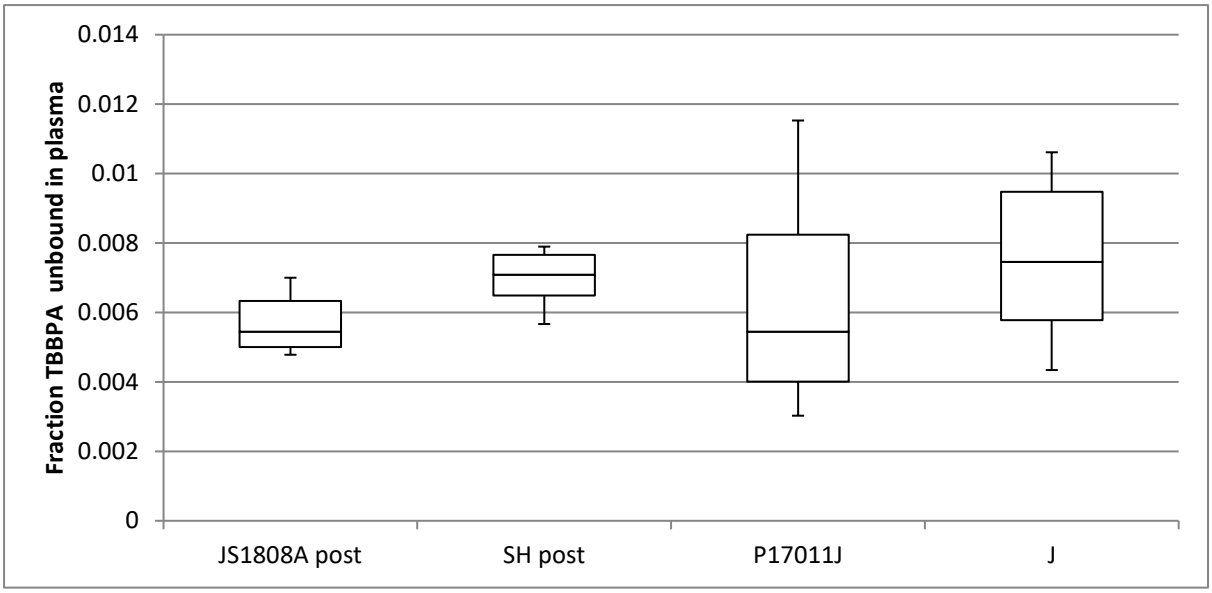


Figure 6.2: *In vitro* fraction of TBBPA unbound in human plasma samples (n = 4). Individual box plots represent measurement error as each dialysis experiment was performed in sextuplicate.

6.4.2 PBTK model calibration

MCMC was used to calibrate the human PBTK model developed for TBBPA. Predictions of TBBPA physicochemcial parameters were used (Table 6.1). Figure 6.3 shows the corresponding fits to plasma and urinary toxicokinetic data of the glucuronidated metabolite following a single oral dose of TBBPA (0.1 mg/ Kg), assuming values of parameters sampled from their posterior distributions. Calibration of the model was assessed through visual inspection of the fits to toxicokinetic data provided by Schauer *et al.* (2006), and assessment of the posterior distributions obtained after convergence.

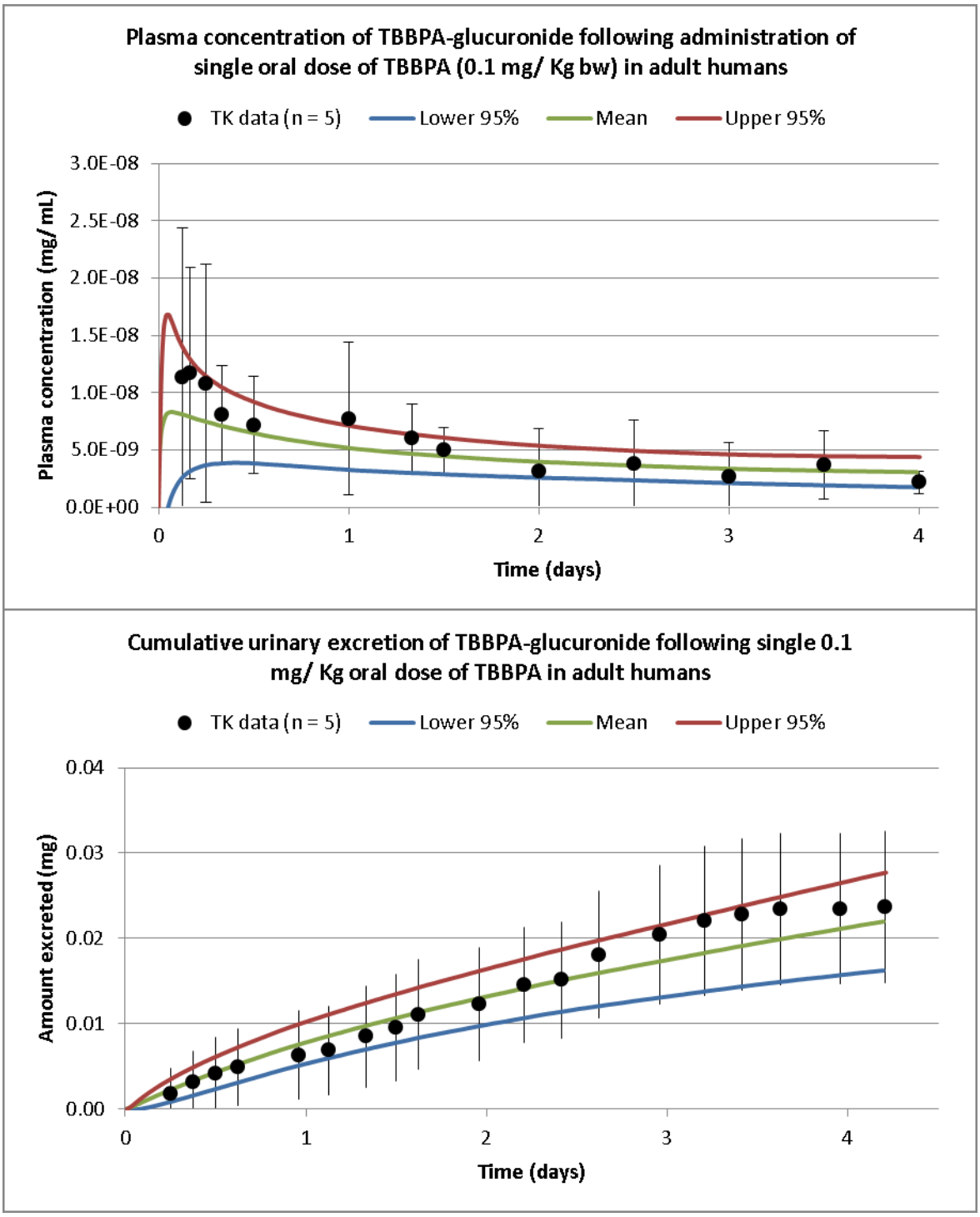


Figure 6.3: Calibration of the human PBTK model to suitable toxicokinetic data following a single oral dose of 0.1 mg/ Kg. Human toxicokinetic data are taken from Schauer *et al.* 2006.

Prior distributions were assigned to biochemical and physicochemical parameters listed in Table 6.1. These were described as uniform because the values of physicochemical parameters (e.g. gut permeability) are dependent on the chemical's characteristics (as well as physiology), therefore

determining relevant priors from the literature is not straightforward. After MCMC convergence, posteriors were obtained. The toxicokinetic data was not informative for several parameters, such as 'PStcm' (the parameter which describes the rate of passive metabolite permeation through tissue membranes) as posteriors appeared similar to their priors. All parameter PSRFs were < 1.2 indicating excellent algorithmic convergence.

Table 6.2: Prior and posterior distributions for biochemical/ physicochemical PBTK model parameters (in natural space).

Parameter‡	Prior*	Posterior shape	Posterior mean‡	Posterior CV	PSRF at 85k iterations
PStcm	0, 0.001	Uniform	0.00051	0.52	1.000200
V_max_liv_e	0, 50	Uniform	27.8	0.43	0.999958
Km_liv_p_e	0, 20	Uniform	9.7	0.54	1.000744
V_max_gut_e	0, 0.0002	Uniform	0.00012	0.36	1.000291
Km_gut_p_e	0, 20	Log normal	3.1	0.83	1.002740
V_max_kid_bm	0, 50	Uniform	25.5	0.52	1.000011
Km_kid_p_bm	0, 20	Uniform	10.0	0.53	1.000133
V_max_kid_am	0, 50	Uniform	25.0	0.53	0.999989
Km_kid_p_am	0, 20	Uniform	9.9	0.54	1.000032
V_max_liv_am	0, 50	Uniform	23.9	0.57	1.000327
Km_liv_p_am	0, 20	Uniform	10.1	0.53	1.000505
PStc_liv_a	0, 1	Uniform	0.5	0.53	1.000057
PStc_kid_a	0, 1	Uniform	0.5	0.54	1.000021
Peff_sto	0, 0.001	Uniform	0.00050	0.54	1.000012
Peff	0, 0.001	Log normal	0.00021	0.82	1.001569

‡ See glossary for description and units (Appendix 2). * Minimum, maximum. N.b. consistent with Schauer *et al*. 2006, body mass was assumed to vary uniformly from 89 to 92 Kg; there were no noticeable differences to its posterior.

Normally distributed priors were assigned to physiological parameters listed in Table 6.3. Posterior distributions of fractional blood flow rates and tissue volumes are generally consistent with prior distributions, suggesting the model structure is a good representation of the biological system it is intended to represent.

Table 6.3: Prior and posterior distributions for PBTK model parameters (in natural space).

Parameter‡	Population mean				Population variability		
	Mean‡		CU		CV		
	Prior	Posterior	Prior	Posterior	Prior	Posterior	PSRF at 85k iterations
Fr_F_kid	0.172	0.198	0.30	0.24	0.50	0.24	1.000074
Fr_F_ski	0.040	0.041	0.30	0.28	0.50	0.48	1.000516
Fr_F_adi	0.111	0.112	0.30	0.29	0.50	0.50	1.000558
Fr_F_gut	0.143	0.147	0.30	0.29	0.50	0.49	0.999968
Fr_F_mus	0.106	0.108	0.30	0.29	0.50	0.48	1.000069
Fr_F_hep	0.087	0.089	0.30	0.28	0.50	0.48	0.999972
Fr_F_spl	0.026	0.027	0.30	0.28	0.50	0.46	0.999952
Fr_F_yel	0.017	0.017	0.30	0.28	0.50	0.50	1.000249
Fr_F_hea	0.041	0.042	0.30	0.29	0.50	0.49	1.000081
Fr_F_bra	0.144	0.148	0.30	0.29	0.50	0.47	0.999951
Fr_F_rep	0.001	0.001	0.30	0.27	0.50	0.50	1.000585
Fr_F_red	0.059	0.061	0.30	0.28	0.50	0.48	0.999971
Fr_V_liv	0.025	0.026	0.20	0.19	0.50	0.39	1.000347
Fr_V_kid	0.004	0.004	0.20	0.20	0.50	0.47	1.000197
Fr_V_nep	0.0001	0.0001	0.20	0.19	0.50	0.56	1.000475
Fr_V_ski	0.030	0.030	0.20	0.19	0.50	0.46	1.000053
Fr_V_adi	0.494	0.494	0.20	0.19	0.50	0.39	1.000034
Fr_V_ven	0.066	0.067	0.20	0.19	0.50	0.45	1.000005
Fr_V_art	0.033	0.034	0.20	0.20	0.50	0.46	1.000012
Fr_V_lun	0.017	0.018	0.20	0.19	0.50	0.44	1.000132
Fr_V_mus	0.315	0.317	0.20	0.20	0.50	0.46	1.000009
Fr_V_spl	0.002	0.002	0.20	0.25	0.50	0.52	1.000175
Fr_V_yel	0.049	0.049	0.20	0.20	0.50	0.45	1.000093
Fr_V_hea	0.005	0.005	0.20	0.19	0.50	0.45	1.000222
Fr_V_bra	0.025	0.025	0.20	0.20	0.50	0.46	1.000111
Fr_V_rep	0.0005	0.0005	0.20	0.19	0.50	0.41	1.000270
Fr_V_red	0.018	0.018	0.20	0.19	0.50	0.43	1.000088

‡ See glossary for description and units (Appendix 2).

6.4.3 Analysis of parameter covariance

The multivariate posterior obtained through model calibration was analysed to identify correlations between model parameters. These are described in Tables 6.4 - 6.6 with Pearson correlation coefficients. Statistically significant correlations are shown in bold (Pearson's r = 4999; $p < 0.05$).

Table 6.4: Correlation matrix of selected human biochemical and physicochemical PBTK model parameters.

	PStcm	V_max_liv_e	Km_liv_p_e	V_max_gut_e	Km_gut_p_e	V_max_kid_bm	Km_kid_p_bm	V_max_kid_am	Km_kid_p_am	V_max_liv_am	Km_liv_p_am	PStc_liv_a	PStc_kid_a	Peff_sto
V_max_liv_e	-0.005													
Km_liv_p_e	-0.017	**0.106**												
V_max_gut_e	0.001	**-0.042**	**0.062**											
Km_gut_p_e	**0.059**	**0.090**	**-0.046**	**0.369**										
V_max_kid_bm	0.002	0.000	0.014	-0.002	0.012									
Km_kid_p_bm	-0.010	-0.003	**0.028**	-0.006	0.001	-0.014								
V_max_kid_am	0.008	**0.031**	0.023	**0.035**	0.011	-0.012	**-0.049**							
Km_kid_p_am	0.019	0.007	0.012	0.011	0.019	-0.003	0.001	0.014						
V_max_liv_am	**-0.047**	-0.027	0.024	-0.012	**-0.100**	-0.005	-0.016	0.020	-0.011					
Km_liv_p_am	0.012	0.024	0.014	-0.027	0.024	-0.004	-0.001	-0.002	0.011	-0.024				
PStc_liv_a	-0.006	**0.031**	-0.005	-0.020	0.023	-0.020	0.004	-0.004	-0.012	-0.015	-0.014			
PStc_kid_a	0.024	-0.014	-0.021	0.020	0.012	0.027	0.002	-0.005	-0.013	0.019	-0.008	0.009		
Peff_sto	**0.049**	0.026	**0.063**	0.021	-0.004	**-0.031**	-0.008	0.012	-0.005	0.012	-0.011	-0.001	**0.030**	
Peff	-0.016	0.026	**-0.130**	-0.003	**-0.529**	-0.014	**-0.044**	0.022	-0.018	**-0.044**	**0.030**	0.015	0.001	**-0.031**

Table 6.5: Correlation matrix of fractional tissue and organ volume variability.

	Fr_V_liv	Fr_V_kid	Fr_V_nep	Fr_V_ski	Fr_V_adi	Fr_V_rob	Fr_V_ven	Fr_V_art	Fr_V_lun	Fr_V_mus	Fr_V_spl	Fr_V_yel	Fr_V_hea	Fr_V_bra	Fr_V_rep
Fr_V_kid	0.002														
Fr_V_nep	-0.020	-0.012													
Fr_V_ski	0.016	0.012	0.001												
Fr_V_adi	0.025	-0.001	-0.027	0.005											
Fr_V_rob	0.003	0.014	-0.017	**-0.034**	0.022										
Fr_V_ven	-0.006	**-0.033**	0.001	0.003	0.000	-0.011									
Fr_V_art	**0.037**	0.000	0.007	0.009	0.008	0.010	-0.016								
Fr_V_lun	0.016	0.000	0.004	-0.011	0.007	-0.004	-0.018	-0.026							
Fr_V_mus	-0.025	0.005	0.017	0.003	**0.036**	0.026	0.002	0.006	-0.024						
Fr_V_spl	-0.019	**-0.040**	0.017	0.001	-0.028	-0.006	-0.013	0.011	0.002	0.013					
Fr_V_yel	0.019	0.026	0.014	0.008	-0.023	-0.014	-0.023	0.024	0.007	0.023	0.010				
Fr_V_hea	0.011	0.002	-0.020	-0.017	0.007	0.015	0.018	0.014	-0.019	0.004	0.012	0.000			
Fr_V_bra	-0.007	0.013	-0.002	0.013	0.004	0.014	-0.021	0.022	0.009	**0.029**	0.005	**0.032**	0.004		
Fr_V_rep	0.009	-0.003	-0.007	0.022	0.001	0.011	-0.015	**0.032**	0.013	**0.032**	-0.018	0.009	0.013	0.001	
Fr_V_red	0.013	-0.018	-0.007	-0.011	-0.014	-0.012	-0.027	-0.007	0.000	0.012	0.009	-0.023	-0.009	0.003	0.008

Table 6.6: Correlation matrix of fractional tissue and organ blood flow rate variability.

	Fr_F_kid	Fr_F_ski	Fr_F_adi	Fr_F_rob	Fr_F_gut	Fr_F_mus	Fr_F_hep	Fr_F_spl	Fr_F_yel	Fr_F_hea	Fr_F_bra	Fr_F_rep
Fr_F_ski	**0.047**											
Fr_F_adi	**0.145**	-0.009										
Fr_F_rob	**0.092**	0.002	0.000									
Fr_F_gut	**0.133**	0.016	**-0.035**	-0.008								
Fr_F_mus	**0.139**	-0.014	0.011	0.023	-0.001							
Fr_F_hep	**0.087**	-0.011	-0.009	0.011	0.002	-0.025						
Fr_F_spl	**0.028**	-0.010	0.009	0.003	**0.030**	0.019	0.000					
Fr_F_yel	0.014	-0.019	0.015	0.015	0.002	-0.013	-0.016	0.001				
Fr_F_hea	0.011	0.003	0.006	-0.019	-0.027	-0.012	-0.004	0.001	-0.014			
Fr_F_bra	**0.144**	-0.015	**-0.038**	0.023	0.000	-0.016	-0.015	**-0.037**	0.027	-0.015		
Fr_F_rep	0.016	-0.009	-0.004	-0.012	-0.021	0.019	0.018	0.004	-0.014	0.008	-0.002	
Fr_F_red	**0.085**	0.001	0.021	-0.003	-0.019	-0.009	-0.003	-0.005	**-0.038**	-0.002	0.013	0.007

6.4.4 Model extrapolation to steady-state

The calibrated PBTK model was used to apply a daily oral RfD exposure of 0.6 mg/ Kg. Analysis of correlated parameter distributions with suitable Monte Carlo sampling suggested the time to achieve steady-state plasma concentration was approximately 150 days (Figure 6.4). This was selected as the time point at which to calculate the biomonitoring equivalent (Figure 6.5).

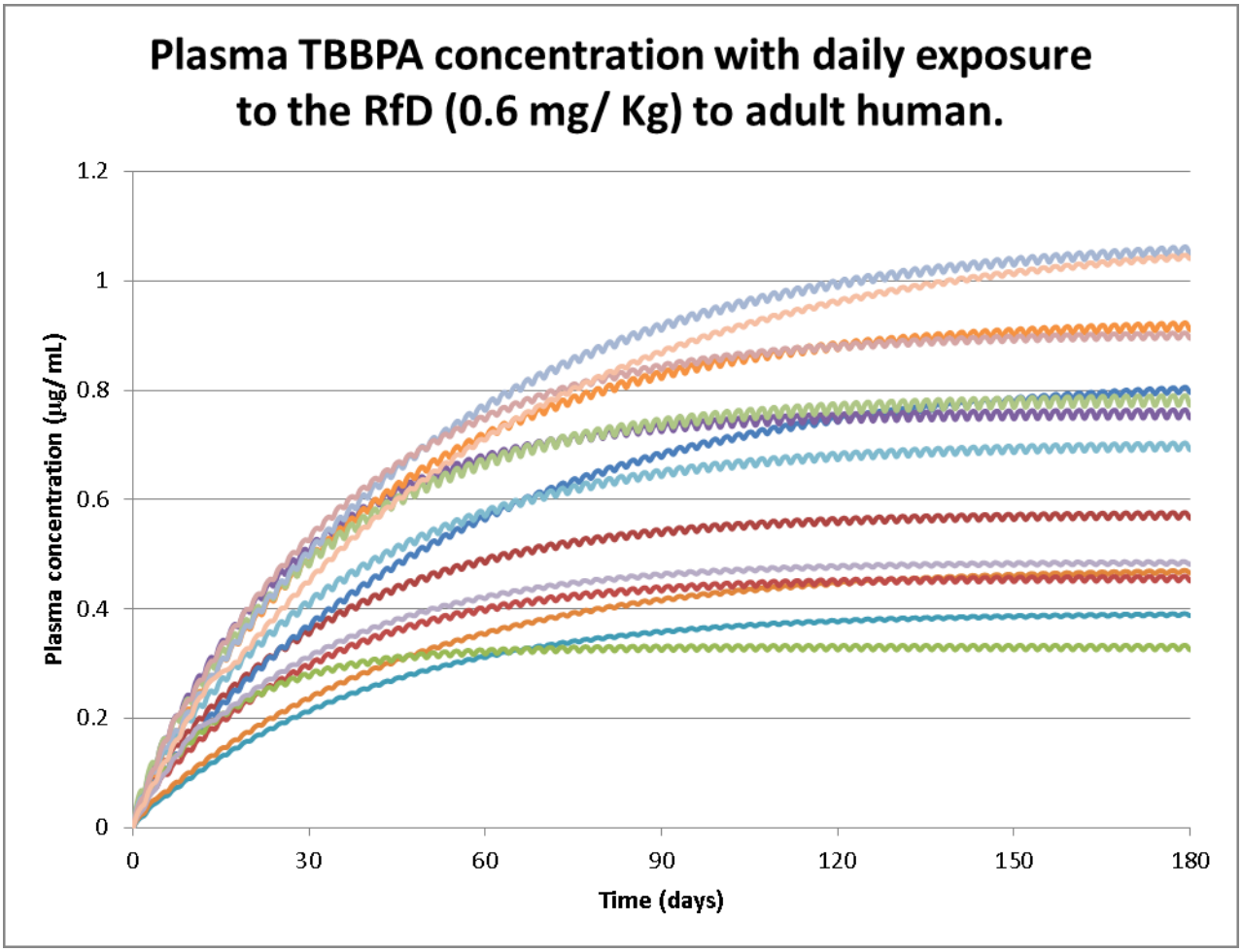


Figure 6.4: Temporal extrapolation of the calibrated human PBTK model for TBBPPA. This shows the time at which steady-state plasma concentration occurs, following daily exposure to the oral reference dose of 0.6 mg/ Kg.

6.4.5 Calculation of the biomonitoring equivalent at steady-state

The distributions in Figure 6.5 reflect possible BE concentrations at in a hypothetical human adult population where all individuals are exposed to the RfD of 0.6 mg/ Kg/ day, for 150 days to achieve steady-state plasma concentrations. The effect of parameter covariance has a statistically significant effect on the prediction of the BE ($p < 0.001$; $\alpha = 0.05$, student's t-test). Indeed, when parameter covariance is used, the range of possible BE concentration is visibly decreased, as well as the median plasma concentration (from 0.21 to 0.17 mg/ g plasma lipids).

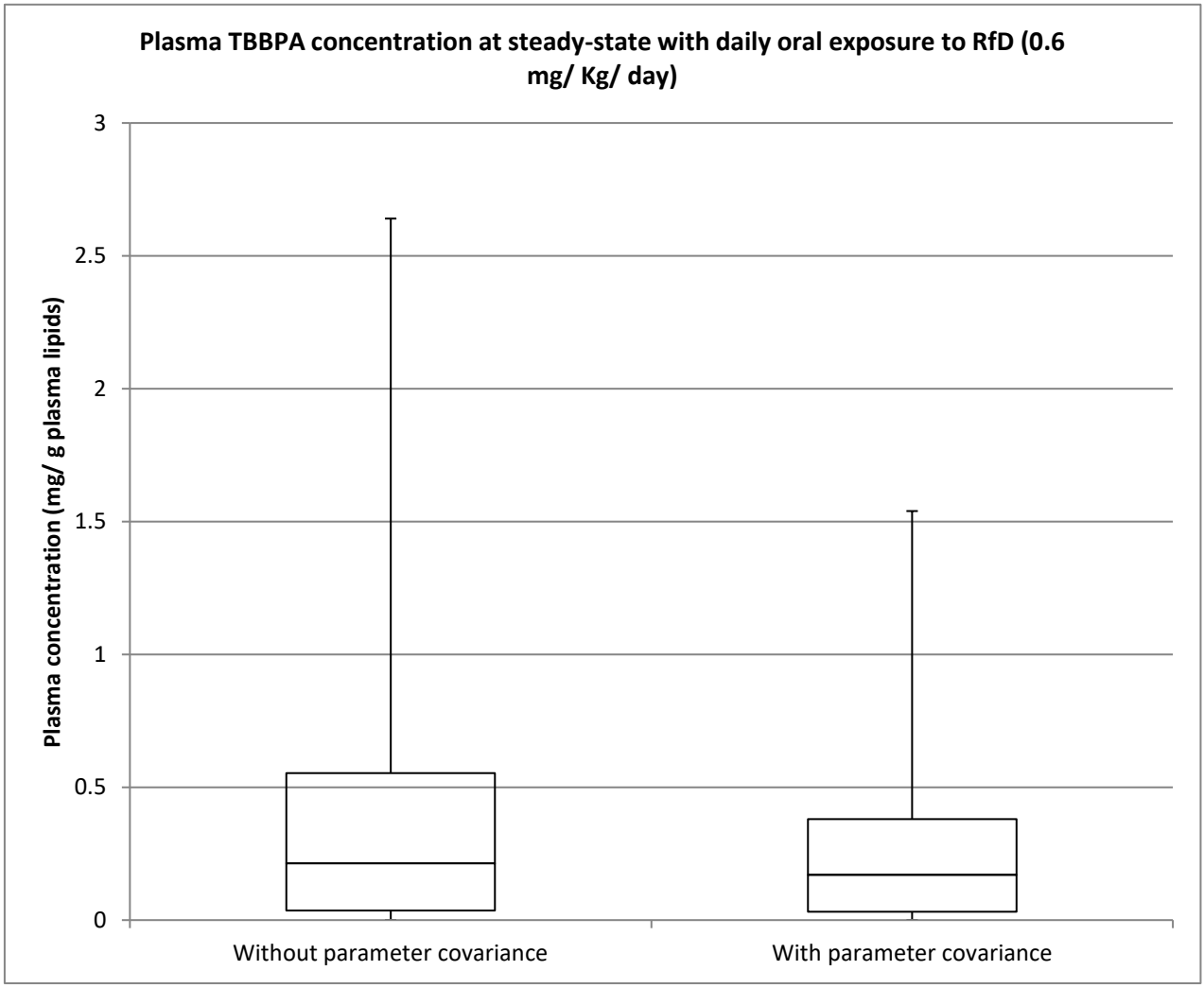


Figure 6.5: Assessment of human plasma TBBPA concentration at steady-state. The calibrated PBTK model for TBBPA was used to predict the plasma concentration at steady-state, for a hypothetical adult population exposed every day to the oral reference dose of 0.6 mg/ Kg; the variability represents the range of possible concentrations in this heterogeneous human population. The effect of parameter covariance significantly affects the model's prediction of the biomonitoring equivalent.

6.4.6 Review of HBM data for TBBPA

The literature review conducted to assess worldwide HBM data available for TBBPA is shown in Figure 6.6. This data was compared to estimates of the BE to facilitate their interpretation for health risk assessment purposes. The reported HBM concentrations are approximately 10,000 fold lower than the biomonitoring equivalent.

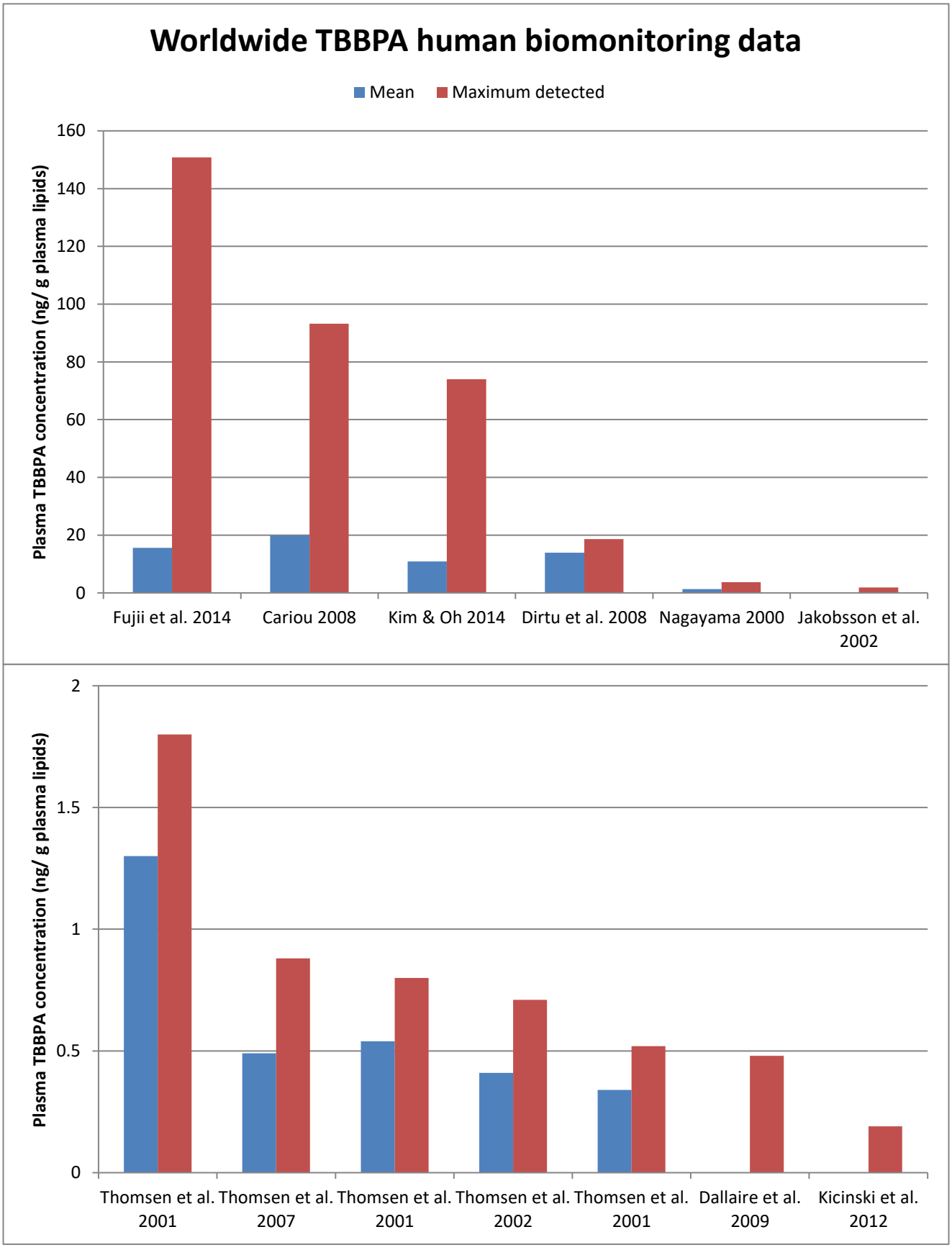


Figure 6.6: Review of worldwide human biomonitoring data available for TBBPA. This is reported as plasma concentrations for the parent compound.

6.5 Discussion

6.5.1 PBTK model calibration

A PBTK model has been built for TBBPA. Successful calibration has been assessed, in part, through visual inspection of fits to the corresponding toxicokinetic data (Figure 6.3). However, because the model is physiologically based, it is also important to assess whether values of selected model parameters are biologically plausible. If they are not, this may indicate deficiencies in the:

1) model structure. If the choice of differential equations does not adequately describe the biological system it is intended to represent, then to compensate, unrealistic parameter values will be selected during the calibration process.
2) choice of prior distributions. Because the posterior is a balance between the prior and data likelihood, inappropriate prior distributions which do not reflect true knowledge of the parameter uncertainty/ variability will generate unrealistic posterior distributions.

Thus, the assessment of successful model calibration also involves the comparison of prior parameter distributions with their posteriors; if they are sufficiently different, this may suggest something is wrong with the model structure and/ or choice of priors. However, in this study, the assignment of suitable prior distributions to model parameters is difficult. The model is intended to represent the human population for which HBM data has been collected. However, this is a worldwide population and therefore very heterogeneous in terms of physiology and xenobiotic biochemistry. Furthermore, when HBM data is collected from such individuals, descriptors of their physiology such as body weight are not usually reported. Therefore prior distributions were intended to represent a general adult population with a high degree of variability, and subsequently, large coefficients of variation of 50 % were used for fractional tissue volumes and perfusion rates (Hack 2006b, Yang *et al.* 2010). These posteriors are generally consistent with their prior

distributions, suggesting the model structure is indeed a good representation of the biological system it is intended to represent (Table 6.3). In terms of biochemical and physicochemical model parameters, the toxicokinetic data is only informative for gut permeability and 'Km' of enterocyte enzymes (Table 6.2). It is likely that if additional TK datasets were used for model calibration, this would allow identification/ calibration of more model parameters and influence the calculated BE.

6.5.2 Analysis of parameter covariance

Analysis of the multivariate posterior distribution obtained through model calibration allowed the identification of significant correlations between model parameters, which are expressed in terms of Pearson correlation coefficients (Tables 6.4 - 6.6). In order for the model to accurately reflect human toxicokinetic processes, it is important to encompass the way in which physiological processes vary in proportion to each other. For example, an individual with a relatively high muscle perfusion rate during exercise may be negatively correlated with a low intestinal perfusion rate. It is recognised that neglecting this kind of parameter covariance can result in highly improbable combinations of parameter values being selected, and therefore unrealistic model physiology being adopted (Bernillon & Bois 2000) leading to improbable model predictions (Bois 2000b). However the identification of parameter covariance to assist PBTK model predictions is not routinely done (Allen *et al.* 1996, El-Masri *et al.* 1999, Al-Subeihi *et al.* 2015); and this is the only known example where it has been used in the derivation of a BE. Part of the challenge is the limited availability of suitable human TK data that can be used to identify parameter covariance, however this is becoming more feasible with the development of 'microdosing' in humans (Section 1.4.3).

6.5.3 Model extrapolation to steady-state

Consistent with guidelines from Hays *et al.* 2007, deriving a BE involves calculating plasma concentrations at steady-state following daily exposure to the oral reference dose (RfD) of 0.6 mg/ Kg bw/ day. Steady-state occurs when plasma concentration remains at a constant level when the rates of chemical absorption and elimination equalise. Model simulations performed with parameter values sampled from their posterior distributions indicate that the time to reach steady-state is approximately 150 days (Figure 6.4). This was used as the time at which to calculate plasma concentrations as the BE. However, the way in which the BE is derived can potentially cause issues for interpretation of HBM data where exposure is acute rather than chronic. This is unlikely to be the case for TBBPA which is primarily an environmental contaminant, and therefore human exposures are likely to occur continuously throughout one's lifeline. Indeed, analysis of the HBM data is likely to reflect historical rather than recent exposure.

6.5.4 Calculation of the biomonitoring equivalent at steady-state

Figure 6.5 shows the BE derived for TBBPA. Parameter covariance has a significant effect on the BE, and appears to narrow the confidence intervals of the prediction as predicted by Portier & Kaplan 1989. Indeed, use of parameter covariance is likely to make the prediction of the BE more accurate for the population of interest. The wide range of the BE partly reflects the use of broad prior distributions for model parameters, which may overestimate the actual population variability. Additionally, it reflects the relatively large degree of parameter uncertainty relating to the mean of parameter distributions. Here, coefficients of uncertainty of 30 % were assigned to blood flows and 20 % to tissue volumes (Mezzetti *et al.* 2003, Hack 2006b). It is anticipated that with additional human TK data for model calibration, this level of uncertainty will decrease and subsequently narrow the BE distribution. Taken together, the BE estimates are likely to be conservative in their

nature; and the lower extreme of the distributions associated with the RfD may represent a 'worst-case' scenario.

6.5.5 Review of HBM data for TBBPA

Figure 6.6 shows a range of human plasma TBBPA concentrations reported in a number of studies conducted across the world, indicating regional differences in exposure levels. Comparison of this HBM data with the calculated BE suggests a low risk of toxicity for these individuals with measured TBBPA plasma concentrations; indeed, the median of the calculated BE is approximately 10,000 fold higher than the reported HBM data. However, there are major limitations relating to the interpretation of HBM data in general. For example, when HBM data is collected from human volunteers, descriptors of their physiology such as age and body weight are not usually reported. However these factors influence toxicokinetics and susceptibility to toxicity. If individual ages were reported with HBM data, then it would be possible to incorporate known age-related physiology into the PBTK model, and subsequently allow the refinement of prior distributions used for model parameters, leading to more relevant predictions for a particular population of interest. Additionally, health status and occupation of volunteers often go unreported, so it is difficult to assess whether HBM data is representative of the general population for whom the risk assessment is performed, and to differentiate exposures which occur primarily in an occupational or environmental setting. Firefighters, for example, are anticipated to receive high exposures to BFRs; indeed, large amounts BFR derivatives are formed in accidental fires (Söderström & Marklund 1999). Therefore it may be useful to routinely collect HBM data from firefighters alongside personal data including age and body weight, to facilitate the assessment of their occupational exposure and health risk.

6.5.6 Summary and conclusions

- A PBTK model has been built for TBBPA and calibrated.
- Possible to identify parameter covariance by calibrating the model to TK data.
- Time to reach steady-state with daily exposure to TBBPA at the RfD is approximately 150 days.
- BE for TBBPA has been calculated, which is affected by parameter covariance.
- Comparison of calculated BE with available HBM data suggests a low risk of toxicity.

6.5.7 Further work

Further work could involve deriving BEs for sub-populations of interest for additional RBFRs for which exposures are likely to be chronic, such as DBDPE, EBTBPE, BTBPE and BEHTBP. This would require the refinement of the model's prior distributions in order to represent the level of variability associated with populations of a particular ethnicity or age group for example.

In this chapter, a forward dosimetry approach was applied to a PBTK model to calculate the steady-state TBBPA plasma concentrations that correspond to an external dose (RfD). However, the reverse approach is also possible, where the measured plasma concentrations (HBM data) are used to estimate external doses which could then be compared to the RfD for risk assessment purposes. This approach has the advantage of generating estimates of external exposure that are directly comparable to existing regulatory guidance values such as the RfD. Typically, however, there is no unique solution to this reverse dosimetry approach because many different exposure scenarios may exist to produce the same biomonitoring level (Rigas *et al.* 2001, Sohn *et al.* 2004). If in some cases a particular exposure scenario (in terms of route, magnitude and timing of doses) can be assumed or derived through questionnaire and other monitoring data, then a solution to the inverse problem

might be possible. Future work could investigate deriving a BE in this way, possibly using human toxicokinetic data in addition to the HBM data through the use of an appropriate statistical model in a similar manner to that described in chapter 5.

Chapter 7: General discussion

7.1 Background to current research

PBTK models have been used extensively by various health protection agencies such as the U.S. EPA to assess environmental chemical exposure to xenobiotics such as methylene chloride; this has improved the assessment of human health risk through better exposure assessment (Andersen *et al.* 1987). More recently, PBTK models have also been used in the pharmaceutical industry to guide the optimisation of certain drug physicochemical properties and dosing regimens to provide an optimised pharmacokinetic profile in humans before first-in-human clinical trials. In both settings, numerous interspecies extrapolations have been performed in order to derive human exposure information without performing human exposure studies. Various methods such as allometric scaling and IVIVE are used however parameter values (such as rate of metabolism) are usually fixed, and thus the impact of interindividual physiological variability that may affect these parameter values, on toxicokinetics cannot be properly assessed. As a result, this then has to be compensated for in risk assessment, for example, a derived biomonitoring equivalent has to be divided by an appropriate uncertainty factor to account for intraspecies variability (Phillips *et al.* 2014). Another approach has been to assign distributions to parameters, although this is usually done without considering parameter covariance (e.g. Al-Subeihi *et al.* 2015), though parameter covariance is well acknowledged (Jamei *et al.* 2009). Recent work has for example identified covariance across the expression levels of various CYP450 enzymes in adult human livers (Achour *et al.* 2014), and running a population PBTK model with and without this covariance affects the PBTK model simulations (Wedagedera *et al.* 2015). However this PBTK model did not consider correlations with other model parameters such as tissue volumes. Another issue in PBTK modelling is the selection of animal model to extrapolate to humans. Ideally, animal model selection should be based on similarities in ADME between both species, but for many xenobiotics (especially novel compounds) this information is not

always available. Thus it is not always clear which animal data to extrapolate from, or what the implications are of extrapolating from an animal model which has dissimilar ADME to humans.

PBTK models can be used for both forward and reverse dosimetry. In forward dosimetry, a PBTK model (f) is used to calculate tissue dose (Ct) from a known external dose (Cd): Ct = f (Cd). In reverse dosimetry, the PBTK model is used to calculate Cd from Ct: Cd = f^{-1}(Ct). Typically, however, the inverse function (f^{-1}) may not exist, or may not be unique or stable, for example small changes in Ct (HBM data) may cause large erroneous changes in Cd (Lyons *et al.* 2008). Because exposure reconstruction is currently performed with HBM data alone (i.e. without toxicokinetic data) (e.g. Allen *et al.* 2007, Lyons *et al.* 2008, Tan *et al.* 2007), it is important to investigate more tractable methods of reconstructing exposure.

7.2 How research questions have been addressed

For the reasons above, this thesis investigated the use of Bayesian analysis to calibrate PBTK models and assess tissue exposures for use in chemical risk assessment. Prototype PBTK models have been developed in Monte Carlo simulation software for B6C3F1 mice, F344 rats, Beagle dogs and humans. These models have been validated by performing discrepancy tests with commercial GastroPlus PBTK software and mass balances. Distributions of values have been used for model parameters to represent population variability and uncertainty regarding ADME processes in order to assess ranges of possible tissue concentrations within populations. These models have been calibrated using Bayesian analysis to various toxicokinetic datasets as well as *in vitro* and HBM data. Several aspects of model development and their effect on exposure assessment were investigated: 1) PBTK model structure, 2) animal model being used for extrapolation to humans, 3) distributions of parameter values and covariance and, 4) inclusion of toxicokinetic and *in vitro* data (alongside HBM data) for exposure reconstruction.

7.3 Findings from research conducted

In this thesis, PBTK models have been developed for TBBPA, haloxyfop and picloram (chapter 3). It was shown that the way in which a PBTK model is built has important impacts on human exposure assessment (chapter 4). Therefore, PBTK model development requires an awareness of the biological processes occurring *in vivo*, so that the model adequately reflects these processes. It was also shown that the animal species being extrapolated from has an important impact on the assessment of human exposure (chapter 4). In particular, it was not necessary to model active transport processes in the dog model (but was in the mouse). This lead to a reduced rate of elimination in the dog model (and in the corresponding human model after extrapolation) and thus elevated systemic burden to haloxyfop following occupational exposure. Thus it is important to identify which animal model makes the most scientific sense to extrapolate to humans which should ideally be based on similarities on ADME.

A statistical model was developed to reconstruct exposure operator exposure to haloxyfop (chapter 5). This statistical model combines various disparate data sources to estimate human exposure (HBM data, mouse toxicokinetic data, human toxicokinetic data and *in vitro* data). While the HBM data is used to quantify unknown external exposure, the mouse and human toxicokinetic data is used to delineate internal processes. The information added to internal PBPK parameters helps to bridge the gap between estimates of external dose and excretion data. By combining toxicokinetic data with HBM data, this 'merges' forward dosimetry with reverse dosimetry, which is likely to increase the stability of the reverse dosimetry (f^{-1}) problem.

From the occupational exposure study that was examined in this thesis (Nolan *et al.* 1991), one operator was potentially at risk of toxicity from his estimated external and internal exposure levels. Additionally, the PTBK and statistical model developed to assess haloxyfop exposure in F344 rats indicated that the gender difference in plasma toxicokinetics in these animals (Smith *et al.* 1982) is likely mediated by transporter differences (chapter 5).

The studies presented provide evidence that parameter covariance has an effect on model predictions, such as systemic exposure (chapter 5) and urinary excretion rates (chapter 6). Thus, population PBTK models should be calibrated to toxicokinetic data in order to identify parameter covariance between all model parameters, before calculations are made with PBTK models for chemical risk assessment. Additionally, a biomonitoring equivalent for TBBPA (which corresponds to an acceptable oral intake rate of 0.6 mg/ Kg body weight) was derived using correlated Monte Carlo sampling (0.23 ± 0.24 SD mg/ g plasma lipids of TBBPA in plasma). Comparison with available HBM data suggests low risk of toxicity for those individuals with measured TBBPA plasma concentrations, ranging from 0.19 ng/ g lipid (Kicinski *et al.* 2012) to 150.8 ng/ g lipid (Fuji *et al.* 2014) (chapter 6).

7.4 Further work

As more human data becomes available, human PBTK modelling (without interspecies extrapolation) seems to be the most appropriate way forward for probabilistic analyses. This is likely to be widely acknowledged as valuable as it complements the replacement, refinement and reduction of animals in research. To this end, various forms of human data can be used such as toxicokinetic data, biochemical, physicochemical and physiological data. Interspecies extrapolation is difficult due to parameter covariance between distributions of parameters, and furthermore there can be subtle (unknown) differences in physiology between animals and humans that affect ADME in the body, for example relative transporter expression levels (Hilgendorf *et al.* 2007). Thus, estimates of human exposure obtained from an extrapolated animal model (without considering these factors, or human toxicokinetic data) should be interpreted with some caution.

Thus, human PBTK models should be continually updated to reflect the availability of new information on human physiology. This might include transporter expression levels in various tissues (not just liver), including their possible induction (particularly CYP1A1) and variability, and also QSAR models to predict which transporters in particular will be able to export or import the substrate; some QSAR models are available for P-glycoprotein (Broccatelli 2012). Furthermore, the model (as

coded) should be updated to allow for pH/ ionisation effects of xenobiotics. For further Bayesian analyses, priors for physicochemical and biochemical parameters should be better defined for specific compounds by performing suitable assays and/ or reviewing the literature to determine their uncertainties and possible ranges of values. In this respect, a database that provides ranges of possible values for these parameters for different xenobiotics would be useful. These updates will improve the predictive capability of PBTK models, allowing the PBTK model to predict with more accuracy the toxicokinetics of a particular exposure scenario that was not used for model calibration.

In terms of exposure reconstruction, it would be useful to experiment with having a human PBTK model, and performing exposure reconstruction with HBM data with and without human toxicokinetic data (through the use of a statistical model), to assess whether toxicokinetic data improves estimates of external exposure. Estimates of external exposure could be validated with passive biomonitoring data and/or results generated by the PROcEED model available from U.S. EPA (Probabilistic Reverse dOsimetry Estimating Exposure Distribution) which similarly uses Bayesian analysis to perform exposure reconstruction (U.S. EPA 2017). If human toxicokinetic data is shown to increase the accuracy of external exposure estimates, then human toxicokinetic data could be collected more routinely as part of human exposure assessment. This could be achieved through microdosing, where trace doses of radiolabelled drugs are administered to volunteers, to minimise the risk of toxicity (Section 1.4.3). Although this would remove the need for animal dosing, values for the PBTK parameters might change between a microdose and a larger occupational or domestic exposure dose. Thus the human PBTK model (calibrated with microdose toxicokinetic data) should only be used for risk assessment when the exposure level is not anticipated to exceed the KMD (the induction of non-linear toxicokinetics) (Section 1.4.1.2).

7.5 Summary

PBTK models are useful computational tools which can be used to assess internal chemical exposure at the site of action. This is very helpful for assessing the risk of toxicity and performing chemical risk

assessments. It is important that these models incorporate interindividual variability and uncertainty regarding ADME processes; as such, distributions of values have been assigned to model parameters in this work. The way in which these distributions vary in proportion to each other affects the model predictions. Thus, future efforts could focus on identifying this parameter covariance before a PBTK model is used for chemical risk assessment.

Bibliography

Abdallah M.A., Harrad S. & Covaci A. (2008). Hexabromocyclododecanes and tetrabromobisphenol-A in indoor air and dust in Birmingham, UK: implications for human exposure. *Environ. Sci. Technol.* **42:** 6855-6861

Abdallah M.A. & Harrad S. (2011). Tetrabromobisphenol-A, hexabromocyclododecane and its degradation products in UK human milk: relationship to external exposure. *Environ. Int.* **37:** 443-448

Achour B., Barber J. & Rostami-Hodjegan A. (2014). Expression of Hepatic Drug-Metabolizing Cytochrome P450 Enzymes and Their Intercorrelations: A Meta-Analysis. *Drug Metab. Dispos.* **42:** 1349-1356

Allen B.C., Covington T.R. & Clewell H.J. (1996). Investigation of the impact of pharmacokinetic variability and uncertainty on risks predicted with a pharmacokinetic model for chloroform. *Toxicology* **111:** 289-303

Allen B.C., Hack C.E. & Clewell H.J. (2007). Use of Markov Chain Monte Carlo analysis with a physiologically-based pharmacokinetic mode of methylmercury to estimate exposures in U.S. women of childbearing age. *Risk Anal.* **27:** 947-958

Al-Subeihi A.A., Alhusainy W., Kiwamoto R., *et al.* (2015). Evaluation of the interindividual human variation in bioactivation of methyleugenol using physiologically based kinetic modeling and Monte Carlo simulations. *Toxicol. Appl. Pharm.* **283:** 117-126

Andersen M.E., Clewell H.J., Gargas M.L., *et al.* (1987). Physiologically based pharmacokinetics and the risk assessment process for methylene chloride. *Toxicol. Appl. Pharm.* **87:** 185-205

Andersen M.E., Clewell H.J. & Frederick C.B. (1995). Applying simulation modeling to problems in toxicology and risk assessment - a short perspective. *Toxicol. Appl. Pharm.* **133:** 181-187

ATSDR (1999). Toxicological Profile for Polychlorinated Biphenyls. Agency for Toxic Substances and Disease Registry, U.S. Department of Health and human Services, Public Health Service, Atlanta, GA.

Aylward L.L., Kirman C.R., Adgate J.L., *et al.* (2012). Interpreting variability in population biomonitoring data: role of elimination kinetics. *J. Expo. Sci. Environ. Epidemiol.* **22:** 398-408

Baldrick P. (2003). Toxicokinetics in preclinical evaluation. *Drug Discov. Today* **8:** 127-133

Barna-Lloyd T., Taylor H.W., Davis N.L., *et al.* (1983). Dowco 543 herbicide: interim report of results through six months in a 12-month dog dietary toxicity study in Beagle dogs. Unpublished report No. TXT:K-131381-(17) from Dow Chemical Company, Midland, Michigan, USA.

Barna-Lloyd T., Taylor H.W., Davis N.L., *et al.* (1984). Dowco 543 herbicide: results of a 12-month dietary toxicity study in Beagle dogs. Unpublished report No. HET K131381-(17) (document 5.3.2.5/01, D12) from Dow Chemical Company, Midland, Michigan, USA.

Barnard S.D., Yano B.L. & Frausion L.E. (1986). Induction of hepatic peroxisome proliferation by haloxyfop - species sensitivity: dogs and monkeys. Unpublished report No. HET K 131381-047 (document 5.8.2.1.2/02 & 03, G04/D12) from Dow Chemical Company, Midland, Michigan, USA.

Bartels M.J. & Smith F.A. (1988) Stereochemical inversion of haloxyfop in the Fisher 344 rat. *Drug Metab. Dispos.* **17:** 286-291

Barton H.A., Pastoor T.P., Baetcke K., *et al.* (2006). The acquisition and application of absorption, distribution, metabolism, and excretion (ADME) data in agricultural chemical safety assessments*. Crit. Rev. Toxicol.* **36:** 9-35

Bauer M., Wagner C.C., Langer O. *et al.* (2008). Microdosing studies in humans: the role of positron emission tomography. *Drugs R&D* **9:** 73-81

Bentley P., Calder I., Elcombe C., *et al.* (1993). Hepatic peroxisome proliferation in rodents and its significance for humans. *Food Chem. Toxicol.* **31:** 857-907

Bernillon P. & Bois F.Y (2000). Statistical issues in toxicokinetic modelling: a Bayesian perspective. *Environ. Health Perspect.* **108:** 883-893

Besis A. & Samara C. (2012). Polybrominated diphenyl ethers (PBDEs) in the indoor and outdoor environments-A review on occurrence and human exposure. *Environ. Pollut.* **169:** 217-229

Bois F.Y. (1999). Analysis of PBPK models for risk characterisation. *Ann. N Y Acad Sci.* **895:** 317-337

Bois F.Y. (2000a). Statistical Analysis of Fisher *et al.* PBPK Model of Trichloroethylene Kinetics. *Environ. Health Perspect.* **108:** 275-282

Bois F.Y. (2000b). Statistical Analysis of Clewell *et al.* PBPK Model of Trichloroethylene Kinetics. *Environ. Health Perspect.* **108:** 307-316

Bois F.Y. (2013). Ch. 25: Bayesian Inference In: Computational Toxicology: Methods in Molecular Biology, Brad Reisfeld and Arthur N. Mayeno (eds.) **930:** 597-636

Bois F. Y., Masoud J. & Clewell H.J. (2010). PBPK modelling of inter-individual variability in the pharmacokinetics of environmental chemicals. *Toxicology* **278:** 256–267

Bois F.Y. & Maszle D.R. (2008). MCSim: A Monte Carlo Simulation Program. User's Manual, software version 5.3.0 Available at: http://www.ofb.net/gnu/mcsim/mcsim_toc.html (accessed 01/11/2014)

Boobis A.R., Cohen S.M., Dellarco V., *et al.* (2006). IPCS framework for analyzing the relevance of a cancer mode of action for humans. *Crit. Rev. Toxicol.* **36:** 781-792

Boobis A.R., Doe J.E., Heinrich-Hirsch B., *et al.* (2008). IPCS framework for analyzing the relevance of a noncancer mode of action for humans. *Crit. Rev. Toxicol.* **38:** 87-96

Bramwell L., Fernandes A., Rose A., *et al.* (2014). PBDEs and PBBs in human serum and breast milk from cohabiting UK couples. *Chemosphere* **116:** 67-74

Broccatelli F. (2012). QSAR Models for P‑Glycoprotein Transport Based on a Highly Consistent Data Set. *J. Chem. Inf. Model.* **52:** 2462-2470

Brown D.J., Overmeire I.V., Goeyens L., *et al.* (2004). Analysis of Ah receptor pathway activation by brominated flame retardants. *Chemosphere.* **55:** 1509-1518

Brown R.P., Delp M.D., Lindstedt S.L., *et al.* (1997). Physiological parameter values for physiologically based pharmacokinetic models. *Toxicol. Ind. Health* **13:** 407-484

Campbell J.L., Clewell R.A., Gentry P.R. *et al.* (2012). Ch. 18. Physiologically Based Pharmacokinetic/ Toxicokinetic Modeling. In: Reisfeld B. & Mayenoo A.N. (eds), Computation Toxicology. Humana Press, New York, p. 457, 473

Canada (2013). Screening assessment report of Phenol, 4,4'-(1-methylethylidene) bis[2,6-dibromo- (Tetrabromobisphenol A, TBBPA; CAS 79–94-7), Ethanol,2,2'-[(1-methylethylidene)bis[(2,6-dibromo-4,1-phenylene)oxy]]bis (known as TBBPA bis(2-hydroxyethyl ether, CAS 4162-45-2) and Benzene, 1,1'-(1-methylethylidene)bis[3,5-dibromo-4-(2-propenyloxy)-(TBBPA bis(allylether, CAS 25327-89-3). Government of Canada, Environment Canada, Health Canada.

Cariou R., Antignac J., Zalko D., *et al.* (2008). Exposure assessment of French women and their newborns to tetrabromobisphenol-A: Occurrence measurements in maternal adipose tissue, serum, breast milk and cord serum. *Chemosphere.* **73:** 1036-1041

Carmichael N.G., Barton H.A., Boobis A.R., *et al.* (2006). Agricultural chemical safety assessment: a multisector approach to the modernization of human safety requirements. *Crit. Rev. Toxicol.* **36:** 1-7

Carrizo D., Grimalt J.O., Fito N.R., *et al.* (2007). Influence of breastfeeding in the accumulation of polybromodiphenyl ethers during the first years of child growth. *Environ. Sci. Technol.* **41:** 4907-4912

Chignell C.F., Han S.K., Mouithys-Mickalad A., *et al.* (2008). EPR studies of *in vivo* radical production by 3,30,5,50-tetrabromobisphenol A (TBBPA) in the Sprague-Dawley rat. *Toxicol. Appl. Pharm.* **230:** 17-22

Chiu W. A., Okino M.S. & Evans M.V. (2009). Characterizing uncertainty and population variability in the toxicokinetics of trichloroethylene and metabolites in mice, rats, and humans using an updated database, physiologically based pharmacokinetic (PBPK) model, and Bayesian approach. *Toxicol. Appl. Pharm.* **241:** 36-60

Clewell H.J. & Andersen M.E. (1996). Use of physiologically based pharmacokinetic modeling to investigate individual versus population risk. *Toxicology* **111:** 315-329

Coecke S., Pelkonen O., Leite S.B., *et al.* (2013). Toxicokinetics as a key to the integrated toxicity risk assessment based primarily on non-animal approaches. *Toxicol. in Vitro* **5:** 1570-1577

Colnot T., Kacew S. & Dekant W. (2014). Mammalian toxicology and human exposures to the flame retardant 2,2′,6,6′‐tetrabromo‐4,4′‐isopropylidenediphenol (TBBPA): implications for risk assessment. *Arch Toxicol.* **88:** 553-573

Combes R.D., Berridge B., Connelly J., *et al.* (2003). Early microdose drug studies in human volunteers can minimise animal testing: proceedings of a workshop organised by Volunteers in Research and Testing. *Eur. J. Pharm. Sci.* **19:** 1-11

Cope R., Kacew S. & Dourson M. (2015). A reproductive, developmental and neurobehavioral study following oral exposure of tetrabromobisphenol A on Sprague-Dawley rats. *Toxicology.* **329:** 49-59

Counts J.L. & Goodman J.I. (1995). Principles underlying dose selection for, and extrapolation from, the carcinogen bioassay: dose influences mechanism. *Regul. Toxicol. Pharm.* **21:** 418-421

Covaci A., Harrad S., Abdallah M.A., *et al.* (2011). Novel brominated flame retardants: a review of their analysis, environmental fate and behaviour. *Environ. Int.* **37:** 532-556

Daley J. (2013). Bioamplification as a bioaccumulation mechanism. PhD thesis. University of Windsor. p.5 Available at: http://scholar.uwindsor.ca/cgi/viewcontent.cgi?article=5757&context=etd (accessed 18/06/2015)

Dallaire R., Ayotte P., Pereg D., *et al.* (2009). Determinants of Plasma Concentrations of Perfluorooctanesulfonate and Brominated Organic Compounds in Nunavik Inuit Adults (Canada) Environ. *Sci. Technol.* **43:** 5130-5136

Dankers A.C., Roelofs M.J., Piersma A.H., *et al.* (2013). Endocrine disruptors differentially target ATP-binding cassette transporters in the blood-testis barrier and affect Leydig cell testosterone secretion *in vitro*. *Toxicol. Sci.* **136:** 382-91

DAS (2018). Product Safety Assessment for Haloxyfop-P Methyl Ester. Available at: http://msdssearch.dow.com/PublishedLiteratureDOWCOM/dh_07cf/0901b803807cfd89.pdf?filepath=productsafety/pdfs/noreg/233-00787.pdf&fromPage=GetDoc (accessed 11/05/2018).

Davies B. & Morris T. (1993). Physiological parameters in laboratory animals and humans. *Pharm. Res.* **10:** 1093 - 1095

Davis J.E. (1980). Minimizing Occupational Exposure to Pesticides: Personal Monitoring. *Residue Rev.* **75:** 33-50

De Buck S.S, Sinha V.K., Fenu L.A., *et al.* (2007). Prediction of Human Pharmacokinetics Using Physiologically Based Modeling: A Retrospective Analysis of 26 Clinically Tested Drugs. Drug *Metab. Dispos.* **35:** 1766-1780

Dirtu A.C., Roosens L., Geens T., *et al.* (2008). Simultaneous determination of bisphenol A, triclosan, and tetrabromobisphenol A in human serum using solid-phase extraction and gas chromatography-electron capture negative-ionization mass spectrometry. *Anal. Bioanal. Chem.* **391:** 1175-1181

Driffield M., Harmer N., Bradley E., *et al.* (2008). Determination of brominated flame retardants in food by LC-MS/MS: diastereoisomer-specific hexabromocyclododecane and tetrabromobisphenol A. *Food Addit. Contam. A.* **25:** 895-903

Duffus J.H. & Worth H.G.J (Eds.) (2006). Fundamental Toxicology. Royal Society of Chemistry, Cambridge, Ch. 3, p.28

Dunnick J.K., Sanders J.M., Kissling G.E., *et al.* (2015). Environmental Chemical Exposure May Contribute to Uterine Cancer Development: Studies with Tetrabromobisphenol A. *Toxicol. Pathol.* **43:** 464-473

EC (2006). Draft: Guidance for the setting and application of acceptable operator exposure levels (AOELs). European Commission, Health & Consumer protection directorate-general; Directorate E.

EC (2010). DG SANCO/11802/1010 Rev.0 Draft guidance to EC 1107/2009.

ECB (2006). European Union Risk Assessment Report – 2,2',6,6'-tetrabromo-4,4' isopropylidenediphenol (tetrabromobisphenol-A or TBBP-A) (CAS: 79–94-7) Part II – human health. Institute for Health and Consumer Protection, European Chemicals Bureau, European Commission Joint Research Centre, 4th Priority List, Luxembourg: Office for Official Publications of the European Communities.

ECB (2008). European Union Risk Assessment Report – 2,2',6,6'-tetrabromo-4,4' isopropylidenediphenol (tetrabromobisphenol-A or TBBP-A) (CAS: 79–94-7) Part I – environment

ECHA (2008). Guidance on information requirements and chemical safety assessment. Chapter R.7.12: Guidance on toxicokinetics. European Chemicals Agency, Helsinki.

EFSA (2009). Conclusion on the peer review of the pesticide risk assessment of the active substance haloxyfop-P (haloxyfop-R). *EFSA J.* **11:** 1348

EFSA (2011). EFSA panel on contaminants in the food chain (CONTAM): scientific opinion on tetrabromobisphenol A (TBBPA) and its derivatives in food EFSA panel on contaminants in the food chain. *EFSA J.* **61:** 2477

EFSA (2012a). Scientific Opinion on Emerging and Novel Brominated Flame Retardants (BFRs) in Food. *EFSA J.* **10:** 2908

EFSA (2012b) Guidance on selected default values to be used by the EFSA Scientific Committee, Scientific Panels and Units in the absence of actual measured data. *EFSA J.* **10:** 2579

EFSA (2014). Guidance on the assessment of exposure of operators, workers, residents and bystanders in risk assessment for plant protection products. *EFSA J.* **10:** 3874

Elcombe B.M. (2002a). Effects of haloxyfop in cultured B6C3F1 mouse hepatocytes. Unpublished report No.CXM 0148 (study ID: GHE-T-1166; document 5.8.2.2.1/01, G11) from Centre for Xenobiotic Research, Ninewells Hospital & Medical School, University of Dundee, UK.

Elcombe B.M. (2002b). Effects of haloxyfop in cultured human hepatocytes. Unpublished report No.CXM 0150 (study ID: GHE-T-1168; document 5.8.2.3/01, G13) from Centre for Xenobiotic Research, Ninewells Hospital & Medical School, University of Dundee, UK.

EU (2002). Directive 2002/95/EC on certain hazardous substances in electrical and electronic equipment.

EU (2004). 24th amendment to the marketing and use Directive 76/769/EEC, Chemicals – Market Restrictions. In: EU (Ed.). Directive 76/769/EEC.

EU (2006). Risk Assessment Report TBBP-A, Part II-Human Health.

EU (2008a). Regulation of Hazardous Substances (RoHS) Directive (2002/95/EC) amendment.

EU (2008b). Communication from the Commission on the results of the risk evaluation and risk reduction strategies for the substances: sodium chromate, sodium dichromate and 2,2',6,6'-tetrabromo-4,4'-isopropylidenediphenol (tetrabromobisphenol A). OJ C; 152: 11-20

EUROPOEM (1997). The Development, Maintenance and Dissemination of a European Predictive Operator Exposure Model (EUROPOEM) Database. Final Report, BIBRA International, Carshalton, UK

Fagerholm U., Johansson M. & Lannernäs H. (1996). Comparison Between Permeability in Rat and Human Jejunum. *Pharm. Res.* **13:** 1336-1342

Fenske R.A. (1993). Dermal Exposure Assessment Technique. *Ann. Occup. Hyg.* **37:** 687-706

Filipsson A.F., Sand S., Nilsson J., *et al.* (2003). The Benchmark Dose Method - Review of Available Models, and Recommendations for Application in Health Risk Assessment. *Crit. Rev. Toxicol.* **33:** 505-542

Fiserova-Bergerova V. (1993). Relevance of Occupational Skin Exposure. *Ann. Occup. Hyg.* **37:** 673-685

Fujii Y., Harada K., Hitomi T., *et al.* (2014). Temporal trend and age-dependent serum concentration of phenolic organohalogen contaminants in Japanese men during 1989-2010. *Environ. Pollut.* **185:** 228-233

Gad S.C. (Ed.) (2007). Animal Models in Toxicology, 2nd Ed.CRC Press, Florida. p.123-130.

Gant T.W., O'Connor C.K., Corbitt R., *et al.* (1995) *In vivo* induction of liver P-glycoprotein expression by xenobiotics in monkeys. *Toxicol. Appl. Pharm.* **133:** 269-276

Garner R.C. & Lappin G. (2006). The phase 0 microdosing concept. *Br. J. Clin. Pharmacol.* **61:** 367-370

Gelman A. & Rubin D.B. (1992). Inference from iterative simulation using multiple sequences. *Stat. Sci.* **4:** 457-511

Gelman A., Bois F.Y. & Jiang J. (1996). Physiological pharmacokinetic analysis using population modeling and informative prior distributions. *J. Am. Stat. Assoc.* **91:** 1400-1412

Gerwick B.C., Jackson L.A., Handley J. *et al.*, (1988). Preemergence and postemergence activities of the (R) and (S) enantiomers of haloxyfop. *Weed Sci.* **36:** 453-456

Geyer C.J. (1992). Practical Markov chain Monte Carlo. *Stat. Sci.* **7:** 473-511

Gilks W.R., Richardson S. & Spiegelhalter D.J. (1996). Introducing Markov chain Monte Carlo. In: Markov chain Monte Carlo in practice. London: Chapman and Hall

Gorzinski S.J., Tollett J.T., Johnson K.A., *et al.* (1982a). Dowco 453: results of 13- and 36-week dietary toxicity studies in B6C3F1 mice. Unpublished report No. HET K 131381-(3)(document 5.3.2.2/01, D09) from Dow Chemical Company, Midland, Michigan, USA.

Gorzinski S.J., Burek J.D., Keyes D.G., *et al.* (1982b). DOWCO 453: Results of 16 and 37-week dietary toxicity studies in Fischer 344 rats. Study No. HET K 131381-(4). Unpublished report prepared by Dow Chemical, Midland, Michigan, USA. Submitted to WHO by Dow Elanco Europe, Wantage, Oxon, United Kingdom.

Grass G.M. (1997). Simulation models to predict oral drug absorption from *in vitro* data. *Adv. Drug Deliv. Rev.* **23:** 199-219

Green N. (2002). Computer systems for the prediction of toxicity: An update. *Adv. Drug. Deliv. Rev.* **54:** 417-431

Griffith F.D. & Long J.W. (1980). Animal toxicity studies with ammonium perfluorooctanoate. *Am. Ind. Hyg. Assoc. J.* **41:** 576-583

Grosse Y., Loomis D., Guyton K.Z., *et al.* (2016). Carcinogenicity of some industrial chemicals. *Lancet Oncol.* **17:** 419-420

Großkopf C., Mielke H., Westphal D., *et al.* (2013). A new model for the prediction of agricultural operator exposure during professional application of plant protection products in outdoor crops. *J. Verbrauch Lebensm* **8:** 143-153

Hack C.E. (2006a). Bayesian analysis of physiologically based toxicokinetic and toxicodynamic models. *Toxicology* **221:** 241-248

Hack E.C., Chiu W.A., Zhao Q.J., *et al.* (2006b). Bayesian population analysis of a harmonised physiologically based pharmacokinetic model of trichloroethylene and its metabolites. *Regul. Toxicol. Pharm.* **46:** 63-83

Hakk H., Larsen G., Bergman Å., *et al.* (2000). Metabolism, excretion and distribution of the flame retardant tetrabromobisphenol-A in conventional and bile-duct cannulated rats. *Xenobiotica* **30:** 881-890

Hamey P.Y. (2001). An Example to Illustrate the Potential Use of Probabilistic Modelling to Estimate Operator Exposure to Pesticides. *Ann. Occup. Hyg*. **45:** 55-64

Hanhijarvi H., Ophaug R. & Singer L. (1982). The sex related difference in perfluorooctanoate excretion in the rat. *Proc. Soc. Exp. Biol. Med.* **171:** 50-55

Hanley T.R., Yano B.L., Berdasco N.M., *et al.* (1985). Haloxyfop: oral teratology study in rabbits (repeat study). Unpublished report No. HET K 131381-042 (document 5.6.2.2/02, F03) from Dow Chemical Company, Midland, Michigan, USA.

Hastings W.K. (1970). Monte-Carlo sampling methods using Markov chains and their applications. *Biometrika* **57:** 97-106

Hayes W.C., Hanley T.R. & Yano B.L. (1983). Dowco 453 sodium salt: oral teratology study in rats and rabbits. Unpublished report No. HET K 131381-028 (document 5.6.2.1/02, F02) from Dow Chemical Company, Midland, Michigan, USA.

Hays S.M., Becker R., Leung H.W., *et al.* (2007). Biomonitoring Equivalents: a screening approach for interpreting biomonitoring results from a public health risk perspective. *Regul. Toxicol. Pharm.* **47:** 96-109

Hays S.M., Pyatt D.W., Kirman C.R., *et al.* (2012). Biomonitoring Equivalents for benzene. *Regul. Toxicol. Pharm.* **62:** 62-73

Heijnen A.M.P., Brink E.J., Lemmens A.G., *et al.* (1993). Ileal pH and apparent absorption of magnesium in rats red on diets containing either lactose or lactulose. *Br. J. Nutr.* **70:** 747-756

Heuvel J. (1991). Tissue distribution, metabolism, and elimination of perfluorooctanoic acid in male and female rats. *J. Biochem. Toxicol.* **6:** 83-92

Hilgendorf C., Ahlin G., Seithel A., *et al.* (2007). Expression of Thirty-six Drug Transporter Genes in Human Intestine, Liver, Kidney, and Organotypic Cell Lines. *Drug Metab. Dispos.* **35:** 1333-1340

Hindmarsh A. (1983). ODEPACK, a systemized collection of ODE solvers. In: Scientific Computing (Stepleman RS, ed). Amsterdam: North-Holland 55-64

Hites R.A. (2004). Polybrominated diphenyl ethers in the environment and in people: a meta-analysis of concentrations. *Environ. Sci. Technol.* **38:** 945-956

Hosseini-Yeganeh M. & McLachlan A.J. (2002). Physiologically based pharmacokinetic model for terbinafine in rats and humans. *Antimicrob. Agents Chemother.* **46:** 2219-28

Huang W., Lee S.A & Yu L.X. (2009). Mechanistic Approaches to Predicting Oral Drug Absorption. *APPS J.* **11:** 217-224

Iakovleva I., Begum A., Brännström K., *et al.* (2016). Tetrabromobisphenol A Is an Efficient Stabilizer of the Transthyretin Tetramer. PLoS ONE 11(4): e0153529. doi:10.1371/journal.pone.0153529

ICH (1995). CPMP/ICH/384/95. Note for guidance on toxicokinetics: a guidance for assessing systemic exposure in toxicology studies.

ICRP (1994). International Commission on Radiological Protection. Human respiratory tract model for radiological protection. ICRP Publication 66; Ann ICRP 24(1-3). Oxford: Pergamon press

ICRP (2006). Human alimentary tract model for radiological protection. ICRP Publication 100. Ann. ICRP 36(1/2).

ICRP (2015). Occupational Intakes of Radionuclides: Part 1. ICRP Publication 130. Ann. ICRP 44(2).

Ings R.M. (1990). Interspecies scaling and comparisons in drug development and toxicokinetics. *Xenobiotica* **20:** 1201-1231

IPCS/WHO (1994). Environmental Health Criteria 152: Polybrominated Biphenyls. Available at: http://www.inchem.org/documents/ehc/ehc/ehc152.htm (accessed 10/11/2014).

Jakobsson K., Thuresson K., Rylander L., *et al.* (2002). Exposure to polybrominated diphenyl ethers and tetrabromobisphenol A among computer technicians. *Chemosphere.* **46:** 709-716

Jamei M., Dickinson G.L. & Rostami-Hodjegan A. (2009). A Framework for Assessing Inter-individual Variability in Pharmacokinetics Using Virtual Human Populations and Integrating General Knowledge of Physical Chemistry, Biology, Anatomy, Physiology and Genetics: A Tale of `Bottom-Up' vs `Top-Down' Recognition of Covariates. *Drug Metab. Pharmacokinet.* **24:** 53-75

Jeffries T., Yano B. & Rao K. (1985). Dowco 453: Three-generation Dietary Reproduction Study in Fischer 344 Rats: HET-K-131381- 012. Unpublished study prepared by Dow Chemical U.S.A. p.25 Available from U.S. EPA (FOIA).

JMPR (2006). Haloxyfop (including haloxyfop-R and haloxyfop-R methyl ester), p. 349

Jonsson F. & Johanson G. (2002). Physiologically Based Modeling of the Inhalation Kinetics of Styrene in Humans Using a Bayesian Population Approach. *Toxicol. Appl. Pharm.* **179:** 35-49

Jonsson F. & Johanson G. (2003). Bayesian population approach to physiological toxicokinetic-toxicodynamic models - an example using the MCSim software. *Toxicol. Lett.* **138:** 143-150

Jurvelin J., Lahtinen T., Kiviranta I., *et al.* (1988). Blood flow, histomorphology and elemental composition of the canine femur after physical training or immobilization. *Acta Physiol. Scand.* **132:** 385-389

Kadono K., Yokoe J., Ogawara K., *et al.* (2002). Analysis and prediction of absorption behavior for theophylline orally administered as powders based on gastrointestinal-transit-absorption (GITA) model. *Drug Metab. Pharmacokinet.* **17:** 307-315.

Kang M.J., Kim J.H., Shin S., *et al.* (2009). Nephrotoxic potential and toxicokinetics of tetrabromobisphenol A in rat for risk assessment. *J. Toxicol. Environ. Health A* **72:** 1439-1445

Kangas J. & Sihvonon S. (1996). Comparison of predictive models for pesticide operator exposure. TemaNord, Copenhagen

Kasperma J., Doumen C., Munrow S., *et al.* (2002). Fire retardant mechanism of aliphatic bromine compounds in polystyrene and polypropylene. *Polym. Degrad. Stabil.* **77:** 325-331

Kefeni K.K., Okonkwo J.O. & Botha B.M., *et al.* (2014). Concentrations of polybromobiphenyls and polybromodiphenyl ethers in home dust: relevance to socio-economic status and human exposure rate. *Sci. Total Environ.* **470-471:** 1250-6

Kenyon E.M. (2012). Ch. 19: Interspecies extrapolation. In: Computational Toxicology: Methods in Molecular Biology, Brad Reisfeld and Arthur N. Mayeno (eds.) 929: 501-520

Kiciński M., Viaene M.K., Hond E.D., *et al.* (2012). Neurobehavioral function and low-level exposure to brominated flame retardants in adolescents: a cross-sectional study. *Environ. Health* **11:** 86

Kim U. & Oh J. (2014). Tetrabromobisphenol A and hexabromocyclododecane flame retardants in infant-mother paired serum samples, and their relationships with thyroid hormones and environmental factors. *Environ. Pollut.* **184:** 193-200

Kitamura S., Junno N., Shigeru O., *et al.* (2002). Thyroid hormonal activity of the flame retardants tetrabromobisphenol A and tetrachlorobisphenol A. *Biochem. Bioph. Res. Co.* **293:** 554-559

Klassen C.C. (2008). Casarett and Doull's Toxicology: the basic science of poisons. 7th edition. USA: McGraw-Hill Companies p. 911

Klaunig J.E., Babich M.A., Baetcke K.P., *et al.* (2003). PPARα Agonist-Induced Rodent Tumors: Modes of Action and Human Relevance. *Crit. Rev. Toxicol.* **33:** 655-780

Knudsen G.A., Sanders J.M., Sadik A.M., *et al.* (2014). Disposition and kinetics of tetrabromobisphenol A in female Wistar Han rats. *Toxicol. Rep.* **1:** 214-233

Knudsen G.A., Hughes M.F., McIntosh K.L., *et al.* (2015). Estimation of Tetrabromobisphenol A (TBBPA) percutaneous uptake in humans using the parallelogram method. *Toxicol. Appl. Pharm.* **289:** 323-329

Knudsen G.A., Hughes M.F., Sanders M., *et al.* (2016). Estimation of human percutaneous bioavailability for two novel brominated flame retardants, 2-ethylhexyl 2,3,4,5-tetrabromobenzoate (EH-TBB) and bis(2-ethylhexyl) tetrabromophthalate (BEH-TEBP). *Toxicol. Appl. Pharm.* **311:** 117-127

Kolmodin-Hedman B. & Akerblom M. (1987). Monitoring of humans for occupational exposure to herbicides. In Hutson, D.H. & Roberts T.R. (Eds.) Herbicides. John Wiley & Sons Ltd

Krieger R.I., Bernard C.E., Dinoff T.M., *et al.* (2001). Biomonitoring of persons exposed to insecticides used in residences. *Ann. Occup. Hyg.* **45:** S143-153

Krishnan A.V., Stathis P., Permuth S.F., *et al.* (1993). Bisphenol A: An estrogenic substance is released from polycarbonate flasks during autoclaving. *Endocrinology* **132:** 2279-2286

Kuester R.K., Solyom A.M., Rodriguez V.P., *et al.* (2007). The Effects of Dose, Route, and Repeated Dosing on the Disposition and Kinetics of Tetrabromobisphenol A in Male F-344 Rats. *Toxicol. Sci.* **96:** 237-245

Kyselova V., Peknicova J., Buckova D., *et al.* (2003). Effects of p-nonylphenol and resveratrol on body and organ weight and *in vivo* fertility of outbred CD-1 mice. *Repr. Biol. Endocrin.* **1:** 1-10

Lai D.Y., Kacew S. & Dekant W. (2015). Tetrabromobisphenol A (TBBPA): Possible modes of action of toxicity and carcinogenicity in rodents. *Food Chem. Toxicol.* **80:** 206-214

Law R.J., Covaci A., Harrad S., *et al.* (2014). Levels and trends of PBDEs and HBCDs in the global environment: status at the end of 2012. *Environ. Int.* **65:** 147-58

Lazarow P.B. & De Duve C. (1976). A fatty acyl-CoA oxidizing system in rat liver peroxisomes; enhancement by clofibrate, a hypo-lipidemic drug. *Proc. Natl. Acad. Sci.* USA **73:** 2043-2046.

Lee H.B. & Peart T.E. (2002). Organic contaminants in Canadian municipal sewage sludge. Part I. Toxic or endocrine disrupting phenolic compounds. *Water Qual. Res.* **37:** 681-696

Lehman A.J. & Fitzhugh O.G. (1954). 100-fold margin of safety. *Assoc. Food Drug Off. U. S. Quant. Bull.* **18:** 33-35

Leo A., Hansch C. & Elkins D. (1971). Partition coefficients and their uses. *Chem. Rev.* **71:** 525-616

Levy R.H. & Moreland T.A. (1984). Rationale for monitoring free drug levels. *Clin. Pharmacokinet.* **9:** 1-9

Lilly P.D., Andersen M.E., Ross T.M., *et al.* (1998). Physiologically Based Pharmacokinetic Description of the Oral Uptake, Tissue Dosimetry, and Rates of Metabolism of Bromodichloromethane in the Male Rat. *Toxicol. Appl. Pharm.* **150:** 205-217

Lindstedt L. & Schaeffer P.J. (2002). Use of allometry in predicting anatomical and physiological parameters of mammals. *Lab Anim.* **36:** 1-19

Lipscomb J.C. & Poet T.S. (2008). *In vitro* measurements of metabolism for application in pharmacokinetic modelling. *Pharmacol. Ther.* **118:** 82 - 103

Loizou G., Spendiff M., Barton H.A., *et al.* (2008). Development of good modelling practice for physiologically based pharmacokinetic models for use in risk assessment: the first steps. *Regul. Toxicol. Pharm.* **50:** 400-411

Lote C.J., McVicar A.J. & Yardley C.P. (1985). Renal extraction and clearance of p-aminohippurate during saline and dextrose infusion in the rat. *J. Physiol.* **383:** 303-313

Lu A.K., Frisella M.E. & Johnson K.C. (1993). Dissolution modeling: Factors affecting the dissolution rates of polydisperse powders. *Pharm. Res.* **10:** 1308-1314

Lukacova V., Bolger M.B., Woltosz W.S., *et al.* (2011). Transporter-based *in vitro-in vivo* extrapolation (IVIVE). Simulations Plus poster, available at: http://www.eposters.net/pdfs/transporter-based-in-vitro-in-vivo-extrapolation-ivive.pdf (accessed 14.06.2015)

Lundehn J.R., Westphal D., Kieczka D., *et al.* (1992). Uniform principles for safeguarding the health of applicators of plant protection products. Mitteilungen aus der Biologischen Bundesanstalt für Land und Forstwirtschaft, Heft 277, Berlin. Available at: www.kemi.se/global/bekampningsmedel/vaxtskyddsmedel/german_model_psd2.xls

Lyons M.A., Yang R., Mayeno A.N., *et al.* (2008). Computational toxicology of chloroform: reverse dosimetry using Bayesian inference, Markov chain Monte Carlo simulation, and human biomonitoring data. *Environ. Health Perspect.* **116:** 1040-1046

Lyons M.A., Reisfield B., Yang R.S.H., *et al.* (2013). A physiologically based pharmacokinetic model of rifampicin in mice. *Antimicrob. Agents Chemother.* **57:** 1763-177

Marsili A., Zavacki A.M., Harney J.W., *et al.* (2011). Physiological role and regulation of iodothyronine deiodinases: a 2011 update. *J. Endocrinol. Invest.* **34:** 395-407

Matthews G. (2002). Operator Exposure to pesticides. *Pesticide Outlook* **6:** 233-237

McClellan R.O. (1999). Human health risk assessment: A historical overview and alternative paths forward. *Inhal. Toxicol.* **11:** 477-518

McConnell E.L., Basit A.W. & Murdan S. (2008). Measurements of rat and mouse gastrointestinal pH, fluid and lymphoid tissue, and implications for in-vivo experiments. *J. Pharm. Pharmacol.* **60:** 63-70.

McLanahan E.D., El-Masri H.A., Sweeney L.M., *et al.* (2012). Physiologically based pharmacokinetic model use in risk assessment - why being published is not enough. *Toxicol. Sci.* **126:** 5-15

Meek B., Renwick A. & Sonich-Mullin C. (2003). Practical application of kinetic data in risk assessment—an IPCS initiative. *Toxicol. Lett.* **138:** 151-160

Metropolis N., Rosenbluth A.W., Rosenbluth M.N., *et al.* (1953). Equations of state calculations by fast computing machines. *J. Chem. Phys.* **21:** 1087-1091

Mezzetti M., Ibrahim J.G., Bois F.Y., *et al.* (2003). A Bayesian compartmental model for the evaluation of 1,3-butadiene metabolism. *J. R. Stat. Soc. C* **52:** 291-305

Millburn P., Smith R.L. & Williams R.T. (1967). Biliary excretion of foreign compounds: biphenyl, stilboestrol and phenolphthalein in the rat: molecular weight, polarity and metabolism as factors in biliary excretion. *Biochem. J.* **105:** 1275 - 1281

Millburn P. (1970). Factors in the Biliary Excretion of Organic Compounds. In: Fishmen W. Editor. Metabolic conjugation and metabolic hydrolysis. New York: Academic. p. 1 - 74

Moody D.E., Reddy J.K., Lake B.G., *et al.*(1991). Peroxisome proliferation and non-genotoxic carcinogenesis: Commentary on a symposium. *Fundam. Appl. Toxicol.* **16:** 233-248

Morris S., Allchin C.R., Zegers B.N., *et al.* (2004). Distribution and Fate of HBCD and TBBPA Brominated Flame Retardants in North Sea Estuaries and Aquatic Food Webs. *Environ. Sci. Technol.* **38:** 5497-5504

Nagayama J. (2000). Comparison between brominated flame retardants and dioxins or organochlorine compounds in blood levels in Japanese adults. *Organohalogen Compounds.* **48:** 27-30

NHANES (2015). Available at: www.cdc.gov.nchs/nhanes.htm (accessed 17/06/2015)

Nigg H.N. & Wade S.E. (1992). Saliva as a Monitoring Medium for Chemicals. *Rev. Environ. Contam. Toxicol.* **129:** 95-119

Nitschke K.D., Hayes W.C., Berdasco N.M., *et al*. (1985). Dowco 453: two-generation dietary reproduction study in Sprague-Dawley rats. Unpublished report No. HET K 131381-039 (document 5.6.1/01, F04) from Dow Chemical Company, Midland, Michigan, USA.

Nolan R.J., Smith F.A., Muller C.J., *et al.* (1980). Kinetics of 14C-labeled picloram in male Fischer 344 rats. Unpublished report No. HET K 38323-22 from Dow Chemical Company, Midland, Michigan, USA.

Nolan R.J., Freshour N.L., Kastl P.E., *et al.* (1983). Picloram: Pharmacokinetics in Human Volunteers. Unpublished report No. HET K-038323-038 from Dow Chemical Company, Midland, Michigan, USA.

Nolan R.J., Campbell R.A., Tollett J.T., *et al.* (1985). DOWCO* 453: Pharmacokinetics in human volunteers following a single oral or dermal dose. Unpublished report No. HET K 131381-037 (document 5.1.5/01, H05) from Dow Chemical Company, Midland, Michigan, USA.

Nolan R.J., Dryzga M.D., Yano B.L., *et al.* (1987). Haloxyfop: Pharmacokinetics following oral administration to male Beagle dogs. Unpublished report No. HET K 131381-061 (document 5.1.3/01,H03) from Dow Chemical Company, Midland, Michigan, USA.

Nolan R.J., Campbell R.A. & Fike R.H. (1991). VERDICT* herbicide field study: quantitation of haloxyfop-methyl absorbed by individuals spraying VERDICT brand herbicide. Unpublished report No. HET M-004570-006 from Dow Chemical Company, Midland, Michigan, USA.

NTP (1993). NTP toxicology and carcinogenesis studies of polybrominated biphenyls (CAS No. 67774-32-7) (Firemaster FF-1(R)) in F344/N Rats and B6C3F1 mice (Feed Studies). *Natl. Toxicol. Program Tech. Rep. Ser.* **398:** 1-235

NTP (2014). Toxicology studies of tetrabromobisphenol A (CAS No. 79-94-7) in F344/NTac rats and B6C3F1/N mice and toxicology and carcinogenesis studies of tetrabromobisphenol A in wistar han [Crl:WI(Han)] rats and B6C3F1/N mice (gavage studies). https://ntp.niehs.nih.gov/ntp/htdocs/lt_rpts/tr587_508.pdf (Accessed April 2017).

OECD (1984). Test guideline 417: toxicokinetics. OECD guidelines for the testing of chemicals.

OECD (1995). Test No. 107: Partition Coefficient (n-octanol/water): Shake Flask Method, OECD Publishing, Paris.

OECD (2007). Test guideline 426: developmental neurotoxicity study. OECD guidelines for the testing of chemicals.

OECD (2009). OECD draft guidance document on the design and conduct of chronic toxicity and carcinogenicity studies, supporting TG 451, 452 and 453. Draft ENV/JM/TG(2009)X.

OECD (2010a). OECD guideline for the testing of chemicals. Toxicokinetics. Organisation for Economic Co-operation and Development. TG 417. p. 1-20.

OECD (2010b). Draft guidance document No. 116 on the design and conduct of chronic toxicity and carcinogenicity studies, supporting TG 451, 452 and 453. 17 December 2010. Series on Testing and Assessment. OECD, Paris.

OECD (2011a). Test Guideline 443: Extended One Generation Reproductive Toxicity Study. OECD Guidelines for the Testing of Chemicals. OECD, Paris.

OECD (2011b). Draft guidance document 151 in support of OECD test guideline 443 on an extended one generation reproductive toxicity study: November 2011. Series on Testing and Assessment. OECD, Paris.

OECD (2016). Test Guideline 422: Combined Repeated Dose Toxicity Study with the Reproduction/ Developmental Toxicity Screening Test. OECD Guidelines for the Testing of Chemicals. OECD, Paris.

Palmer C.N., Hsu M.H., Griffin K.J., *et al.* (1998). Peroxisome proliferator activated receptor-alpha expression in human liver. *Mol. Pharmacol.* **53:** 14-22

Paltiel H.J., Diamond D.A., Canzio J.D., *et al.* (2002). Testicular volume: Comparison of orchidometer and US measurements in dogs. *Radiology* **222:** 114-119

Perkins J.M. (2004). *In vitro* percutaneous absorption of [14-C] haloxyfop R methyl ester formulated as an emulsifiable concentration EF-1400 and field dilutions through rat and human skin using flow-through diffusion cells. Unpublished report No. V5456 from Dow Chemical Company, Midland, Michigan, USA.

PHED (1992). Notice of Availability of the Pesticide Handlers Exposure Database Version 1.1 through VERSAR, Inc., Arlington, VA, USA, Federal Register, 57(107), 23403–23404, June 3, Washington, DC, USA.

Phillips M.B., Sobus J.R., George B.J., *et al.* (2014). A new method for generating distributions of biomonitoring equivalents to support exposure assessment and prioritization. *Regul. Toxicol. Pharm.* **69:** 434-442

Poddalgoda D., Macey K., Jayawardene I., *et al.* (2016). Derivation of biomonitoring equivalent for inorganic tin for interpreting population-level biomonitoring data. *Regul. Toxicol. Pharm.* **81:** 430-436

Poet T.S., Weitz K.K., Gies R.A., *et al.* (2002). PBPK modelling of percutaneous absorption of perchloroethylene from a soil matrix in rats and humans. *Toxicol. Sci.* **67:** 17-31

Portier C.J. & Kaplan N.L. (1989). Variability of safe dose estimates when using complicated models of the carcinogenic process. *Fundam. Appl. Toxicol.* **13:** 533-544

Poulin P. & Theil F.P. (2000). A priori prediction of tissue:plasma partition coefficients of drugs to facilitate the use of physiologically-based pharmacokinetic models in drug discovery. *J. Pharm. Sci.* **89:** 16-35

Poulin P. & Theil F.P. (2002). Prediction of pharmacokinetics prior to *in vivo* studies. 1. Mechanism-based prediction of volume of distribution. *J. Pharm. Sci.* **91:** 129-56

PSD (1992). UK Predictive Operator Exposure Model (POEM). A Users Guide. Pesticide Safety Directorate, Ministry of Agriculture, Fisheries and Food, York.

Raftogianis R., Creveling C., Weinshilboum R., *et al.* (2000). Estrogen metabolism by conjugation. *J. Natl. Cancer Inst. Monogr.* **27:** 113-124

Rasoulpour R.J., Ellis-Hutchings R.G., Terry C., *et al.* (2012). A novel mode-of action mediated by the fetal muscle nicotinic acetylcholine receptor resulting in developmental toxicity in rats. *Toxicol. Sci.* **127:** 522-534

Renwick A.G. (1991). Safety factors and establishment of acceptable daily intake. *Food Addit. Contam.* **8:** 135-150

Renwick A.G. (1993). Data-derived safety factors for the evaluation of food additives and environmental contaminants. *Food Addit. Contam.* **10:** 275-305

Renwick A.G. & Lazarus N.R. (1998). Human variability and noncancer risk assessment - An analysis of the default uncertainty factor. *Regul. Toxicol. Pharm.* **27:** 3-20

Rhomberg L.R., Baetcke K., Blancato J., *et al.* (2007). Issues in the design and interpretation of chronic toxicity and carcinogenicity studies in rodents: approaches to dose selection. *Crit. Rev. Toxicol.* **37:** 729-837

Rigas M.L, Okino M.S. & Quackenboss J.J. (2001). Use of a pharmacokinetic model to assess chlorpyrifos exposure and dose in children, based on urinary biomarker measurements. *Toxicol. Sci.* **61:** 374-381

Rodriguez C., Noe V., Cabrero A., *et al.* (2000). Differences in the formation of PPARalpha-RXR/acoPPRE complexes between responsive and nonresponsive species upon fibrate administration. *Mol. Pharmacol.* **58:** 185-193

Saghir S.A., Mendrala A.L., Bartels M.J., *et al.* (2006). Strategies to assess systemic exposure of chemicals in subchronic/chronic diet and drinking water studies. *Toxicol. Appl. Pharm.* **211:** 245-260

Saghir S.A., Rick D.L., Clark A.J., *et al.* (2011). Integration of toxicokinetics into guideline studies of a new agrochemical. *Toxicologist* **120:** 2107

Sakai H., Kim E.Y., Petrov E.A., *et al.* (2009). Transactivation Potencies of Baikal Seal Constitutive Active/Androstane Receptor by Persistent Organic Pollutants and Brominated Flame Retardants. *Environ. Sci. Technol.* **43:** 6391-6397

Samuelsen M., Olsen C., Holme J.A., *et al.* (2001). Estrogen-like properties of brominated analogs of bisphenol A in the MCF-7 human breast cancer cell line. *Cell Biol. Toxicol.* **17:** 139-151

Schanker L.S., Shore P.A., Brodie B.B., *et al.* (1957). Absorption of Drugs from the Stomach I. The Rat. *J. Pharmacol. Exp. Ther.* **120:** 528-539.

Schauer U.M., Volkel W. & Dekant W. (2006). Toxicokinetics of tetrabromobisphenol a in humans and rats after oral administration. *Toxicol. Sci.* **91:** 49-58

Schecter A., Papke O., Tung K.C., *et al.* (2005). Polybrominated diphenyl ether flame retardants in the U.S. population: current levels, temporal trends, and comparison with dioxins, dibenzofurans, and polychlorinated biphenyls. *J. Occup. Environ. Med.* **47:** 199-211

Schecter A., Harris T.R, Shah N., *et al.* (2008). Brominated flame retardants in US food. *Mol. Nutr. Food Res*. **52:** 266-272

Scortichini B.H., Bohl R.W. & Engdahl G.W. (1987). Measurement of potential airborne and dermal exposures to haloxyfop-methyl by individuals mixing and spraying Verdict herbicide, Freehand, Michigan and Hallandale, Minnesota, July 28 and 30, August 12 and 13, 1986. Unpublished report No. HEH2.1-1-182(56) from Dow Chemical Company, Midland, Michigan, USA.

Sellström U. & Jansson B. (1995). Analysis of tetrabromobisphenol A in a product and environmental samples. *Chemosphere* **31:** 3085-3092

Shelia A.P. (2012). Physiologically-Based Pharmacokinetic (PBPK) Modeling and Simulations: Principles, Methods, and Applications in the Pharmaceutical Industry. USA: John Wiley & Sons. p. 79-83, 172-173

Simulations Plus (2013a). Advanced absorption, pharmacokinetic and pharmacodynamic simulation software. Version 8.5. Available at: http://www.simulations-plus.com/Products (accessed 01/11/2014)

Simulations Plus (2013b). Manual: Simulation Software for Drug Discovery and Development. User's manual, software version 8.5. Simulations Plus, inc. p. 147-206

Sjödin A., Carlsson H., Thuresson K., *et al.* (2001). Flame Retardants in Indoor Air at an Electronics Recycling Plant and at Other Work Environments. *Environ. Sci. Technol.* **35:** 448-454

Slikker W.Jr., Andersen M.E., Bogdanffy M.S., *et al.* (2004a). Dose-dependent transitions in mechanisms of toxicity: case studies. *Toxicol. Appl. Pharm.* **201:** 226-294

Slikker W.Jr., Andersen M.E., Bogdanffy M.S., *et al.* (2004b). Dose-dependent transitions in mechanisms of toxicity. *Toxicol. Appl. Pharm.* **201:** 203-225

Smith F.A., Hermann E.A., Dryzga M.D., *et al.* (1982). The pharmacokinetics of 14C-Dowco* 453 in Fischer 344 rats. Unpublished report No. HET K 131381-(26) (document 5.1.1/01, H01) from Dow Chemical Company, Midland, Michigan, USA.

Smith F.A., Kropscott B.E. & Kastl P.E. (1984). The pharmacokinetics of DOWCO* 453 in the B6C3F1 mouse. Unpublished report No. HET K 131381-(26) (document 5.1.2/01, H02) from Dow Chemical Company, Midland, Michigan, USA.

Smith J.H., Birchall A., Etherington G., *et al.* (2014). A revised model for the deposition and clearance of inhaled particles in human extra-thoracic airways. *Radiat. Prot. Dosim.* **158:** 135-47

Snipes R.L. (1997). Intestinal absorptive surface in mammals of different sizes. *Adv. Anat. Embryol. Cell Biol.* **138:** 1-90

Söderström G. & Marklund S. (1999). Fire of a flame retarded TV. *Organohalogen Compounds* **41:** 469-472

Sohn M.D., McKone T.E & Blancato J.N. (2004). Reconstructing population exposures from dose biomarkers: inhalation of trichloroethylene (TCE) as a case study. *J. Expo. Anal. Env. Epid.* **14:** 204-213

Stapleton H.M., Klosterhaus S., Eagle S., *et al.* (2009). Detection of organophosphate flame retardants in furniture foam and U.S. house dist. *Environ. Sci. Technol.* **43:** 7490-7495

Stapleton H.M., Klosterhaus S., Keller A., *et al.* (2011). Identification of flame retardants in polyurethane foam collected from baby products. *Environ. Sci. Technol.* **45:** 5323-5331

Stoltenberg D.E., Gronwald J.W., Wyse D.L., *et al.* (1989). Effect of sethoxydim and haloxyfop on acetyl-coenzyme A carboxylase activity in Festuca species. *Weed Sci.* **37:** 512-516

Stuart H., Ibarra C., Abdallah M., *et al.* (2008). Concentrations of brominated flame retardants in dust from United Kingdom cars, homes and offices: causes of variability and implications for human exposure. *Environ. Int.* **34:** 1170-1175

Tan Y.M., Liao K.H. & Clewell H.J. (2007). Reverse dosimetry: interpreting trihalomethanes biomonitoring data using physiologically based pharmacokinetic modeling. *J. Expo. Sci. Environ. Epidemiol.* **17:** 591-603

Tanner G.A. & Isenberg M.T. (1970). Secretion of p-aminohippurate by rat kidney proximal tubules. *Am. J. Physiol.* **219:** 889-892

Tardif R., Charest-Tardif G., Brodeur J., *et al.* (1997). Physiologically based pharmacokinetic modelling of a ternary mixture of alkyl benzenes in rats and humans. *Toxicol. Appl. Pharm.* **144:** 120-134

Teeguarden J.G. & Barton H.A. (2004). Computational modeling of serum-binding proteins and clearance in extrapolations across life stages and species for endocrine active compounds. *Risk Anal.* **24:** 751-770

Terry C., Hays S., McCoy A.T., *et al.* (2016). Implementing a framework for integrating toxicokinetics into human health risk assessment for agrochemicals. *Regul. Toxicol. Pharm.* **75:** 89-104

Thomas R.S., Yang R.S.H., Morgan D.G., *et al.* (1996). PBPK modeling/ Monte Carlo simulation of methylene chloride kinetic changes in mice in relation to age and acute, subchronic, and chronic inhalation exposure. *Environ. Health Perspect.* **104:** 858-865

Thomsen C., Lundanes E. & Becher G. (2001). Brominated flame retardants in plasma samples from three different occupational groups in Norway. *J. Environ. Monit.* **3:** 366-370

Thomsen C., Lundanes E. & Becher G. (2002). Brominated Flame Retardants in Archived Serum Samples from Norway: A Study on Temporal Trends and the Role of Age. *Environ. Sci. Technol.* **36:** 1414-1418

Thomsen C., Liane V.H. & Becher G. (2007). Automated solid-phase extraction for the determination of polybrominated diphenyl ethers and polychlorinated biphenyls in serum—application on archived Norwegian samples from 1977 to 2003. *J. Chromatogr. B* **846:** 252-263

Thornhill E.W., Matthews G.A. & Clayton J.S. (1996). Potential operator exposure to insecticides: a comparison between knapsack and CDA spinning disc sprayers. Proceedings of the Brighton Conference. **3:** 1175-1180

Tollett J.T., Yano B.L., Campbell R.A., *et al.* (1983). Dowco 453 acid: results of a 6-month and 1-year interim sacrifice of a 2-year dietary chronic toxicity-oncogenicity study in CDF Fischer 344 rats. Unpublished report No. HET K 131381-(18a) (document 5.5.1/01, I03) from Dow Chemical Company, Midland, Michigan, USA.

Tollett J.T., Yano B.L., Cieszlak F.S., *et al.* (1985). Dowco 453: 2-year dietary chronic toxicity oncogenicity study in B6C3F1 mice. Unpublished report No. HET K 131381-(26) (document 5.5.2/01,I02) from Dow Chemical Company, Midland, Michigan, USA.

Tugwood J.D., Holden P.R., James N.H., *et al.* (1998). A PPAR alpha cDNA cloned from guinea pig liver encodes a protein with similar properties to the mouse PPAR alpha: Implications for species differences in response to peroxisome proliferators. *Arch. Toxicol.* **72:** 169- 177

Tyagi S., Gupta P., Saini A.S., *et al.* (2011). The peroxisome proliferator-activated receptor: A family of nuclear receptors role in various diseases. *J. Adv. Techno. Res.* **2:** 236-240

U.S. EPA (1992). Worker Protection Standard (Final Rule), Federal Register, 57(163), 38102-38166, August 21, Washington, DC, USA.

U.S. EPA (1995). Reregistration Eligibility Decision (RED): Picloram. Washington, D.C.

U.S. EPA (1998). Reregistration Eligibility Decision (RED): Triclopyr. Washington, D.C.

U.S. EPA (2002). Children's total exposure to persistent pesticides and other persistent organic pollutants (CTEPP). US Environmental Protection Agency, National Exposure Research Laboratory, Research Triangle Park, NC.

U.S. EPA (2011). Glossary. Available at: http://ofmpub.epa.gov/sor_internet/registry/termreg/searchandretrieve/glossariesandkeywordlists/search.do?details=&glossaryName=IRIS%20Glossary (accessed 30.04.2015)

U.S. EPA (2017). PROcEED. Available at: https://www.epa.gov/chemical-research/probabilistic-reverse-dosimetry-estimating-exposure-distribution-proceed (accessed 16/10/2017)

U.S. EPA (2018). Search for Registered Pesticide Products. Available at: https://www.epa.gov/safepestcontrol/search-registered-pesticide-products (accessed 11/05/2018)

U.S. OSHA (1994). Permissible Exposure Limits for Air Contaminants, U.S. Department of Labor, Washington, D.C. Available at: https://www.osha.gov/pls/oshaweb/owadisp.show_document?p_table=standards&p_id=9992 (accessed 30.04.2015)

Van Hemmen J.J. (1992). Agricultural pesticide exposure data bases for risk assessment. *Rev. Environ. Contam. T.* **126:** 1-85

Van Hemmen J.J. (1998). Pesticide worker exposure assessment for registration purposes. *Occupational Hygiene* **4:** 243-257

Walgren J.E., Kurtz D.T. & McMillan J.M. (2000). Expression of PPAR (alpha) in human hepatocytes and activation by trichloroacetate and dichloroacetate. *Res. Commun. Mol. Pathol. Pharmacol.* **108:** 116-132

Wang W., Abualnaja K.O., Asimakopoulos A.G., *et al.* (2015). A comparative assessment of human exposure to tetrabromobisphenol A and eight bisphenols including bisphenol A via indoor dust ingestion in twelve countries. *Environ. Int.* **83:** 183-191

Wang X., Santostefano M.J., DeVito M.J., *et al.* (2000). Extrapolation of a PBPK model for dioxins across dosage regimen, gender, strain, and species. *Toxicol. Sci.* **56:** 49-60

Ward R.C., Travis C.C., Hetrick D.M., *et al.* (1988). Pharmacokinetics of tetrachloroethylene. *Toxicol. Appl. Pharm.* **93:** 108-117

Watanabe I., Kashimoto T. & Tatsukawa R. (1983). Identification of the flame retardant tetrabromobisphenol-A in the river sediment and the mussel collected in Osaka. *Bull. Environ. Contam. Toxicol.* **31:** 48-52

Watanabe K.H. & Bois F.Y. (1996). Interspecies Extrapolation of Physiological Pharmacokinetic Parameter Distributions. *Risk Anal.* **16:** 741-754

Wedagedera J.R., Abduljalil K., Cain T., *et al*. (2015). Towards more Realistic Clinical Trial Simulation: Establishing Inter-Correlations between Several Cytochrome P450 Enzyme Abundances in Human Liver. Cetara poster, available at: https://www.certara.com/wp-content/uploads/Resources/Posters/Wedagedera_2015_PAGE_CYP450.pdf (accessed 31/10/2017)

Weijs L., Covaci A., Yang R., *et al.* (2012). Computational toxicology: Physiologically based pharmacokinetic models (PBPK) for lifetime exposure and bioaccumulation of polybrominated diphenyl ethers (PBDEs) in marine mammals. *Environ. Pollut.* **163:** 134-141

West G.B., Woodruff W.H. & Brown J.H. (2002). Allometric scaling of metabolic rate from molecules and mitochondria to cells and mammals. *Proc. Natl. Acad. Sci. U.S.A.* **99:** 2473-2478

WHO (2005). Harmonization Project Document No. 2: Chemical-specific adjustment factors for interspecies differences and human variability: guidance document for use on data in dose/ concentration-response assessment.

Wikoff D., Thompson C., Perry C., *et al.* (2014). Development of toxicity values and exposure estimates for tetrabromobisphenol A: application in a margin of exposure assessment. *J. Appl. Toxicol.* **35:** 1292-1308

Wilson J.P. (1967). Surface area of the small intestine in man. *Gut* **8:** 618-21

Wilson T.M., Brown P.J., Sternbach D.D., *et al.* (2000). The PPARs from orphan receptors to drug discovery. *J. Med. Chem.* **43:** 527-550

Wolfe H.R. (1976). Field exposure to airborne pesticides. In: Air Pollution from Pesticides and Agricultural Processes, Lee R.E., ed., pp. 137-161. CRC Press, Boca Raton, FL.

Yang P. & Pursch M. (2015). Hydrophilic interaction liquid chromatography for the separation of acidic agricultural compounds. *J. Sep. Sci.* **1:** 1-7

Yang Y., Xu X. & Georgopoulos P.G. (2010). A Bayesian population PBPK model for multiroute chloroform exposure. *J. Expo. Sci. Env. Epid.* **20:** 326-341

Yano B.L., Campbell R.A. & Tollett J.T. (1984). Dowco 453: 2-year dietary chronic toxicity-oncogenicity study in CDF Fischer 344 rats. Unpublished report No. HET K 131381-(18b) (document 5.5.2/01, I01) from Dow Chemical Company, Midland, Michigan, USA.

Yano B.L., Marler R.J., Sorrells R.M., *et al.* (1987). Haloxyfop: 13-week oral toxicity study in Cynomolgus monkeys. Unpublished report No. HET K 131381-058 (T-1242) (document 5.3.2.4/01 & 5.8.2.1.2/06, D11) from Dow Chemical Company, Midland, Michigan, USA.

Ylinen M., Kojo A., Hanhijarvi H., *et al.* (1990). Disposition of perfluorooctanoic acid in the rat after single and subchronic administration. *Bull. Environ. Contam. Toxicol.* **44:** 46-53

Zakeri-Milani P., Valizadeh H., Tajerzadeh H., *et al.* (2007). Predicting human intestinal permeability using single-pass intestinal perfusion in rat. *J. Pharm. Pharmaceut. Sci.* **10:** 373

Zalko D., Prouillac C., Riu A., *et al.* (2006). Biotransformation of the flame retardant tetrabromo-bisphenol A by human and rat sub-cellular liver fractions. *Chemosphere* **64:** 318-327

Appendix 1: Model equations

Equations 1-10, 13, 19, 23-28, 31, 34, 39, 42-43 and 49-52 reproduced with permission of the rights holder, Simulations Plus Inc.

Perfusion-limited tissue model

Equation [1] describes the rate of change in the amount of chemical across a tissue described as perfusion-limited. V_{tis} x dCt_{tis}/dt gives quantity in the tissue over time, which is calculated as the rate entering the tissue in blood (F_{tis} x C_{art}) minus the rate leaving, F_{tis} x ((Ct_{tis} x Rbp) / Kp_{tis}) (i.e. the concentration at the venous end of the tissue), and the rate of metabolism (terms RHS). As Kp (the tissue partition coefficient) increases, the rate leaving the tissue decreases as more chemical accumulates in the tissue. The term Rbp (blood/ plasma concentration ratio) is used to convert the plasma concentration to blood concentration by correcting for binding to erythrocytes. C_{art} and Ct_{tis} are calculated iteratively and their values from the previous iteration are used to solve [1]. The rate of metabolism includes $f_{ut,tis}$ (fraction unbound in tissue) as it is assumed only the unbound chemical fraction is metabolised. Linear Michaelis-Menten enzyme kinetics are used, as it assumed environmental exposure levels elicit sub-Km tissue doses. Furthermore, the rate of metabolism is treated as a summation (sigma) of all parallel metabolic pathways. Appendix 2 contains a glossary of terms.

$$V_{tis}\ x\ \frac{dCt_{tis}}{dt} = F_{tis}\left(C_{art} - \frac{Ct_{tis}\ x\ R_{bp}}{Kp_{tis}}\right) - \sum^{nEnz}\left[\frac{V_{\max_w_tis_e}\ x\ Ct_{tis}\ x\ f_{ut,tis}}{K_{m_tis_e}\ +\ \left(Ct_{tis}\ x\ f_{ut,tis}\right)}\right] \quad [1]$$

Equation [2] is used to calculate the V_{max} of tissue enzyme scaled to the whole tissue.

$$V_{\max_w_tis_e} = V_max_tis_e\ x\ Enz_exp_tis_e\ x\ D_tis\ x\ V_tis \quad [2]$$

Equation [3] is Poulin & Theil's homogenous method for calculating Kps (Poulin & Theil 2000), which assumes passive diffusion of the chemical into tissue and instantaneously distributes homogenously within. The equation considers the tissue as a mixture of lipids, water and proteins at tissue physiological pH (7.4) which bind the chemical.

$$Kp_{tis} = \frac{\left[K_{tis}\ x\ \left(V_{nlt} + 0.3V_{pht}\right)\right] + \left(V_{wt}\ x\ 0.7V_{pht}\right)}{\left[K_{tis}\ x\ \left(V_{nlp} + 0.3V_{php}\right)\right] + \left(V_{wp}\ x\ 0.7V_{php}\right)}\ x\ \frac{f_{up,adj}}{f_{ut,tis}} \quad [3]$$

Equation [4] is used to obtain the partition coefficient (K_{tis}) from its log value (logP_tis)

$$K_{tis} = 10^{logP_tis} \quad [4]$$

Equation [5] is the Poulin equation used to calculate fraction unbound in tissue ($f_{ut,tis}$) (Poulin & Theil 2002).

$$f_{ut,tis} = \frac{1}{1 + \left[\frac{(1 - f_{up,adj})}{f_{up,adj}}\ x\ RAtp_{tis}\right]} \quad [5]$$

GastroPlus (Simulations Plus 2013b) derived equation [6]. It calculates $f_{up,adj}$, i.e. the fraction unbound in plasma adjusted for binding to plasma lipids. This is particularly relevant to BFRs which are anticipated to bind plasma lipids due to high lipophilicity. It is assumed that during rapid equilibrium dialysis, experimental

f_{up} ($f_{up,exp}$) is a measure of chemical binding only to plasma albumin (Section 4.82), however binding to plasma lipids is also potentially possible. It is also assumed that logP_pla is a measure of chemical partitioning into plasma lipids.

$$f_{up,adj} = \frac{1}{\left[10^{logP_pla} x \left(\frac{V_{nlp} + V_{php}}{V_{wp}}\right)\right] + 1 + \frac{(1 - f_{up,exp})}{f_{up,exp}}} \quad [6]$$

Perfusion-limited adipose

Equation [7] is used to convert the octanol/ water partition coefficient to the vegetable oil/ water partition coefficient (Poulin & Theil 2002). Equations involving logP_adi are subsequently calculated as described above.

$$logP_adi = (1.115\ x\ logP_tis) - 1.35 \quad [7]$$

$$K_{adi} = 10^{logP_adi} \quad [8]$$

$$f_{ut,adi} = \frac{1}{1 + \left[\frac{(1 - f_{up,adj})}{f_{up,adj}}\ x\ RAtp_{adi}\right]} \quad [9]$$

$$Kp_{adi} = \frac{\left[K_{adi}\ x\ (V_{nlt} + 0.3V_{pht})\right] + (V_{wt}\ x\ 0.7V_{pht})}{\left[K_{adi}\ x\ (V_{nlp} + 0.3V_{php})\right] + (V_{wp}\ x\ 0.7V_{php})}\ x\ \frac{f_{up,adj}}{f_{ut,adi}} \quad [10]$$

Perfusion-limited kidney

The perfusion-limited kidney extends the tissue model in several ways. The rate of chemical entering the kidney vascular space decreases given glomerular filtration (GFR) into kidney tubule, as it is assumed only protein-unbound chemical undergoes ultrafiltration. Hence, C_{art} is multiplied with $f_{up,exp}$ (instead of $f_{up,adj}$) as it is assumed that chemical bound to plasma lipids can enter kidney tubule via ultrafiltration (equation 6). The chemical can also enter kidney tubule via passive diffusion and/ or active transport across the kidney apical membrane, which interfaces kidney cells with kidney tubule. Fick's first law of passive diffusion is implemented, where the rate of diffusion is dependent on the concentration difference across the membrane multiplied by the membrane's permeability ($PStc_{kid,api}$). It is assumed only the unbound chemical can passively diffuse across the membrane, and is the only substrate for transporters therein. Equation 12 currently depicts an efflux transporter, although can be expanded to include influx transporters if necessary. The rate of active transport shares the same first-order kinetics with enzymes (equation 11).

$$V_{kid}\ x\ \frac{dCt_{kid}}{dt} = F_{kid}\left(C_{art} - \frac{Ct_{kid}\ x\ R_{bp}}{Kp_{kid}}\right) - perm_kid_api - \sum^{nEnz}\left[\frac{V_{\max_w_kid_e}\ x\ Ct_{kid}\ x\ f_{ut,tis}}{K_{m_kid_e} + (Ct_{kid}\ x\ f_{ut,tis})}\right] \quad [11]$$

$$perm_kid_api = PStc_{kid,api}\left(Ct_{kid,u} - C_{tub,u}\right) + \sum^{nTra}\left[\frac{V_{\max_w_kid_api}\ x\ Ct_{kid}\ x\ f_{ut,tis}}{K_{m_kid_api} + \left(Ct_{kid}\ x\ f_{ut,tis}\right)}\right] \quad [12]$$

$$V_{\max_w_kid_api} = V_max_kid_api\ x\ Tra_exp_kid_api\ x\ D_kid\ x\ V_kid \quad [13]$$

Equation [14] illustrates that unbound concentration in the kidney tubule is the product of total concentration and fraction unbound therein.

$$C_{tub,u} = C_{tub}\ x\ f_{utub} \quad [14]$$

Assuming f_{utub}= 1 due to protein absence therein, $C_{tub,u}$ (from equation 11) becomes C_{tub}:

$$perm_kid_api = PStc_{kid,api}x\ \left(\left(Ct_{kid}x\ f_{ut,tis}\right) - C_{tub}\right) + \sum^{nTra}\left[\frac{V_{\max_w_kid_api}\ x\ Ct_{kid}\ x\ f_{ut,tis}}{K_{m_kid_api} + \left(Ct_{kid}\ x\ f_{ut,tis}\right)}\right] \quad [15]$$

Equation 16 shows the quantity of chemical in kidney tubule over time is the rate entering (i.e. equation 15) minus the rate leaving, i.e. the urine flow rate (QUR).

$$V_{tub}\ x\ \frac{dC_{tub}}{dt} = perm_kid_{api} + \left(GFR\ x\ fup_{exp}x\ C_{art}\right) - \left(QUR\ x\ Q_{tub}\right) \quad [16]$$

Hence the cumulative amount excreted in urine is given as:

$$dt(Q_{uri}) = QUR\ x\ Q_{tub} \quad [17]$$

<u>Perfusion-limited liver</u>

The perfusion-limited liver extends the tissue model in several ways. There are three modelled routes of chemical entry to the liver vascular space: hepatic artery, splenic vein and 'gut blood' (equation 18). The chemical can be metabolised inside hepatocytes. A compartment for bile canaliculi is modelled, and the chemical can enter via passive diffusion and/ or active transport across the liver apical membrane interfacing hepatocytes with canaliculi. Currently an efflux transporter is modelled (equation 20).

$$V_{liv}\ x\ \frac{dCt_{liv}}{dt} = \left(F_{gut}\ x\ Ct_gut_blo\right) + \left(F_{hep}\ x\ C_{art}\right) + \left(F_{spl}\ x\ C_{spl_v}\right) + F_{liv}\left(C_{art} - \frac{Ct_{liv}\ x\ R_{bp}}{Kp_{liv}}\right) - perm_liv_api - \sum^{nEnz}\left[\frac{V_{\max_w_liv_e}\ x\ Ct_{liv}\ x\ f_{ut,tis}}{K_{m_liv_e} + \left(Ct_{liv}\ x\ f_{ut,tis}\right)}\right] \quad [18]$$

Equation [19] gives quantity metabolised in hepatocytes over time.

$$dt(Q_liv_met) = \sum^{nEnz}\left[\frac{V_{max_w_liv_e}\ x\ Ct_{liv}\ x\ f_{ut,tis}}{K_{m_liv_e} + \left(Ct_{liv}\ x\ f_{ut,tis}\right)}\right] \quad [19]$$

$$perm_liv_api = PStc_{liv,api}\left(Ct_{liv,u} - Ct_{can,u}\right) + \sum^{nTra}\left[\frac{V_{\max_w_liv_api}\ x\ Ct_{liv}\ x\ f_{ut,tis}}{K_{m_liv_api}\ +\ \left(Ct_{liv}\ x\ f_{ut,tis}\right)}\right] \quad [20]$$

$$Ct_{can,u} = Ct_{can}\ x\ f_{ub} \quad [21]$$

Assuming f_{ub}= 0 due to binding bile salts, then $Ct_{can,u}$ becomes zero (i.e. no passive diffusion from canaliculi to hepatocytes):

$$perm_liv_api = \left(PStc_{liv,api}\ x\ Ct_{liv} x\ f_{ut}\right) + \sum^{nTra}\left[\frac{V_{\max_w_liv_api}\ x\ Ct_{liv}\ x\ f_{ut,tis}}{K_{m_liv_api}\ +\ \left(Ct_{liv}\ x\ f_{ut,tis}\right)}\right] \quad [22]$$

Equation [23] gives the quantity excreted in bile over time. Because rats have no gall bladder a continuous bile flow to the duodenum is modelled, where it appears instantaneously (equation 45), i.e. a bile flow rate is not used.

$$dt(Q_{bile})\ = perm_liv_api \quad [23]$$

Alternatively the amount entering bile can be specified as a fraction (F_{bcl}) of that metabolised inside hepatocytes:

$$dt(Q_{bile}) = F_{bcl}\ x\ \sum^{nEnz}\left[\frac{V_{max_w_liv_e}\ x\ Ct_{liv}\ x\ f_{ut,tis}}{K_{m_liv_e}\ +\ \left(Ct_{liv}\ x\ f_{ut,tis}\right)}\right] \quad [24]$$

<u>Permeability-limited tissue model</u>

Equation [25] describes the rate of change in the amount of chemical across a tissue described as permeability-limited. In contrast to perfusion-limited tissues, chemical distribution throughout the tissue (i.e. extracellular and intracellular spaces) is not instantaneous because permeation through the basolateral membrane is relatively slow. The LHS terms give the total quantity across both the vascular and extracellular spaces of the tissue. Thus the rate entering this 'combined' compartment is given as F_{tis} x C_{art}, and the rate leaving is given as F_{tis} x ((C_{e_tis} x Rbp) / Kp_{tis})) in addition to perm_tis_bas, i.e. permeability through the tissue basolateral membrane which interfaces extracellular with intracellular spaces.

$$\left(V_{tis_e} + V_{tis_v}\ \frac{R_{bp}}{Kp_{tis}}\right)\ x\ \ \frac{dC_{e_tis}}{dt} = F_{tis}\ \left(C_{art} - \frac{C_{e_tis}\ x\ R_{bp}}{Kp_{tis}}\right) - perm_tis_bas \quad [25]$$

$$perm_tis_bas = PStc_{tis,bas}\ x\ ((C_{e_{tis}}\ x\ fup_adj_tis_e)\ -\ (C_{i_tis}\ x\ f_{ut,tis})) \quad [26]$$

Equation [27] calculates the intracellular concentration in terms of amount entering via passive diffusion minus the rate of metabolism occurring therein.

$$V_{tis_i}\ x\ \frac{dC_{i_tis}}{dt} = perm_tis_bas\ -\ \sum^{nEnz}\left[\frac{V_{\max_w_tis_e}\ x\ C_{i_tis}\ x\ f_{ut,tis}}{K_{m_tis_e}\ +\ \left(C_{i_tis}\ x\ f_{ut,tis}\right)}\right] \quad [27]$$

Equation [28] is Poulin & Theil's extracellular method for calculating Kps (Poulin & Theil 2000). Kp is calculated as adjusted fraction unbound in plasma ($f_{up,adj}$) over fraction unbound in tissue ($f_{ut,tis}$) - both of which are calculated as for perfusion-limited tissues.

$$Kp_{tis} = \frac{f_{up,adj}}{f_{ut,tis}}\ ;\quad N.b.\ \ Kp_{adi} = \frac{f_{up,adj}}{f_{ut,adi}} \quad [28]$$

Equation [29] calculates the adjusted fraction unbound in tissue extracellular space (f_{up,adj,tis_e}) used in equation [26].

$$f_{up,adj,tis_e} = \frac{f_{up,adj}}{Kp_{tis}} \quad [29]$$

The permeability-surface area product of tissue basolateral membrane ($PStc_{tis,bas}$) is calculated by scaling PStc according to the tissue's volume and the fraction of membrane which is basolateral (F_bm_tis). The remaining portion is the apical membrane. F_bm_tis is assumed to equal 1 for all tissues except kidney and liver where values of 0.500 and 0.667 are assumed, respectively.

$$PStc_{tis,bas} = PStc \; x \; F_bm_tis \; x \; V_{tis_i} \; ; \quad N.b. \quad PStc_{tis,api} = PStc \; x \; (1 - F_bm_tis) \; x \; V_{tis_i} \quad [30]$$

Permeability-limited kidney

The kidneys (and liver) are treated as special cases as the permeability through the apical membrane is modelled in addition to basolateral membrane permeability. Subsequently, the amount within the intracellular compartment is described in terms of movement across both apical and basolateral membranes (equation 32). Once inside kidney tubule, same processes operate as for perfusion-limited kidney (equations 35 - 36).

$$\left(V_{kid_e} + V_{kid_v} \frac{R_{bp}}{Kp_{kid}}\right) x \; \frac{dC_{e_kid}}{dt} = F_{kid} \left(C_{art} - \frac{C_{e_kid} \; x \; R_{bp}}{Kp_{kid}}\right) - perm_kid_bas \quad [31]$$

$$V_{kid_i} \; x \; \frac{dC_{i_kid}}{dt} = perm_kid_bas - \; perm_kid_api - \sum^{nEnz} \left[\frac{V_{\max_w_kid_e} \; x \; C_{i_kid} \; x \; f_{ut,tis}}{K_{m_kid_e} \; + \; \left(C_{i_kid} \; x \; f_{ut,tis}\right)}\right] \quad [32]$$

$$perm_kid_bas = \; PStc_{kid,bas} \; x \; \left(\left(C_{e_kid} \; x \; f_{up_adj_kid_e}\right) - \; \left(C_{i_kid} \; x \; f_{ut,tis}\right)\right) + \sum^{nTra} \left[\frac{V_{max_w_kid_bas} \; x \; C_{e_kid} \; x \; f_{up_adj_kid_e}}{K_{m_kid_bas} \; + \; \left(C_{e_kid} \; x \; f_{up_adj_kid_e}\right)}\right] \quad [33]$$

$$perm_kid_api \; = \; PStc_{kid,api} \; x \; ((Ci_kid \; x \; f_{ut,tis}) \; - \; C_tub)) + \sum^{nTra} \left[\frac{V_{max_w_kid_api} \; x \; C_{i_kid} \; x \; f_{ut,tis}}{K_{m_kid_api} \; + \; \left(C_{i_kid} \; x \; f_{ut,tis}\right)}\right] \quad [34]$$

$$V_{tub} \; x \; \frac{dC_{tub}}{dt} = \; perm_{kid,api} \; + \; (GFR \; x \; f_{up,exp} \; x \; C_art) - \; (QUR \; x \; Q_{tub}) \quad [35]$$

$$dt(Q_uri) \; = \; QUR \; x \; Q_{tub} \quad [36]$$

Permeability-limited liver

Equations 37-43 illustrate aforementioned concepts which are applied to the liver.

$$\left(V_{liv_e} + V_{liv_v}\,\frac{R_{bp}}{Kp_{liv}}\right) x\ \frac{dC_{e_liv}}{dt} = (F_{gut}\ x\ Ct_gut_blo) +\ (F_{hep}\ x\ C_{art}) +\ (F_{spl}\ x\ C_{spl_v}) + F_{liv}\ \left(C_{art} - \frac{C_{e_liv}\ x\ R_{bp}}{Kp_{liv}}\right) - perm_liv_bas \quad [37]$$

$$V_{liv_i}\ x\ \frac{dC_{i_liv}}{dt} = perm_liv_bas - perm_liv_api - \sum^{nEnz}\left[\frac{V_{\max_w_liv_e}\ x\ C_{i_liv}\ x\ f_{ut,tis}}{K_{m_liv_e} +\ \left(C_{i_liv}\ x\ f_{ut,tis}\right)}\right] \quad [38]$$

$$dt(Q_liv_met) =\ \sum^{nEnz}\left[\frac{V_{max_w_liv_e}\ x\ C_{i_liv}\ x\ f_{ut,tis}}{K_{m_liv_e} +\ \left(C_{i_liv}\ x\ f_{ut,tis}\right)}\right] \quad [39]$$

$$perm_liv_bas =\ PStc_{liv,bas}\ x\ \left(\left(C_{e_liv}\ x\ f_{up_adj_liv}\right) - \left(C_{i_liv}\ x\ f_{ut,tis}\right)\right) +\ \sum^{nTra}\left[\frac{V_{max_w_liv_bas}\ x\ C_{e_liv}\ x\ f_{up_adj_liv_e}}{K_{m_liv_bas} +\ \left(C_{e_liv}\ x\ f_{up_adj_liv_e}\right)}\right] \quad [40]$$

$$perm_liv_api =\ \left(PStc_{liv,api}\ x\ C_{i_liv} x\ f_{ut,tis}\right) +\ \sum^{nTra}\left[\frac{V_{max_w_liv_api}\ x\ C_{i_liv}\ x\ f_{ut,tis}}{K_{m_liv_api} +\ \left(C_{i_liv}\ x\ f_{ut,tis}\right)}\right] \quad [41]$$

$$dt(Q_{bile}) =\ perm_liv_api \quad [42]$$

$$dt(Q_{bile}) =\ F_{bcl}\ x\ \sum^{nEnz}\left[\frac{V_{max_w_liv_e}\ x\ C_{i_liv}\ x\ f_{ut,tis}}{K_{m_liv_e} +\ \left(C_{i_liv}\ x\ f_{ut,tis}\right)}\right] \quad [43]$$

Gastro-intestinal tract (GIT) model

For simplicity, a selection of key equations is described for the GIT model.

Duodenum

Equation [44] calculates the quantity within duodenum lumen as the incoming transit rate from the stomach (Kt_s x Q_sto_{und}) minus the outgoing duodenum transit rate (Kt_{duo} x Q_duo_{und}) and dissolution rate (DR_{duo}). This equation is used for ingestion of solid matter which dissolves before absorption into 'gut blood'. The dissolved portion enters an identical duodenum lumen compartment specifically for dissolved material. Equation adapted from Shelia 2012.

$$V_{duo,lum}\ x\ \frac{dC_duo_{und}}{dt} = (Kt_s\ x\ Q_sto_{und})\ -\ DR_{duo} -\ (Kt_{duo}\ x\ Q_duo_{und}) \quad [44]$$

Equation [45] shows the amount in the duodenum dissolved compartment has multiple routes of chemical entry including Q_{bile} x EHC. Q_{bile} is calculated in equations 23 and 42. Enterohepatic circulation (EHC) can be set to 1 ('on') or 0 ('off') depending on, e.g. whether *in vivo* evidence for EHC is available. Permeability

across the enterocyte apical membrane (which interfaces with duodenum lumen) is modelled (perm_duo_api) in terms of passive diffusion and active (efflux) transport (equation 47). Equation adapted from Shelia 2012.

$$V_{duo,lum}\ x\ \frac{dC_duo_{dis}}{dt} = (Kt_s\ x\ Q_sto_{dis})\ + DR_{duo} + (Q_{bile}\ x\ EHC) - (Kt_{duo}\ x\ Q_duo_{dis}) - perm_duo_api \quad [45]$$

Equation [46] calculates the amount in duodenum enterocytes as the difference between apical and basolateral permeabilities. The basolateral membrane interfaces enterocyte with 'gut blood' compartment.

$$V_{ent_duo}\ x\ \frac{dC_ent_duo}{dt} = perm_duo_api\ -\ perm_duo_bas \quad [46]$$

$$perm_duo_api\ =\ Ka_{duo}\ x\ V_{duo,lum}\ x\ \left(C_duo_{dis} -\ \left(C_ent_duo\ x\ f_{ut,tis}\right)\right) - \sum^{nTra}\left[\frac{V_{max_w_duo_api}\ x\ C_ent_duo\ x\ f_{ut,tis}}{K_{m_duo_api}\ +\ \left(C_ent_duo\ x\ f_{ut,tis}\right)}\right] \quad [47]$$

Equation [48] calculates the permeability across the duodenum enterocyte basolateral membrane, which is currently described in terms of passive diffusion. Ka_e_{duo} is calculated in equation [56].

$$perm_duo_bas\ =\ Ka_e_{duo}\ x\ V_{ent_duo}\ x\ (C_ent_duo\ -\ (Ct_gut_blo\ x\ fup_adj)) \quad [48]$$

Equation [49] calculates the dissolution rate using the Johnson model (Lu *et al.* 1993). Dissolution rates specific to each gut compartment are calculated.

$$DR_{duo} = \frac{Deff}{\rho\ x\ h\ x\ r}\ x\ \left[\frac{(1+2S)}{S}\right]\ x\ (Cs\ -\ C_duo_{dis})\ x\ Q_duo_{und} \quad [49]$$

Absorption into enterocytes

In equation [50], the surface area to volume ratio of the duodenum lumen ($SA{:}V_{duo,lum}$) is calculated by considering the shape of the gut as a cylinder. Hence surface area (2 x π x radius x length) and volume (π x radius^2 x length) are calculated which simplifies:

$$SA{:}\,V_{duo,lum} = \frac{2\ x\ \pi\ x\ R_{duo,lum}\ x\ L_{duo}}{\pi\ x\ {R_{duo,lum}}^2\ x\ L_{duo}} = \frac{2}{R_{duo,lum}} \quad [50]$$

Subsequently, in equation [51], the oral absorption constant for duodenum (Ka_{duo}) is calculated and used in equation [47]. As indicated $SA{:}V_{duo,lum}$, endothelial gut wall permeability (Peff) and surface area enhancement factor for duodenum (SEF_duo) are used to calculate Ka_{duo}. SEF_duo is used to account for changes in the surface area along the enterocyte apical membrane (e.g. due to microvilli and intestinal folds) and pH, thus is unitless. This relationship is known as the 'Theoretical SA/V Model' in GastroPlus.

$$Ka_{duo}\ =\ \frac{2}{R_{duo,lum}}\ x\ Peff\ x\ SEF_duo \quad [51]$$

Absorption into gut blood

To calculate the absorption constant between enterocyte and 'gut blood' compartment (Ka_e_{duo}), the outer surface area of the gut compartment is calculated:

$$SA_{duo} = 2\ x\ \pi\ x\ R_{duo,lum}\ x\ L_{duo} \quad [52]$$

With individual gut lumen and enterocyte volumes, it is necessary to recalculate the total radius (R):

$$Vol_{duo} = V_{duo,lum} + V_{ent_duo} = \pi\ x\ R^2 x\ L_{duo} \quad [53]$$

$$\therefore R = \sqrt{\left(\frac{V_{duo,lum} + V_{ent_duo}}{\pi\ x\ L_{duo}}\right)} \quad [54]$$

Substituting [54] into [52],

$$SA_{duo,lum+ent} = 2\ x\ \pi\ x \sqrt{\left(\frac{V_{duo,lum} + V_{ent_{duo}}}{\pi\ x\ L_{duo}}\right)}\ x\ L_{duo} \quad [55]$$

Subsequently in equation [56], Ka_e_{duo} is calculated as the surface area (cm^2; equation 55) multiplied by Peff (cm/ sec). Unlike equation [51], SEF is omitted because along GIT, physiological characteristics of gut outer membrane are assumed relatively constant unlike the inner GIT membrane.

$$Ka_e_{duo} = 2\ x\ \pi\ x \sqrt{\left(\frac{V_{duo,lum} + V_{ent_duo}}{\pi\ x\ L_{duo}}\right)}\ x\ L_{duo}\ x\ Peff \quad [56]$$

Equation [57] is used to calculate the quantity in the 'gut blood' compartment over time. The chemical enters via blood flow (F_gut x C_art) and basolateral GIT membrane permeabilities. The rate leaving the gut blood compartment is (F_gut x Ct_gut_blo).

$$V_{gut,blo}\ x\ \frac{dCt_{gut,blo}}{dt} = perm_sto + perm_duo_bas + perm_SI_bas + perm_col_bas + (F_gut\ x\ C_art) - (F_gut\ x\ Ct_gut_blo) \quad [57]$$

Equation [58] calculates fraction absorbed (Q_Fa), displayed as a percentage. It is calculated from the amount absorbed through the apical membrane of GIT enterocytes. This is consistent with the U.S. Food and Drug Administration (FDA) definition of Q_Fa, as metabolism can occur within enterocytes (although not currently modelled).

$$dt(Q_Fa) = \frac{perm_duo_api + perm_SI_api + perm_col_api}{Intake}\ x\ 100 \quad [58]$$

Equation [59] calculates fraction absorbed into 'portal vein' (Q_FDp) more specifically 'gut blood'. It is calculated from the amount absorbed through the basolateral membrane of GIT enterocytes.

$$dt(Q_FDp) = \frac{perm_sto + perm_duo_bas + perm_SI_bas + perm_col_bas}{Intake}\ x\ 100 \quad [59]$$

Equation [60] calculates bioavailability (Q_F). It is calculated using Q_FDp minus the amount metabolised in liver. Thus without liver metabolism, Q_F equals Q_FDp.

$$dt(Q_F) = \frac{(Q_FDp - Q_liv_met)}{Intake}\ x\ 100 \quad [60]$$

Dermal absorption model

$$dt(Q_{_ski_i}) = perm_ski_b - perm_ski_a \quad [61]$$

$$dt(Q_{_liq}) = \ Dose_{dermal} \ + \ perm_ski_a \ - \ (Q_{liq} \ x \ Cry) \quad [62]$$

$$\left(V_{ski_e} + V_{ski_v} \ \frac{R_{bp}}{Kp_{ski}}\right) \ x \ \frac{dC_{e_ski}}{dt} = F_{ski} \ \left(C_{art} - \ \frac{C_{e_ski} \ x \ R_{bp}}{Kp_{ski}}\right) - perm_ski_b \quad [63]$$

$$perm_ski_b = \ PStc_{ski,bas} \ x \ \left(\left(C_{e_ski} \ x \ f_{up_adj_ski_e}\right) - \ \left(C_{i_ski} \ x \ f_{ut,tis}\right)\right) \quad [64]$$

The perm_ski_a equation, which describes the rate at which the dermal dose permeates through the skin, was taken from Poet *et al.* 2002.

$$perm_ski_a = \ Perm_{co} \ x \ SA \ x \ \left(\left(C_{i_ski} \ \div Kp_{ski_liq}\right) - \ C_{surf}\right) \quad [65]$$

$$Fa_{skin} = \ -\frac{perm_ski_a}{Dose_{dermal}} \ x \ 100 \quad [66]$$

Calibration to kidney and liver tissue concentration data (where the sample was homogeneous) requires their homogenous concentrations to be calculated:

$$C_{kid} \ = \ \frac{dt(Q_kid_e) \ + \ dt(Q_kid_i) \ + \ dt(Q_tub)}{V_kid_i \ + \ V_kid_e \ + \ V_tub} \quad [67]$$

$$C_{liv} \ = \ \frac{dt(Q_liv_e) \ + \ dt(Q_liv_i)}{V_liv_i \ + \ V_liv_e} \quad [68]$$

Systemic exposure (which relates to the AOEL) is based on the mass balance equation, and is calculated as follows:

$$dt(Systemic \ exposure) = \frac{dt(Mass \ Balance) - dt(Q_{external})}{Body \ Mass} \quad [69]$$

First-order precipitation occurs in the gut lumen if the local concentration exceeds the chemical's solubility (Simulations Plus 2013b). The precipitation rate is proportional to the difference between the chemical's solubility (Cs), and the concentration of dissolved chemical in the gut lumen (C_{lumen}).

$$dt(Q_{precip}) = \ \frac{1}{PrecipTime} \ (C_{lumen} - \ C_s) \quad [70]$$

Appendix 2: Glossary of terms

C_{art} = arterial blood concentration (mg / mL)
C_{lumen} = concentration of dissolved chemical in a specific gut lumen compartment (mg / mL)
C_{ven} = venous blood concentration (mg / mL)
C_duo_{und} = undissolved concentration in duodenum (mg / mL)
C_duo_{dis} = dissolved concentration in duodenum (mg / mL)
C_{max} = maximum concentration reached in venous plasma (mg / mL)
Ct_{can} = concentration in liver canaliculi (mg / mL)
$Ct_{can,u}$ = unbound concentration in liver canaliculi (mg / mL)
C_{e_kid} = concentration in extracellular compartment of kidney (mg / mL)
C_ent_duo = concentration in duodenum enterocytes (mg / mL)
C_{i_kid} = concentration in intracellular compartment of kidney (mg / mL)
C_{e_tis} = concentration in extracellular compartment of tissue (mg / mL)
C_{i_tis} = concentration in intacellular compartment of tissue (mg / mL)
$C_{i_tis(m)}$ = concentration of metabolite in intracellular compartment of tissue (mg / mL)
Cry = Rate of crystallisation (mg/ sec)
Cs = solubility (mg / mL)
C_surf = Concentration on skin surface (mg/ mL)
C_{spl_v} = concentration at venous end of spleen (mg / mL)
Ct_gut_blo = concentration in gut blood (mg / mL)
Ct_{kid} = concentration in kidney tissue (mg / mL)
$Ct_{kid,u}$ = unbound concentration in kidney tissue (mg / mL)
Ct_{liv} = concentration in liver tissue (mg / mL)
$Ct_{liv,u}$ = unbound concentration in liver tissue (mg / mL)
Ct_{tis} = homogenous concentration in tissue (mg / mL)
C_{tis_v} = concentration at venous end of tissue (mg / mL)
Ct_{tub} = concentration in kidney tubule (mg / mL)
$Ct_{tub,u}$ = unbound concentration in kidney tubule (mg / mL)
Deff = diffusion coefficient in aqueous media (cm^2 / sec)
DR_{duo} = dissolution rate in duodenum (mg / sec)
D_tis = density of tissue (g / mL)
D_kid = density of kidney (g / mL)
EHC = enterohepatic circulation (1 [on] or 0 [off])
Enz_exp_tis_e = enzyme expression in tissue (mg-enzyme/ g-tissue)
Fa_skin = Fraction absorbed through skin (%)
F_{bcl} = fraction biliary clearance
F_bm_tis = fraction basolateral membrane of tissue
F_{gut} = flow to gut (mL / sec)
F_{hep} = hepatic artery flow (mL / sec)
F_{liv} = flow to liver (mL / sec)
F_{kid} = flow to kidney (mL / sec)
F_{spl} = flow to spleen (mL / sec)
F_{tis} = flow to tissue (mL / sec)
f_{ub} = fraction unbound in bile
$f_{up,adj}$ = adjusted fraction unbound in plasma
$f_{up_adj_tis}$ = adjusted fraction unbound in tissue
$f_{up_adj_kid}$ = adjusted fraction unbound in kidney
$f_{ut,adi}$ = fraction unbound in adipose tissue
f_{utub} = fraction unbound in kidney tubule
$f_{up,exp}$ = experimental fraction unbound in plasma
$f_{ut,tis}$ = fraction unbound in tissue
Fvec_mus = fractional volume of muscle which is extracellular space
Fvec_rob = fractional volume of rest-of-body compartment which is extracellular space
GFR = glomerular filtration rate (mL / sec)
h = diffusion layer thickness (cm)
Intake = dose (mg)
K_{adi} = partition coefficient at pH 7.4 in vegetable oil and water (no units)

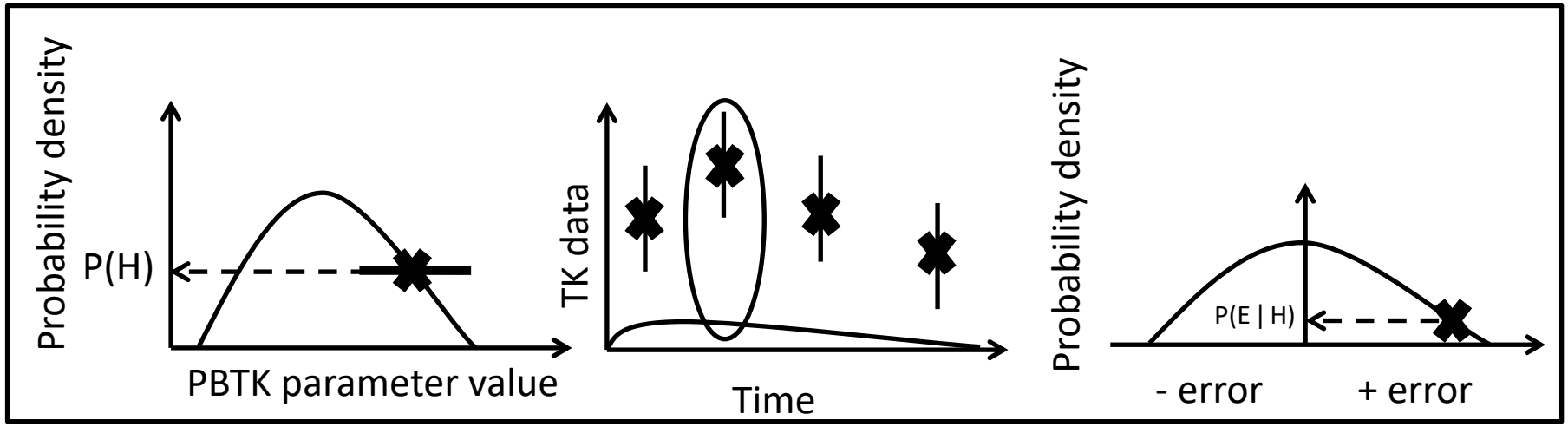
Ka_{duo} = duodenum absorption constant
Ka_e_{duo} = duodenum enterocyte absorption constant
K_m_duo_api = Km of transporter in duodenum enterocyte apical membrane (µg / mL)
K_m_kid_api = Km of transporter in kidney apical membrane (µg / mL)
K_m_kid_bas = Km of transporter in kidney basolateral membrane (µg / mL)
K_m_kid_e = Km of enzyme in kidney (µg / mL)
K_m_liv_api = Km of transporter in liver apical membrane (µg / mL)
K_m_liv_e = Km of enzyme in liver (µg / mL)
K_m_tis_e = Km of enzyme in tissue (µg / mL)
K_m_tis_api/bas = Km of transporter in tissue apical or basolateral membrane (µg / mL)
Kp_{adi} = adipose partition coefficient (no units)
Kp_{kid} = kidney partition coefficient (no units)
Kp_{liv} = liver partition coefficient (no units)
Kp_{ski_liq} =skin: liquid partition coefficient
Kp_{tis} = tissue partition coefficient (no units)
K_{tis} = partition coefficient in octanol and water (no units)
Kt_{duo} = duodenum transit time (hr)
Kt_s = stomach transit time (hr)
L_{duo} = length of duodenum segment (cm)
logP_adi = logarithm of vegetable oil:water partition coefficient of neutral drug molecules for adipose (no units)
logP_pla = logP_tis value at pH of plasma (pH 7.4) (no units)
logP_tis = logarithm of octanol:water partition coefficient of neutral drug molecules for tissue (no units)
ρ = density (g / mL)
Peff = effective permeability of gastro-intestinal tract; small intestine to colon (cm / sec)
Peff_sto = effective permeability of stomach (cm / sec)
$Perm_{co}$ = skin permeability coefficient (mg/ sec/ cm^2 -skin)
Perm_tis_api/bas = flux through tissue apical or basolateral membrane (mg/ sec)
PrecipTime = time for precipitate to form (sec)
PStc = permeability-surface area product (mL/ sec/ mL-tissue)
$PStc_{liv,api}$ = permeability-surface area product of liver apical membrane (mL / sec)
$PStc_{kid,api}$ = permeability-surface area product of kidney apical membrane (mL / sec)
$PStc_{kid,bas}$ = permeability-surface area product of kidney basolateral membrane (mL / sec)
$PStc_{tis,api/bas}$ = permeability-surface area product of tissue apical or basolateral membrane (mL / sec)
Qbile = quantity in bile (mg)
Q_duo_{und} = undissolved quantity in duodenum (mg)
Q_duo_{dis} = dissolved quantity in duodenum (mg)
Q_F = Bioavailability (%)
Q_Fa = Fraction absorbed into apical membrane enterocytes (%)
Q_FDP = Fraction drug absorbed into portal vein (%)
Q_{liq} = quantity in liquid on skin (mg)
Q_liv_met = quantity metabolised in liver (mg)
Qprecip = quantity of precipitate formed (mg)
Q_sto_{und} = undissolved quantity in stomach (mg)
Q_sto_{dis} = dissolved quantity in stomach (mg)
Q_{tis_i} = quantity in tissue intracellular compartment (mg)
Q_{tis_e} = quantity in tissue extracellular compartment (mg)
Q_{tub} = quantity in kidney tubule (mg)
QUR = urine flow rate (mL / sec)
Q_uri = quantity in urine (mg)
r = radius of spherical particles (cm)
$RATp_{tis}$ = ratio of albumin concentration in tissue over plasma
$RATp_{adi}$ = ratio of albumin concentration in adipose over plasma
R_{bp} = blood: plasma concentration ratio
R_SI = average radius of small intestine (cm)
$R_{duo,lum}$ = radius of duodenum lumen (cm)
S = shape factor (length / diameter)
SA = surface area of skin exposed to liquid (cm^2)

$SA:V_{duo,lum}$ = surface area:volume ratio of duodenum lumen
SEF_duo = surface area enhancement factor for duodenum (no units)

Tra_exp_kid_api = transporter expression level in kidney apical membrane (mg-transporter/g-tissue)
Tra_exp_liv_bas = transporter expression in liver basolateral membrane (mg-transporter/g-tissue)
V_adi = volume of adipose tissue (mL)
V_art = volume of arterial blood (mL)
$V_{duo,lum}$ = volume of duodenum lumen (mL)
$V_{ent,duo}$ = volume of duodenum enterocytes (mL)
$V_{gut,blo}$ = volume of gut blood (mL)
V_max_tis_e = *in vitro* enzyme Vmax of tissue (mg / sec/mg-enzyme)
V_{max}_w_duo_api = V_{max} of transporter in duodenum enterocyte apical membrane scaled to whole tissue (mg / sec)
V_{max}_w_kid_api = V_{max} of transporter in kidney apical membrane scaled to whole tissue (mg / sec)
V_{max}_w_kid_bas = V_{max} of transporter in kidney basolateral membrane scaled to whole tissue (mg / sec)
V_{max}_w_kid_e = V_{max} of kidney enzyme scaled to whole tissue (mg / sec)
V_{max}_w_liv_api = V_{max} of transporter in liver apical membrane scaled to whole tissue (mg / sec)
V_{max}_w_liv_e = V_{max} of liver enzyme scaled to whole tissue (mg / sec)
V_{max}_w_tis_api/bas = V_{max} of transporter in tissue apical or basolateral membrane scaled to whole tissue (mg / sec)
V_{max}_w_tis_e = V_{max} of tissue enzyme scaled to whole tissue (mg / sec)

SEF_SI = surface area enhancement factor for gastro-intestinal tract; small intestine to colon (no units)
SEF_col = surface area enhancement factor for colon (no units)
V_{kid} = volume of kidney (mL)
V_{kid_e} = volume of kidney extracellular compartment (mL)
V_{kid_i} = volume of kidney intracellular compartment (mL)
V_{kid_v} = volume of kidney vascular compartment (mL)
V_liq = volume of liquid applied to skin (mL)
V_liv = volume of liver (mL)
V_max_tis_api = *in vitro* Vmax of transporter in apical membrane of tissue (mg / sec/mg-transporter)
V_mus = volume of muscle (mL)
V_{nlp} = fraction neutral lipid content of plasma
V_{nlt} = fraction neutral lipid content of wet tissue weight
V_{php} = fraction phospholipid content of plasma
V_{pht} = fraction polar lipid content of wet tissue weight
V_rob = volume of rest of body (mL)
V_sto = volume of stomach (mL)
V_{tis} = volume of tissue (mL)
V_{tis_e} = volume of tissue extracellular compartment (mL)
V_{tis_i} = volume of tissue intracellular compartment (mL)
V_{tis_v} = volume of tissue vascular compartment (mL)
V_{tub} = volume of kidney tubule (mL)
V_ven = volume of venous blood (mL)
V_{wp} = fraction water content of plasma
V_{wt} = fraction water content of wet tissue weight

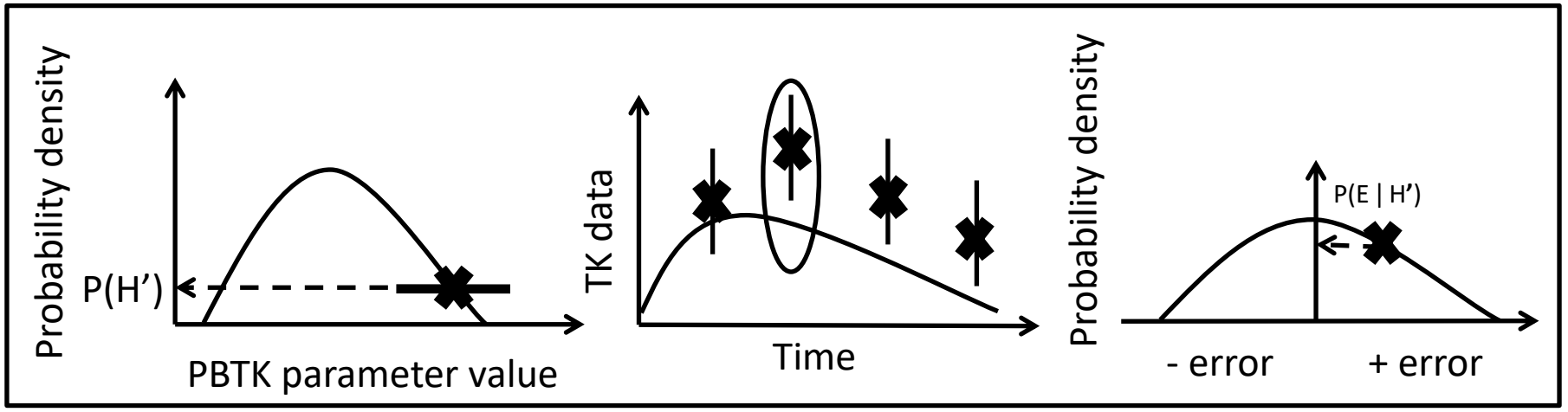
Appendix 3 (Appendix Figure 3.1):



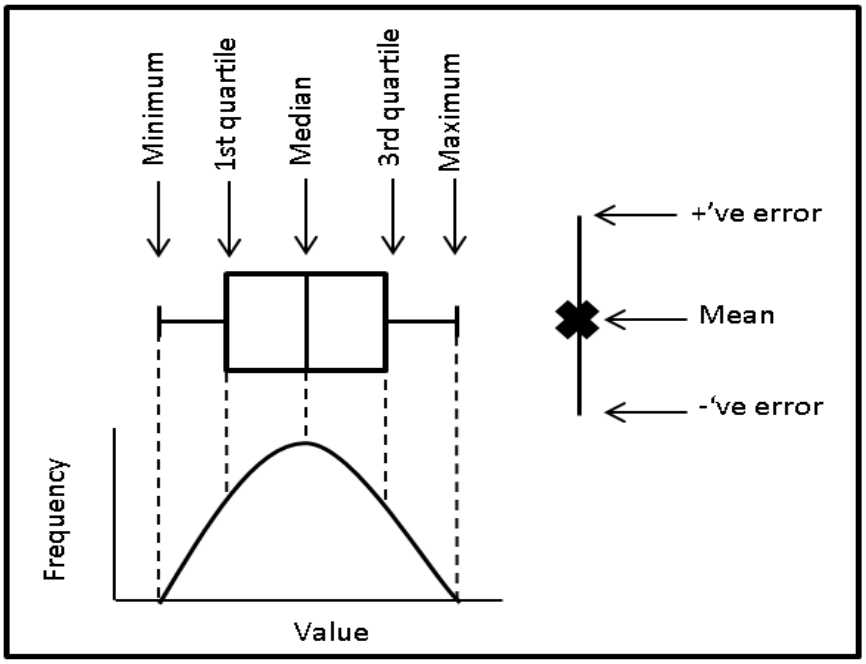
Step 1: randomly select value from the proposal distribution (bold line) within PBTK parameter distribution.

Step 2: run simulation with PBTK model. Error bars reflect natural variation and measurement uncertainty.

Step 3: calculate P(H) x P(E | H) for each TK datum, then multiply probabilities to arrive with single probability density value.



In iteration two (lower row), the proposal probability density P(H') x P(E | H') is greater than the current probability density, P(H) x P(E | H), even though (in this case) P(H') alone is lower, so the sampling vector accepts the move. After a sufficient number of iterations, the sampler reaches equilibrium, and thus samples taken from the proposal distribution are samples from the posterior distribution.



Appendix Figure 3.2: Data visualisation for distributions. Box plot represents confidence intervals in model predictions, i.e. estimates of both variability and uncertainty in toxicokinetics of haloxyfop. The first quartile is the 25th percentile (i.e. 25 % of the data falls below this data point). The second quartile (the median), is the data point at which 50 % of the data is below, and 50 % of the data is above. The third quartile is the 75th percentile. These box plots represent confidence levels of the model's prediction; for normal distributions, the most certain point estimate is the median (normally distributed), or the mode (lognormally distributed). Error bars on toxicokinetic data describe the standard deviation on the data - i.e. the variability in the population, and the measurement uncertainty of the data from individuals.

Appendix 4:

Appendix Table 4.1: Adverse effect levels for haloxyfop-methyl ester relevant to risk assessment

Species	Study	Toxicological effect(s) at LOAEL	NOAEL (mg/ Kg bw/ day)	LOAEL (mg/ Kg bw/ day)	References
Mouse (B6C3F1)	36 weeks[1]	Increased serum AP activity (M* & F) and decreased cytoplasmic vacuolation of proximal convoluted tubule cells (M).	0.2	2.0	Gorzinski *et al.* 1982a
	2 years[1]	Increased serum AP activity at 12 months and increased liver weight (M*), reduced kidney weights (F*), carcinogenicity (M* & F*).	0.065	0.6	Tollet *et al.* 1985
Rat	16 weeks (F344)[1,2]	Increased serum AP activity (M*), increased liver, heart and kidney weights (M* & F*).	0.2	2.0	Gorzinski *et al.* 1892b
	2 years (F344)[1]	Increased serum ALT at 6 and 12 months, decrease in serum [globulin] (M*), increased liver weights and hypertrophy (M).	0.065	0.1	Tollett *et al.* 1983, Yano *et al*. 1984
	Reproductive toxicity (S-D)[1]	Decreased F1a and F1b pup weights at age 14* and 21 days*, decreased body weights of F2a pups age 21 days.	0.065	1.0	Nitschke *et al.* 1985
	3 weeks, developmental toxicity (F344)[2]	Delayed ossification in foetuses*.	1.0	7.5	Hayes *et al*. 1983
Rabbit	4 weeks, developmental toxicity (New Zealand)[2]	Unexplained maternal mortality.	7.5	15.0	Hanley *et al.* 1985
Beagle dog	1 year[1]	Increased serum ALT and AST activities at 12 months (F*), serum [cholesterol] decreased at 1, 6, 9 and 12 months (M*).	0.5	5.0	Barna-Lloyd *et al.* 1983, 1984
Cynomolgus Monkey	13 weeks[3]	Increased kidney weight (M), hepatocellular hypertrophy (M and F), hypertrophy of thyrocytes (F).	2.0	10.0	Yano *et al.* 1987

*Statistically significant effect. **NOAEL)** no observable adverse effect level. **LOAEL)** lowest observable adverse effect level. **1):** Dietary-, **2)** Gavage- **3)** Nasogastric- administration. Table adapted from JMPR 2006.

Appendix 5: The haloxyfop toxicokinetic and HBM data (reproduced with permission of the rights holder, Dow AgroSciences)

Beagle dog TK data (Nolan *et al.* 1987)

In a GLP- compliant study, two Beagle dogs were administered single oral doses (1.99 mg/ Kg; dog AFFX5 and 2.74 mg/ Kg; dog ZIX5) of ^{14}C-labelled haloxyfop (radiochemical purity > 99%). Plasma, faeces and urine TK data were collected over 8 days. Autopsies were done day 8, and concentrations in various tissues determined (liver, kidney and perirenal fat). Radioactivity was quantified using liquid scintillation spectrometry.

^{14}C-Haloxyfop was rapidly and completely absorbed into the blood plasma. Peak plasma concentrations (mean 23 µg/ g-plasma) occurred 30 minutes post-dose. GC and HPLC analysis indicated all plasma radioactivity was unchanged haloxyfop. Plasma clearance appeared to be biphasic with an initial phase lasting 6 - 8 hrs (half-life of 1 - 2 hrs) and the terminal phase having a half-life of 34 hrs. After 8 days, 76.9 % of the administered radioactivity was found in faeces and 10 % in urine. In faeces, most of the excretion was unchanged haloxyfop, although an unidentified metabolite accounted for 8 % of the radioactivity. In urine, unchanged haloxyfop was present, but a metabolite accounted for 50 - 68 % of the radioactivity and was unaffected by acid hydrolysis.

Mouse TK data (Smith *et al.* 1984)

In a GLP- compliant study, a single oral dose of ^{14}C-labelled haloxyfop (radiochemical purity 98.5 %) was administered to B6C3F1 mice (21 female, 21 male). The dose was haloxyfop sodium salt in water (5 mg/ Kg). 3 males and 3 females were sacrificed at each time point (6, 12, 24, 46, 72, 96 and 168 hours after dosing) allowing collection of kidney, liver and plasma TK data. Mice were housed in metabolism cages permitting collection of urine and faeces TK data at 24-hour intervals. Rodent chow and water were provided *ad libitum*, except mice were fasted 3 hours before and 2 - 3 hours after dosing. Radioactivity in the samples collected was quantified using liquid scintillation spectrometry.

No significant sex differences were observed in the TK data. Both male and female blood plasma data showed monophasic plasma clearance, with a mean half-life of 43 hours indicating chronic systemic burden. HPLC analysis indicated that both sexes excrete haloxyfop in both bile and urine (as the parent compound, a glucuronide conjugate and another unidentified conjugate). Biliary excretion via the faeces is the major route of excretion of ^{14}C activity for both genders, indicating haloxyfop undergoes enterohepatic circulation (EHC). Males and females excreted 66% and 60% of the dose, respectively, in faeces 7 days post-dose. Haloxyfop was excreted relatively slowly in urine: males and females excreted 18% and 24% of the dose, respectively, in urine 7 days post-dose.

Human TK data (Nolan *et al.* 1985)

Male Caucasians (31 - 52 years old, weighing 73 - 97 Kg) deemed healthy (based on medical history and a physician's examination) participated. A single oral dose of ^{14}C-labelled haloxyfop (chemical purity 99.8 %) was administered to four Caucasians. The dose was haloxyfop sodium salt in water

(0.2 mg/ Kg), diluted into 100 mL of apple juice to mask haloxyfop's taste. This was ingested 8:00 - 9:00 am, approximately 30 minutes after a light breakfast to reduce possible gastric upset. A single dermal dose of ^{14}C-labelled haloxyfop-methyl ester (chemical purity 99.6 %) was administered to four other Caucasians at rest. The dose was haloxyfop sodium salt in xylene (0.8 mg/ Kg), applied to approximately 100 cm^2 of the forearm until complete evaporation. The participants were instructed to bathe 12 hours later. For both oral and dermal exposure studies, blood samples were collected at 0.5, 1, 2, 4, 6, 8, 10, 12, 24, 32, 48, 72, 144, 240, 384 and 504 hours post-dose. Over this duration, volunteers collected urine voided during specified 24-hour intervals.

Orally administered haloxyfop was rapidly absorbed: peak plasma concentrations (range 1.4 - 2.2 μg haloxyfop-P/ g-plasma) were observed between 4 and 12 hours post-dose. The concentration of haloxyfop-P in plasma decreased with a half-life of 6.3 days (range 4.8 - 9.3 days). Urine was the primary excretion route: by 21 days, an average of 79 % of the oral dose was excreted in urine as the parent compound primarily, and/ or conjugates capable of hydrolysis to haloxyfop-P.

Haloxyfop-methyl ester was slowly absorbed through skin: peak plasma concentrations (range 0.1 - 0.2 μg haloxyfop/ g-plasma) were observed 3 days post-dose. The concentration of haloxyfop-P in plasma decreased with a half-life of 5.8 days (range 5.3 - 7.4 days). Based on the amount of haloxyfop-P excreted in urine approximately 3 % of the dermal dose was absorbed; on average, 2.4 % (range 1.6 - 3.3 %) of which was excreted in urine (by 21 days).

Operator HBM data (Nolan *et al*. 1991)

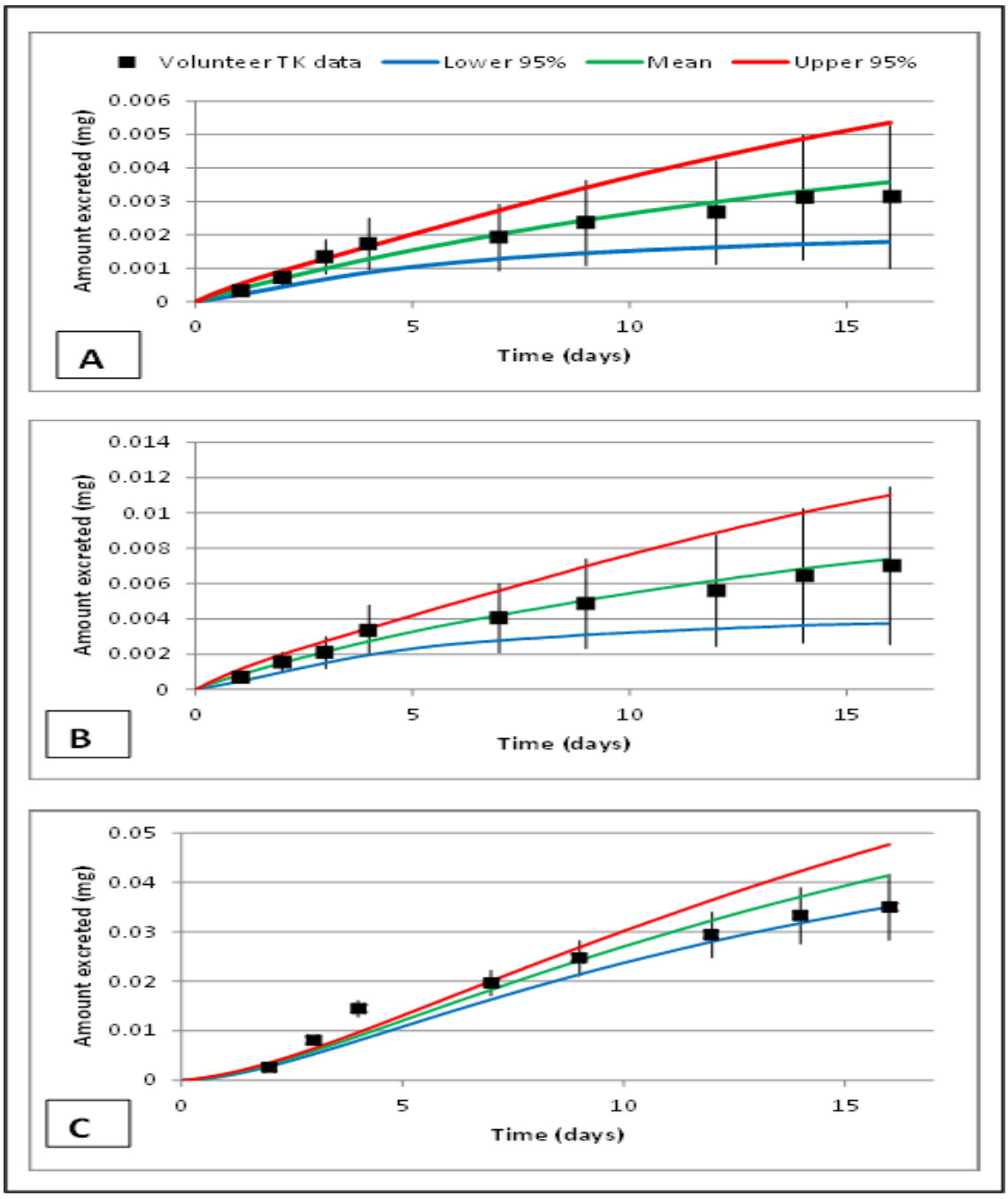
The purpose of this non-GLP compliant study was to use urinary haloxyfop-P excretion to quantify haloxyfop-methyl ester absorbed by individuals applying Verdict™ herbicide. Eight experienced male applicators (age 21 - 55 years) participated. They were examined by a physician to exclude those taking chronic medication, or with liver, kidney or cardiovascular disease. Participants were asked to abstain from alcohol and acute medication 24 hours before and 24 hours after applying Verdict. The participants followed proposed label directions, and wore long-sleeved coveralls, goggles and waterproof gloves whilst mixing and loading. Only coveralls were worn during application. Details of mixing, loading, application, site conditions and amounts of haloxyfop-methyl ester found in the breathing zone and on patches attached to participant's clothing are reported (Scortichini & Bohl 1987). Each participant mixed 9.46 Kg of Verdict (2.27 Kg haloxyfop-methyl ester), and applied 1,818 litres of diluted Verdict to 0.081 Km^2 of fallow crop land using an open cab or tractor-drawn boom spray. The participants were asked to collect all urine voided during two days before spraying, spray day, and 1, 2, 3, 6, 8, 11, 13 and 15 days post-spray.

Urinary haloxyfop-P was measured by GCMS; the limit of quantification (LOQ) ranged from 0.080 - 0.47 ng/ mL depending on the interference level found in pre-spray urine samples. Three individuals (G.B., G.D. and J.Q.) excreted quantifiable haloxyfop-P in their urine samples. Only 2 of the urine specimens submitted by G.D. contained sufficient haloxyfop-P to quantify; haloxyfop-P concentrations (and those of J.Q. urine samples) were close to the LOQ. Only G.B.'s urine samples contained haloxyfop-P concentrations substantially above the LOQ. Urinary haloxyfop-P was used to calculate the amount of haloxyfop-methyl ester absorbed, according to a compartmental TK model (Nolan *et al.* 1985). The 8 applicators absorbed an average of 0.31 ± 0.46 μg haloxyfop-methyl ester/

Kg body weight (range < 0.04 - 1.4 µg haloxyfop-methyl ester/ Kg body weight). This average overestimates true exposure because the estimates for the five individuals (who excreted insufficient haloxyfop-P for quantification) are based on the LOQ. Furthermore, it is influenced by G.B. who absorbed more haloxyfop-methyl ester than all other participants combined.

Reverse dosimetry (fits to HBM data)

The sampled MCMC parameter values derived from the reverse dosimetry fit the urinary HBM data from Nolan *et al.* 1991.



Appendix Figure 5.1: Uncertainty analysis of urinary excretion of haloxyfop-P with human PBTK model, calibrated with HBM data. A) Operators J.H., M.D., D.R. & G.D. (based on LoQ), **B)** operator J.Q., and **C)** operator G.B. HBM data is taken from Nolan *et al.* 1991, and reproduced with permission of the rights holder, Dow AgroSciences.

Appendix 6: Correlation matrices of PBTK model parameters (chapter 5)

Appendix Table 6.1: Correlation matrix of mouse-human PBTK model parameters.

Values shown in bold are statistically significant correlations, Pearson's r (999), $p < 0.05$. N.b. every third iteration was used to prevent interference from auto-correlation (Chiu *et al.* 2009).
Black: species non-specific parameters, **green:** mouse-specific parameters, **blue:** human-specific parameters.

	PStc	*V_max_liv_e*	*Km_liv_p_e*	*V_max_kid_a*	*Km_kid_p_a*	*V_max_liv_b*	*Km_liv_p_b*	*V_max_liv_a*	*Km_liv_p_a*	*fup_exp*	*logP_pla*	*Cry*	*Peff_sto (h)*	*Peff (h)*	*Kp_ski_fab (h)*	*Perm_co (h)*	*Peff_sto (m)*
V_max_liv_e	**-0.35**																
Km_liv_p_e	-0.02	**0.38**															
V_max_kid_a	**0.59**	**-0.26**	**-0.07**														
Km_kid_p_a	0.06	0.03	**-0.10**	**0.66**													
V_max_liv_b	0.00	**0.07**	**0.14**	**-0.14**	**-0.14**												
Km_liv_p_b	**0.16**	**0.07**	**0.12**	-0.04	**-0.09**	**0.69**											
V_max_liv_a	**-0.52**	**0.11**	**-0.10**	**-0.42**	**-0.13**	0.02	**-0.38**										
Km_liv_p_a	**-0.47**	**0.20**	**-0.07**	**-0.53**	**-0.20**	**-0.16**	-0.05	**0.70**									
fup_exp	0.02	**-0.10**	**0.12**	**-0.51**	**-0.43**	**0.11**	0.06	0.02	**0.12**								
logP_pla	0.00	0.03	**0.07**	0.00	-0.01	-0.03	0.00	-0.02	0.01	0.01							
Cry	**0.62**	**-0.25**	0.05	**0.44**	**0.07**	0.02	**0.08**	**-0.45**	**-0.48**	**0.11**	0.01						
Peff_sto (h)	-0.03	-0.04	0.02	**-0.08**	**-0.11**	**0.11**	**0.09**	-0.02	-0.01	0.05	0.02	0.04					
Peff (h)	**0.12**	0.01	0.00	-0.02	**-0.08**	0.00	**-0.07**	**-0.09**	**-0.08**	**0.16**	-0.04	**0.22**	**0.24**				
Kp_ski_fab (h)	0.05	-0.01	0.02	**0.17**	**0.15**	0.02	-0.02	**-0.20**	**-0.32**	-0.01	0.02	**0.59**	0.00	**0.08**			
Perm_co (h)	**-0.55**	**0.17**	0.04	**-0.22**	0.06	**-0.09**	**-0.11**	**0.13**	**0.11**	**-0.13**	-0.04	**-0.08**	**0.11**	-0.05	**0.33**		
Peff_sto (m)	0.05	**0.08**	0.02	0.00	0.03	**-0.30**	**0.20**	**-0.26**	**0.24**	-0.04	0.05	-0.06	0.06	**0.09**	**-0.15**	**-0.08**	
Peff (m)	**-0.25**	-0.01	**-0.13**	-0.04	**0.14**	**-0.49**	**-0.47**	**0.13**	**0.10**	**-0.15**	0.02	**-0.12**	0.05	**0.13**	0.00	**0.14**	**0.27**

Appendix Table 6.2: Correlation matrix of rat PBTK model parameters.

Values shown in bold are statistically significant correlations, Pearson's r (999), $p < 0.05$. **Black:** gender non-specific parameters, **green:** female parameters, **blue:** male parameters.

	PStc	*logP_pla*	*logP_tis*	*Peff_sto*	*Peff*	*SEF_C1*	*SEF_C2_7*	*SEF_c*	*V_max_kid_a*	*Km_kid_p_a*	*V_max_kid_b*	*Km_kid_p_b*	*V_max_liv_a*	*Km_liv_p_a*	*V_max_liv_b*
logP_pla	0.01														
logP_tis	-0.03	0.02													
Peff_sto	**-0.06**	-0.04	0.02												
Peff	0.04	0.01	0.03	0.00											
SEF_C1	**0.09**	0.00	**-0.08**	-0.01	0.00										
SEF_C2_7	**-0.08**	0.05	-0.02	-0.01	**-0.11**	**-0.16**									
SEF_c	**-0.06**	0.00	-0.01	**-0.10**	**-0.08**	**-0.16**	-0.01								
V_max_kid_a	**0.17**	-0.03	0.03	-0.01	-0.02	**0.07**	**-0.06**	0.01							
Km_kid_p_a	**0.13**	-0.02	0.00	-0.01	-0.03	**0.09**	**-0.07**	0.06	**0.70**						
V_max_kid_b	**0.08**	-0.03	0.01	-0.03	-0.02	-0.04	**0.13**	**-0.11**	**0.09**	-0.03					
Km_kid_p_b	**0.09**	-0.01	0.00	-0.05	-0.02	-0.04	**0.10**	**-0.08**	0.05	-0.02	**0.91**				
V_max_liv_a	**0.08**	0.01	0.03	**-0.14**	**0.29**	**0.16**	-0.03	-0.06	**0.28**	0.04	**0.34**	**0.25**			
Km_liv_p_a	0.00	-0.05	-0.05	**0.07**	**-0.12**	0.00	-0.02	-0.01	**-0.11**	**-0.07**	**0.18**	**0.21**	**0.14**		
V_max_liv_b	-0.02	-0.02	-0.03	-0.02	0.03	0.06	0.03	**-0.07**	-0.01	-0.03	**0.44**	**0.39**	**0.10**	**0.28**	
Km_liv_p_b	-0.05	-0.01	**-0.07**	**0.08**	**-0.15**	0.02	0.02	-0.04	**-0.13**	-0.06	**0.26**	**0.29**	**-0.25**	**0.38**	**0.83**
V_max_kid_a	0.01	0.02	-0.05	-0.01	**0.10**	0.06	-0.01	**-0.14**							
Km_kid_p_a	**0.17**	**0.06**	-0.03	-0.03	**0.14**	0.04	-0.05	-0.05	**0.59**						
V_max_kid_b	**-0.31**	-0.04	-0.03	0.03	-0.01	0.01	-0.01	**-0.09**	**0.57**	0.02					
Km_kid_p_b	**-0.11**	-0.03	0.04	0.00	0.01	0.00	**-0.08**	0.00	**0.09**	0.02	**0.60**				
V_max_liv_a	**0.13**	-0.04	-0.02	**-0.07**	**0.42**	**0.27**	**-0.12**	**-0.07**	**0.18**	0.05	**0.10**	**0.08**			
Km_liv_p_a	-0.06	**-0.09**	**-0.09**	**0.11**	**-0.09**	0.04	**0.06**	-0.03	**-0.06**	**-0.15**	0.02	**0.09**	**0.42**		
V_max_liv_b	-0.06	0.00	0.02	0.04	**0.19**	**0.11**	**-0.18**	-0.04	**0.15**	0.03	**0.11**	0.00	**0.14**	**-0.23**	
Km_liv_p_b	**-0.20**	0.01	0.02	**0.11**	**-0.17**	**-0.10**	-0.06	0.04	0.01	**-0.07**	0.06	0.00	**-0.32**	**-0.13**	**0.79**

Appendix 7: PBTK model computer code to simulate toxicokinetics of TBBPA (and its glucuronide conjugate) (MCSim V.5.3)

N.b. Permission not received to reproduce values of physiological parameters as generated from rights holder Simulations Plus, Inc. These are available at Simulations Plus (2013a). Values for model parameters can be respecified in corresponding input file (not shown). HRTM and adapted HATM model codes and parameter values reproduced with permission of the rights holder, ICRP.

```
States = {
Q_sto_und,Q_C1_und,Q_C2_7_und,Q_col_und,Q_
sto_dis,Q_C1_dis,Q_C2_7_dis,Q_col_dis,Q_fec,Q_
ent_C1_abs,Q_ent_C2_7_abs,Q_ent_col_abs,Q_bil
,Q_Fa,Q_FDp,C1_tot,C2_7_tot,Ccol_tot,Q_sto_abs
,Q_ent_C1,Q_ent_C2_7,Q_ent_col,Q_gut_blo,Q_ki
d_met,Q_liv_met,Q_ski_met,Q_adi_met,Q_rob_m
et,Q_lun_met,Q_mus_met,Q_spl_met,Q_yel_met,
Q_hea_met,Q_bra_met,Q_rep_met,Q_red_met,Q
_cl_tot,Q_kid,Q_nep,Q_uri,Q_liv,Q_adi,Q_rob,Q_l
un,Q_mus,Q_spl,Q_yel,Q_hea,Q_bra,Q_rep,Q_red
,Q_ven,Q_art,Q_ski,Q_fab,Intake,Q_Crystal,
# Permeability-limited model (1st metabolite)
Q_sto_dism,Q_C1_dism,Q_C2_7_dism,Q_col_dism
,Q_fecm,Q_ent_C1_absm,Q_ent_C2_7_absm,Q_e
nt_col_absm,Q_bilm,Q_Fam,Q_FDpm,C1_totm,C2
_7_totm,Ccol_totm,Q_sto_absm,Q_ent_C1m,Q_e
nt_C2_7m,Q_ent_colm,Q_gut_blom,Q_kid_im,Q_
kid_em,Q_kid_totm,Q_nepm,Q_urim,Q_liv_em,Q_
liv_im,Q_liv_totm,Q_ski_em,Q_ski_im,Q_ski_totm
,Q_adi_em,Q_adi_im,Q_adi_totm,Q_rob_em,Q_ro
b_im,Q_rob_totm,Q_lun_em,Q_lun_im,Q_lun_tot
m,Q_mus_em,Q_mus_im,Q_mus_totm,Q_spl_em,
Q_spl_im,Q_spl_totm,Q_yel_em,Q_yel_im,Q_yel_
totm,Q_hea_em,Q_hea_im,Q_hea_totm,Q_bra_e
m,Q_bra_im,Q_bra_totm,Q_rep_em,Q_rep_im,Q_
rep_totm,Q_red_em,Q_red_im,Q_red_totm,Q_ve
nm,Q_artm,Q_GITm,
# Permeability-limited model (2nd metabolite)
Q_sto_dism2,Q_C1_dism2,Q_C2_7_dism2,Q_col_
dism2,Q_fecm2,Q_ent_C1_absm2,Q_ent_C2_7_ab
sm2,Q_ent_col_absm2,Q_bilm2,Q_Fam2,Q_FDpm
2,C1_totm2,C2_7_totm2,Ccol_totm2,Q_sto_absm
2,Q_ent_C1m2,Q_ent_C2_7m2,Q_ent_colm2,Q_g
ut_blom2,Q_kid_im2,Q_kid_em2,Q_kid_totm2,Q_
nepm2,Q_urim2,Q_liv_em2,Q_liv_im2,Q_liv_totm
2,Q_ski_em2,Q_ski_im2,Q_ski_totm2,Q_adi_em2,
Q_adi_im2,Q_adi_totm2,Q_rob_em2,Q_rob_im2,
Q_rob_totm2,Q_lun_em2,Q_lun_im2,Q_lun_totm
2,Q_mus_em2,Q_mus_im2,Q_mus_totm2,Q_spl_
em2,Q_spl_im2,Q_spl_totm2,Q_yel_em2,Q_yel_i
m2,Q_yel_totm2,Q_hea_em2,Q_hea_im2,Q_hea_
totm2,Q_bra_em2,Q_bra_im2,Q_bra_totm2,Q_re
p_em2,Q_rep_im2,Q_rep_totm2,Q_red_em2,Q_r
ed_im2,Q_red_totm2,Q_venm2,Q_artm2,Q_GITm
2,
# ICRP lung model
A,A_T,A_bnd,I,I_T,I_bnd,LNTH,LNTH_T,LNTH_bnd,
bb,bb_T,bb_bnd,bb_seq,bb_seq_T,bb_seq_bnd,BB
,BB_T,BB_bnd,BB_seq,BB_seq_bnd,BB_seq_T,ET2,
ET2_T,ET2_bnd,ET_seq,ET_seq_T,ET_seq_bnd,LNE
T,LNET_bnd,LNET_T,ET1,NB,Q_sto_I, Q_sto_T,
Q_C1_I, Q_C1_T, Q_C2_7_I, Q_C2_7_T, Q_col_I,
Q_col_T,
};
# ICRP lung model
# Lung absorption (ICRP Type F) from Table 3.2
ICRP 130
Fr = 1;
Sr = 30;
Ss = 0;
Fb = 0; # fraction bound
Sb = 0; # rate of bound material to Q_gut_blo
f1 = 0.0005; # used to calculate Lum_blo rate (in
initialise)
# Regional deposition from Table 3.1 ICRP 130

DEP_A = 0.0532; # 'AI' - alveolar-instititial
DEP_bb = 0.011; # bronchiolar
DEP_BB = 0.0178; # bronchial
DEP_ET2 = 0.2582; # posterior nasal passage
DEP_ET1 = 0.4794; # anterior nasal passage
# Aerosol particle transport rates
RT_A_I = 0.001;
RT_I_LNTH = 0.00003;
RT_A_bb = 0.002;
RT_bb_BB = 0.2;
RT_bbseq_LNTH = 0.001;
RT_BBseq_LNTH = 0.001;
RT_BB_ET2 = 10;
RT_ETseq_LNET = 0.001;
RT_ET2_St = 100;
RT_ET1_NB = 0.6;
RT_ET1_ET2 = 1.5;
# Aersol absorption rates derived from fr,sr and ss
SP = 0;   # sp, spt & st are rates at which inhaled
particles dissolve and are initialised.
SPT = 0;
ST = 0;
Lum_blo = 0;
# Intake rates
Inhalation = 0;
Solution_ingested = 0;
Solid_ingested = 0;
```

```
Clothes = 0;
# Dermal absorption model
Perm_co = 1; # skin permeability coefficient (mg/ sec/ cm2 of skin)
SA = 1; # surface area of skin exposed (cm2)
Kp_ski_fab = 1; # skin: medium partition coefficient (no units)
V_fab = 1; # volume of medium (cm3)
Cry = 1; # rate of crystallisation (mg/ sec)
# Gut parameters
EHC = 1; # Enterohepatic circulation. 1 is on, 0 is off.
Fbcl = 1; # fraction of that metabolised which enters bile canaliculi
Stoichiometry = 1; # used for tracking 2nd metabolite/ conjugate
Peff_sto = 1; # effective stomach permeability (cm/ sec)
Peff = 1; # effective permeability of intestinal tract (cm/ sec)
SEF_s = 1; # surface area enhancement factors (no units)
SEF_C1 = 1;
SEF_C2_7 = 1;
SEF_c = 1;
pi = 3.14;
L_sto = 1; # lengths of gut segments (cm)
L_C1 = 1;
L_C2_7 = 1;
L_col = 1;
R_sto = 1;
R_C1 = 1; # radius of duodenum (cm)
R_C2_7 = 1;
R_col = 1;
V_sto = 1;
V_C1 = 1; # volume of duodenum (cm3)
V_C2_7 = 1;
V_col = 1;
V_gut_blo = 1; # volume of portal blood
Kt_s_p = 1; # Stomach transit rate (hrs)
Kt_1_p = 1;
Kt_2_7_p = 1;
Kt_c_p = 1;
V_ent_sto = 1;
V_ent_C1 = 1; # volume of enterocytes in duodenum (cm3)
V_ent_C2_7 = 1;
V_ent_col = 1;
D_ent_C1 = 1; # density of enterocyte compartment in duodenum (g/ cm3)

D_ent_C2_7 = 1;
D_ent_col = 1;
# Parameters for dissolution and precipitation rates in gut
Deff = 1; # diffusion coefficient (cm2/ sec)
p = 1; # particle density (g/ mL)
h = 1; # diffusion layer thickness (cm)
S = 1; # shape factor (no units)
Cs = 1; # solubility at pH 7.0 (mg/ mL)
r = 1; # radius of particles (cm)
PrecipTime = 1; # precipitation time (sec)
# Body parameters
F_total = 1; # total blood flow (i.e. cardiac output)
# Tissue blood flow rates as fractions of cardiac output
Fr_F_kid = 1; # kidney
Fr_F_ski = 1; # skin
Fr_F_adi = 1; # adipose
Fr_F_rob = 1; # rest of body
Fr_F_gut = 1; # gut
Fr_F_mus = 1; # muscle
Fr_F_hep = 1; # hepatic artery
Fr_F_spl = 1; # spleen
Fr_F_yel = 1; # yellow marrow
Fr_F_hea = 1; # heart
Fr_F_bra = 1; # brain
Fr_F_rep = 1; # reproductive organs
Fr_F_red = 1; # red marrow
# Tissue volumes as fractions of body weight
Fr_V_liv = 1;
Fr_V_kid = 1;
Fr_V_nep = 1; # kidney nephron
Fr_V_ski = 1;
Fr_V_adi = 1;
Fr_V_rob = 1;
Fr_V_ven = 1; # venous blood
Fr_V_art = 1; # arterial blood
Fr_V_lun = 1;
Fr_V_mus = 1;
Fr_V_spl = 1; # volume of spleen
Fr_V_yel = 1; # yellow marrow
Fr_V_hea = 1;
Fr_V_bra = 1;
Fr_V_rep = 1;
Fr_V_red = 1;
# Fractional composition of each tissue
Fvec_liv = 1; # fractional volume which is extracellularspace
Fvv_liv = 1;   # fractional volume which is vascular space
Fvec_kid = 1;
Fvv_kid = 1;
Fvec_ski = 1;
Fvv_ski = 1;
Fvec_adi = 1;
Fvv_adi = 1;
Fvec_rob = 1;
Fvv_rob = 1;
Fvec_lun = 1;
Fvv_lun = 1;
Fvec_mus = 1;
Fvv_mus = 1;
Fvec_spl = 1;
```

```
Fvv_spl = 1;
Fvec_yel = 1;
Fvv_yel = 1;
Fvec_hea = 1;
Fvv_hea = 1;
Fvec_bra = 1;
Fvv_bra = 1;
Fvec_rep = 1;
Fvv_rep = 1;
Fvec_red = 1;
Fvv_red = 1;
# Parameters for calculating Kp (Poulin
homogenous method)
logP_tis = 1; # logP values for all tisues but adipose
and yellow marrow.
logP_pla = 1; # logP value at pH of plasma (pH =
7.4)
Vnlt_kid = 1; # fractional neutral lipid content of
wet tissue weight
Vpht_kid = 1; # fractional polar lipid content of wet
tissue weight
Vwt_kid = 1; # fractional water content of wet
tissue weight
Vnlt_liv = 1;
Vpht_liv = 1;
Vwt_liv = 1;
Vnlt_ski = 1;
Vpht_ski = 1;
Vwt_ski = 1;
Vnlt_adi = 1;
Vpht_adi = 1;
Vwt_adi = 1;
Vnlt_mus = 1;
Vpht_mus = 1;
Vwt_mus = 1;
Vnlt_spl = 1;
Vpht_spl = 1;
Vwt_spl = 1;
Vnlt_yel = 1;
Vpht_yel = 1;
Vwt_yel = 1;
Vnlt_hea = 1;
Vpht_hea = 1;
Vwt_hea = 1;
Vnlt_bra = 1;
Vpht_bra = 1;
Vwt_bra = 1;
Vnlt_rep = 1;
Vpht_rep = 1;
Vwt_rep = 1;
Vnlt_red = 1;
Vpht_red = 1;
Vwt_red = 1;
Vnlt_rob = 1;
Vpht_rob = 1;
Vwt_rob = 1;
Vnlt_lun = 1;
Vpht_lun = 1;
Vwt_lun = 1;
Vphp = 1; # fraction phospholipid content of
plasma
Vwp = 1; # fraction water content of plasma
Vnlp = 1; # fraction neutral lipid content of plasma
D_kid = 1; # density of kidney (g/ mL)
D_liv = 1;
D_ski = 1;
D_adi = 1;
D_rob = 1;
D_lun = 1;
D_mus = 1;
D_spl = 1;
D_yel = 1;
D_hea = 1;
D_bra = 1;
D_rep = 1;
D_red = 1;
D_blo = 1; # blood
D_ent = 1; # enterocytes
D_gut_lum = 1; # gut lumen
Rbp = 1; # blood/ plasma concentration ratio
fup_exp = 1; # experimental fraction unbound in
plasma (i.e.value from in vitro assay).
PStc_liv_a = 1;
PStc_kid_a = 1;
RAtp_tis = 1; # tissue/ plasma albumin ratio for all
tissues except adipose and yellow marrow
RAtp_adi = 1; # tissue/ plasma albumin ratio for
adipose and yellow marrow
QUR_p = 1; # urinary flow rate (mL/ sec)
GFR = 1; # glomerular filtration rate (mL / sec)
# Transporters (in apical membrane of kidney and
liver)
V_max_liv_a = 1; # in vitro vmax (mg/ sec/ mg of
transporter)
Tra_exp_liv_a = 1; # transporter expression level
(mg of transporter/ g of tissue)
Km_liv_p_a = 1; # Km of transporter (mg/ L)
V_max_kid_a = 1;
Tra_exp_kid_a = 1;
Km_kid_p_a = 1;
# Transporters (in apical membrane of
enterocytes)
V_max_gut_C1_a = 1;
Tra_exp_gut_C1_a = 1;
Km_gut_p_C1_a = 1;
V_max_gut_C2_7_a = 1;
Tra_exp_gut_C2_7_a = 1;
Km_gut_p_C2_7_a = 1;
V_max_gut_col_a = 1;
Tra_exp_gut_col_a = 1;
Km_gut_p_col_a = 1;
# Enzymes
V_max_kid_e = 1; # in vitro vmax (mg/ sec/ mg of
enzyme)
```

```
V_max_liv_e = 1;
V_max_ski_e = 1;
V_max_adi_e = 1;
V_max_rob_e = 1;
V_max_lun_e = 1;
V_max_mus_e = 1;
V_max_spl_e = 1;
V_max_yel_e = 1;
V_max_hea_e = 1;
V_max_bra_e = 1;
V_max_rep_e = 1;
V_max_red_e = 1;
V_max_gut_e = 1;
Enz_exp_kid_e = 1; # enzyme expression level (mg of enzyme/ g of tissue)
Enz_exp_liv_e = 1;
Enz_exp_ski_e = 1;
Enz_exp_adi_e = 1;
Enz_exp_rob_e = 1;
Enz_exp_lun_e = 1;
Enz_exp_mus_e = 1;
Enz_exp_spl_e = 1;
Enz_exp_yel_e = 1;
Enz_exp_hea_e = 1;
Enz_exp_bra_e = 1;
Enz_exp_rep_e = 1;
Enz_exp_red_e = 1;
Enz_exp_gut_e = 1;
Km_kid_p_e = 1; # Km of enzyme (mg/ L)
Km_liv_p_e = 1;
Km_ski_p_e = 1;
Km_adi_p_e = 1;
Km_rob_p_e = 1;
Km_lun_p_e = 1;
Km_mus_p_e = 1;
Km_spl_p_e = 1;
Km_yel_p_e = 1;
Km_hea_p_e = 1;
Km_bra_p_e = 1;
Km_rep_p_e = 1;
Km_red_p_e = 1;
Km_gut_p_e = 1;
Mass_iv = 1; # body mass of subject(s) dosed via intravenous route
Mass_oral = 1;
Mass_inhale = 1;
Mass_fabric = 1; # (dosed via dermal route)
Recov_iv = 1; # Rec
Recov_oral = 1; # fractional recovery of dose post administration
Recov_inhale = 1;
Recov_fabric = 1;
# Permeability-limited model (1st metabolite)
fup_expm = 1;
EHCm = 1;
Rbpm = 1;
logP_plam = 1;
logP_tism = 1;
PStcm = 1; # global PStc value (mL/sec/ mL of tissue).
F_bm_kid = 1; # fraction (of tissue cell volume) that is basolateral membrane
F_bm_liv = 1;
F_bm_ski = 1;
F_bm_adi =1;
F_bm_rob = 1;
F_bm_lun = 1;
F_bm_mus = 1;
F_bm_spl = 1;
F_bm_yel = 1;
F_bm_hea = 1;
F_bm_bra = 1;
F_bm_rep = 1;
F_bm_red = 1;
# Transporters in kidney basolateral membrane
V_max_kid_bm = 1;
Tra_exp_kid_bm = 1;
Km_kid_p_bm = 1;
# Transporters in kidney apical membrane
V_max_kid_am = 1;
Tra_exp_kid_am = 1;
Km_kid_p_am = 1;
# Transporters in liver basolateral membrane
V_max_liv_bm = 1;
Tra_exp_liv_bm = 1;
Km_liv_p_bm = 1;
# Transporters in liver apical membrane
V_max_liv_am = 1;
Tra_exp_liv_am = 1;
Km_liv_p_am = 1;
# Transporters in apical membrane of enterocytes
V_max_gut_C1_am = 1;
Tra_exp_gut_C1_am = 1;
Km_gut_p_C1_am = 1;
V_max_gut_C2_7_am = 1;
Tra_exp_gut_C2_7_am = 1;
Km_gut_p_C2_7_am = 1;
V_max_gut_col_am = 1;
Tra_exp_gut_col_am = 1;
Km_gut_p_col_am = 1;
# Permeability-limited model (2nd metabolite)
fup_expm2 = 1;
EHCm2 = 1;
Rbpm2 = 1;
logP_plam2 = 1;
logP_tism2 = 1;
# Transporters
V_max_kid_bm2 = 1;
Tra_exp_kid_bm2 = 1;
Km_kid_p_bm2 = 1;
V_max_kid_am2 = 1;
Tra_exp_kid_am2 = 1;
Km_kid_p_am2 = 1;
V_max_liv_bm2 = 1;
```

```
Tra_exp_liv_bm2 = 1;
Km_liv_p_bm2 = 1;
V_max_liv_am2 = 1;
Tra_exp_liv_am2 = 1;
Km_liv_p_am2 = 1;
V_max_gut_C1_am2 = 1;
Tra_exp_gut_C1_am2 = 1;
Km_gut_p_C1_am2 = 1;
V_max_gut_C2_7_am2 = 1;
Tra_exp_gut_C2_7_am2 = 1;
Km_gut_p_C2_7_am2 = 1;
V_max_gut_col_am2 = 1;
Tra_exp_gut_col_am2 = 1;
Km_gut_p_col_am2 = 1;

Outputs = {
Fa_skin, MB1, MB2, MB3, MB4, MB5, MB6, MB7,
MB8, MB9, MassBalance, SE1, SE2, SE3, SE4, SE5,
SE6, SE7, SE8, SE9, SystemicExposure, In,
On_Off_sto_p, On_Off_C1_p, On_Off_C2_7_p,
On_Off_col_p, On_Off_sto_d,
On_Off_C1_d,On_Off_C2_7_d, On_Off_col_d,
PR_C_sto, PR_C_C1, PR_C_C2_7, PR_C_col,
DR_C_sto, DR_C_C1, DR_C_C2_7, DR_C_col,
Qstound, QC1und, QC2_7und, Qcolund,
Qstodis,QC1dis,QC2_7dis,Qcoldis, C_sto_und,
C_C1_und,C_C2_7_und,C_col_und,
C_sto_dis,C_C1_dis,C_C2_7_dis,C_col_dis,
QentC1abs, QentC2_7abs,
Qentcolabs, DR,PR,
Ka_s,Ka_1,Ka_2_7,Ka_c,C_ent_C1,C_ent_C2_7,C_e
nt_col,Ct_gut_blo,Fa,FDp,F,Qbil,QentC1,
QentC2_7,Qentcol,Qstoabs,C1tot,C2_7tot,Ccoltot,
Qkidmet,Qlivmet,Qskimet,Qadimet,Qrobmet,Qlun
met,
Qmusmet,Qsplmet,Qyelmet,Qheamet,Qbramet,Qr
epmet,Qredmet,Qcltot,fut_tis,fut_adi,Kp_liv,Kp_ki
d,Kp_ski,Kp_adi,Kp_rob,Kp_lun,Kp_mus,Kp_spl,Kp
_yel,Kp_hea,Kp_bra,Kp_rep,Kp_red,fup_adj,Qkid,
Qnep,Quri,Qliv,Qski,Qadi,Qrob,Qlun,Qmus,Qspl,Q
yel,Qhea,Qbra,Qrep,Qred,Ct_kid,C_nep,Ct_liv,Ct_a
di,Ct_rob,Ct_lun,Ct_mus,Ct_spl,Ct_yel,Ct_hea,Ct_
bra,Ct_rep,Ct_red,Ct_kid_u,Ct_liv_u,Ct_adi_u,Ct_r
ob_u,Ct_lun_u,Ct_mus_u,Ct_spl_u,Ct_yel_u,Ct_hea_u,Ct_bra_u,Ct_rep_u,Ct_red_u,C_ven,C_art,Vmax_w_liv_a,Vmax_w_kid_a,Km_liv_a,Km_kid_a,Vmax_w_gut_e,Vmax_w_kid_e,Vmax_w_liv_e,Vmax_w_ski_e,Vmax_w_adi_e,Vmax_w_rob_e,Vmax_w_lun_e,Vmax_w_mus_e,Vmax_w_spl_e,Vmax_w_yel_e,Vmax_w_hea_e,Vmax_w_bra_e,Vmax_w_rep_e,Vmax_w_red_e,Km_gut_e,Km_kid_e,Km_liv_e,Km_ski_e,Km_adi_e,Km_rob_e,Km_lun_e,Km_mus_e,Km_spl_e,Km_yel_e,Km_hea_e,Km_bra_e,Km_rep_e,Km_red_e,Vmax_w_gut_C1_a,Vmax_w_gut_C2_7_a,Vmax_w_gut_col_a,Km_gut_C1_a,Km_gut_C2_7_a,Km_gut_col_a,QUR,perm_kid_a,perm_liv_a,perm_sto,perm_C1_a,perm_C2_7_a,perm_col_a,perm_C1_b,perm_C2_7_b,perm_col_b,Qfec,C_vpl,C_vpl_u,Ka_e_sto,Ka_e_C1,
Ka_e_C2_7,Ka_e_col,V_gut_lum,V_ent,Ani_mass,Kt_s,Kt_1,
Kt_2_7, Kt_c,SigSL,
SigSL2,SigSL3,SigSL4,SigSL5,C_surf,Qven,Qart,Qgutblo,Ct_ski_u,Ct_ski,Qfab,Flow_Scaler,F_ven,
F_lun,F_art,F_liv, F_kid, F_ski, F_adi, F_rob, F_gut,
F_mus, F_hep, F_spl, F_yel, F_hea, F_bra, F_rep,
F_red, F_total_QC,V_liv, V_kid, V_nep, V_ski,
V_adi, V_rob, V_ven, V_art, V_lun, V_mus,
V_spl,V_yel,V_hea,V_bra, V_rep, V_red,
Vol_Scaler,Q_stoI, Q_stoT, Q_C1I, Q_C1T,
Q_C2_7I, Q_C2_7T, Q_colI, Q_colT,
# Permeability-limited model (1st metabolite)
Qstodism,QC1dism,QC2_7dism,Qcoldism,C_sto_dism,C_C1_dism,C_C2_7_dism,C_col_dism,QentC1absm,QentC2_7absm,Qentcolabsm,C_ent_C1m,C_ent_C2_7m,C_ent_colm,Ct_gut_blom,Fam,FDpm,rm,Qbilm,QentC1m,QentC2_7m,Qentcolm,Qstoabsm,C1totm,C2_7totm,Ccoltotm,fut_tism,fut_adim,Kp_livm,Kp_kidm,Kp_skim,Kp_adim,Kp_robm,Kp_lunm,Kp_musm,Kp_splm,Kp_yelm,Kp_heam,Kp_bram,Kp_repm,Kp_redm,fup_adjm,fup_adj_livm,fup_adj_kidm,fup_adj_skim,fup_adj_adim,fup_adj_robm,fup_adj_lunm,fup_adj_musm,fup_adj_splm,fup_adj_yelm,fup_adj_heam,fup_adj_bram,fup_adj_repm,fup_adj_redm,Qlivtotm,Qlivem,Qlivim,Qkidtotm,Qkidem,Qkidim,Qurim,Qnepm,Qskitotm,Qskiem,Qskiim,Qaditotm,Qadiem,Qadiim,Qrobtotm,Qrobem,Qrobim,Qluntotm,Qlunem,Qlunim,Qmustotm,Qmusem,Qmusim,Qspltotm,Qsplem,Qsplim,Qyeltotm,Qyelem,Qyelim,Qheatotm,Qheaem,Qheaim,Qbratotm,Qbraem,Qbraim,Qreptotm,Qrepem,Qrepim,Qredtotm,Qredem,Qredim,V_liv_e,V_liv_v,V_liv_i,V_liv_xm,V_liv_xm2,
V_kid_e,V_kid_v,V_kid_i,V_kid_xm,V_kid_xm2,
V_ski_e,V_ski_v,V_ski_i,V_ski_x,V_ski_xm,V_ski_xm2,
V_adi_e,V_adi_v,V_adi_i,V_adi_xm,V_adi_xm2,V_rob_e,V_rob_v,V_rob_i,V_rob_xm,V_rob_xm2,
V_lun_e,
V_lun_v,V_lun_i,V_lun_xm,V_lun_xm2,V_mus_e,V_mus_v,V_mus_i,V_mus_xm,V_mus_xm2,V_spl_e,
V_spl_v,
V_spl_i,V_spl_xm,V_spl_xm2,V_yel_e,V_yel_v,V_yel_i,V_yel_xm,V_yel_xm2,V_hea_e,V_hea_v,V_hea_i,V_hea_xm,V_hea_xm2,V_bra_e,V_bra_v,V_bra_i,V_bra_xm,V_bra_xm2,V_rep_e,V_rep_v,V_rep_i,V_rep_xm,V_rep_xm2,V_red_e,V_red_v,V_red_i,
V_red_xm,V_red_xm2,Ci_liv_um,Ce_liv_um,Ce_livm,Ci_livm, Ci_kid_um,Ce_kid_um,
Ce_kidm,Ci_kidm,C_nepm,
Ci_ski_um,Ce_ski_um,Ce_skim,Ci_skim,
Ci_adi_um,Ce_adi_um,Ce_adim, Ci_adim,
Ci_rob_um,Ce_rob_um,Ce_robm,Ci_robm,
```

```
Ci_lun_um,Ce_lun_um,Ce_lunm,Ci_lunm,Ci_mus_
um,Ce_mus_um,
Ce_musm,Ci_musm,Ci_spl_um,Ce_spl_um,Ce_spl
m,Ci_splm,Ci_yel_um,Ce_yel_um,Ce_yelm,Ci_yelm
,Ci_hea_um,
Ce_hea_um,Ce_heam,Ci_heam,Ci_bra_um,Ce_bra
_um,Ce_bram,Ci_bram,Ci_rep_um,Ce_rep_um,Ce
_repm,Ci_repm,Ci_red_um,Ce_red_um,Ce_redm,C
i_redm,C_venm,C_artm,Vmax_w_kid_bm,Vmax_w
_liv_bm,Vmax_w_kid_am,Vmax_w_liv_am,Km_kid
_bm,Km_kid_am,Km_liv_bm,Km_liv_am,Vmax_w_
gut_C1_am,Vmax_w_gut_C2_7_am,Vmax_w_gut_
col_am,Km_gut_C1_am,Km_gut_C2_7_am,Km_gut
_col_am,perm_kid_bm,perm_kid_am,perm_liv_b
m,perm_liv_am,perm_skim,perm_adim,perm_rob
m,perm_lunm,perm_musm,perm_splm,perm_yel
m,perm_heam,perm_bram,perm_repm,perm_red
m,perm_stom,perm_C1_am,perm_C2_7_am,perm
_col_am, perm_C1_bm, perm_C2_7_bm,
perm_col_bm,
PStc_kid_bm,PStc_kid_am,PStc_liv_bm,PStc_liv_a
m, PStc_skim,PStc_adim,
PStc_robm,PStc_lunm,PStc_musm,PStc_splm,PStc
_yelm,PStc_heam,PStc_bram,PStc_repm,PStc_red
m,Qfecm,C_vplm,C_vpl_um, SigSLm, SigSL2m,
SigSL3m,SigSL4m,perm_ski,Qvenm,Qartm,Qgutblo
m,
# Permeability-limited model (2nd metabolite)
Qstodism2,QC1dism2,QC2_7dism2,Qcoldism2,C_sto
_dism2,C_C1_dism2,C_C2_7_dism2,C_col_dism2,
QentC1absm2,QentC2_7absm2,Qentcolabsm2,C_e
nt_C1m2,C_ent_C2_7m2,C_ent_colm2,Ct_gut_blo
m2,Fam2,FDpm2,rm2,Qbilm2,QentC1m2,QentC2_
7m2,Qentcolm2,Qstoabsm2,C1totm2,C2_7totm2,
Ccoltotm2,fut_tism2,fut_adim2,Kp_livm2,Kp_kidm
2,Kp_skim2,Kp_adim2,Kp_robm2,Kp_lunm2,Kp_m
usm2,Kp_splm2,Kp_yelm2,Kp_heam2,Kp_bram2,K
p_repm2,Kp_redm2,fup_adjm2,fup_adj_livm2,fup
_adj_kidm2,fup_adj_skim2,fup_adj_adim2,fup_adj
_robm2,fup_adj_lunm2,fup_adj_musm2,fup_adj_s
plm2,fup_adj_yelm2,fup_adj_heam2,fup_adj_bra
m2,fup_adj_repm2,fup_adj_redm2,Qlivtotm2,Qliv
em2,Qlivim2,Qkidtotm2,Qkidem2,Qkidim2,Qurim2
,Qnepm2,Qskitotm2,Qskiem2,Qskiim2,Qaditotm2,
Qadiem2,Qadiim2,Qrobtotm2,Qrobem2,Qrobim2,
Qluntotm2,Qlunem2,Qlunim2,Qmustotm2,Qmuse
m2,Qmusim2,Qspltotm2,Qsplem2,Qsplim2,Qyelto
tm2,Qyelem2,Qyelim2,Qheatotm2,Qheaem2,Qhea
im2,Qbratotm2,Qbraem2,Qbraim2,Qreptotm2,Qre
pem2,Qrepim2,Qredtotm2,Qredem2,Qredim2,Ci_l
iv_um2,Ce_liv_um2,Ce_livm2,Ci_livm2,Ci_kid_um
2,Ce_kid_um2,Ce_kidm2,Ci_kidm2,C_nepm2,Ci_sk
i_um2,Ce_ski_um2,Ce_skim2,Ci_skim2,Ci_adi_um
2,Ce_adi_um2,Ce_adim2,Ci_adim2,Ci_rob_um2,Ce
_rob_um2,Ce_robm2,Ci_robm2,Ci_lun_um2,Ce_lu
n_um2,Ce_lunm2,Ci_lunm2,Ci_mus_um2,Ce_mus
_um2,Ce_musm2,Ci_musm2,Ci_spl_um2,Ce_spl_u
m2,Ce_splm2,Ci_splm2,Ci_yel_um2,Ce_yel_um2,C
e_yelm2,Ci_yelm2,Ci_hea_um2,Ce_hea_um2,Ce_h
eam2,Ci_heam2,Ci_bra_um2,Ce_bra_um2,Ce_bra
m2,Ci_bram2,Ci_rep_um2,Ce_rep_um2,Ce_repm2
,Ci_repm2,Ci_red_um2,Ce_red_um2,Ce_redm2,Ci
_redm2,C_venm2,C_artm2,Vmax_w_kid_bm2,Vm
ax_w_liv_bm2,Vmax_w_kid_am2,Vmax_w_liv_am
2,Km_kid_bm2,Km_kid_am2,Km_liv_bm2,Km_liv_
am2,Vmax_w_gut_C1_am2,Vmax_w_gut_C2_7_a
m2,Vmax_w_gut_col_am2,
Km_gut_C1_am2,Km_gut_C2_7_am2,Km_gut_col_
am2,perm_kid_bm2,perm_kid_am2,perm_liv_bm
2,perm_liv_am2,perm_skim2,perm_adim2,perm_r
obm2,perm_lunm2,perm_musm2,perm_splm2,per
m_yelm2,perm_heam2,perm_bram2,perm_repm2
,perm_redm2,perm_stom2,perm_C1_am2,perm_C
2_7_am2,perm_col_am2,perm_C1_bm2,perm_C2
_7_bm2,perm_col_bm2,
PStc_kid_bm2,PStc_kid_am2,PStc_liv_bm2,PStc_li
v_am2,PStc_skim2,
PStc_adim2,PStc_robm2,PStc_lunm2,PStc_musm2,
PStc_splm2,PStc_yelm2,PStc_heam2,PStc_bram2,
PStc_repm2,PStc_redm2,Qfecm2,C_vplm2,C_vpl_
um2,Qvenm2,Qartm2,Qgutblom2,
# ICRP lung model
A1, A_T1, A_bnd1, I1, I_T1, I_bnd1, LNTH1,
LNTH_T1, LNTH_bnd1, BB1, BB_T1, BB_bnd1,
BB_seq1, BB_seq_T1, BB_seq_bnd1, bb1, bb_T1,
bb_bnd1, bb_seq1,bb_seq_T1, bb_seq_bnd1,
ET21, ET2_T1, ET2_bnd1, ET_seq1, ET_seq_T1,
ET_seq_bnd1, LNET1, LNET_T1, LNET_bnd1, ET11,
NB1,
#-----------------------
};
Inputs = {Fabric, Solution_ingest, Solid_ingest,
Inhale, Q_iv, Q_ivm, Q_ivm2,};
Initialize {
# ICRP lung model
SP = (Ss + Fr) * (Sr - Ss);
SPT = (1 - Fr) * (Sr - Ss);
ST = Ss;
Lum_blo = (6 * f1) / (1-f1); # rate from GIT lumen
to Q_gut_blood.
# Gut
Kt_s = 1 / (Kt_s_p * 3600);
Kt_1 = 1 / (Kt_1_p * 3600);
Kt_2_7 = 1 / (Kt_2_7_p * 3600);
Kt_c = 1 / (Kt_c_p * 3600);
# Ka per gut compartment (lumen to enterocyte)
Ka_s = (2/R_sto)* SEF_s * Peff_sto;
Ka_1 = (2/R_C1) * SEF_C1 * Peff;
Ka_2_7 = (2/R_C2_7) * SEF_C2_7 * Peff;
Ka_c = (2/R_col) * SEF_c * Peff;
# Ka per gut compartment (enterocyte to gut
blood)
Ka_e_sto = 2 * pi * sqrt((V_ent_sto + V_sto) / (pi *
L_sto)) * L_sto * Peff_sto; # surface area x Peff
```

```
Ka_e_C1 = 2 * pi * sqrt((V_ent_C1 + V_C1) / (pi *
L_C1)) * L_C1 * Peff;
Ka_e_C2_7 = 2 * pi * sqrt((V_ent_C2_7 + V_C2_7)
/ (pi * L_C2_7)) * L_C2_7 * Peff;
Ka_e_col = 2 * pi * sqrt((V_ent_col + V_col) / (pi *
L_col)) * L_col * Peff;
DR = (Deff/(p * h * r)) * ((1 + (2 * S))/ S); #
dissolution rate
PR = (1/PrecipTime); # precipitation rate
# Body
Flow_Scaler = 1 / (Fr_F_kid + Fr_F_ski + Fr_F_adi +
Fr_F_rob + Fr_F_gut + Fr_F_mus + Fr_F_hep +
Fr_F_spl + Fr_F_yel + Fr_F_hea + Fr_F_bra +
Fr_F_rep + Fr_F_red);
# Blood flows (mL/ sec)
F_kid = Flow_Scaler * Fr_F_kid * F_total;
F_ski = Flow_Scaler * Fr_F_ski * F_total;
F_adi = Flow_Scaler * Fr_F_adi * F_total;
F_rob = Flow_Scaler * Fr_F_rob * F_total;
F_gut = Flow_Scaler * Fr_F_gut * F_total;
F_mus = Flow_Scaler * Fr_F_mus * F_total;
F_hep = Flow_Scaler * Fr_F_hep * F_total;
F_spl = Flow_Scaler * Fr_F_spl * F_total;
F_yel = Flow_Scaler * Fr_F_yel * F_total;
F_hea = Flow_Scaler * Fr_F_hea * F_total;
F_bra = Flow_Scaler * Fr_F_bra * F_total;
F_rep = Flow_Scaler * Fr_F_rep * F_total;
F_red = Flow_Scaler * Fr_F_red * F_total;
F_ven = F_total;
F_lun = F_total;
F_art = F_total;
F_liv = (Fr_F_gut * F_total) + (Fr_F_hep * F_total) +
(Fr_F_spl * F_total); # flow to liver.
# Calculate total flow (quality control; should equal
F_total specified).
F_total_QC = (Flow_Scaler * Fr_F_kid * F_total) +
(Flow_Scaler * Fr_F_ski * F_total) + (Flow_Scaler *
Fr_F_adi * F_total) + (Flow_Scaler * Fr_F_rob *
F_total) + (Flow_Scaler * Fr_F_gut * F_total) +
(Flow_Scaler * Fr_F_mus * F_total) + (Flow_Scaler
* Fr_F_hep * F_total) + (Flow_Scaler * Fr_F_spl *
F_total) + (Flow_Scaler * Fr_F_yel * F_total) +
(Flow_Scaler * Fr_F_hea * F_total) + (Flow_Scaler
* Fr_F_bra * F_total) + (Flow_Scaler * Fr_F_rep *
F_total) + (Flow_Scaler * Fr_F_red * F_total);
# Tissue volumes
Vol_Scaler = 1 / (Fr_V_liv + Fr_V_kid + Fr_V_nep +
Fr_V_ski + Fr_V_adi + Fr_V_rob + Fr_V_ven +
Fr_V_art + Fr_V_lun + Fr_V_mus + Fr_V_spl +
Fr_V_yel + Fr_V_hea + Fr_V_bra + Fr_V_rep +
Fr_V_red);
V_liv = Vol_Scaler * Fr_V_liv * Mass_oral;
V_kid = Vol_Scaler * Fr_V_kid * Mass_oral;
V_nep = Vol_Scaler * Fr_V_nep * Mass_oral;
V_ski = Vol_Scaler * Fr_V_ski * Mass_oral;
V_adi = Vol_Scaler * Fr_V_adi * Mass_oral;
V_rob = Vol_Scaler * Fr_V_rob * Mass_oral;
V_ven = Vol_Scaler * Fr_V_ven * Mass_oral;
V_art = Vol_Scaler * Fr_V_art * Mass_oral;
V_lun = Vol_Scaler * Fr_V_lun * Mass_oral;
V_mus = Vol_Scaler * Fr_V_mus * Mass_oral;
V_spl = Vol_Scaler * Fr_V_spl * Mass_oral;
V_yel = Vol_Scaler * Fr_V_yel * Mass_oral;
V_hea = Vol_Scaler * Fr_V_hea * Mass_oral;
V_bra = Vol_Scaler * Fr_V_bra * Mass_oral;
V_rep = Vol_Scaler * Fr_V_rep * Mass_oral;
V_red = Vol_Scaler * Fr_V_red * Mass_oral;
QUR = (1 / (V_nep / QUR_p)); # urine flow rate
# Transporters for parent compound (apical
transporters only given perfusion-limited model)
Vmax_w_liv_a = V_max_liv_a * Tra_exp_liv_a *
D_liv * V_liv;
Km_liv_a = Km_liv_p_a / 1000;
Vmax_w_kid_a = V_max_kid_a * Tra_exp_kid_a *
D_kid * V_kid;
Km_kid_a = Km_kid_p_a / 1000;
Vmax_w_gut_C1_a = V_max_gut_C1_a *
Tra_exp_gut_C1_a * D_ent_C1 * V_ent_C1;
Km_gut_C1_a = Km_gut_p_C1_a / 1000;
Vmax_w_gut_C2_7_a = V_max_gut_C2_7_a *
Tra_exp_gut_C2_7_a * D_ent_C2_7 * V_ent_C2_7;
Km_gut_C2_7_a = Km_gut_p_C2_7_a / 1000;
Vmax_w_gut_col_a = V_max_gut_col_a *
Tra_exp_gut_col_a * D_ent_col * V_ent_col;
Km_gut_col_a = Km_gut_p_col_a / 1000;
# Enzymes for parent compound
Vmax_w_kid_e = V_max_kid_e * Enz_exp_kid_e *
D_kid * V_kid;
Vmax_w_liv_e = V_max_liv_e * Enz_exp_liv_e *
D_liv * V_liv;
Vmax_w_ski_e = V_max_ski_e * Enz_exp_ski_e *
D_ski * V_ski;
Vmax_w_adi_e = V_max_adi_e * Enz_exp_adi_e *
D_adi * V_adi;
Vmax_w_rob_e = V_max_rob_e * Enz_exp_rob_e
* D_rob * V_rob;
Vmax_w_lun_e = V_max_lun_e * Enz_exp_lun_e *
D_lun * V_lun;
Vmax_w_mus_e = V_max_mus_e *
Enz_exp_mus_e * D_mus * V_mus;
Vmax_w_spl_e = V_max_spl_e * Enz_exp_spl_e *
D_spl * V_spl;
Vmax_w_yel_e = V_max_yel_e * Enz_exp_yel_e *
D_yel * V_yel;
Vmax_w_hea_e = V_max_hea_e * Enz_exp_hea_e
* D_hea * V_hea;
Vmax_w_bra_e = V_max_bra_e * Enz_exp_bra_e *
D_bra * V_bra;
Vmax_w_rep_e = V_max_rep_e * Enz_exp_rep_e
* D_rep * V_rep;
Vmax_w_red_e = V_max_red_e * Enz_exp_red_e
* D_red * V_red;
Vmax_w_gut_e = V_max_gut_e * Enz_exp_gut_e *
D_ent_C2_7 * V_ent_C2_7;
```

```
Km_kid_e = Km_kid_p_e / 1000;
Km_liv_e = Km_liv_p_e / 1000;
Km_ski_e = Km_ski_p_e / 1000;
Km_adi_e = Km_adi_p_e / 1000;
Km_rob_e = Km_rob_p_e / 1000;
Km_lun_e = Km_lun_p_e / 1000;
Km_mus_e = Km_mus_p_e / 1000;
Km_spl_e = Km_spl_p_e / 1000;
Km_yel_e = Km_yel_p_e / 1000;
Km_hea_e = Km_hea_p_e / 1000;
Km_bra_e = Km_bra_p_e / 1000;
Km_rep_e = Km_rep_p_e / 1000;
Km_red_e = Km_red_p_e / 1000;
Km_gut_e = Km_gut_p_e / 1000;
# Calculation of tissue Kp
fup_adj = 1/((pow(10,logP_pla)*((Vnlp +
Vphp)/Vwp)) + 1 + ((1 - fup_exp)/fup_exp)); #
adjusted fup (accounts for lipid binding in plasma)
logP_adi = (1.115 * logP_tis) - 1.35;
K_adi = pow(10,logP_adi);
K_tis = pow(10,logP_tis);
# Poulin equation for fut
fut_tis = (1/((((1 - fup_adj)/fup_adj) * RAtp_tis) +
1)); # fut_tis is for all tissues but adipose and
yellow marrow
fut_adi = (1/((((1 - fup_adj)/fup_adj) * RAtp_adi) +
1));
# Poulin & Theil (homogneous) method for Kp
calculation
Kp_liv = ((K_tis * (Vnlt_liv + (0.3 * Vpht_liv))) +
(Vwt_liv + (0.7 * Vpht_liv))) / ((K_tis * (Vnlp + (0.3
* Vphp))) + (Vwp + (0.7 * Vphp))) * (fup_adj /
fut_tis);
Kp_kid = ((K_tis * (Vnlt_kid + (0.3 * Vpht_kid))) +
(Vwt_kid + (0.7 * Vpht_kid))) / ((K_tis * (Vnlp + (0.3
* Vphp))) + (Vwp + (0.7 * Vphp))) * (fup_adj /
fut_tis);
Kp_ski = ((K_tis * (Vnlt_ski + (0.3 * Vpht_ski))) +
(Vwt_ski + (0.7 * Vpht_ski))) / ((K_tis * (Vnlp + (0.3
* Vphp))) + (Vwp + (0.7 * Vphp))) * (fup_adj /
fut_tis);
Kp_adi = ((K_adi * (Vnlt_adi + (0.3 * Vpht_adi))) +
(Vwt_adi + (0.7 * Vpht_adi))) / ((K_adi * (Vnlp +
(0.3 * Vphp))) + (Vwp + (0.7 * Vphp))) * (fup_adj /
fut_adi); # n.b. fut_adi & K_adi
Kp_yel = ((K_adi * (Vnlt_yel + (0.3 * Vpht_yel))) +
(Vwt_yel + (0.7 * Vpht_yel))) / ((K_adi * (Vnlp +
(0.3 * Vphp))) + (Vwp + (0.7 * Vphp))) * (fup_adj /
fut_adi); # n.b. fut_adi & K_adi
Kp_rob = ((K_tis * (Vnlt_rob + (0.3 * Vpht_rob))) +
(Vwt_rob + (0.7 * Vpht_rob))) / ((K_tis * (Vnlp +
(0.3 * Vphp))) + (Vwp + (0.7 * Vphp))) * (fup_adj /
fut_tis);
Kp_lun = ((K_tis * (Vnlt_lun + (0.3 * Vpht_lun))) +
(Vwt_lun + (0.7 * Vpht_lun))) / ((K_tis * (Vnlp +
(0.3 * Vphp))) + (Vwp + (0.7 * Vphp))) * (fup_adj /
fut_tis);
Kp_mus = ((K_tis * (Vnlt_mus + (0.3 * Vpht_mus)))
+ (Vwt_mus + (0.7 * Vpht_mus))) / ((K_tis * (Vnlp +
(0.3 * Vphp))) + (Vwp + (0.7 * Vphp))) * (fup_adj /
fut_tis);
Kp_spl = ((K_tis * (Vnlt_spl + (0.3 * Vpht_spl))) +
(Vwt_spl + (0.7 * Vpht_spl))) / ((K_tis * (Vnlp + (0.3
* Vphp))) + (Vwp + (0.7 * Vphp))) * (fup_adj /
fut_tis);
Kp_hea = ((K_tis * (Vnlt_hea + (0.3 * Vpht_hea))) +
(Vwt_hea + (0.7 * Vpht_hea))) / ((K_tis * (Vnlp +
(0.3 * Vphp))) + (Vwp + (0.7 * Vphp))) * (fup_adj /
fut_tis);
Kp_bra = ((K_tis * (Vnlt_bra + (0.3 * Vpht_bra))) +
(Vwt_bra + (0.7 * Vpht_bra))) / ((K_tis * (Vnlp +
(0.3 * Vphp))) + (Vwp + (0.7 * Vphp))) * (fup_adj /
fut_tis);
Kp_rep = ((K_tis * (Vnlt_rep + (0.3 * Vpht_rep))) +
(Vwt_rep + (0.7 * Vpht_rep))) / ((K_tis * (Vnlp +
(0.3 * Vphp))) + (Vwp + (0.7 * Vphp))) * (fup_adj /
fut_tis);
Kp_red = ((K_tis * (Vnlt_red + (0.3 * Vpht_red))) +
(Vwt_red + (0.7 * Vpht_red))) / ((K_tis * (Vnlp +
(0.3 * Vphp))) + (Vwp + (0.7 * Vphp))) * (fup_adj /
fut_tis);
# Berezhkovskiy method for Kp calculation
#Kp_liv = ((K_tis * (Vnlt_liv + (0.3 * Vpht_liv))) +
((Vwt_liv / fut_tis) + (0.7 * Vpht_liv))) / ((K_tis *
(Vnlp + (0.3 * Vphp))) + ((Vwp / fup_adj) + (0.7 *
Vphp)));
#Kp_kid = ((K_tis * (Vnlt_kid + (0.3 * Vpht_kid))) +
((Vwt_kid / fut_tis) + (0.7 * Vpht_kid))) / ((K_tis *
(Vnlp + (0.3 * Vphp))) + ((Vwp / fup_adj) + (0.7 *
Vphp)));
#Kp_ski = ((K_tis * (Vnlt_ski + (0.3 * Vpht_ski))) +
((Vwt_ski / fut_tis) + (0.7 * Vpht_ski))) / ((K_tis *
(Vnlp + (0.3 * Vphp))) + ((Vwp / fup_adj) + (0.7 *
Vphp)));
#Kp_adi = ((K_adi * (Vnlt_adi + (0.3 * Vpht_adi))) +
((Vwt_adi / fut_tis) + (0.7 * Vpht_adi))) / ((K_adi *
(Vnlp + (0.3 * Vphp))) + ((Vwp / fup_adj) + (0.7 *
Vphp))); # n.b. fut_adi & K_adi
#Kp_yel = ((K_adi * (Vnlt_yel + (0.3 * Vpht_yel))) +
((Vwt_yel / fut_tis) + (0.7 * Vpht_yel))) / ((K_adi *
(Vnlp + (0.3 * Vphp))) + ((Vwp / fup_adj) + (0.7 *
Vphp))); # n.b. fut_adi & K_adi
#Kp_rob = ((K_tis * (Vnlt_rob + (0.3 * Vpht_rob))) +
((Vwt_rob / fut_tis) + (0.7 * Vpht_rob))) / ((K_tis *
(Vnlp + (0.3 * Vphp))) + ((Vwp / fup_adj) + (0.7 *
Vphp)));
#Kp_lun = ((K_tis * (Vnlt_lun + (0.3 * Vpht_lun))) +
((Vwt_lun / fut_tis) + (0.7 * Vpht_lun))) / ((K_tis *
(Vnlp + (0.3 * Vphp))) + ((Vwp / fup_adj) + (0.7 *
Vphp)));
#Kp_mus = ((K_tis * (Vnlt_mus + (0.3 *
Vpht_mus))) + ((Vwt_mus / fut_tis) + (0.7 *
Vpht_mus))) / ((K_tis * (Vnlp + (0.3 * Vphp))) +
((Vwp / fup_adj) + (0.7 * Vphp)));
```

```
#Kp_spl = ((K_tis * (Vnlt_spl + (0.3 * Vpht_spl))) +
((Vwt_spl / fut_tis) + (0.7 * Vpht_spl))) / ((K_tis *
(Vnlp + (0.3 * Vphp))) + ((Vwp / fup_adj) + (0.7 *
Vphp)));
#Kp_hea = ((K_tis * (Vnlt_hea + (0.3 * Vpht_hea)))
+ ((Vwt_hea / fut_tis) + (0.7 * Vpht_hea))) / ((K_tis
* (Vnlp + (0.3 * Vphp))) + ((Vwp / fup_adj) + (0.7 *
Vphp)));
#Kp_bra = ((K_tis * (Vnlt_bra + (0.3 * Vpht_bra))) +
((Vwt_bra / fut_tis) + (0.7 * Vpht_bra))) / ((K_tis *
(Vnlp + (0.3 * Vphp))) + ((Vwp / fup_adj) + (0.7 *
Vphp)));
#Kp_rep = ((K_tis * (Vnlt_rep + (0.3 * Vpht_rep))) +
((Vwt_rep / fut_tis) + (0.7 * Vpht_rep))) / ((K_tis *
(Vnlp + (0.3 * Vphp))) + ((Vwp / fup_adj) + (0.7 *
Vphp)));
#Kp_red = ((K_tis * (Vnlt_red + (0.3 * Vpht_red))) +
((Vwt_red / fut_tis) + (0.7 * Vpht_red))) / ((K_tis *
(Vnlp + (0.3 * Vphp))) + ((Vwp / fup_adj) + (0.7 *
Vphp)));
# Quality control
V_gut_lum = V_sto + V_C1 + V_C2_7 + V_col;
V_ent = V_ent_sto + V_ent_C1 + V_ent_C2_7 +
V_ent_col;
Ani_mass = (D_kid * V_kid) + (D_liv * V_liv) +
(D_ski * V_ski) + (D_adi * V_adi) + (D_rob * V_rob)
+ (D_lun * V_lun) + (D_mus * V_mus) + (D_spl *
V_spl) + (D_yel * V_yel) + (D_hea * V_hea) +
(D_bra * V_bra) + (D_rep * V_rep) + (D_red *
V_red) + (D_ent * V_ent) + (D_gut_lum *
V_gut_lum) + (D_blo * (V_ven + V_art));
# Permeability-limited model (1st metabolite)
fup_adjm = 1/((pow(10,logP_plam)*((Vnlp +
Vphp)/Vwp)) + 1 + ((1 - fup_expm)/fup_expm));
logP_adim = (1.115 * logP_tism) - 1.35;
K_adim = pow(10,logP_adim);
K_tism = pow(10,logP_tism);
# Transporters for metabolite
Vmax_w_kid_bm = V_max_kid_bm *
Tra_exp_kid_bm * D_kid * V_kid; # Whole-body
Vmax for kidney (mg/ sec)
Km_kid_bm = Km_kid_p_bm / 1000; # Km (mg/
mL)
Vmax_w_kid_am = V_max_kid_am *
Tra_exp_kid_am * D_kid * V_kid;
Km_kid_am = Km_kid_p_am / 1000;
Vmax_w_liv_bm = V_max_liv_bm *
Tra_exp_liv_bm * D_liv * V_liv;
Km_liv_bm = Km_liv_p_bm / 1000;
Vmax_w_liv_am = V_max_liv_am *
Tra_exp_liv_am * D_liv * V_liv;
Km_liv_am = Km_liv_p_am / 1000;
Vmax_w_gut_C1_am = V_max_gut_C1_am *
Tra_exp_gut_C1_am * D_ent_C1 * V_ent_C1;
Km_gut_C1_am = Km_gut_p_C1_am / 1000;
Vmax_w_gut_C2_7_am = V_max_gut_C2_7_am *
Tra_exp_gut_C2_7_am * D_ent_C2_7 *
V_ent_C2_7;
Km_gut_C2_7_am = Km_gut_p_C2_7_am / 1000;
Vmax_w_gut_col_am = V_max_gut_col_am *
Tra_exp_gut_col_am * D_ent_col * V_ent_col;
Km_gut_col_am = Km_gut_p_col_am / 1000;
fut_tism = (1/((((1 - fup_adjm)/fup_adjm) *
RAtp_tis) + 1));
fut_adim = (1/((((1 - fup_adjm)/fup_adjm) *
RAtp_adi) + 1));
# Poulin & Theil (extracellular) method for
permeability-limited tissues
Kp_livm = fup_adjm / fut_tism;
Kp_kidm = fup_adjm / fut_tism;
Kp_skim = fup_adjm / fut_tism;
Kp_adim = fup_adjm / fut_adim; # n.b. fut_adi
Kp_yelm = fup_adjm / fut_adim; # n.b. fut_adi
Kp_robm = fup_adjm / fut_tism;
Kp_lunm = fup_adjm / fut_tism;
Kp_musm = fup_adjm / fut_tism;
Kp_splm = fup_adjm / fut_tism;
Kp_heam = fup_adjm / fut_tism;
Kp_bram = fup_adjm / fut_tism;
Kp_repm = fup_adjm / fut_tism;
Kp_redm = fup_adjm / fut_tism;

# Berezhkovskiy method for Kp calculation
#Kp_livm = ((K_tism * (Vnlt_liv + (0.3 * Vpht_liv)))
+ ((Vwt_liv / fut_tism) + (0.7 * Vpht_liv))) /
((K_tism * (Vnlp + (0.3 * Vphp))) + ((Vwp /
fup_adjm) + (0.7 * Vphp)));
#Kp_kidm = ((K_tism * (Vnlt_kid + (0.3 *
Vpht_kid))) + ((Vwt_kid / fut_tism) + (0.7 *
Vpht_kid))) / ((K_tism * (Vnlp + (0.3 * Vphp))) +
((Vwp / fup_adjm) + (0.7 * Vphp)));
#Kp_skim = ((K_tism * (Vnlt_ski + (0.3 * Vpht_ski)))
+ ((Vwt_ski / fut_tism) + (0.7 * Vpht_ski))) /
((K_tism * (Vnlp + (0.3 * Vphp))) + ((Vwp /
fup_adjm) + (0.7 * Vphp)));
#Kp_adim = ((K_adim * (Vnlt_adi + (0.3 *
Vpht_adi))) + ((Vwt_adi / fut_tism) + (0.7 *
Vpht_adi))) / ((K_adim * (Vnlp + (0.3 * Vphp))) +
((Vwp / fup_adjm) + (0.7 * Vphp))); # n.b. fut_adi &
K_adi
#Kp_yelm = ((K_adim * (Vnlt_yel + (0.3 *
Vpht_yel))) + ((Vwt_yel / fut_tism) + (0.7 *
Vpht_yel))) / ((K_adim * (Vnlp + (0.3 * Vphp))) +
((Vwp / fup_adjm) + (0.7 * Vphp))); # n.b. fut_adi &
K_adi
#Kp_robm = ((K_tism * (Vnlt_rob + (0.3 *
Vpht_rob))) + ((Vwt_rob / fut_tism) + (0.7 *
Vpht_rob))) / ((K_tism * (Vnlp + (0.3 * Vphp))) +
((Vwp / fup_adjm) + (0.7 * Vphp)));
#Kp_lunm = ((K_tism * (Vnlt_lun + (0.3 *
Vpht_lun))) + ((Vwt_lun / fut_tism) + (0.7 *
```

```
Vpht_lun))) / ((K_tism * (Vnlp + (0.3 * Vphp))) +
((Vwp / fup_adjm) + (0.7 * Vphp)));
#Kp_musm = ((K_tism * (Vnlt_mus + (0.3 *
Vpht_mus))) + ((Vwt_mus / fut_tism) + (0.7 *
Vpht_mus))) / ((K_tism * (Vnlp + (0.3 * Vphp))) +
((Vwp / fup_adjm) + (0.7 * Vphp)));
#Kp_splm = ((K_tism * (Vnlt_spl + (0.3 *
Vpht_spl))) + ((Vwt_spl / fut_tism) + (0.7 *
Vpht_spl))) / ((K_tism * (Vnlp + (0.3 * Vphp))) +
((Vwp / fup_adjm) + (0.7 * Vphp)));
#Kp_heam = ((K_tism * (Vnlt_hea + (0.3 *
Vpht_hea))) + ((Vwt_hea / fut_tism) + (0.7 *
Vpht_hea))) / ((K_tism * (Vnlp + (0.3 * Vphp))) +
((Vwp / fup_adjm) + (0.7 * Vphp)));
#Kp_bram = ((K_tism * (Vnlt_bra + (0.3 *
Vpht_bra))) + ((Vwt_bra / fut_tism) + (0.7 *
Vpht_bra))) / ((K_tism * (Vnlp + (0.3 * Vphp))) +
((Vwp / fup_adjm) + (0.7 * Vphp)));
#Kp_repm = ((K_tism * (Vnlt_rep + (0.3 *
Vpht_rep))) + ((Vwt_rep / fut_tism) + (0.7 *
Vpht_rep))) / ((K_tism * (Vnlp + (0.3 * Vphp))) +
((Vwp / fup_adjm) + (0.7 * Vphp)));
#Kp_redm = ((K_tism * (Vnlt_red + (0.3 *
Vpht_red))) + ((Vwt_red / fut_tism) + (0.7 *
Vpht_red))) / ((K_tism * (Vnlp + (0.3 * Vphp))) +
((Vwp / fup_adjm) + (0.7 * Vphp)));
# Fraction unbound in tissue given fup_adj in
plasma.
fup_adj_livm = fup_adjm / Kp_livm;
fup_adj_kidm = fup_adjm / Kp_kidm;
fup_adj_skim = fup_adjm / Kp_skim;
fup_adj_adim = fup_adjm / Kp_adim;
fup_adj_robm = fup_adjm / Kp_robm;
fup_adj_lunm = fup_adjm / Kp_lunm;
fup_adj_musm = fup_adjm / Kp_musm;
fup_adj_splm = fup_adjm / Kp_splm;
fup_adj_yelm = fup_adjm / Kp_yelm;
fup_adj_heam = fup_adjm / Kp_heam;
fup_adj_bram = fup_adjm / Kp_bram;
fup_adj_repm = fup_adjm / Kp_repm;
fup_adj_redm = fup_adjm / Kp_redm;
# Volumes of tissue compartments
V_liv_e = Fvec_liv * V_liv; # volume extracellular
compartment
V_liv_v = Fvv_liv * V_liv;  # volume vascular
compartment
V_liv_i = V_liv - (V_liv_e + V_liv_v); # volume
intracellular compartment
V_liv_xm = V_liv_e + (V_liv_v * (Rbpm / Kp_livm));
# denominator of Q_e to find C_e
V_kid_e = Fvec_kid * V_kid;
V_kid_v = Fvv_kid * V_kid;
V_kid_i = V_kid - (V_kid_e + V_kid_v);
V_kid_xm = V_kid_e + (V_kid_v * (Rbpm /
Kp_kidm));
V_ski_e = Fvec_ski * V_ski;
V_ski_v = Fvv_ski * V_ski;
V_ski_i = V_ski - (V_ski_e + V_ski_v);
V_ski_x = V_ski + (V_ski_v * (Rbp / Kp_ski));
V_ski_xm = V_ski_e + (V_ski_v * (Rbpm /
Kp_skim));
V_adi_e = Fvec_adi * V_adi;
V_adi_v = Fvv_adi * V_adi;
V_adi_i = V_adi - (V_adi_e + V_adi_v);
V_adi_xm = V_adi_e + (V_adi_v * (Rbpm /
Kp_adim));
V_rob_e = Fvec_rob * V_rob;
V_rob_v = Fvv_rob * V_rob;
V_rob_i = V_rob - (V_rob_e + V_rob_v);
V_rob_xm = V_rob_e + (V_rob_v * (Rbpm /
Kp_robm));
V_lun_e = Fvec_lun * V_lun;
V_lun_v = Fvv_lun * V_lun;
V_lun_i = V_lun - (V_lun_e + V_lun_v);
V_lun_xm = V_lun_e + (V_lun_v * (Rbpm /
Kp_lunm));
V_mus_e = Fvec_mus * V_mus;
V_mus_v = Fvv_mus * V_mus;
V_mus_i = V_mus - (V_mus_e + V_mus_v);
V_mus_xm = V_mus_e + (V_mus_v * (Rbpm /
Kp_musm));
V_spl_e = Fvec_spl * V_spl;
V_spl_v = Fvv_spl * V_spl;
V_spl_i = V_spl - (V_spl_e + V_spl_v);
V_spl_xm = V_spl_e + (V_spl_v * (Rbpm /
Kp_splm));
V_yel_e = Fvec_yel * V_yel;
V_yel_v = Fvv_yel * V_yel;
V_yel_i = V_yel - (V_yel_e + V_yel_v);
V_yel_xm = V_yel_e + (V_yel_v * (Rbpm /
Kp_yelm));
V_hea_e = Fvec_hea * V_hea;
V_hea_v = Fvv_hea * V_hea;
V_hea_i = V_hea - (V_hea_e + V_hea_v);
V_hea_xm = V_hea_e + (V_hea_v * (Rbpm /
Kp_heam));
V_bra_e = Fvec_bra * V_bra;
V_bra_v = Fvv_bra * V_bra;
V_bra_i = V_bra - (V_bra_e + V_bra_v);
V_bra_xm = V_bra_e + (V_bra_v * (Rbpm /
Kp_bram));
V_rep_e = Fvec_rep * V_rep;
V_rep_v = Fvv_rep * V_rep;
V_rep_i = V_rep - (V_rep_e + V_rep_v);
V_rep_xm = V_rep_e + (V_rep_v * (Rbpm /
Kp_repm));
V_red_e = Fvec_red * V_red;
V_red_v = Fvv_red * V_red;
V_red_i = V_red - (V_red_e + V_red_v);
V_red_xm = V_red_e + (V_red_v * (Rbpm /
Kp_redm));
# Tissue-specific PStc values (scaled according to
tissue cell volumes)
```

```
PStc_kid_bm = PStcm * F_bm_kid * V_kid_i; # PStc of kidney basolateral membrane
PStc_kid_am = PStcm * (1 - F_bm_kid) * V_kid_i; # PStc of kidney apical membrane
PStc_liv_bm = PStcm * F_bm_liv * V_liv_i;
PStc_liv_am = PStcm * (1 - F_bm_liv) * V_liv_i;
PStc_skim = PStcm * F_bm_ski * V_ski_i;
PStc_adim = PStcm * F_bm_adi * V_adi_i;
PStc_robm = PStcm * F_bm_rob * V_rob_i;
PStc_robm = PStcm * F_bm_rob * V_rob_i;
PStc_lunm = PStcm * F_bm_lun * V_lun_i;
PStc_musm = PStcm * F_bm_mus * V_mus_i;
PStc_splm = PStcm * F_bm_spl * V_spl_i;
PStc_yelm = PStcm * F_bm_yel * V_yel_i;
PStc_heam = PStcm * F_bm_hea * V_hea_i;
PStc_bram = PStcm * F_bm_bra * V_bra_i;
PStc_repm = PStcm * F_bm_rep * V_rep_i;
PStc_redm = PStcm * F_bm_red * V_red_i;
# Permeability-limited PBTK model (2nd metbaoiite)
# for Berezhkovskiy method for Kp calculation
fup_adjm2 = 1/((pow(10,logP_plam2)*((Vnlp + Vphp)/Vwp)) + 1 + ((1 - fup_expm2)/fup_expm2));
logP_adim2 = (1.115 * logP_tism2) - 1.35;
K_adim2 = pow(10,logP_adim2);
K_tism2 = pow(10,logP_tism2);
# Transporters for metabolite
Vmax_w_kid_bm2 = V_max_kid_bm2 * Tra_exp_kid_bm2 * D_kid * V_kid; # Vmax for whole kidney (mg/ sec)
Km_kid_bm2 = Km_kid_p_bm2 / 1000; # Km for kidney (mg/ mL)
Vmax_w_kid_am2 = V_max_kid_am2 * Tra_exp_kid_am2 * D_kid * V_kid;
Km_kid_am2 = Km_kid_p_am2 / 1000;
Vmax_w_liv_bm2 = V_max_liv_bm2 * Tra_exp_liv_bm2 * D_liv * V_liv;
Km_liv_bm2 = Km_liv_p_bm2 / 1000;
Vmax_w_liv_am2 = V_max_liv_am2 * Tra_exp_liv_am2 * D_liv * V_liv;
Km_liv_am2 = Km_liv_p_am2 / 1000;
Vmax_w_gut_C1_am2 = V_max_gut_C1_am2 * Tra_exp_gut_C1_am2 * D_ent_C1 * V_ent_C1;
Km_gut_C1_am2 = Km_gut_p_C1_am2 / 1000;
Vmax_w_gut_C2_7_am2 = V_max_gut_C2_7_am2 * Tra_exp_gut_C2_7_am2 * D_ent_C2_7 * V_ent_C2_7;
Km_gut_C2_7_am2 = Km_gut_p_C2_7_am2 / 1000;
Vmax_w_gut_col_am2 = V_max_gut_col_am2 * Tra_exp_gut_col_am2 * D_ent_col * V_ent_col;
Km_gut_col_am2 = Km_gut_p_col_am2 / 1000;
fut_tism2 = (1/((((1 - fup_adjm2)/fup_adjm2) * RAtp_tis) + 1));
fut_adim2 = (1/((((1 - fup_adjm2)/fup_adjm2) * RAtp_adi) + 1));
# Poulin & Theil (extracellular) method for permeability-limited tissues
Kp_livm2 = fup_adjm2 / fut_tism2;
Kp_kidm2 = fup_adjm2 / fut_tism2;
Kp_skim2 = fup_adjm2 / fut_tism2;
Kp_adim2 = fup_adjm2 / fut_adim2;
Kp_yelm2 = fup_adjm2 / fut_adim2;
Kp_robm2 = fup_adjm2 / fut_tism2;
Kp_lunm2 = fup_adjm2 / fut_tism2;
Kp_musm2 = fup_adjm2 / fut_tism2;
Kp_splm2 = fup_adjm2 / fut_tism2;
Kp_heam2 = fup_adjm2 / fut_tism2;
Kp_bram2 = fup_adjm2 / fut_tism2;
Kp_repm2 = fup_adjm2 / fut_tism2;
Kp_redm2 = fup_adjm2 / fut_tism2;
# Berezhkovskiy method for Kp calculation
#Kp_livm2 = ((K_tism2 * (Vnlt_liv + (0.3 * Vpht_liv))) + ((Vwt_liv / fut_tism2) + (0.7 * Vpht_liv))) / ((K_tism2 * (Vnlp + (0.3 * Vphp))) + ((Vwp / fup_adjm2) + (0.7 * Vphp)));
#Kp_kidm2 = ((K_tism2 * (Vnlt_kid + (0.3 * Vpht_kid))) + ((Vwt_kid / fut_tism2) + (0.7 * Vpht_kid))) / ((K_tism2 * (Vnlp + (0.3 * Vphp))) + ((Vwp / fup_adjm2) + (0.7 * Vphp)));
#Kp_skim2 = ((K_tism2 * (Vnlt_ski + (0.3 * Vpht_ski))) + ((Vwt_ski / fut_tism2) + (0.7 * Vpht_ski))) / ((K_tism2 * (Vnlp + (0.3 * Vphp))) + ((Vwp / fup_adjm2) + (0.7 * Vphp)));
#Kp_adim2 = ((K_adim2 * (Vnlt_adi + (0.3 * Vpht_adi))) + ((Vwt_adi / fut_tism2) + (0.7 * Vpht_adi))) / ((K_adim2 * (Vnlp + (0.3 * Vphp))) + ((Vwp / fup_adjm2) + (0.7 * Vphp))); # n.b. fut_adi & K_adi
#Kp_yelm2 = ((K_adim2 * (Vnlt_yel + (0.3 * Vpht_yel))) + ((Vwt_yel / fut_tism2) + (0.7 * Vpht_yel))) / ((K_adim2 * (Vnlp + (0.3 * Vphp))) + ((Vwp / fup_adjm2) + (0.7 * Vphp))); # n.b. fut_adi & K_adi
#Kp_robm2 = ((K_tism2 * (Vnlt_rob + (0.3 * Vpht_rob))) + ((Vwt_rob / fut_tism2) + (0.7 * Vpht_rob))) / ((K_tism2 * (Vnlp + (0.3 * Vphp))) + ((Vwp / fup_adjm2) + (0.7 * Vphp)));
#Kp_lunm2 = ((K_tism2 * (Vnlt_lun + (0.3 * Vpht_lun))) + ((Vwt_lun / fut_tism2) + (0.7 * Vpht_lun))) / ((K_tism2 * (Vnlp + (0.3 * Vphp))) + ((Vwp / fup_adjm2) + (0.7 * Vphp)));
#Kp_musm2 = ((K_tism2 * (Vnlt_mus + (0.3 * Vpht_mus))) + ((Vwt_mus / fut_tism2) + (0.7 * Vpht_mus))) / ((K_tism2 * (Vnlp + (0.3 * Vphp))) + ((Vwp / fup_adjm2) + (0.7 * Vphp)));
#Kp_splm2 = ((K_tism2 * (Vnlt_spl + (0.3 * Vpht_spl))) + ((Vwt_spl / fut_tism2) + (0.7 * Vpht_spl))) / ((K_tism2 * (Vnlp + (0.3 * Vphp))) + ((Vwp / fup_adjm2) + (0.7 * Vphp)));
#Kp_heam2 = ((K_tism2 * (Vnlt_hea + (0.3 * Vpht_hea))) + ((Vwt_hea / fut_tism2) + (0.7 *
```

```
Vpht_hea))) / ((K_tism2 * (Vnlp + (0.3 * Vphp))) +
((Vwp / fup_adjm2) + (0.7 * Vphp)));
#Kp_bram2 = ((K_tism2 * (Vnlt_bra + (0.3 *
Vpht_bra))) + ((Vwt_bra / fut_tism2) + (0.7 *
Vpht_bra))) / ((K_tism2 * (Vnlp + (0.3 * Vphp))) +
((Vwp / fup_adjm2) + (0.7 * Vphp)));
#Kp_repm2 = ((K_tism2 * (Vnlt_rep + (0.3 *
Vpht_rep))) + ((Vwt_rep / fut_tism2) + (0.7 *
Vpht_rep))) / ((K_tism2 * (Vnlp + (0.3 * Vphp))) +
((Vwp / fup_adjm2) + (0.7 * Vphp)));
#Kp_redm2 = ((K_tism2 * (Vnlt_red + (0.3 *
Vpht_red))) + ((Vwt_red / fut_tism2) + (0.7 *
Vpht_red))) / ((K_tism2 * (Vnlp + (0.3 * Vphp))) +
((Vwp / fup_adjm2) + (0.7 * Vphp)));
fup_adj_livm2 = fup_adjm2 / Kp_livm2;
fup_adj_kidm2 = fup_adjm2 / Kp_kidm2;
fup_adj_skim2 = fup_adjm2 / Kp_skim2;
fup_adj_adim2 = fup_adjm2 / Kp_adim2;
fup_adj_robm2 = fup_adjm2 / Kp_robm2;
fup_adj_lunm2 = fup_adjm2 / Kp_lunm2;
fup_adj_musm2 = fup_adjm2 / Kp_musm2;
fup_adj_splm2 = fup_adjm2 / Kp_splm2;
fup_adj_yelm2 = fup_adjm2 / Kp_yelm2;
fup_adj_heam2 = fup_adjm2 / Kp_heam2;
fup_adj_bram2 = fup_adjm2 / Kp_bram2;
fup_adj_repm2 = fup_adjm2 / Kp_repm2;
fup_adj_redm2 = fup_adjm2 / Kp_redm2;
V_liv_xm2 = V_liv_e + (V_liv_v * (Rbpm2 /
Kp_livm2));
V_kid_xm2 = V_kid_e + (V_kid_v * (Rbpm2 /
Kp_kidm2));
V_ski_xm2 = V_ski_e + (V_ski_v * (Rbpm2 /
Kp_skim2));
V_adi_xm2 = V_adi_e + (V_adi_v * (Rbpm2 /
Kp_adim2));
V_rob_xm2 = V_rob_e + (V_rob_v * (Rbpm2 /
Kp_robm2));
V_lun_xm2 = V_lun_e + (V_lun_v * (Rbpm2 /
Kp_lunm2));
V_mus_xm2 = V_mus_e + (V_mus_v * (Rbpm2 /
Kp_musm2));
V_spl_xm2 = V_spl_e + (V_spl_v * (Rbpm2 /
Kp_splm2));
V_yel_xm2 = V_yel_e + (V_yel_v * (Rbpm2 /
Kp_yelm2));
V_hea_xm2 = V_hea_e + (V_hea_v * (Rbpm2 /
Kp_heam2));
V_bra_xm2 = V_bra_e + (V_bra_v * (Rbpm2 /
Kp_bram2));
V_rep_xm2 = V_rep_e + (V_rep_v * (Rbpm2 /
Kp_repm2));
V_red_xm2 = V_red_e + (V_red_v * (Rbpm2 /
Kp_redm2));
# Tissue-specific PStc values
PStc_kid_bm2 = PStcm * F_bm_kid * V_kid_i;
PStc_kid_am2 = PStcm * (1 - F_bm_kid) * V_kid_i;
PStc_liv_bm2 = PStcm * F_bm_liv * V_liv_i;
PStc_liv_am2 = PStcm * (1 - F_bm_liv) * V_liv_i;
PStc_skim2 = PStcm * F_bm_ski * V_ski_i;
PStc_adim2 = PStcm * F_bm_adi * V_adi_i;
PStc_robm2 = PStcm * F_bm_rob * V_rob_i;
PStc_robm2 = PStcm * F_bm_rob * V_rob_i;
PStc_lunm2 = PStcm * F_bm_lun * V_lun_i;
PStc_musm2 = PStcm * F_bm_mus * V_mus_i;
PStc_splm2 = PStcm * F_bm_spl * V_spl_i;
PStc_yelm2 = PStcm * F_bm_yel * V_yel_i;
PStc_heam2 = PStcm * F_bm_hea * V_hea_i;
PStc_bram2 = PStcm * F_bm_bra * V_bra_i;
PStc_repm2 = PStcm * F_bm_rep * V_rep_i;
PStc_redm2 = PStcm * F_bm_red * V_red_i;
}
Dynamics {
# Concentrations in gut lumen
C_sto_dis = Q_sto_dis / V_sto;
C_C1_dis = Q_C1_dis / V_C1;
C_C2_7_dis = Q_C2_7_dis / V_C2_7;
C_col_dis = Q_col_dis / V_col;
On_Off_sto_p = (C_sto_dis < Cs ? 0:1); # for
precipitation
On_Off_C1_p = (C_C1_dis < Cs ? 0:1);
On_Off_C2_7_p = (C_C2_7_dis < Cs ? 0:1);
On_Off_col_p = (C_col_dis < Cs ? 0:1);
PR_C_sto = C_sto_dis - Cs;
PR_C_C1 = C_C1_dis - Cs;
PR_C_C2_7 = C_C2_7_dis - Cs;
PR_C_col = C_col_dis - Cs;
On_Off_sto_d = (Cs < C_sto_dis ? 0:1); # for
dissolution
On_Off_C1_d = (Cs < C_C1_dis ? 0:1);
On_Off_C2_7_d = (Cs < C_C2_7_dis ? 0:1);
On_Off_col_d = (Cs < C_col_dis ? 0:1);
DR_C_sto = Cs - C_sto_dis;
DR_C_C1 = Cs - C_C1_dis;
DR_C_C2_7 = Cs - C_C2_7_dis;
DR_C_col = Cs - C_col_dis;
# Concentrations in enterocytes
C_ent_C1 = Q_ent_C1 / V_ent_C1;
C_ent_C2_7 = Q_ent_C2_7 / V_ent_C2_7;
C_ent_col = Q_ent_col / V_ent_col;
Ct_gut_blo = Q_gut_blo / V_gut_blo;
C_sto_und = Q_sto_und / V_sto;
C_C1_und = Q_C1_und / V_C1;
C_C2_7_und = Q_C2_7_und / V_C2_7;
C_col_und = Q_col_und / V_col;
C_surf = Q_fab / V_fab; # concentration on skin
surface
# Concentrations in body tissues
Ct_kid = Q_kid / V_kid;
Ct_kid_u = (Q_kid / V_kid) * fut_tis;
C_nep = Q_nep / V_nep;
Ct_liv = Q_liv / V_liv;
Ct_liv_u = (Q_liv / V_liv) * fut_tis;
Ct_ski = Q_ski / V_ski_x;
Ct_ski_u = (Q_ski / V_ski_x) * fut_tis;
```

```
Ct_adi = Q_adi / V_adi;
Ct_adi_u = (Q_adi / V_adi) * fut_adi;
Ct_rob = Q_rob / V_rob;
Ct_rob_u = (Q_rob / V_rob) * fut_tis;
Ct_lun = Q_lun / V_lun;
Ct_lun_u = (Q_lun / V_lun) * fut_tis;
Ct_mus = Q_mus / V_mus;
Ct_mus_u = (Q_mus / V_mus) * fut_tis;
Ct_spl = Q_spl / V_spl;
Ct_spl_u = (Q_spl / V_spl) * fut_tis;
Ct_yel = Q_yel / V_yel;
Ct_yel_u = (Q_yel / V_yel) * fut_adi;
Ct_hea = Q_hea / V_hea;
Ct_hea_u = (Q_hea / V_hea) * fut_tis;
Ct_bra = Q_bra / V_bra;
Ct_bra_u = (Q_bra / V_bra) * fut_tis;
Ct_rep = Q_rep / V_rep;
Ct_rep_u = (Q_rep / V_rep) * fut_tis;
Ct_red = Q_red / V_red;
Ct_red_u = (Q_red / V_red) * fut_tis;
# Concentration at venous ends of tissues
C_liv_v = ((Ct_liv * Rbp) / Kp_liv);
C_kid_v = ((Ct_kid * Rbp) / Kp_kid);
C_ski_v = ((Ct_ski * Rbp) / Kp_ski);
C_adi_v = ((Ct_adi * Rbp) / Kp_adi);
C_rob_v = ((Ct_rob * Rbp) / Kp_rob);
C_lun_v = ((Ct_lun * Rbp) / Kp_lun);
C_mus_v = ((Ct_mus * Rbp) / Kp_mus);
C_spl_v = ((Ct_spl * Rbp) / Kp_spl);
C_yel_v = ((Ct_yel * Rbp) / Kp_yel);
C_hea_v = ((Ct_hea * Rbp) / Kp_hea);
C_bra_v = ((Ct_bra * Rbp) / Kp_bra);
C_rep_v = ((Ct_rep * Rbp) / Kp_rep);
C_red_v = ((Ct_red * Rbp) / Kp_red);
C_ven = Q_ven / V_ven; # concentration in venous
blood
C_art = Q_art / V_art; # concentration in arterial
blood
C_vpl = C_ven / Rbp; # concentration in venous
plasma
C_vpl_u = (C_ven / Rbp) * fup_adj; # unbound
concentration in venous plasma
# Flux through liver and kidney apical membranes
perm_liv_a = (PStc_liv_a * (Ct_liv * fut_tis)) +
((Vmax_w_liv_a * Ct_liv * fut_tis) / (Km_liv_a +
(Ct_liv * fut_tis)));
perm_kid_a = (PStc_kid_a * ((Ct_kid * fut_tis) -
C_nep)) + ((Vmax_w_kid_a * Ct_kid * fut_tis) /
(Km_kid_a + (Ct_kid * fut_tis)));
# Flux through enterocyte membranes
perm_sto = (Ka_e_sto * V_sto * (C_sto_dis -
Ct_gut_blo)); # (n.b. no enterocytes in stomach!)
perm_C1_a = (Ka_1 * V_C1 * (C_C1_dis -
(C_ent_C1 * fut_tis))) - ((Vmax_w_gut_C1_a *
C_ent_C1 * fut_tis) / (Km_gut_C1_a + (C_ent_C1 *
fut_tis)));
perm_C1_b = (Ka_e_C1 * V_ent_C1 * (C_ent_C1 -
(Ct_gut_blo * fup_adj)));
perm_C2_7_a = (Ka_2_7 * V_C2_7 * (C_C2_7_dis -
(C_ent_C2_7 * fut_tis))) - ((Vmax_w_gut_C2_7_a *
C_ent_C2_7 * fut_tis) / (Km_gut_C2_7_a +
(C_ent_C2_7 * fut_tis)));
perm_C2_7_b = (Ka_e_C2_7 * V_ent_C2_7 *
(C_ent_C2_7 - (Ct_gut_blo * fup_adj)));
perm_col_a = (Ka_c * V_col * (C_col_dis -
(C_ent_col * fut_tis))) - ((Vmax_w_gut_col_a *
C_ent_col * fut_tis) / (Km_gut_col_a + (C_ent_col
* fut_tis)));
perm_col_b = (Ka_e_col * V_ent_col * (C_ent_col -
(Ct_gut_blo * fup_adj)));
# Permeability-limited model (1st metabolite)
# Concentrations in gut
C_sto_dism = Q_sto_dism / V_sto;
C_C1_dism = Q_C1_dism / V_C1;
C_C2_7_dism = Q_C2_7_dism / V_C2_7;
C_col_dism = Q_col_dism / V_col;
C_ent_C1m = Q_ent_C1m / V_ent_C1;
C_ent_C2_7m = Q_ent_C2_7m / V_ent_C2_7;
C_ent_colm = Q_ent_colm / V_ent_col;
Ct_gut_blom = Q_gut_blom / V_gut_blo;
# Concentrations in body tissues
Ci_kidm = Q_kid_im / V_kid_i;
Ce_kidm = Q_kid_em / V_kid_xm;
Ce_kid_um = (Q_kid_em / V_kid_xm) *
fup_adj_kidm;
Ci_kid_um = (Q_kid_im / V_kid_i) * fut_tism;
C_nepm = Q_nepm / V_nep;
Ci_livm = Q_liv_im / V_liv_i;
Ce_livm = Q_liv_em / V_liv_xm;
Ce_liv_um = (Q_liv_em / V_liv_xm) * fup_adj_livm;
Ci_liv_um = (Q_liv_im / V_liv_i) * fut_tism;
Ci_skim = Q_ski_im / V_ski_i;
Ce_skim = Q_ski_em / V_ski_xm;
Ce_ski_um = (Q_ski_em / V_ski_xm) *
fup_adj_skim;
Ci_ski_um = (Q_ski_im / V_ski_i) * fut_tism;
Ci_adim = Q_adi_im / V_adi_i;
Ce_adim = Q_adi_em / V_adi_xm;
Ce_adi_um = (Q_adi_em / V_adi_xm) *
fup_adj_adim;
Ci_adi_um = (Q_adi_im / V_adi_i) * fut_adim;
Ci_robm = Q_rob_im / V_rob_i;
Ce_robm = Q_rob_em / V_rob_xm;
Ce_rob_um = (Q_rob_em / V_rob_xm) *
fup_adj_robm;
Ci_rob_um = (Q_rob_im / V_rob_i) * fut_tism;
Ci_lunm = Q_lun_im / V_lun_i;
Ce_lunm = Q_lun_em / V_lun_xm;
Ce_lun_um = (Q_lun_em / V_lun_xm) *
fup_adj_lunm;
Ci_lun_um = (Q_lun_im / V_lun_i) * fut_tism;
Ci_musm = Q_mus_im / V_mus_i;
Ce_musm = Q_mus_em / V_mus_xm;
```

```
Ce_mus_um = (Q_mus_em / V_mus_xm) *
fup_adj_musm;
Ci_mus_um = (Q_mus_im / V_mus_i) * fut_tism;
Ci_splm = Q_spl_im / V_spl_i;
Ce_splm = Q_spl_em / V_spl_xm;
Ce_spl_um = (Q_spl_em / V_spl_xm) *
fup_adj_splm;
Ci_spl_um = (Q_spl_im / V_spl_i) * fut_tism;
Ci_yelm = Q_yel_im / V_yel_i;
Ce_yelm = Q_yel_em / V_yel_xm;
Ce_yel_um = (Q_yel_em / V_yel_xm) *
fup_adj_yelm;
Ci_yel_um = (Q_yel_im / V_yel_i) * fut_adim; #
n.b. fut_adi
Ci_heam = Q_hea_im / V_hea_i;
Ce_heam = Q_hea_em / V_hea_xm;
Ce_hea_um = (Q_hea_em / V_hea_xm) *
fup_adj_heam;
Ci_hea_um = (Q_hea_im / V_hea_i) * fut_tism;
Ci_bram = Q_bra_im / V_bra_i;
Ce_bram = Q_bra_em / V_bra_xm;
Ce_bra_um = (Q_bra_em / V_bra_xm) *
fup_adj_bram;
Ci_bra_um = (Q_bra_im / V_bra_i) * fut_tism;
Ci_repm = Q_rep_im / V_rep_i;
Ce_repm = Q_rep_em / V_rep_xm;
Ce_rep_um = (Q_rep_em / V_rep_xm) *
fup_adj_repm;
Ci_rep_um = (Q_rep_im / V_rep_i) * fut_tism;
Ci_redm = Q_red_im / V_red_i;
Ce_redm = Q_red_em / V_red_xm;
Ce_red_um = (Q_red_em / V_red_xm) *
fup_adj_redm;
Ci_red_um = (Q_red_im / V_red_i) * fut_tism;
C_liv_vm = ((Ce_livm * Rbpm) / Kp_livm);
C_kid_vm = ((Ce_kidm * Rbpm) / Kp_kidm);
C_ski_vm = ((Ce_skim * Rbpm) / Kp_skim);
C_adi_vm = ((Ce_adim * Rbpm) / Kp_adim);
C_rob_vm = ((Ce_robm * Rbpm) / Kp_robm);
C_lun_vm = ((Ce_lunm * Rbpm) / Kp_lunm);
C_mus_vm = ((Ce_musm * Rbpm) / Kp_musm);
C_spl_vm = ((Ce_splm * Rbpm) / Kp_splm);
C_yel_vm = ((Ce_yelm * Rbpm) / Kp_yelm);
C_hea_vm = ((Ce_heam * Rbpm) / Kp_heam);
C_bra_vm = ((Ce_bram * Rbpm) / Kp_bram);
C_rep_vm = ((Ce_repm * Rbpm) / Kp_repm);
C_red_vm = ((Ce_redm * Rbpm) / Kp_redm);
C_venm = Q_venm / V_ven;
C_artm = Q_artm / V_art;
C_vplm = C_venm / Rbpm;
C_vpl_um = (C_venm / Rbpm) * fup_adjm;
perm_kid_bm = (PStc_kid_bm * ((Ce_kidm *
fup_adj_kidm) - (Ci_kidm * fut_tism))) +
((Vmax_w_kid_bm * Ce_kidm * fup_adj_kidm) /
(Km_kid_bm + (Ce_kidm * fup_adj_kidm))); #
influx transporter in basolateral membrane
perm_kid_am = (PStc_kid_am * ((Ci_kidm *
fut_tism) - C_nepm)) + ((Vmax_w_kid_am *
Ci_kidm * fut_tism) / (Km_kid_am + (Ci_kidm *
fut_tism))); # efflux transporter in apical
membrane
perm_liv_bm = (PStc_liv_bm * ((Ce_livm *
fup_adj_livm) - (Ci_livm * fut_tism))) +
((Vmax_w_liv_bm * Ce_livm * fup_adj_livm) /
(Km_liv_bm + (Ce_livm * fup_adj_livm)));
perm_liv_am = (PStc_liv_am * (Ci_livm * fut_tism))
+ ((Vmax_w_liv_am * Ci_livm * fut_tism) /
(Km_liv_am + (Ci_livm * fut_tism))); # efflux
transporter in apical membrane
# Flux through single-membrane tissues
perm_ski = Perm_co * SA * ((Ct_ski / Kp_ski_fab) -
C_surf);
perm_skim = (PStc_skim * ((Ce_skim *
fup_adj_skim) - (Ci_skim * fut_tism)));
perm_adim = (PStc_adim * ((Ce_adim *
fup_adj_adim) - (Ci_adim * fut_adim)));
perm_robm = (PStc_robm * ((Ce_robm *
fup_adj_robm) - (Ci_robm * fut_tism)));
perm_lunm = (PStc_lunm * ((Ce_lunm *
fup_adj_lunm) - (Ci_lunm * fut_tism)));
perm_musm = (PStc_musm * ((Ce_musm *
fup_adj_musm) - (Ci_musm * fut_tism)));
perm_splm = (PStc_splm * ((Ce_splm *
fup_adj_splm) - (Ci_splm * fut_tism)));
perm_yelm = (PStc_yelm * ((Ce_yelm *
fup_adj_yelm) - (Ci_yelm * fut_adim)));
perm_heam = (PStc_heam * ((Ce_heam *
fup_adj_heam) - (Ci_heam * fut_tism)));
perm_bram = (PStc_bram * ((Ce_bram *
fup_adj_bram) - (Ci_bram * fut_tism)));
perm_repm = (PStc_repm * ((Ce_repm *
fup_adj_repm) - (Ci_repm * fut_tism)));
perm_redm = (PStc_redm * ((Ce_redm *
fup_adj_redm) - (Ci_redm * fut_tism)));
# Flux through enterocyte membranes
perm_stom = (Ka_e_sto * V_sto * (C_sto_dism -
Ct_gut_blom)); # (n.b. no enterocytes in stomach!)
perm_C1_am = (Ka_1 * V_C1 * (C_C1_dism -
(C_ent_C1m * fut_tism))) - ((Vmax_w_gut_C1_am
* C_ent_C1m * fut_tism) / (Km_gut_C1_am +
(C_ent_C1m * fut_tism)));
perm_C1_bm = (Ka_e_C1 * V_ent_C1 *
(C_ent_C1m - (Ct_gut_blom * fup_adjm)));

perm_C2_7_am = (Ka_2_7 * V_C2_7 *
(C_C2_7_dism - (C_ent_C2_7m * fut_tism))) -
((Vmax_w_gut_C2_7_am * C_ent_C2_7m *
fut_tism) / (Km_gut_C2_7_am + (C_ent_C2_7m *
fut_tism)));
perm_C2_7_bm = (Ka_e_C2_7 * V_ent_C2_7 *
(C_ent_C2_7m - (Ct_gut_blom * fup_adjm)));
perm_col_am = (Ka_c * V_col * (C_col_dism -
(C_ent_colm * fut_tism))) - ((Vmax_w_gut_col_am
```

```
* C_ent_colm * fut_tism) / (Km_gut_col_am +
(C_ent_colm * fut_tism)));
perm_col_bm = (Ka_e_col * V_ent_col *
(C_ent_colm - (Ct_gut_blom * fup_adjm)));
# Permeability-limited model (2nd metabolite)
C_sto_dism2 = Q_sto_dism2 / V_sto;
C_C1_dism2 = Q_C1_dism2 / V_C1;
C_C2_7_dism2 = Q_C2_7_dism2 / V_C2_7;
C_col_dism2 = Q_col_dism2 / V_col;
C_ent_C1m2 = Q_ent_C1m2 / V_ent_C1;
C_ent_C2_7m2 = Q_ent_C2_7m2 / V_ent_C2_7;
C_ent_colm2 = Q_ent_colm2 / V_ent_col;
Ct_gut_blom2 = Q_gut_blom2 / V_gut_blo;
Ci_kidm2 = Q_kid_im2 / V_kid_i;
Ce_kidm2 = Q_kid_em2 / V_kid_xm2;
Ce_kid_um2 = (Q_kid_em2 / V_kid_xm2) *
fup_adj_kidm2;
Ci_kid_um2 = (Q_kid_im2 / V_kid_i) * fut_tism2;
C_nepm2 = Q_nepm2 / V_nep;
Ci_livm2 = Q_liv_im2 / V_liv_i;
Ce_livm2 = Q_liv_em2 / V_liv_xm2;
Ce_liv_um2 = (Q_liv_em2 / V_liv_xm2) *
fup_adj_livm2;
Ci_liv_um2 = (Q_liv_im2 / V_liv_i) * fut_tism2;
Ci_skim2 = Q_ski_im2 / V_ski_i;
Ce_skim2 = Q_ski_em2 / V_ski_xm2;
Ce_ski_um2 = (Q_ski_em2 / V_ski_xm2) *
fup_adj_skim2;
Ci_ski_um2 = (Q_ski_im2 / V_ski_i) * fut_tism2;
Ci_adim2 = Q_adi_im2 / V_adi_i;
Ce_adim2 = Q_adi_em2 / V_adi_xm2;
Ce_adi_um2 = (Q_adi_em2 / V_adi_xm2) *
fup_adj_adim2;
Ci_adi_um2 = (Q_adi_im2 / V_adi_i) * fut_adim2;
Ci_robm2 = Q_rob_im2 / V_rob_i;
Ce_robm2 = Q_rob_em2 / V_rob_xm2;
Ce_rob_um2 = (Q_rob_em2 / V_rob_xm2) *
fup_adj_robm2;
Ci_rob_um2 = (Q_rob_im2 / V_rob_i) * fut_tism2;
Ci_lunm2 = Q_lun_im2 / V_lun_i;
Ce_lunm2 = Q_lun_em2 / V_lun_xm2;
Ce_lun_um2 = (Q_lun_em2 / V_lun_xm2) *
fup_adj_lunm2;
Ci_lun_um2 = (Q_lun_im2 / V_lun_i) * fut_tism2;
Ci_musm2 = Q_mus_im2 / V_mus_i;
Ce_musm2 = Q_mus_em2 / V_mus_xm2;
Ce_mus_um2 = (Q_mus_em2 / V_mus_xm2) *
fup_adj_musm2;
Ci_mus_um2 = (Q_mus_im2 / V_mus_i) *
fut_tism2;
Ci_splm2 = Q_spl_im2 / V_spl_i;
Ce_splm2 = Q_spl_em2 / V_spl_xm2;
Ce_spl_um2 = (Q_spl_em2 / V_spl_xm2) *
fup_adj_splm2;
Ci_spl_um2 = (Q_spl_im2 / V_spl_i) * fut_tism2;
Ci_yelm2 = Q_yel_im2 / V_yel_i;
Ce_yelm2 = Q_yel_em2 / V_yel_xm2;
Ce_yel_um2 = (Q_yel_em2 / V_yel_xm2) *
fup_adj_yelm2;
Ci_yel_um2 = (Q_yel_im2 / V_yel_i) * fut_adim2;
Ci_heam2 = Q_hea_im2 / V_hea_i;
Ce_heam2 = Q_hea_em2 / V_hea_xm2;
Ce_hea_um2 = (Q_hea_em2 / V_hea_xm2) *
fup_adj_heam2;
Ci_hea_um2 = (Q_hea_im2 / V_hea_i) * fut_tism2;
Ci_bram2 = Q_bra_im2 / V_bra_i;
Ce_bram2 = Q_bra_em2 / V_bra_xm2;
Ce_bra_um2 = (Q_bra_em2 / V_bra_xm2) *
fup_adj_bram2;
Ci_bra_um2 = (Q_bra_im2 / V_bra_i) * fut_tism2;
Ci_repm2 = Q_rep_im2 / V_rep_i;
Ce_repm2 = Q_rep_em2 / V_rep_xm2;
Ce_rep_um2 = (Q_rep_em2 / V_rep_xm2) *
fup_adj_repm2;
Ci_rep_um2 = (Q_rep_im2 / V_rep_i) * fut_tism2;
Ci_redm2 = Q_red_im2 / V_red_i;
Ce_redm2 = Q_red_em2 / V_red_xm2;
Ce_red_um2 = (Q_red_em2 / V_red_xm2) *
fup_adj_redm2;
Ci_red_um2 = (Q_red_im2 / V_red_i) * fut_tism2;
C_liv_vm2 = ((Ce_livm2 * Rbpm2) / Kp_livm2);
C_kid_vm2 = ((Ce_kidm2 * Rbpm2) / Kp_kidm2);
C_ski_vm2 = ((Ce_skim2 * Rbpm2) / Kp_skim2);
C_adi_vm2 = ((Ce_adim2 * Rbpm2) / Kp_adim2);
C_rob_vm2 = ((Ce_robm2 * Rbpm2) / Kp_robm2);
C_lun_vm2 = ((Ce_lunm2 * Rbpm2) / Kp_lunm2);
C_mus_vm2 = ((Ce_musm2 * Rbpm2) /
Kp_musm2);
C_spl_vm2 = ((Ce_splm2 * Rbpm2) / Kp_splm2);
C_yel_vm2 = ((Ce_yelm2 * Rbpm2) / Kp_yelm2);
C_hea_vm2 = ((Ce_heam2 * Rbpm2) / Kp_heam2);
C_bra_vm2 = ((Ce_bram2 * Rbpm2) / Kp_bram2);
C_rep_vm2 = ((Ce_repm2 * Rbpm2) / Kp_repm2);
C_red_vm2 = ((Ce_redm2 * Rbpm2) / Kp_redm2);
C_venm2 = Q_venm2 / V_ven;
C_artm2 = Q_artm2 / V_art;
C_vplm2 = C_venm2 / Rbpm2;
C_vpl_um2 = (C_venm2 / Rbpm2) * fup_adjm2;
perm_kid_bm2 = (PStc_kid_bm2 * ((Ce_kidm2 *
fup_adj_kidm2) - (Ci_kidm2 * fut_tism2))) +
((Vmax_w_kid_bm2 * Ce_kidm2 * fup_adj_kidm2)
/ (Km_kid_bm2 + (Ce_kidm2 * fup_adj_kidm2)));
perm_kid_am2 = (PStc_kid_am2 * ((Ci_kidm2 *
fut_tism2) - C_nepm2)) + ((Vmax_w_kid_am2 *
Ci_kidm2 * fut_tism2) / (Km_kid_am2 + (Ci_kidm2
* fut_tism2)));
perm_liv_bm2 = (PStc_liv_bm2 * ((Ce_livm2 *
fup_adj_livm2) - (Ci_livm2 * fut_tism2))) +
((Vmax_w_liv_bm2 * Ce_livm2 * fup_adj_livm2) /
(Km_liv_bm2 + (Ce_livm2 * fup_adj_livm2)));
perm_liv_am2 = (PStc_liv_am2 * (Ci_livm2 *
fut_tism2)) + ((Vmax_w_liv_am2 * Ci_livm2 *
fut_tism2) / (Km_liv_am2 + (Ci_livm2 *
fut_tism2)));
```

```
perm_skim2 = (PStc_skim2 * ((Ce_skim2 *
fup_adj_skim2) - (Ci_skim2 * fut_tism2)));
perm_adim2 = (PStc_adim2 * ((Ce_adim2 *
fup_adj_adim2) - (Ci_adim2 * fut_adim2)));
perm_robm2 = (PStc_robm2 * ((Ce_robm2 *
fup_adj_robm2) - (Ci_robm2 * fut_tism2)));
perm_lunm2 = (PStc_lunm2 * ((Ce_lunm2 *
fup_adj_lunm2) - (Ci_lunm2 * fut_tism2)));
perm_musm2 = (PStc_musm2 * ((Ce_musm2 *
fup_adj_musm2) - (Ci_musm2 * fut_tism2)));
perm_splm2 = (PStc_splm2 * ((Ce_splm2 *
fup_adj_splm2) - (Ci_splm2 * fut_tism2)));
perm_yelm2 = (PStc_yelm2 * ((Ce_yelm2 *
fup_adj_yelm2) - (Ci_yelm2 * fut_adim2)));
perm_heam2 = (PStc_heam2 * ((Ce_heam2 *
fup_adj_heam2) - (Ci_heam2 * fut_tism2)));
perm_bram2 = (PStc_bram2 * ((Ce_bram2 *
fup_adj_bram2) - (Ci_bram2 * fut_tism2)));
perm_repm2 = (PStc_repm2 * ((Ce_repm2 *
fup_adj_repm2) - (Ci_repm2 * fut_tism2)));
perm_redm2 = (PStc_redm2 * ((Ce_redm2 *
fup_adj_redm2) - (Ci_redm2 * fut_tism2)));
perm_stom2 = (Ka_e_sto * V_sto * (C_sto_dism2 -
Ct_gut_blom2));
perm_C1_am2 = (Ka_1 * V_C1 * (C_C1_dism2 -
(C_ent_C1m2 * fut_tism2))) -
((Vmax_w_gut_C1_am2 * C_ent_C1m2 *
fut_tism2) / (Km_gut_C1_am2 + (C_ent_C1m2 *
fut_tism2)));
perm_C1_bm2 = (Ka_e_C1 * V_ent_C1 *
(C_ent_C1m2 - (Ct_gut_blom2 * fup_adjm2)));
perm_C2_7_am2 = (Ka_2_7 * V_C2_7 *
(C_C2_7_dism2 - (C_ent_C2_7m2 * fut_tism2))) -
((Vmax_w_gut_C2_7_am2 * C_ent_C2_7m2 *
fut_tism2) / (Km_gut_C2_7_am2 +
(C_ent_C2_7m2 * fut_tism2)));
perm_C2_7_bm2 = (Ka_e_C2_7 * V_ent_C2_7 *
(C_ent_C2_7m2 - (Ct_gut_blom2 * fup_adjm2)));
perm_col_am2 = (Ka_c * V_col * (C_col_dism2 -
(C_ent_colm2 * fut_tism2))) -
((Vmax_w_gut_col_am2 * C_ent_colm2 *
fut_tism2) / (Km_gut_col_am2 + (C_ent_colm2 *
fut_tism2)));
perm_col_bm2 = (Ka_e_col * V_ent_col *
(C_ent_colm2 - (Ct_gut_blom2 * fup_adjm2)));
# ICRP lung model
# Alveoli
dt (A) = (DEP_A * (Inhale * ((Inhalation
/(1000/Mass_inhale)) * Recov_inhale))) -
(A*(SPT+SP)) - (A*RT_A_I) - (A*RT_A_bb);
dt (A_T) = (A*SPT) - (A_T*ST) - (A_T * RT_A_I) -
(A_T*RT_A_bb);
dt (A_bnd) = ((Fb*SP) * A) + ((Fb * ST) *A_T) -
(Sb*A_bnd);
# Interstium (lung cells surrounding alveoli)
dt (I) = (A*RT_A_I) - (I*(SP+SPT)) - (I*RT_I_LNTH);
dt (I_T) = (A_T * RT_A_I) + (I * SPT) - (I_T*ST) -
(I_T*RT_I_LNTH);
dt (I_bnd) = (Fb * (SP * I + ST * I_T)) - (Sb * I_bnd);
# Lymph nodes
dt (LNTH) = (I * RT_I_LNTH) + (bb_seq *
RT_bbseq_LNTH) + (BB_seq * RT_BBseq_LNTH) -
(LNTH * (SPT+SP));
dt (LNTH_T) = (LNTH * SPT) + (I_T*RT_I_LNTH) +
(bb_seq_T * RT_bbseq_LNTH) + (BB_seq_T *
RT_BBseq_LNTH) - (LNTH_T*ST);
dt (LNTH_bnd) = (Fb*(SP*LNTH + ST*LNTH_T)) -
(Sb*LNTH_bnd);
# Bronchial region
dt (BB) = (0.998 * DEP_BB * (Inhale * ((Inhalation
/(1000/Mass_inhale)) * Recov_inhale))) +
(bb*RT_bb_BB) - (BB*(SPT +SP+RT_BB_ET2));
dt (BB_T) = (BB*SPT) + (bb_T*RT_bb_BB) -
(BB_T*ST) - (BB_T*RT_BB_ET2);
dt (BB_bnd) = (Fb*(SP*BB + ST*BB_T)) -
(Sb*BB_bnd);
dt (BB_seq) = (0.002 * DEP_BB * (Inhale *
((Inhalation /(1000/Mass_inhale)) *
Recov_inhale))) -
(BB_seq*(SP+SPT+RT_BBseq_LNTH));# SP-
BB_seq*SPT-BB_seq*RT_BBseq_LNTH;
dt (BB_seq_T) = (BB_seq*SPT) -
(BB_seq_T*(ST+RT_BBseq_LNTH));
dt (BB_seq_bnd) = (Fb*(SP*BB_seq +
ST*BB_seq_T)) - (Sb*BB_seq_bnd);
# Bronchiolar region
dt (bb) = (0.998 * DEP_bb * (Inhale * ((Inhalation
/(1000/Mass_inhale)) * Recov_inhale))) +
(RT_A_bb*A) - (bb*(RT_bb_BB+SPT+SP));
dt (bb_T) = (bb*SPT) + (RT_A_bb*A_T) -
(bb_T*(RT_bb_BB+ST));
dt (bb_bnd) = (Fb*(SP*bb + ST*bb_T)) -
(Sb*bb_bnd);
dt (bb_seq) = (0.002 * DEP_bb * (Inhale *
((Inhalation /(1000/Mass_inhale)) *
Recov_inhale))) -
(bb_seq*(RT_bbseq_LNTH+SPT+SP));
dt (bb_seq_T) = (bb_seq*SPT) -
(bb_seq_T*(RT_bbseq_LNTH+ST));
dt (bb_seq_bnd) = (Fb*(SP*bb_seq +
ST*bb_seq_T)) - (Sb*bb_seq_bnd);
# Nose
dt (ET2) = (0.998 * DEP_ET2 * (Inhale * ((Inhalation
/(1000/Mass_inhale)) * Recov_inhale))) +
(RT_BB_ET2*BB) + (RT_ET1_ET2*ET1) -
(ET2*(RT_ET2_St+SPT+SP));
dt (ET2_T) = (ET2*SPT) + (BB_T*RT_BB_ET2) -
(ET2_T*(RT_ET2_St+ST));
dt (ET2_bnd) = (Fb*(SP*ET2 + ST*ET2_T)) -
(Sb*ET2_bnd);
# Extrathoracic region
dt (ET_seq) = (0.002 * DEP_ET2 * (Inhale *
((Inhalation /(1000/Mass_inhale)) *
```

```
Recov_inhale))) -
(ET_seq*(RT_ETseq_LNET+SPT+SP));
dt (ET_seq_T) = (ET_seq*SPT) -
(ET_seq_T*(RT_ETseq_LNET+ST));
dt (ET_seq_bnd) = (Fb*(SP*ET_seq +
ST*ET_seq_T)) - (Sb*ET_seq_bnd);

# Lymph nodes in extrathoracic region
dt (LNET) = (ET_seq*RT_ETseq_LNET) -
(LNET*(SPT+SP));
dt (LNET_T) = (LNET*SPT) + (ET_seq_T *
RT_ETseq_LNET) - (LNET_T * ST);
dt (LNET_bnd) = (Fb*(SP*LNET + ST*LNET_T)) -
(Sb*LNET_bnd);
# Mouth
dt (ET1) =  (DEP_ET1 * (Inhale * ((Inhalation
/(1000/Mass_inhale)) * Recov_inhale))) - (ET1 *
(RT_ET1_ET2 + RT_ET1_NB));
dt (NB) = (ET1 * RT_ET1_NB);
# Inhaled material into gut
# Stomach
dt(Q_sto_I) = (ET2 * RT_ET2_St) - (Kt_s * Q_sto_I) -
(Q_sto_I * Lum_blo);
dt(Q_sto_T) = (ET2_T * RT_ET2_St) - (Kt_s *
Q_sto_T) - (Q_sto_T * Lum_blo);
# Duodenum
dt(Q_C1_I) = (Kt_s * Q_sto_I) - (Kt_1 * Q_C1_I) -
(Q_C1_I * Lum_blo);
dt(Q_C1_T) = (Kt_s * Q_sto_T) - (Kt_1 * Q_C1_T) -
(Q_C1_T * Lum_blo);
# Jejunum 1 to Ileum 4
dt(Q_C2_7_I) = (Kt_1 * Q_C1_I) - (Kt_2_7 *
Q_C2_7_I) - (Q_C2_7_I * Lum_blo);
dt(Q_C2_7_T) = (Kt_1 * Q_C1_T) - (Kt_2_7 *
Q_C2_7_T) - (Q_C2_7_T * Lum_blo);
# Colon
dt(Q_col_I) = (Kt_2_7 * Q_C2_7_I) - (Kt_c *
Q_col_I) - (Q_col_I * Lum_blo);
dt(Q_col_T) = (Kt_2_7 * Q_C2_7_T) - (Kt_c *
Q_col_T) - (Q_col_T * Lum_blo);
# Gut
# Stomach
dt(Q_sto_und) = (Solid_ingested * ((Solid_ingest
/(1000/Mass_oral)) * Recov_oral)) - (On_Off_sto_d
* DR * DR_C_sto * Q_sto_und) + (On_Off_sto_p *
PR * PR_C_sto) - (Kt_s * Q_sto_und);
dt(Q_sto_dis) =  (Solution_ingested *
((Solution_ingest /(1000/Mass_oral)) *
Recov_oral)) + (On_Off_sto_d * DR * DR_C_sto *
Q_sto_und) - (On_Off_sto_p * PR * PR_C_sto) -
(Kt_s * Q_sto_dis) - perm_sto;
dt(Q_sto_abs) = perm_sto;
# Duodenum
dt(Q_C1_und) = (Kt_s * Q_sto_und) -
(On_Off_C1_d * DR * DR_C_C1 * Q_C1_und) +
(On_Off_C1_p * PR * PR_C_C1) - (Kt_1 *
Q_C1_und);
dt(Q_C1_dis) = (Kt_s * Q_sto_dis) + (perm_liv_am
* EHCm) + (On_Off_C1_d * DR * DR_C_C1 *
Q_C1_und) - (On_Off_C1_p * PR * PR_C_C1) +
((PStc_liv_a * (Ct_liv * fut_tis)) + ((Vmax_w_liv_a *
Ct_liv * fut_tis) / (Km_liv_a + (Ct_liv * fut_tis)))) -
(Kt_1 * Q_C1_dis) - perm_C1_a;
dt(Q_ent_C1) = perm_C1_a - perm_C1_b;
dt(Q_ent_C1_abs) = perm_C1_a;
dt(C1_tot) = dt(Q_C1_dis) + dt(Q_ent_C1);
# Jejunum 1 to Ileum 4
dt(Q_C2_7_und) = (Kt_1 * Q_C1_und) -
(On_Off_C2_7_d * DR * DR_C_C2_7 *
Q_C2_7_und) + (On_Off_C2_7_p * PR *
PR_C_C2_7) - (Kt_2_7 * Q_C2_7_und);
dt(Q_C2_7_dis) = (Kt_1 * Q_C1_dis) +
(On_Off_C2_7_d * DR * DR_C_C2_7 *
Q_C2_7_und) - (On_Off_C2_7_p * PR *
PR_C_C2_7) - (Kt_2_7 * Q_C2_7_dis) -
perm_C2_7_a;
dt(Q_ent_C2_7) = perm_C2_7_a - perm_C2_7_b  -
((Vmax_w_gut_e * C_ent_C2_7 * fut_tis) /
(Km_gut_e + (C_ent_C2_7 * fut_tis)));
dt(Q_ent_C2_7_abs) = perm_C2_7_a;
dt(C2_7_tot) = dt(Q_C2_7_dis) + dt(Q_ent_C2_7);
# Colon
dt(Q_col_und) = (Kt_2_7 * Q_C2_7_und) -
(On_Off_col_d  * DR * DR_C_col * Q_col_und) +
(On_Off_col_p * PR * PR_C_col) - (Kt_c *
Q_col_und);
dt(Q_col_dis) = (Kt_2_7 * Q_C2_7_dis) +
(On_Off_col_d  * DR * DR_C_col * Q_col_und) -
(On_Off_col_p * PR * PR_C_col) - (Kt_c *
Q_col_dis) - perm_col_a;
dt(Q_ent_col) = perm_col_a - perm_col_b;
dt(Q_ent_col_abs) = perm_col_a;
dt(Ccol_tot) = dt(Q_col_dis) + dt(Q_ent_col);
dt(Q_fec) = (Kt_c * (Q_col_dis + Q_col_und)) +
(Kt_c * (Q_col_T + Q_col_I));
# Portal Vein
dt (Q_Fa) = perm_C1_a + perm_C2_7_a +
perm_col_a;
dt(Q_FDp) = perm_sto + perm_C1_b +
perm_C2_7_b + perm_col_b;
dt(Q_gut_blo) = ((Q_sto_I * Lum_blo) + (Q_sto_T *
Lum_blo) + (Q_C1_I * Lum_blo) + (Q_C1_T *
Lum_blo) + (Q_C2_7_I * Lum_blo) + (Q_C2_7_T *
Lum_blo) + (Q_col_I * Lum_blo) + (Q_col_T *
Lum_blo)) + perm_sto + perm_C1_b +
perm_C2_7_b + perm_col_b + (F_gut * C_art) -
(F_gut * Ct_gut_blo);
# Body tissues
# Kidney
dt(Q_kid) = (F_kid * C_art) - (F_kid * C_kid_v) -
perm_kid_a - ((Vmax_w_kid_e * Ct_kid * fut_tis) /
(Km_kid_e + (Ct_kid * fut_tis)));
dt(Q_nep) = perm_kid_a + (GFR * fup_exp * C_art)
- (QUR * Q_nep);
```

```
dt(Q_uri) = (QUR * Q_nep);
dt(Q_kid_met) = ((Vmax_w_kid_e * Ct_kid *
fut_tis) / (Km_kid_e + (Ct_kid * fut_tis)));
# Liver
dt(Q_liv_met) = Stoichiometry * ((Vmax_w_liv_e *
Ct_liv * fut_tis) / (Km_liv_e + (Ct_liv * fut_tis)));
dt(Q_bil) = perm_liv_a + ((Vmax_w_liv_e * Ct_liv *
fut_tis) / (Km_liv_e + (Ct_liv * fut_tis))); # for
quality control.
dt(Q_liv) = (F_gut * Ct_gut_blo) + (F_hep * C_art) +
(F_spl * C_spl_v) - (F_liv * C_liv_v) - perm_liv_a -
((Vmax_w_liv_e * Ct_liv * fut_tis) / (Km_liv_e +
(Ct_liv * fut_tis)));
# Skin
dt(Q_ski_met) = 0;#((Vmax_w_ski_e * Ce_ski *
fut_tis) / (Km_ski_e + (Ce_ski * fut_tis)));
dt(Q_ski) = (F_ski * C_art) - (F_ski * C_ski_v) -
perm_ski;
dt(Q_fab) = (Clothes * ((Fabric
/(1000/Mass_fabric)) * Recov_fabric)) + perm_ski -
(Q_fab * Cry);
dt(Q_Crystal) = (Q_fab * Cry);
# Adipose
dt(Q_adi_met) = ((Vmax_w_adi_e * Ct_adi *
fut_adi) / (Km_adi_e + (Ct_adi * fut_adi))); # n.b.
fut_adi
dt(Q_adi) = (F_adi * C_art) - (F_adi * C_adi_v) -
((Vmax_w_adi_e * Ct_adi * fut_adi) / (Km_adi_e +
(Ct_adi * fut_adi))); # n.b. fut_adi
# Skeletal Muscle
dt(Q_mus_met) = ((Vmax_w_mus_e * Ct_mus *
fut_tis) / (Km_mus_e + (Ct_mus * fut_tis)));
dt(Q_mus) = (F_mus * C_art) - (F_mus * C_mus_v)
- ((Vmax_w_mus_e * Ct_mus * fut_tis) /
(Km_mus_e + (Ct_mus * fut_tis)));
# Spleen
dt(Q_spl_met) = ((Vmax_w_spl_e * Ct_spl *
fut_tis) / (Km_spl_e + (Ct_spl * fut_tis)));
dt(Q_spl) = (F_spl * C_art) - (F_spl * C_spl_v) -
((Vmax_w_spl_e * Ct_spl * fut_tis) / (Km_spl_e +
(Ct_spl * fut_tis)));
# Yellow Marrow
dt(Q_yel_met) = ((Vmax_w_yel_e * Ct_yel *
fut_adi) / (Km_yel_e + (Ct_yel * fut_adi))); # n.b.
fut_yel
dt(Q_yel) = (F_yel * C_art) - (F_yel * C_yel_v) -
((Vmax_w_yel_e * Ct_yel * fut_adi) / (Km_yel_e +
(Ct_yel * fut_adi))); # n.b. fut_adi
# Heart
dt(Q_hea_met) = ((Vmax_w_hea_e * Ct_hea *
fut_tis) / (Km_hea_e + (Ct_hea * fut_tis)));
dt(Q_hea) = (F_hea * C_art) - (F_hea * C_hea_v) -
((Vmax_w_hea_e * Ct_hea * fut_tis) / (Km_hea_e
+ (Ct_hea * fut_tis)));
# Brain
dt(Q_bra_met) = ((Vmax_w_bra_e * Ct_bra *
fut_tis) / (Km_bra_e + (Ct_bra * fut_tis)));
dt(Q_bra) = (F_bra * C_art) - (F_bra * C_bra_v) -
((Vmax_w_bra_e * Ct_bra * fut_tis) / (Km_bra_e +
(Ct_bra * fut_tis)));
# Reproductive Organs
dt(Q_rep_met) = ((Vmax_w_rep_e * Ct_rep *
fut_tis) / (Km_rep_e + (Ct_rep * fut_tis)));
dt(Q_rep) = (F_rep * C_art) - (F_rep * C_rep_v) -
((Vmax_w_rep_e * Ct_rep * fut_tis) / (Km_rep_e +
(Ct_rep * fut_tis)));
# Red Marrow
dt(Q_red_met) = ((Vmax_w_red_e * Ct_red *
fut_tis) / (Km_red_e + (Ct_red * fut_tis)));
dt(Q_red) = (F_red * C_art) - (F_red * C_red_v) -
((Vmax_w_red_e * Ct_red * fut_tis) / (Km_red_e +
(Ct_red * fut_tis)));
# Rest of body
dt(Q_rob_met) = ((Vmax_w_rob_e * Ct_rob *
fut_tis) / (Km_rob_e + (Ct_rob * fut_tis)));
dt(Q_rob) = (F_rob * C_art) - (F_rob * C_rob_v) -
((Vmax_w_rob_e * Ct_rob * fut_tis) / (Km_rob_e +
(Ct_rob * fut_tis)));
# Venous blood
dt(Q_ven) = ((Q_iv /(1000/Mass_iv)) * Recov_iv) +
(F_liv * C_liv_v) + (F_kid * C_kid_v) + (F_ski *
C_ski_v) + (F_adi * C_adi_v) + (F_rob * C_rob_v) +
(F_mus * C_mus_v) + (F_yel * C_yel_v) + (F_hea *
C_hea_v) + (F_bra * C_bra_v) + (F_rep * C_rep_v)
+ (F_red * C_red_v) - (F_ven * C_ven);
# Lung
dt(Q_lun_met) = ((Vmax_w_lun_e * Ct_lun *
fut_tis) / (Km_lun_e + (Ct_lun * fut_tis)));
dt(Q_lun) = (F_lun * C_ven) - (F_lun * C_lun_v) -
((Vmax_w_lun_e * Ct_lun * fut_tis) / (Km_lun_e +
(Ct_lun * fut_tis)));
# Arterial blood
dt(Q_art) = (F_lun * C_lun_v) - (F_art * C_art) +
(((1-Fb) * SP * (A + I + LNTH + BB + BB_seq + bb +
bb_seq + ET2 + ET_seq + LNET)) + ((1-Fb) * ST *
(A_T +I_T +LNTH_T +BB_T + BB_seq_T + bb_T +
bb_seq_T+ET2_T+ET_seq_T+LNET_T)) + (Sb *
(A_bnd +I_bnd +LNTH_bnd +BB_bnd +
BB_seq_bnd + bb_bnd +
bb_seq_bnd+ET2_bnd+ET_seq_bnd+LNET_bnd))) -
(GFR * fup_exp * C_art);
dt(Q_cl_tot) = dt(Q_kid_met) + dt(Q_liv_met) +
dt(Q_ski_met) + dt(Q_adi_met) + dt(Q_rob_met) +
dt(Q_lun_met) + dt(Q_mus_met) + dt(Q_spl_met)
+ dt(Q_yel_met) + dt(Q_hea_met) +
dt(Q_bra_met) + dt(Q_rep_met) + dt(Q_red_met);
# Permeability-limited model (1st metabolite)
# Gut
dt(Q_sto_dism) = -(Kt_s * Q_sto_dism) -
perm_stom;
dt(Q_sto_absm) = perm_stom;
dt(Q_C1_dism) = (Kt_s * Q_sto_dism) - (Kt_1 *
Q_C1_dism) - perm_C1_am;
dt(Q_ent_C1m) = perm_C1_am - perm_C1_bm;
```

```
dt(Q_ent_C1_absm) = perm_C1_am;
dt(C1_totm) = dt(Q_C1_dism) + dt(Q_ent_C1m);
dt(Q_C2_7_dism) = (Kt_1 * Q_C1_dism) - (Kt_2_7
* Q_C2_7_dism) - perm_C2_7_am;
dt(Q_ent_C2_7m) = perm_C2_7_am -
perm_C2_7_bm + ((Vmax_w_gut_e * C_ent_C2_7
* fut_tis) / (Km_gut_e + (C_ent_C2_7 * fut_tis)));
dt(Q_ent_C2_7_absm) = perm_C2_7_am;
dt(C2_7_totm) = dt(Q_C2_7_dism) +
dt(Q_ent_C2_7m);
dt(Q_col_dism) = (Kt_2_7 * Q_C2_7_dism) - (Kt_c
* Q_col_dism) - perm_col_am;
dt(Q_ent_colm) = perm_col_am - perm_col_bm;
dt(Q_ent_col_absm) = perm_col_am;
dt(Ccol_totm) = dt(Q_col_dism) + dt(Q_ent_colm);
dt(Q_fecm) = Kt_c * Q_col_dism;
dt(Q_GITm) = dt(Q_C1_dism) + dt(Q_ent_C1m) +
dt(Q_C2_7_dism) + dt(Q_ent_C2_7m) +
dt(Q_col_dism) + dt(Q_ent_colm);
dt (Q_Fam) = perm_C1_am + perm_C2_7_am +
perm_col_am;
dt(Q_FDpm) = perm_stom + perm_C1_bm +
perm_C2_7_bm + perm_col_bm;
dt(Q_gut_blom) = perm_stom + perm_C1_bm +
perm_C2_7_bm + perm_col_bm + (F_gut *
C_artm) - (F_gut * Ct_gut_blom);
# Body tissues
dt(Q_kid_im) = perm_kid_bm - perm_kid_am;
dt(Q_nepm) = perm_kid_am + (GFR * fup_expm *
C_artm) - (QUR * Q_nepm);
dt(Q_urim) = (QUR * Q_nepm);
dt(Q_kid_em) = (F_kid * C_artm) - (F_kid *
C_kid_vm) - perm_kid_bm;
dt(Q_kid_totm) = dt(Q_kid_em) + dt(Q_kid_im);
dt(Q_liv_im) = perm_liv_bm - perm_liv_am +
(((Vmax_w_liv_e * Ct_liv * fut_tis) / (Km_liv_e +
(Ct_liv * fut_tis))) * EHC);
dt(Q_bilm) = 0;
dt(Q_liv_em) = (F_gut * Ct_gut_blom) + (F_hep *
C_artm) + (F_spl * C_spl_vm) - (F_liv * C_liv_vm) -
perm_liv_bm;
dt(Q_liv_totm) = dt(Q_liv_em) + dt(Q_liv_im);
dt(Q_ski_em) = (F_ski * C_artm) - (F_ski *
C_ski_vm) - perm_skim;
dt(Q_ski_im) =  perm_skim;# + ((Vmax_w_ski_e *
Ct_ski * fut_tis) / (Km_ski_e + (Ct_ski * fut_tis))); #
input from parent model
dt(Q_ski_totm) = dt(Q_ski_em) + dt(Q_ski_im);
dt(Q_adi_im) = perm_adim;# + ((Vmax_w_adi_e *
Ct_adi * fut_adi) / (Km_adi_e + (Ct_adi *
fut_adi))); # input from parent model
dt(Q_adi_em) = (F_adi * C_artm) - (F_adi *
C_adi_vm) - perm_adim;
dt(Q_adi_totm) = dt(Q_adi_em) + dt(Q_adi_im);
dt(Q_mus_im) = perm_musm;# +
((Vmax_w_mus_e * Ct_mus * fut_tis) /
(Km_mus_e + (Ct_mus * fut_tis))); # input from
parent model
dt(Q_mus_em) = (F_mus * C_artm) - (F_mus *
C_mus_vm) - perm_musm;
dt(Q_mus_totm) = dt(Q_mus_em) +
dt(Q_mus_im);
dt(Q_spl_im) = perm_splm;# + ((Vmax_w_spl_e *
Ct_spl * fut_tis) / (Km_spl_e + (Ct_spl * fut_tis))); #
input from parent model
dt(Q_spl_em) = (F_spl * C_artm) - (F_spl *
C_spl_vm) - perm_splm;
dt(Q_spl_totm) = dt(Q_spl_em) + dt(Q_spl_im);
dt(Q_yel_im) = perm_yelm;# + ((Vmax_w_yel_e *
Ct_yel * fut_adi) / (Km_yel_e + (Ct_yel * fut_adi)));
# input from parent model, n.b. fut_adi
dt(Q_yel_em) = (F_yel * C_artm) - (F_yel *
C_yel_vm) - perm_yelm;
dt(Q_yel_totm) = dt(Q_yel_em) + dt(Q_yel_im);
dt(Q_hea_im) = perm_heam;# + ((Vmax_w_hea_e
* Ct_hea * fut_tis) / (Km_hea_e + (Ct_hea *
fut_tis))); # input from parent model
dt(Q_hea_em) = (F_hea * C_artm) - (F_hea *
C_hea_vm) - perm_heam;
dt(Q_hea_totm) = dt(Q_hea_em) + dt(Q_hea_im);
dt(Q_bra_im) = perm_bram;# + ((Vmax_w_bra_e *
Ct_bra * fut_tis) / (Km_bra_e + (Ct_bra * fut_tis)));
# input from parent model
dt(Q_bra_em) = (F_bra * C_artm) - (F_bra *
C_bra_vm) - perm_bram;
dt(Q_bra_totm) = dt(Q_bra_em) + dt(Q_bra_im);
dt(Q_rep_im) = perm_repm;# + ((Vmax_w_rep_e *
Ct_rep * fut_tis) / (Km_rep_e + (Ct_rep * fut_tis)));
# input from parent model
dt(Q_rep_em) = (F_rep * C_artm) - (F_rep *
C_rep_vm) - perm_repm;
dt(Q_rep_totm) = dt(Q_rep_em) + dt(Q_rep_im);
dt(Q_red_im) = perm_redm;# + ((Vmax_w_red_e *
Ct_red * fut_tis) / (Km_red_e + (Ct_red * fut_tis)));
# input from parent model
dt(Q_red_em) = (F_red * C_artm) - (F_red *
C_red_vm) - perm_redm;
dt(Q_red_totm) = dt(Q_red_em) + dt(Q_red_im);
dt(Q_rob_im) = perm_robm;# + ((Vmax_w_rob_e
* Ct_rob * fut_tis) / (Km_rob_e + (Ct_rob *
fut_tis))); # input from parent model
dt(Q_rob_em) = (F_rob * C_artm) - (F_rob *
C_rob_vm) - perm_robm;
dt(Q_rob_totm) = dt(Q_rob_em) + dt(Q_rob_im);
dt(Q_venm) = ((Q_ivm /(1000/Mass_iv)) *
Recov_iv) + (F_liv * C_liv_vm) + (F_kid * C_kid_vm)
+ (F_ski * C_ski_vm) + (F_adi * C_adi_vm) + (F_rob
* C_rob_vm) + (F_mus * C_mus_vm) + (F_yel *
C_yel_vm) + (F_hea * C_hea_vm) + (F_bra *
C_bra_vm) + (F_rep * C_rep_vm) + (F_red *
C_red_vm) - (F_ven * C_venm);
```

```
dt(Q_lun_im) = perm_lunm;# + ((Vmax_w_lun_e *
Ct_lun * fut_tis) / (Km_lun_e + (Ct_lun * fut_tis)));
# input from parent model
dt(Q_lun_em) = (F_lun * C_venm) - (F_lun *
C_lun_vm) - perm_lunm;
dt(Q_lun_totm) = dt(Q_lun_em) + dt(Q_lun_im);
dt(Q_artm) = (F_lun * C_lun_vm) - (F_art *
C_artm) - (GFR * fup_expm * C_artm);

# Permeability-limited model (2nd metabolite)
# Gut
dt(Q_sto_dism2) = -(Kt_s * Q_sto_dism2) -
perm_stom2;
dt(Q_sto_absm2) = perm_stom2;
dt(Q_C1_dism2) = (Kt_s * Q_sto_dism2) +
(perm_liv_am2 * EHCm2) - (Kt_1 * Q_C1_dism2) -
perm_C1_am2;
dt(Q_ent_C1m2) = perm_C1_am2 -
perm_C1_bm2;
dt(Q_ent_C1_absm2) = perm_C1_am2;
dt(C1_totm2) = dt(Q_C1_dism2) +
dt(Q_ent_C1m2);
dt(Q_C2_7_dism2) = (Kt_1 * Q_C1_dism2) -
(Kt_2_7 * Q_C2_7_dism2) - perm_C2_7_am2;
dt(Q_ent_C2_7m2) = perm_C2_7_am2 -
perm_C2_7_bm2;
dt(Q_ent_C2_7_absm2) = perm_C2_7_am2;
dt(C2_7_totm2) = dt(Q_C2_7_dism2) +
dt(Q_ent_C2_7m2);
dt(Q_col_dism2) = (Kt_2_7 * Q_C2_7_dism2) -
(Kt_c * Q_col_dism2) - perm_col_am2;
dt(Q_ent_colm2) = perm_col_am2 -
perm_col_bm2;
dt(Q_ent_col_absm2) = perm_col_am2;
dt(Ccol_totm2) = dt(Q_col_dism2) +
dt(Q_ent_colm2);
dt(Q_fecm2) = Kt_c * Q_col_dism2;
dt(Q_GITm2) = dt(Q_C1_dism2) + dt(Q_ent_C1m2)
+ dt(Q_C2_7_dism2) + dt(Q_ent_C2_7m2) +
dt(Q_col_dism2) + dt(Q_ent_colm2);
dt (Q_Fam2) = perm_C1_am2 + perm_C2_7_am2 +
perm_col_am2;
dt(Q_FDpm2) = perm_stom2 + perm_C1_bm2 +
perm_C2_7_bm2 + perm_col_bm2;
dt(Q_gut_blom2) = perm_stom2 + perm_C1_bm2
+ perm_C2_7_bm2 + perm_col_bm2 + (F_gut *
C_artm2) - (F_gut * Ct_gut_blom2);
# Body tissues
dt(Q_kid_im2) = perm_kid_bm2 - perm_kid_am2;
dt(Q_nepm2) = perm_kid_am2 + (GFR *
fup_expm2 * C_artm2) - (QUR * Q_nepm2);
dt(Q_urim2) = (QUR * Q_nepm2);
dt(Q_kid_em2) = (F_kid * C_artm2) - (F_kid *
C_kid_vm2) - perm_kid_bm2;
dt(Q_kid_totm2) = dt(Q_kid_em2) +
dt(Q_kid_im2);
dt(Q_liv_im2) = perm_liv_bm2 - perm_liv_am2;
dt(Q_bilm2) = 0;
dt(Q_liv_em2) = (F_gut * Ct_gut_blom2) + (F_hep
* C_artm2) + (F_spl * C_spl_vm2) - (F_liv *
C_liv_vm2) - perm_liv_bm2;
dt(Q_liv_totm2) = dt(Q_liv_em2) + dt(Q_liv_im2);
dt(Q_ski_em2) = (F_ski * C_artm2) - (F_ski *
C_ski_vm2) - perm_skim2;
dt(Q_ski_im2) =  perm_skim2;# + ((Vmax_w_ski_e
* Ct_ski * fut_tis) / (Km_ski_e + (Ct_ski * fut_tis)));
# input from parent model
dt(Q_ski_totm2) = dt(Q_ski_em2) + dt(Q_ski_im2);
dt(Q_adi_im2) = perm_adim2; # +
((Vmax_w_adi_e * Ct_adi * fut_adi) / (Km_adi_e +
(Ct_adi * fut_adi))); # input from parent model
dt(Q_adi_em2) = (F_adi * C_artm2) - (F_adi *
C_adi_vm2) - perm_adim2;
dt(Q_adi_totm2) = dt(Q_adi_em2) +
dt(Q_adi_im2);
dt(Q_mus_im2) = perm_musm2; #  +
((Vmax_w_mus_e * Ct_mus * fut_tis) /
(Km_mus_e + (Ct_mus * fut_tis))); # input from
parent model
dt(Q_mus_em2) = (F_mus * C_artm2) - (F_mus *
C_mus_vm2) - perm_musm2;
dt(Q_mus_totm2) = dt(Q_mus_em2) +
dt(Q_mus_im2);
dt(Q_spl_im2) = perm_splm2; # + ((Vmax_w_spl_e
* Ct_spl * fut_tis) / (Km_spl_e + (Ct_spl * fut_tis)));
# input from parent model
dt(Q_spl_em2) = (F_spl * C_artm2) - (F_spl *
C_spl_vm2) - perm_splm2;
dt(Q_spl_totm2) = dt(Q_spl_em2) +
dt(Q_spl_im2);
dt(Q_yel_im2) = perm_yelm2; # + ((Vmax_w_yel_e
* Ct_yel * fut_adi) / (Km_yel_e + (Ct_yel *
fut_adi))); # input from parent model, n.b. fut_adi
dt(Q_yel_em2) = (F_yel * C_artm2) - (F_yel *
C_yel_vm2) - perm_yelm2;
dt(Q_yel_totm2) = dt(Q_yel_em2) +
dt(Q_yel_im2);
dt(Q_hea_im2) = perm_heam2; # +
((Vmax_w_hea_e * Ct_hea * fut_tis) / (Km_hea_e
+ (Ct_hea * fut_tis))); # input from parent model
dt(Q_hea_em2) = (F_hea * C_artm2) - (F_hea *
C_hea_vm2) - perm_heam2;
dt(Q_hea_totm2) = dt(Q_hea_em2) +
dt(Q_hea_im2);
dt(Q_bra_im2) = perm_bram2; # +
((Vmax_w_bra_e * Ct_bra * fut_tis) / (Km_bra_e +
(Ct_bra * fut_tis))); # input from parent model
dt(Q_bra_em2) = (F_bra * C_artm2) - (F_bra *
C_bra_vm2) - perm_bram2;
dt(Q_bra_totm2) = dt(Q_bra_em2) +
dt(Q_bra_im2);
dt(Q_rep_im2) = perm_repm2; # +
((Vmax_w_rep_e * Ct_rep * fut_tis) / (Km_rep_e +
(Ct_rep * fut_tis))); # input from parent model
```

```
dt(Q_rep_em2) = (F_rep * C_artm2) - (F_rep *
C_rep_vm2) - perm_repm2;
dt(Q_rep_totm2) = dt(Q_rep_em2) +
dt(Q_rep_im2);
dt(Q_red_im2) = perm_redm2; # +
((Vmax_w_red_e * Ct_red * fut_tis) / (Km_red_e +
(Ct_red * fut_tis))); # input from parent model
dt(Q_red_em2) = (F_red * C_artm2) - (F_red *
C_red_vm2) - perm_redm2;
dt(Q_red_totm2) = dt(Q_red_em2) +
dt(Q_red_im2);
dt(Q_rob_im2) = perm_robm2; # +
((Vmax_w_rob_e * Ct_rob * fut_tis) / (Km_rob_e +
(Ct_rob * fut_tis))); # input from parent model
dt(Q_rob_em2) = (F_rob * C_artm2) - (F_rob *
C_rob_vm2) - perm_robm2;
dt(Q_rob_totm2) = dt(Q_rob_em2) +
dt(Q_rob_im2);
dt(Q_venm2) = ((Q_ivm2 /(1000/Mass_iv)) *
Recov_iv) + (F_liv * C_liv_vm2) + (F_kid *
C_kid_vm2) + (F_ski * C_ski_vm2) + (F_adi *
C_adi_vm2) + (F_rob * C_rob_vm2) + (F_mus *
C_mus_vm2) + (F_yel * C_yel_vm2) + (F_hea *
C_hea_vm2) + (F_bra * C_bra_vm2) + (F_rep *
C_rep_vm2) + (F_red * C_red_vm2) - (F_ven *
C_venm2);
dt(Q_lun_im2) = perm_lunm2; # +
((Vmax_w_lun_e * Ct_lun * fut_tis) / (Km_lun_e +
(Ct_lun * fut_tis))); # input from perf model
dt(Q_lun_em2) = (F_lun * C_venm2) - (F_lun *
C_lun_vm2) - perm_lunm2;
dt(Q_lun_totm2) = dt(Q_lun_em2) +
dt(Q_lun_im2);
dt(Q_artm2) = (F_lun * C_lun_vm2) - (F_art *
C_artm2) - (GFR * fup_expm2 * C_artm2);
# Intake through all routes of absorption, used to
calculate F, Fdp and Fa.
dt(Intake) = (Clothes * ((Fabric
/(1000/Mass_fabric)) * Recov_fabric)) +
(Solid_ingested * ((Solid_ingest
/(1000/Mass_oral)) * Recov_oral)) +
(Solution_ingested * ((Solution_ingest
/(1000/Mass_oral)) * Recov_oral)) + (Inhale *
((Inhalation /(1000/Mass_inhale)) * Recov_inhale))
+ ((Q_iv /(1000/Mass_iv)) * Recov_iv);
}

CalcOutputs {
MB1 = Q_sto_dis + Q_C1_dis + Q_ent_C1 +
Q_C2_7_dis + Q_ent_C2_7 + Q_col_dis +
Q_ent_col + Q_sto_und + Q_C1_und +
Q_C2_7_und + Q_col_und + Q_fec + Q_gut_blo;
MB2 = Q_kid + Q_nep + Q_uri + Q_ven + Q_art;
MB3 = Q_liv + Q_fab + Q_Crystal + Q_ski + Q_rob +
Q_adi + Q_lun + Q_mus + Q_spl + Q_yel + Q_hea +
Q_bra + Q_rep + Q_red;
MB4 = A + A_T + A_bnd + I + I_T + I_bnd + LNTH +
LNTH_T + LNTH_bnd + BB + BB_T + BB_bnd +
BB_seq + BB_seq_T + BB_seq_bnd + bb + bb_T +
bb_bnd + bb_seq + bb_seq_T + bb_seq_bnd + ET2
+ ET2_T + ET2_bnd + ET_seq + ET_seq_T +
ET_seq_bnd + LNET + LNET_T + LNET_bnd + ET1 +
NB + Q_sto_I + Q_sto_T + Q_C1_I + Q_C1_T +
Q_C2_7_I + Q_C2_7_T + Q_col_I + Q_col_T;
MB5 = Q_kid_met + Q_ski_met + Q_adi_met +
Q_rob_met + Q_lun_met + Q_mus_met +
Q_spl_met + Q_yel_met + Q_hea_met +
Q_bra_met + Q_rep_met + Q_red_met;
MB6 = Q_sto_dism + Q_C1_dism + Q_ent_C1m +
Q_C2_7_dism + Q_ent_C2_7m + Q_col_dism +
Q_ent_colm + Q_fecm;
MB7 = Q_gut_blom + Q_kid_totm + Q_nepm +
Q_urim + Q_venm + Q_artm + Q_bilm +
Q_liv_totm + Q_ski_totm + Q_rob_totm +
Q_adi_totm + Q_lun_totm + Q_mus_totm +
Q_spl_totm + Q_yel_totm + Q_hea_totm +
Q_bra_totm + Q_rep_totm + Q_red_totm;
MB8 = Q_sto_dism2 + Q_C1_dism2 + Q_ent_C1m2
+ Q_C2_7_dism2 + Q_ent_C2_7m2 + Q_col_dism2
+ Q_ent_colm2 + Q_fecm2;
MB9 = Q_gut_blom2 + Q_kid_totm2 + Q_nepm2 +
Q_urim2 + Q_venm2 + Q_artm2 + Q_bilm2 +
Q_liv_totm2 + Q_ski_totm2 + Q_rob_totm2 +
Q_adi_totm2 + Q_lun_totm2 + Q_mus_totm2 +
Q_spl_totm2 + Q_yel_totm2 + Q_hea_totm2 +
Q_bra_totm2 + Q_rep_totm2 + Q_red_totm2; #
Omit Qlivmet as it enters metabolism models. If
EHC = 0 include Qbil.
MassBalance = ((MB1 + MB2 + MB3 + MB4 + MB5
+ MB6 + MB7 + MB8 + MB9) / (Mass_oral / 1000));
# Quality control
# Calculate systemic exposure
SE1 = Q_ent_C1 + Q_ent_C2_7 + Q_ent_col +
Q_gut_blo;
SE2 = Q_kid + Q_nep + Q_ven + Q_art;
SE3 = Q_liv + Q_ski + Q_rob + Q_adi + Q_lun +
Q_mus + Q_spl + Q_yel + Q_hea + Q_bra + Q_rep +
Q_red;
SE4 = A_T + A_bnd + I_T + I_bnd + LNTH_T +
LNTH_bnd + BB_T + BB_bnd + BB_seq_T +
BB_seq_bnd + bb_T + bb_bnd + bb_seq_T +
bb_seq_bnd + ET2_T + ET2_bnd + ET_seq_T +
ET_seq_bnd + LNET_T + LNET_bnd;
SE5 = Q_kid_met + Q_ski_met + Q_adi_met +
Q_rob_met + Q_lun_met + Q_mus_met +
Q_spl_met + Q_yel_met + Q_hea_met +
Q_bra_met + Q_rep_met + Q_red_met;
SE6 = Q_ent_C1m + Q_ent_C2_7m + Q_ent_colm;
SE7 = Q_gut_blom + Q_kid_totm + Q_nepm +
Q_venm + Q_artm + Q_liv_totm + Q_ski_totm +
Q_rob_totm + Q_adi_totm + Q_lun_totm +
Q_mus_totm + Q_spl_totm + Q_yel_totm +
```

```
Q_hea_totm + Q_bra_totm + Q_rep_totm +
Q_red_totm;
SE8 = Q_ent_C1m2 + Q_ent_C2_7m2 +
Q_ent_colm2;
SE9 = Q_gut_blom2 + Q_kid_totm2 + Q_nepm2 +
Q_venm2 + Q_artm2 + Q_liv_totm2 + Q_ski_totm2
+ Q_rob_totm2 + Q_adi_totm2 + Q_lun_totm2 +
Q_mus_totm2 + Q_spl_totm2 + Q_yel_totm2 +
Q_hea_totm2 + Q_bra_totm2 + Q_rep_totm2 +
Q_red_totm2;
SystemicExposure = ((SE1 + SE2 + SE3 + SE4 + SE5 +
SE6 + SE7 + SE8 + SE9) / (Mass_fabric / 1000));
Fa = (Q_Fa / Intake) * 100; # Fraction absorbed
into apical membrane enterocytes (%)
FDp = (Q_FDp / Intake) * 100; # Fraction drug
absorbed into portal vein (%)
F = ((Q_FDp - Q_liv_met) / Intake) * 100; #
Bioavailability (%)
Fa_skin = (-perm_ski / Clothes) * 100;
In = Intake;
QCrystal = Q_Crystal;
Qven = Q_ven;
Qart = Q_art;
Qgutblo = Q_gut_blo;
Qstound = Q_sto_und;
QC1und =  Q_C1_und;
QC2_7und =  Q_C2_7_und;
Qcolund = Q_col_und;
Qstodis = Q_sto_dis;
QC1dis = Q_C1_dis;
QC2_7dis = Q_C2_7_dis;
Qcoldis = Q_col_dis;
Qbil = Q_bil;
QentC1abs = Q_ent_C1_abs;
QentC2_7abs = Q_ent_C2_7_abs;
Qentcolabs = Q_ent_col_abs;
C1tot = C1_tot;
C2_7tot = C2_7_tot;
Ccoltot = Ccol_tot;
Qfec = Q_fec;
Qstoabs = Q_sto_abs;
QentC1 = Q_ent_C1;
QentC2_7 = Q_ent_C2_7;
Qentcol = Q_ent_col;
Qnep = Q_nep;
Quri = Q_uri;
Qfab = Q_fab;
Qkid = Q_kid;
Qliv = Q_liv;
Qski = Q_ski;
Qadi = Q_adi;
Qrob = Q_rob;
Qlun = Q_lun;
Qmus = Q_mus;
Qspl = Q_spl;
Qyel = Q_yel;
Qhea = Q_hea;
Qbra = Q_bra;
Qrep = Q_rep;
Qred = Q_red;
Qkidmet = Q_kid_met;
Qlivmet = Q_liv_met;
Qskimet = Q_ski_met;
Qadimet = Q_adi_met;
Qrobmet = Q_rob_met;
Qlunmet = Q_lun_met;
Qmusmet = Q_mus_met;
Qsplmet = Q_spl_met;
Qyelmet = Q_yel_met;
Qheamet = Q_hea_met;
Qbramet = Q_bra_met;
Qrepmet = Q_rep_met;
Qredmet = Q_red_met;
Qcltot = Q_cl_tot;
# Permeability-limitied model (1st metabolite)
Fam = (Q_Fam / Intake) * 100;
FDpm = (Q_FDpm / Intake) * 100;
Qvenm = Q_venm;
Qartm = Q_artm ;
Qgutblom = Q_gut_blom ;
Qstodism = Q_sto_dism;
QC1dism = Q_C1_dism;
QC2_7dism = Q_C2_7_dism;
Qcoldism = Q_col_dism;
Qbilm = Q_bilm;
QentC1absm = Q_ent_C1_absm;
QentC2_7absm = Q_ent_C2_7_absm;
Qentcolabsm = Q_ent_col_absm;
C1totm = C1_totm;
C2_7totm = C2_7_totm;
Ccoltotm = Ccol_totm;
Qfecm = Q_fecm;
Qstoabsm = Q_sto_absm;
QentC1m = Q_ent_C1m;
QentC2_7m = Q_ent_C2_7m;
Qentcolm = Q_ent_colm;

QGITm = Q_GITm;
Qurim = Q_urim;
Qnepm = Q_nepm;
Qlivtotm = Q_liv_totm;
Qkidtotm = Q_kid_totm;
Qskitotm = Q_ski_totm;
Qaditotm = Q_adi_totm;
Qrobtotm = Q_rob_totm;
Qluntotm = Q_lun_totm;
Qmustotm = Q_mus_totm;
Qspltotm = Q_spl_totm;
Qyeltotm = Q_yel_totm;
Qheatotm = Q_hea_totm;
Qbratotm = Q_bra_totm;
Qreptotm = Q_rep_totm;
Qredtotm = Q_red_totm;
Qlivem = Q_liv_em;
```

```
Qkidem = Q_kid_em;
Qskiem = Q_ski_em;
Qadiem = Q_adi_em;
Qrobem = Q_rob_em;
Qlunem = Q_lun_em;
Qmusem = Q_mus_em;
Qsplem = Q_spl_em;
Qyelem = Q_yel_em;
Qheaem = Q_hea_em;
Qbraem = Q_bra_em;
Qrepem = Q_rep_em;
Qredem = Q_red_em;
Qlivim = Q_liv_im;
Qkidim = Q_kid_im;
Qskiim = Q_ski_im;
Qadiim = Q_adi_im;
Qrobim = Q_rob_im;
Qlunim = Q_lun_im;
Qmusim = Q_mus_im;
Qsplim = Q_spl_im;
Qyelim = Q_yel_im;
Qheaim = Q_hea_im;
Qbraim = Q_bra_im;
Qrepim = Q_rep_im;
Qredim = Q_red_im;
# Permeability-limitied model (2nd metabolite)
Fam2 = (Q_Fam2 / Intake) * 100;
FDpm2 = (Q_FDpm2 / Intake) * 100;
Qvenm2 = Q_venm2;
Qartm2 = Q_artm2;
Qgutblom2 = Q_gut_blom2;
Qstodism2 = Q_sto_dism2;
QC1dism2 = Q_C1_dism2;
QC2_7dism2 = Q_C2_7_dism2;
Qcoldism2 = Q_col_dism2;
Qbilm2 = Q_bilm2;
QentC1absm2 = Q_ent_C1_absm2;
QentC2_7absm2 = Q_ent_C2_7_absm2;
Qentcolabsm2 = Q_ent_col_absm2;
C1totm2 = C1_totm2;
C2_7totm2 = C2_7_totm2;
Ccoltotm2 = Ccol_totm2;
Qfecm2 = Q_fecm2;
Qstoabsm2 = Q_sto_absm2;
QentC1m2 = Q_ent_C1m2;
QentC2_7m2 = Q_ent_C2_7m2;
Qentcolm2 = Q_ent_colm2;
QGITm2 = Q_GITm2;
Qurim2 = Q_urim2;
Qnepm2 = Q_nepm2;
Qlivtotm2 = Q_liv_totm2;
Qkidtotm2 = Q_kid_totm2;
Qskitotm2 = Q_ski_totm2;
Qaditotm2 = Q_adi_totm2;
Qrobtotm2 = Q_rob_totm2;
Qluntotm2 = Q_lun_totm2;
Qmustotm2 = Q_mus_totm2;
Qspltotm2 = Q_spl_totm2;
Qyeltotm2 = Q_yel_totm2;
Qheatotm2 = Q_hea_totm2;
Qbratotm2 = Q_bra_totm2;
Qreptotm2 = Q_rep_totm2;
Qredtotm2 = Q_red_totm2;
Qlivem2 = Q_liv_em2;
Qkidem2 = Q_kid_em2;
Qskiem2 = Q_ski_em2;
Qadiem2 = Q_adi_em2;
Qrobem2 = Q_rob_em2;
Qlunem2 = Q_lun_em2;
Qmusem2 = Q_mus_em2;
Qsplem2 = Q_spl_em2;
Qyelem2 = Q_yel_em2;
Qheaem2 = Q_hea_em2;
Qbraem2 = Q_bra_em2;
Qrepem2 = Q_rep_em2;
Qredem2 = Q_red_em2;
Qlivim2 = Q_liv_im2;
Qkidim2 = Q_kid_im2;
Qskiim2 = Q_ski_im2;
Qadiim2 = Q_adi_im2;
Qrobim2 = Q_rob_im2;
Qlunim2 = Q_lun_im2;
Qmusim2 = Q_mus_im2;
Qsplim2 = Q_spl_im2;
Qyelim2 = Q_yel_im2;
Qheaim2 = Q_hea_im2;
Qbraim2 = Q_bra_im2;
Qrepim2 = Q_rep_im2;
Qredim2 = Q_red_im2;
# ICRP lung model
A1 = A;
A_T1 = A_T;
A_bnd1 = A_bnd;
I1 = I;
I_T1 = I_T;
I_bnd1 = I_bnd;
LNTH1 = LNTH;
LNTH_T1 = LNTH_T;
LNTH_bnd1 = LNTH_bnd;
BB1 = BB;
BB_T1 = BB_T;
BB_bnd1 = BB_bnd;
BB_seq1 = BB_seq;
BB_seq_T1 = BB_seq_T;
BB_seq_bnd1 = BB_seq_bnd;
bb1 = bb;
bb_T1 = bb_T;
bb_bnd1 = bb_bnd;
bb_seq1 = bb_seq;
bb_seq_T1 = bb_seq_T;
bb_seq_bnd1 = bb_seq_bnd;
ET21 = ET2;
ET2_T1 = ET2_T;
ET2_bnd1 = ET2_bnd;
```

```
ET_seq1 = ET_seq;
ET_seq_T1 = ET_seq_T;
ET_seq_bnd1 = ET_seq_bnd;
LNET1 = LNET;
LNET_T1 = LNET_T;
LNET_bnd1 = LNET_bnd;
ET11 = ET1;
NB1 = NB;
Q_stoI = Q_sto_I;
Q_stoT = Q_sto_T;
Q_C1I = Q_C1_I;
Q_C1T = Q_C1_T;
Q_C2_7I = Q_C2_7_I;
Q_C2_7T = Q_C2_7_T;
Q_colI = Q_col_I;
Q_colT = Q_col_T;
}
```

Appendix 8: Permissions to reprint third-party extracts

02.06.2018

To Whom It May Concern,

I am completing my PhD thesis at Imperial College London entitled 'Developing physiologically-based toxicokinetic models to assess human exposure to brominated flame retardants and herbicides'.

I seek the permission of Dow AgroSciences to reprint in my thesis the extracts that appear in the table appended below.

I would like to include these extracts in my thesis which will be added to Spiral, Imperial's institutional repository http://spiral.imperial.ac.uk/ and made available to the public under a Creative Commons Attribution-NonCommercial-NoDerivs licence.

If you are happy to grant me all the permissions requested, please return a signed copy of this letter. If you wish to grant only some of the permissions requested, please list these and then sign.

Yours sincerely,

Alex Cooper

Alex Cooper

Permission granted for the use requested above:

I confirm that I am the copyright holder of the extract above and hereby give permission to include it in your thesis which will be made available, via the internet, for non-commercial purposes under the terms of the user licence.

Signed: Manoj

Name: MANOJ AGGARWAL

Organisation: DOW AGROSCIENCES

Job title: Toxicologist

Source of work	Name of work	Type of work	Page number	Reprinted extracts to appear in PhD thesis
Nolan R.J., Smith F.A., Muller C.J., et al. (1980). Kinetics of 14C-labeled picloram in male Fischer 344 rats. Unpublished report No. HET K 38323-22 from Dow Chemical Company, Midland, Michigan, USA.	Figure 2: Concentration of radioactivity in the plasma expressed as ug eq 14C-picloram/g following intravenous administration of 14 and 160 mg 14C-Picloram/kg to 3 and 2 rats, respectively.	Figure	31	• rat picloram TK data (Figures 3.12-3.15) • executive summary of study (Section 3.3.6.1)
	Figure 3: Concentration of radioactivity in plasma expressed as ug eq 14C-picloram/g following oral administration of 9.6 and 1634 mg 14C-Picloram/kg.	Figure	32	
	Table 5: Excretion of radioactivity in the urine expressed as MG EQ picloram following administration of 14C-labeled picloram	Table	29	
	Abstract (descriptive summary with conclusions)	Abstract	Front cover	
Nolan R.J., Campbell R.A., Tollett J.T., et al. (1985). DOWCO* 453: Pharmacokinetics in human volunteers following a single oral or dermal dose. Unpublished report No. HET K 131381-037 (document 5.1.5/01, H05) from Dow Chemical Company, Midland, Michigan, USA.	Table 3: Volume and concentrations of creatinine and DOWCO 453 in Urine Specimens collected by male volunteers given 0.1 mg/ Kg oral dose of DOWCO 453	Table	A-3	• human haloxyfop TK data (Figure 4.9) • executive summary of study (Appendix 5 & Table 4.2)
	Table 4: Volume and concentrations of creatinine and DOWCO 453 in Urine Specimens collected by male volunteers given 0.8 mg/ Kg dermal dose of DOWCO 453	Table	A-5	
	Abstract (descriptive summary with conclusions)	Abstract	Front cover	
Nolan R.J., Dryzga M.D., Yano B.L., et al. (1987). Haloxyfop: Pharmacokinetics following oral administration to male Beagle dogs. Unpublished report No. HET K 131381-061 (document 5.1.3/01,H03) from Dow Chemical Company, Midland, Michigan, USA.	Abstract (descriptive summary with conclusions)	Abstract	Front cover	• executive summary of study (Appendix 5 & Table 4.2)
Nolan R.J., Campbell R.A. & Fike R.H. (1991). VERDICT* herbicide field study: quantitation of haloxyfop-methyl absorbed by individuals spraying VERDICT brand herbicide. Unpublished report No. HET M-004570-006 from Dow Chemical Company, Midland, Michigan, USA.	Table 2: Urine volumes and creatinine and haloxyfop concentrations excreted by applicators from Freeland, MI.	Table	17	• human biomonitoring data for haloxyfop (Appendix Figure 5.1) • executive summary of study (Appendix 5 & Table 4.2)
	Abstract (descriptive summary with conclusions)	Abstract	Front cover	
Smith F.A., Hermann E.A., Dryzga M.D., et al. (1982). The pharmacokinetics of 14C-Dowco* 453 in Fisher 344 rats. Unpublished report No. HET K 131381-(26) (document 5.1.1/01, H01) from Dow Chemical Company, Midland, Michigan, USA.	Table 3: Tissue 14C concentrations (ug eq/g plasma) after a single oral dose of 0.1 mg 14C-DOWCO 453/ Kg to male fischer 344 rats.	Table	20	• rat haloxyfop TK data (Figures 5.10-5.12) • executive summary of study (Section 5.3.5)
	Table 4: Tissue 14C concentrations after a single oral dose of 0.1 mg 14C-DOWCO 453/ Kg to female fischer 344 rats.	Table	21	
	Figure 2: Plasma concentrations of 14C activity from female fisher 344 rats administered a 10 mg/kg dose of 14C-DOWCO 453 by either the intravenous or oral route of administration	Figure	24	
	Figure 3: Plasma concentrations of radioactivity from male fischer 344 rats administered a single oral 0.1 mg/kg dose of 14C-DOWCO 453.	Figure	25	
	Abstract (descriptive summary with conclusions)	Abstract	Front cover	
Smith F.A., Kropscott B.E. & Kastl P.E. (1984). The pharmacokinetics of DOWCO* 453 in the B6C3F1 mouse. Unpublished report No. HET K 131381-(26) (document 5.1.2/01, H02) from Dow Chemical Company, Midland, Michigan, USA.	Figure 1: Plasma, liver and kidney concentration of male and female B6C3F1 mice administered a 5 mg/kg dose of 14C-DOWCO 453 by the oral route of administration.	Figure	11	• mouse haloxyfop TK data (Figure 4.8) • executive summary of study (Appendix 5 & Table 4.2)
	Figure 2: Combined male and female urine or feces excretion curves after a 5 mg/kg single oral dose of DOWCO 453 to male and female B6C3F1 mice.	Figure	12	
	Abstract (descriptive summary with conclusions)	Abstract	Front cover	

11.06.2018

To Whom It May Concern,

I am completing my PhD thesis at Imperial College London entitled 'Developing physiologically-based toxicokinetic models to assess human exposure to brominated flame retardants and herbicides'.

I seek your permission to reprint, in my thesis, appropriately referenced extracts from: 'ICRP, 2015. Occupational Intakes of Radionuclides: Part 1. ICRP Publication 130. Ann. ICRP 44(2)'. These extracts are presented in the table appended below.

I would also like to reprint the computer code for the human respiratory tract model (HRTM) and an adapted code for the human alimentary tract model (HATM), using the open source modelling package 'MCSim'.

I would like to include these extracts in my thesis which will be added to Spiral, Imperial's institutional repository http://spiral.imperial.ac.uk/ and made available to the public under a Creative Commons Attribution-NonCommercial-NoDerivs licence.

If you are happy to grant me all the permissions requested, please return a signed copy of this letter. If you wish to grant only some of the permissions requested, please list these and then sign.

Yours sincerely,

Alex Cooper

Alex Cooper

Permission granted for the use requested above:

I confirm that I am the copyright holder of the extracts below and hereby give permission to include it in your thesis which will be made available, via the internet, for non-commercial purposes under the terms of the user licence.

Signed: 藤田 博喜

Name: Hiroki Fujita

Organisation: ICRP

Job title: Assistant Scientific Secretary

Table of extracts from ICRP, 2015. Occupational Intakes of Radionuclides: Part 1. ICRP Publication 130. Ann. ICRP 44(2).

Name of work	Work	Page number	Manner of reproduction
Table 3.1. Regional deposition of inhaled aerosols with an activity median aerodynamic diameter of 5 mm in the Reference Worker* (% of inhaled activity).	Table	62	Within text & computer code
Fig. 3.4. Compartment model representing time-dependent particle transport from each respiratory tract region in the revised Human Respiratory Tract Model.	Figure	65	Copy of figure
Fig. 3.5. Alternative compartment models representing time dependent absorption into blood (dissolution and uptake).	Figure	67	Copy of figure
Table 3.2. Default absorption parameter values for Type F, M, and S materials in the revised Human Respiratory Tract Model.	Table	71	Within text & computer code

7.07.2018

To Whom It May Concern,

I am completing my PhD thesis at Imperial College London entitled 'Developing physiologically-based toxicokinetic models to assess human exposure to brominated flame retardants and herbicides'.

I seek your permission to reprint, in my thesis, extracts from the GastroPlus™ software user's manual (version 8.5). I have attached the relevant section from manual for your convenience. These extracts are presented in the table appended below.

I would also like to reprint *in silico* predictions from ADMET Predictor™, and values generated for physiological model parameters including tissue/ plasma albumin ratios.

I would like to include the extracts in my thesis which will be added to Spiral, Imperial's institutional repository http://spiral.imperial.ac.uk/ and made available to the public under a Creative Commons Attribution-NonCommercial-NoDerivs licence.

If you are happy to grant me all the permissions requested, please return a signed copy of this letter. If you wish to grant only some of the permissions requested, please list these and then sign.

Yours sincerely,

Alex Cooper

Alex Cooper

Permission granted for the use requested above:

I confirm that I am the copyright holder of the extract above and hereby give permission to include it in your thesis which will be made available, via the internet, for non-commercial purposes under the terms of the user licence.

List of permissions granted:

- *in silico* predictions from ADMET Predictor™
- extracts from GastroPlus™ user's manual (specified below)

Signed: John DiBella

Name: John DiBella

Organisation: Simulations Plus, Inc.

Job title: President, Lancaster Division

Table of extracts from GastroPlus™ user's manual (version 8.5)

Name of work	Work	Page number
Perfusion-limited tissue	Figure	186
Permeability-limited tissue	Figure	188
Perfusion-limited kidney	Figure	192
Permeability-limited kidney	Figure	192
ACAT Model Compartments	Figure 4-2	149
Equation for non-eliminating perfusion-limited tissue	Equation 4-53	186
Equation for eliminating perfusion-limited tissue	Equation 4-54	186
Equation for intrinsic tissue clearance	Equation 4-56	187
Equation for whole tissue Vmax	Equation (in text)	187
Equations for permeability-limited tissue	Equations (4-57 to 4-59)	188
Equations for biliary clearance	Equation 4-60 to 4-62	189-190
Equation for fraction unbound in tissue	Equation 4-65	193
Equation for homogeneous Kps	Equation 4-66	193
Equation for conversion of octanol/water partition coefficient to vegetable oil/water distribution coefficient	Equation 4-67	194
Equation for Kp for perfusion-limited tissues	Equation 4-68a	194
Equation for Kp for permeability-limited tissues	Equation 4-68b	194
Berezhkovskiy method of Kp calculation	Equation 4-69	194
Equation to calculate the "corrected" fraction unbound in plasma	Equation 4-78	200
Johnson equation for dissolution rate	Equation 4-3	155
Equation for first-order precipitation	Equation 4-16	159
Equation for absorption rate coefficient	Equation 4-23	163
Equation for passive absorption into the enterocyte subcompartments	Equation 4-24	164
Equation used for theoretical SA/V Model	Equation (in text)	169